VRIJE UNIVERSITEIT

METAL ORIGIN AND FLUID EVOLUTION IN THE ZALDIVAR PORPHYRY COPPER DEPOSIT, CHILE

AN ORTHOMAGMATIC MODEL

ACADEMISCH PROEFSCHRIFT

ter verkrijging van de graad van doctor aan
de Vrije Universiteit Amsterdam,
op gezag van de rector magnificus
prof.dr. T. Sminia,
in het openbaar te verdedigen
ten overstaan van de promotiecommissie
van de faculteit der Aard- en Levenswetenschappen
op donderdag 6 juni 2002 om 13.45 uur
in de aula van de universiteit,
De Boelelaan 1105

door

Eduardo Antonio Campos-Sepulveda

geboren te Talcahuano, Chile

promotor:	prof. dr. J. L. R. Touret
copromotoren:	prof. dr. R. D. Vis (✝)

The achievement of a great result by patient work is the best possible object-lesson for struggling humanity, for the results of genius, however admirable, can rarely be instructive.

El logro de un gran resultado producto del trabajo paciente, es la mejor lección que se puede otorgar a la humanidad luchadora, si bien los genios obtienen logros admirables, estos rara vez resultan instructivos.

Explorer Cap. Robert F. Scott,
Antarctic expedition to the South Pole, 1910.

Dedicated to my dearest
Marcia and María José

The research reported in this thesis was carried out at the

Department of petrology and Department of Isotopic Geology
Faculty of Earth and Life Sciences
Vrije Universiteit Amsterdam
De Boelelaan 1085
1081 HV Amsterdam
The Netherlands

And

PIXE facility
Faculty of Sciences division Physics and Astronomy
Vrije Universiteit Amsterdam
De Boelelaan 1083
1081 HV Amsterdam
The Netherlands

This thesis work was supported by: The Vrije Universiteit Amsterdam, The Netherlands, Universidad de Concepción, Chile and Compañía Minera Zaldívar, Chile.

Netherlands Research School of Sedimentary Geology (NSG) publication no. 20020406

ISBN: 90-807115-1-9

Reading Committee:
Prof. dr. Christoph A. Heinrich (ETH Zentrum, Zürich)
Prof. dr. Paul A. M. Andriessen (Vrije Universiteit, Amsterdam)
Dr. Maria Luce Frezzotti (Universita' Di Siena)
Drs. Ernst A. J. Burke (Vrije Universiteit, Amsterdam)
Dr. Waldo Vivallos (Servicio Nacional de Geología y Minería, Chile)

Cover: Aerial photograpy of the Zaldívar porphyry copper deposit, june 2001, provided by Compañía Minera Zaldívar

Contents

CHAPTER 1
INTRODUCTION

CHAPTER 2
THE ZALDÍVAR DEPOSIT

CHAPTER 3
SAMPLING AND METHODS OF INVESTIGATION

CHAPTER 4
PETROLOGY AND GEOCHEMISTRY

CHAPTER 5
MINERAL INCLUSIONS IN QUARTZ PHENOCRYSTS

CHAPTER 6
MELT INCLUSIONS

CHAPTER 7
MAGMATIC MULTISOLID MS-TYPE FLUID INCLUSIONS

CHAPTER 8
HYDROTHERMAL FLUID INCLUSIONS

CHAPTER 9
TERMOCHRONOLOGY

CHAPTER 10
DISCUSSION OF ANALYTICAL RESULTS

CHAPTER 11
GEODYNAMIC EVOLUTION AND METALLOGENETIC MODEL FOR THE ZALDÍVAR DEPOSIT

APPENDICES

Acknowledgements

First of all I would like to express my deepest gratitude to my promotor prof. dr. Jacques L. R. Touret, for his enthusiasm, motivation, and most of all for bringing numerous original ideas that improved the final outcome of this research. It has been a pleasure and an honor to work with you and with the people of your group at the Vrije Universiteit.

Also thanks to my co-promotor dr. Ronal D. Vis who thought me most of what I now know about the PIXE and who past away in 2000.

I am deeply indebted towards Jan Donner former member of the Vrije Universiteit (VU) and Ricardo Reich from the Universidad de Concepción (UdeC), as they offered me the chance of coming to Amsterdam to carry out PhD research, and made it all possible. Luis Arturo Quinzio is also thanked for his continued support, he made the first contact with the staff from the Zaldívar mine and arranged the first field work. My thanks also to Sergio Quadri, Bernabe Ribas and Santiago Collao from the UdeC for all their support.

Furthermore I would like to thank the members of the reading committee, dr. Maria Luce Frezzotti, prof. dr. Chistoph A. Heinrich, prof. dr. Paul A. M. Andriessen, dr. Waldo Vivallos and drs. Ernst A. J. Burke. I deeply appreciate their interest in my research and their willingness to read the manuscript. Most of all I am very grateful for the discussions and comments that helped to improve the final version.

Compania Minera Zaldívar is thanked for supporting this research, providing access to the mine, drill hole samples, maps and unpublished reports. My appreciation to Jorge Aceituno and Patricio Morales chief geologist and geologist from Zaldívar mine respectively. The geologist Jaime Delgado is especially thanked for guiding me and sharing with me his wide knowledge in the geology of the Zaldívar deposit during field work, and most of all for accepting to be my direct connection with the mine during all these years.

This study would never have been accomplished without the help of many people at the VU. Igor Nikogosian (melt inclusions), Ernst Burke (Raman), Jan Wijbrans (^{40}Ar/^{39}Ar geochronology), Paul Andriessen (zircon fission tracks), Wim Lustenhouwer (electron microprobe and Linkam stage), Saskia Karst (electron microscope and EDS analysis), Wynanda Koot and Bouk Lacet (sample preparation), Ronald Vis, Mark Huisman and Rob van der Geer (PIXE facility), Tineke Vogel-Eisses and Roel van Elsas (mineral separation). Each one of them is here by gratefully acknowledged for their dedication, fruitful comments and efforts to achieve the most out of their techniques.

Thanks to Kees, Frank, Marek, Bin and Gareth. Also I appreciate the friendship from my Dutch colleagues Klaudia and Claudia, Leisellote, Marlees, Peter, Bernd, Margo, Karen, Carlo, Martijn and Onno. Especially to my good friend Yvette for always having time to help me out with the Dutch translations, but most of all for stopping almost everyday at my door just to have a little morning talk. Also to Bart who always found a way to make the Dutch language more difficult for me, “alles kit”. Jurgen, I am indebted to you for the ticket you give me for the Ajax game, please give me the chance to pay you back…..in Chile.

Arnd, thank you very much because you always had the time talk and question my work, which was very helpful to me, I hope soon you will be back in Chile. The same to you Tibor, always ready to listen and make comments, good luck in Antofagsta, and I hope to see you in Concepción. Nina, the other member of the German group, thank you for the conversations, to bad you will miss the promotion.

Glen is thanked for shearing with me countless beers at the borrel every Thursday evening, also for been always there to help me out with my English.

My gratitude to Alex for taking the time to read the whole manuscript whilst on vacation, I really appreciate that.

To the Italian girls Valentina, Giovanna and Barbara for always smiling, and being cheerful, even during time of great stress, thanks for always bringing a good atmosphere with you.

To the French ladies, Stephanie good luck and success in your research. Melanie, I still remember the mussels you made so long ago, thank you for that.

Thanks to my Spanish colleagues Daniel and Conxita. I deeply appreciate the friendship of Jorge and Joaquim, to both of you nothing more than thanks for being such good friends. I am sure that Marcia and María José share the same fillings.

Thanks to my friends outside of the VU, they made our living in The Netherlands much easier, Thomas and Liliana, Luis and Gladys, Rudy and Oini, Marcos and Estela, David.

Valoro profundamente la amistad de mis colegas de la Universidad de Concepción María Mardones, Liuba González, Ramiro Bonilla, Oscar Figueroa, Harry Esterio. Muy especialmente agradezco a Lydia Esparza por su permanente y desinteresado apoyo.

En este último párrafo quiero agradecer a mis padres Rosa y Juan, mamá finalmente tienes un Doctor en la familia. Gracias también a Sergio y Ruth por estar siempre dispuestos a ayudarnos en lo que fuera necesario.

Estos agradecimientos jamás podrían estar completos sin antes dedicar unas líneas en forma muy especial a mis damas, Marcia y María José, ellas han sido parte fundamental de este trabajo por su permanente apoyo, les estaré eternamente agradecidos. A ellas dedico este libro, fruto de un esfuerzo compartido.

I would like to finish this acknowledgment with words from the Chilean poet Pablo Neruda, novel prize winner 1971.

I tell you all: I have come here
to learn from you,
from each one of you, from all,
because what will be the goodness
of the land, for what reason
where made the sea and the roads,
but to go around looking and learning
from all human beings a little…

Samenvatting

De Zaldívar koperporfier (KP) ertsafzetting is gelegen in de Atacama woestijn in Noord-Chili, 5 km ten noorden van het reusachtige Escondida KP ertslichaam. Beide afzettingen zijn even oud, en zijn gevormd in de Laat-Eocene – Vroeg-Oligocene *West Fissure* structurele gordel die meerdere van ‘s werelds grootste KP afzettingen bevat. Deze ertsen staan in verband met eilandenboogmagmatisme dat gekoppeld is aan de subductie van oceanische korst onder de Zuid-Amerikaanse plaat. Door ontwatering van de opgeslokte plaat is magma gevormd dat, na wisselwerking met binnen- en buitenkorst via processen van smelten, assimilatie, opslag en homogenisatie (in het Engels: *MASH*), uiteindelijk op een ondiep niveau is terechtgekomen.

De hier vermelde waarnemingen aan de Zaldívar ertsafzetting ondersteunen de hypothese voor een magmatische bron van de metalen in een KP systeem (orthomagmatisch model). De hypogene mineralisatie is genetisch verbonden met het Llamo porfier, een granodiorietachtig intrusieflichaam met een kristallisatie-ouderdom van 38,7 ± 1,3 miljoen jaar (U/Pb in zirkoon), de jongste intrusieve eenheid die dagzoomt in de mijn.

Kwartsfenokristen in het Llamo porfier begonnen te groeien tijdens de vroege stadia van magmakristallisatie, en zij groeiden door tot in de laat-magmatische stadia. In ieder stadium hebben die fenokristen een verscheidenheid van magmatische en hydrothermale fasen (smelt-, mineraal- en fluïde insluitsels) opgenomen die behulpzaam zijn bij de reconstructie van de complexe opeenvolging van magmatische en post-magmatische gebeurtenissen tijdens de evolutie van dit porfiersysteem.

Het belangrijkste magmatische stadium is vertegenwoordigd door goed bewaarde smeltinsluitsels en even oude hoge-temperatuur fluïde insluitsels met talrijke dochtermineralen (Engels: *multisolid inclusions, MS*). De samenstelling van de smeltinsluitsels, verkregen van snel afgekoeld glas na verhitting tot 1100°C, wijst op een SiO_2-rijke rhyolietachtige samenstelling met een hoog tot zeer hoog kopergehalte (0,03 tot 0,50 gewichts-%). De hoogste koperwaarden (tot aan 1,5 gewichts-%) zijn gemeten in insluitsels met zwarte stippen die bestaan uit druppels van koperchloride. Bij kamertemperatuur bevatten de *MS* insluitsels alleen gas en een complex aggregaat van vaste fasen. Deze vaste fasen smelten geleidelijk weg bij verhitting, samengaand met de vorming van vloeistof. De laatste vaste fase verdwijnt tussen 300 en 550°C, en de dan tweefasige (vloeistof/gas) insluitsels homogeniseren pas bij een waarlijk magmatische temperatuur, tot aan 1000°C. *In situ*, niet-destructieve, kwalitatieve analysen met PIXE hebben aangetoond dat de ingesloten fluïda zeer dichte chloridenzoutoplossingen zijn, vooral van Na, K, Fe, Cu, Mg en Mn. Zij vertegenwoordigen de eerste fluïda die uit het moedermagma gestoten zijn, ver vóór het einde van de magmatische kristallisatie.

Deze resultaten bewijzen dat het moeder-intrusieflichaam de belangrijkste bron van koper is. Het nauwe verband tussen koper en chloor in de smelt- en *MS*-insluitsels geeft bovendien aan dat de metalen in een zeer vroeg stadium van de evolutie van het porfier van het kristalliserende magma afgescheiden zijn, in de vorm van chloridenrijke oplossingen.

Het magmatische stadium werd gevolgd door een belangrijk magma-gerelateerd hydrothermaal systeem, dat gekarakteriseerd is door overvloedige, gelijktijdig bestaande, hoogsalinische en gasrijke waterige fluïde insluitsels. PIXE analysen van de zoutoplossingen wijst ook op de aanwezigheid van Fe, Cu, Mg en Mn, waarschijnlijk als aanwijzing dat deze fluïda de oorspronkelijke, magmatische mineralisatie herverdeeld hebben.

De homogenisatietemperatuur van deze insluitsels varieert sterk (600 – 250°C), maar een groot kookevenement heeft plaatsgevonden bij 400°C op een diepte van 1.5 km. De globale samenstelling van deze post-magmatische waterige fluïda ontwikkelde zich van een complex Na-Cl-K-Fe-H_2O systeem naar een eenvoudiger Na-Cl-Fe-H_2O systeem. De jongste fluïda in het Zaldívar gebied zijn lage-temperatuur (< 200°C) insluitsels van bijna zuiver water, zeer waarschijnlijk van een hydrothermaal systeem dat overheerst werd door grondwater. Deze jongste fluïda schijnen niet bijgedragen te hebben aan de mineralisatie.

^{40}Ar/^{39}Ar thermochronologie aan biotiet van het Llamo porfier toont aan dat de meeste van de bestudeerde monsters ongeveer 35,5 miljoen jaar geleden afgekoeld zijn tot onder de afsluitingstemperatuur van biotiet (~ 350°C); bovendien houden de betrouwbare plateau-ouderdommen in dat een nieuwe verhitting later nooit heeft plaatsgevonden. Omdat de afsluitingstemperatuur van biotiet voor het ^{40}Ar/^{39}Ar systeem sterk overeenkomt met de onderste temperatuurwaarden gevonden in de aan magma gerelateerde hydrothermale fluïda (~ 350°C), vertegenwoordigen de ^{40}Ar/^{39}Ar ouderdommen het einde van het belangrijkste mineraliserende hydrothermale systeem.

De kristallisatie-ouderdom van 38,7 ± 1,3 miljoen jaar (U/Pb in zirkoon) eerder bepaald aan het Llamo porfier, alsmede de ^{40}Ar/^{39}Ar ouderdommen en de microthermometrie gegevens verkregen in de voorliggende studie, versterken de opvatting dat de tijdsspanne tussen de kristallisatie van de porfierachtige intrusieflichamen en het ophouden van de belangrijkste gebeurtenis van mineralisatie/verwering in de Zaldívar ertsafzetting 1 tot 2 miljoen jaar bedragen heeft. Tenslotte geven de uniforme ouderdommen van ongeveer 29 miljoen jaar, bepaald met splijtsporen in zirkoon, het tijdstip aan waarop het hele Zaldívar complex afkoelde tot onder ~ 250°C.

Abstract

The Zaldívar porphyry copper deposit (PCD) is located in the Atacama Desert of Northern Chile, 5 km north of the giant Escondida PCD. Both deposits are coeval and are emplaced within the Late Eocene-Early Oligocene West Fissure Structural Belt that includes several of the world's largest PCDs. These deposits are associated with arc magmatism related to the subduction of oceanic crust beneath the South American plate. The magmas generated by dehydration of the subducted slab interacted with the lower and upper crust through processes of melting, assimilation, storage and homogenization (MASH) until they were finally emplaced at shallow levels.

The observations on the Zaldívar deposit reported here support the hypothesis of a magmatic source of metals in a porphyry copper system (orthomagmatic model). The hypogene mineralization is genetically related to the Llamo intrusive, that shows a crystallization age of 38.7 ± 1.3 Ma (U/Pb in zircon), representing the youngest intrusive unit outcropping in the mine.

Quartz phenocrysts in the Llamo intrusive started to grow during the early stages of magma crystallization, and their growth continued until the late-magmatic stages. In each stage they have trapped a variety of magmatic and hydrothermal phases (melt, mineral and fluid inclusions) that are helpful to reconstruct the complex succession of magmatic and post-magmatic events related to the evolution of this porphyry system.

The main magmatic stage is represented by well-preserved melt inclusions and contemporaneous high-temperature multisolid fluid inclusions (MS). The composition of melt inclusions, obtained from quenched glasses after heating to 1100°C, indicates a silica-rich rhyolitic composition with a high to very high copper content (0.03 to 0.50 wt %). The highest copper values (up to 1.5 wt %) were measured in inclusions showing black dots consisting of Cu-chloride droplets.

At room temperature, MS inclusions contain only gas and a complex aggregate of solid phases. These solid phases dissolve progressively upon heating, with concomitant liquid formation. The last solid dissolves between 300° and 550°C, and the biphase (liquid/vapor) inclusions homogenize at truly magmatic temperatures, up to 1000°C. *In-situ*, non-destructive qualitative compositional analyses by PIXE have shown that the trapped fluids are dense chloride brines dominated by Na, K, Fe, Cu, Mg and Mn. They represent the first fluids expelled from the parental magma, well before the end of the magmatic crystallization.

These results show that the parental intrusive represents the main source of copper. Furthermore, the close copper-chlorine association in the melt and MS-inclusions indicates that the metals were separated from the crystallizing magma at a very early stage of the porphyry evolution, in the form of chloride-rich solutions.

The magmatic stage was followed by an important magma-related hydrothermal system, characterized by abundant coexisting high-salinity and vapor-rich aqueous fluid inclusions. PIXE analysis of the brines also indicates the occurrence of Fe, Cu, Mg and Mn in solution, probably indicating that these fluids redistributed the initial, magmatic mineralization.

Homogenization temperatures cover a wide range (600° - 250°C), but a major boiling event could be identified at about 400°C and 1.5 km depth. The overall compositions from these post-magmatic aqueous fluids evolved from a complex Na-Cl-K-Fe-H_2O to a more simple Na-Cl-H_2O system.

The latest fluids identified in the Zaldívar area are characterized by low-temperature (<200°C), almost pure water aqueous fluids, most likely a hydrothermal system dominated by groundwater. This latest fluid does not seem to have contribute to the mineralization.

$^{40}Ar/^{39}Ar$ thermochronology of biotite from Llamo porphyry indicates that most of the studied samples cooled through the biotite closure temperature (~350°C) about 36.5 Ma ago; in

addition the homogeneous plateau ages imply that later reheating has never occurred. As the closure temperature for the $^{40}Ar/^{39}Ar$ system in biotite is closely similar to the lower temperature values defined in the magma-related hydrothermal fluids (~350°C), the $^{40}Ar/^{39}Ar$ ages represent the termination of the main mineralizing hydrothermal system.

The 38.7 ± 1.3 Ma crystallization age (U/Pb in zircon) previously defined for the Llamo porphyry, in combination with $^{40}Ar/^{39}Ar$ ages and microthermometry data obtained in the present study, reinforce the conception that the timespan between the crystallization of the porphyritic intrusives and the ceasing of the main mineralization-alteration event at the Zaldívar deposit was not longer than 2 Ma. Finally, the uniform zircon fission-track ages of about 29 Ma for the Zaldívar deposit indicate the time when the whole site cooled below ~250°C.

Resumen

El pórfido cuprífero Zaldívar se ubica en el desierto de Atacama del norte de Chile, a unos 5 kilómetros al norte del mega yacimiento de cobre Escondida. Ambos depósitos son contemporáneos y se emplazan dentro de la franja estructural falla Oeste de edad Eoceno Superior-Oligoceno Inferior, a la cual se asocian algunos de los mayores pórfidos cupríferos a escala mundial.

Los yacimientos tipo pórfido cuprífero se encuentran genéticamente relacionados al magmatismo de arco asociado al proceso de subducción de la corteza oceánica bajo la placa continental. Los magmas generados por deshidratación de la placa subductada, interactuan con la corteza inferior y superior mediante procesos de fusión parcial, asimilación, almacenamiento y homogeneización (MASH, por sus siglas en ingles), hasta que son finalmente emplazados a poca profundidad en la corteza superior.

El yacimiento Zaldívar, presenta una serie de evidencias que soportan la hipótesis de un origen magmático para los metales en depósitos tipo pórfido cuprífero (modelo ortomagmático) En primer termino, la mineralización hipógena se encuentra genéticamente relacionada al pórfido Llamo, que presenta una edad de cristalización de 38.7 ± 1.3 Ma (U/Pb en circones), y constituye el intrusivo más joven que aflora en la mina.

Los fenocristales de cuarzo en el pórfido Llamo, comenzaron a desarrollarse durante las etapas tempranas de cristalización magmática, y su formación prosiguió de manera continua hasta las etapas magmáticas tardías. En cada etapa estos fenocristales atraparon una variedad de remanentes magmáticos e hidrotermales (inclusiones vítreas, inclusiones minerales e inclusiones fluidas) los cuales permiten caracterizar eventos magmáticos y postmagmáticos relacionados con la evolución de este sistema porfídico.

La etapa magmática principal está representada por inclusiones vítreas e inclusiones fluidas multi-sólidas (MS) de alta temperatura, aparentemente contemporáneas. La composición de las inclusiones vítreas, obtenida de vidrios sobre enfriados (quenched) luego de ser calentados hasta 1100°C, indican una composición riolítica rica en sílice con altos contenidos de cobre (0.03 a 0.50 % en peso). Los valores más elevados de cobre (hasta 1.5 % en peso) se midieron en vidrios que contenían microinclusiones cuya composición corresponde a Cu+Cl.

A temperatura ambiente, las inclusiones tipo MS contienen una burbuja y múltiples fases sólidas, estas últimas se disuelven progresivamente al calentar la inclusión, y simultáneamente aparece un volumen creciente de líquido. El último sólido se disuelve entre los 300° y 550°C, y la inclusión ahora bifásica (líquido/vapor) homogeneiza a temperaturas magmáticas, hasta 1030°C.

Análisis composicionales cualitativos no destructivos, realizados en inclusiones tipo MS mediante PIXE, han mostrado que los fluidos atrapados en estas inclusiones corresponden a densas salmueras cloruradas ricas en Na, K, Fe, Cu, Mg y Mn. Estos salmueras representan los primeros fluidos en ser separados del magma parental, mucho antes de finalice la cristalización del magma.

Los resultados obtenidos demuestran que el intrusivo parental representa la fuente principal de cobre. Más aún, la estrecha relación cobre-cloruro en las inclusiones vítreas y del tipo MS, indican que los metales fueron separados como soluciones cloruradas en una etapa temprana de la cristalización magmática durante la evolución del sistema porfídico Zaldívar.

Luego de la etapa magmática, en el yacimiento se produce una intensa actividad hidrotermal relacionada al enfriamiento del magma parental, los fluidos hidrotermales se encuentra bien caracterizados por abundantes inclusiones fluidas de alta-salinidad y otras ricas en gas, las cuales son coexistentes. Análisis cuantitativos de las inclusiones salinas muestran la ocurrencia de Fe, Cu, Mg y Mn en solución, probablemente una indicación de que estos fluidos redistribuyeron la mineralización magmática inicial.

Las temperaturas de homogeneización de las inclusiones fluidas hidrotermales presentan un amplio rango, sin embargo, un evento de ebullición mayor se ha definido alrededor de los 400°C a una profundidad de 1.5 km. La composición general de estos fluidos acuosos postmagmáticos evolucionó desde un sistema complejo tipo Na-Cl-K-Fe-H_2O a uno más simple tipo Na-Cl-H_2O.

Los fluidos hidrotermales tardíos identificados en el área de Zaldívar corresponden a agua prácticamente pura y de baja temperatura (< 200°C). Este sistema hidrotermal muy probablemente se encontraba dominado por agua meteórica y aparentemente no tienen relación alguna con la mineralización.

Dataciones $^{40}Ar/^{39}Ar$ en biotitas en el pórfido Llamo, indican que la mayoría de las muestras estudiadas se enfriaron bajo la temperatura de cierre de este sistema isotópico (ca. 350°C) hace unos 36.5 Ma además, los plateaus de edades resultan bastante homogéneos lo que implicaría que no ha ocurrido un recalentamiento con posterioridad a esa edad. Al ser la temperatura de cierre para el sistema $^{40}Ar/^{39}Ar$ en biotitas muy similar a las temperaturas menores definidas para el evento hidrotermal principal (ca. 350°C), las edades $^{40}Ar/^{39}Ar$ se relacionan directamente con el cese de la mineralización asociada a este sistema hidrotermal.

La edad de cristalización definida para el pórfido Llamo (38.7 ± 1.3 Ma), en combinación con las edades $^{40}Ar/^{39}Ar$ y los datos de microtermometría obtenidos en el presente estudio, refuerza el concepto de que el tiempo transcurrido entre la cristalización del intrusivo porfídico y el término del evento principal de mineralización-alteración en el yacimiento Zaldívar, no fue superior a 2 Ma. Finalmente, las edades de 29 Ma definidas por trazas de fisión en circón, indican el momento a partir del cual el yacimiento Zaldívar se enfrió por debajo de los ~250°C.

Chapter 1

Introduction

1.1 Introduction

Porphyry copper deposits (PCDs) are among the most notable ore deposits in the world from the viewpoint of size and/or grade. They represent the world's largest accumulations and principal resource of Cu and Mo, and because of the engineering amenability they can be mined on a large scale with low-cost extractive methods. Several PCDs are the basis of some of the world's largest mining operations (e.g., Chuquicamata, El Teniente, both located in Chile). These deposits occur in a series of extensive, narrow, linear metallogenic provinces throughout the world. Chile being one of the most important countries for this type of mineralization in the Andes of South America.

For decades, PCDs have been extensively researched, as a consequence the knowledge of general processes of ore formation are well understood, however the comprehension of some key particular processes such as the origin of metals and metal-bearing fluids is far from complete. To explain the provenance of copper and other metals two contrasting theories have been proposed, one is the hydrothermal model (e. g., Norton, 1978; Cathles, 1977) which suggest that a major part of the metals are scavenged from the surrounding rocks by a convective fluid system, initiated and sustained by the heat of the intrusion. The second correspond to the orthomagmatic model (e.g., Fournier, 1967; Henley and McNabb, 1978), which proposed that parental magmas are the primary source of metals and volatile components. Metals are brought near the surface by "fertile" magmas originated by dehydration of the subducted slab (e.g., Sillitoe, 1972; Sawkins, 1984), metals can later be redistributed by related late-magmatic hydrothermal processes.

Because the combined effects of magmatic and hydrothermal processes, eventually overprinted by supergene events, produce PCDs, any remaining features of the early magmatic evolutionary stages are difficult to find as normally they are strongly overprinted by subsequent events. However, because quartz phenocrysts are most frequently not affected by hydrothermal or supergene alteration, this mineral will potentially be the most adequate source of well-preserved magmatic remnants that can provide information on the primary magmatic processes involved in the generation of PCDs.

The aim of this investigation is to provide direct evidence that would more rigorously relate magmatic processes with the origin of metals in porphyry copper systems. Also to investigate the mechanism by which those metals are sequestered from the crystallizing magma, and to characterize the composition of early magmatic fluids exsolved from the cooling parental intrusive body before they subsequently evolved towards mineralizing hydrothermal solution.

It will be also important to characterize the compositional evolution of magma-related hydrothermal mineralizing fluids, and to evaluate the possibilities of defining the timescale for hydrothermal processes.

1.2 Outline of the thesis

Following this introductory chapter, the thesis is structured into eleven chapters, each concentrating in a different aspect of the study. Supplementary information such as geochemical and microthermometry data are provided in the Appendices.
The chapters have the following subjects:

Chapter one gives an introduction to study and the aims of the present research, it also summarizes the knowledge of porphyry copper deposits including some basic concepts such as tectonic and geological settings, global and temporal distribution, and the origin of fluids and metals. Special attention is given to the relationship between hydrothermal alteration and mineralization. This chapter ends with a short discussion on the distribution of porphyry coppers deposits in Chile.

Chapter two begins with a literature study that introduces the reader into the regional geological setting of the Zaldívar porphyry copper deposit. Then a detailed geological description is given for the Zaldívar mine.

Chapter three presents an overview of the sampling procedure and sample preparation. Also describe the different analytical techniques and procedures utilized during this study.

Chapter four contains a detailed petrographic description of the samples collected at Zaldívar mine as well as whole rock major elements geochemistry for each unit rock outcropping in the mine area.

Chapter five investigate the composition of mineral inclusions hosted in quartz phenocrysts by EMP analysis, also characterize by microthermometry the brines that appears closely associated to the mineral inclusions.

Chapter six presents the characterization of melts inclusions trapped in igneous quartz phenocrysts and provides microthermometric data as well as major element composition of quenched glasses. Microthermometry of melt inclusions was carried out in a heating/quenching stage, and quenched glass composition was defined by electron microprobe.

Chapter seven defines and characterizes the multisolid fluid inclusions (MS-type) with a major emphasis in the microthermometry and chemical composition of the trapped fluids. To better characterize the MS inclusions, several analytical techniques were used including heating/quenching stage, cooling/heating stage, PIXE, RAMAN and SEM microanalysis, and EDX analysis.

Chapter eight deals with the characterization, microthermometry and compositional study of aqueous fluid inclusions related to the main and late hydrothermal event in the Zaldívar ore deposit. Aqueous fluid inclusions were characterized by means of microscopic observation and microthermometry on a cooling/heating stage. PIXE, RAMAN and SEM microanalysis defined qualitative chemical compositions.

Chapter nine explores the timescale involved in the genesis of the Zaldívar porphyry copper deposit. In this chapter ^{40}Ar/^{39}Ar isotope systematics are used to date magmatic biotite phenocrysts that may shed light on the date of late-magmatic events. This chapter also presents the fission track dating methods and concepts used for age calculation, calibration and interpretation.

Chapter ten provides an overview of the data obtained during this study, discusses their implications of the genesis of the ore deposit and draw some general conclusions based on their interpretation.

Chapter eleven describes the geodynamic evolution in the area of the Zaldívar deposit and the distinguishing features that characterize Llamo porphyry. This chapter concludes with the presentation of a model for the evolution of the Zaldívar porphyry copper deposit.

1.3 An overview of porphyry copper deposits

1.3.1 Introduction

Because PCDs represent an important economic resource and are major exploration and exploitation targets, they have been a principal subject for intensive and extensive scientific and engineering research during the last 30 years. The investigation and exploration efforts have produced an enormous collection of papers on the geology of PCDs around the world, which have been summarized in the noteworthy works of Titley and Hicks (1966), Lowell and Guilbert (1970), Sillitoe (1973), Gustafson and Hunt (1975), Gustafson and Titley (1978), Einaudi et al., (1978), Gustafson (1978), and Titley and Beane (1981), among others.

The aim of this chapter is to provide a descriptive overview of PCDs, remarking all those features that are relevant to their general understanding. The review is largely based on the papers from the authors mentioned above.

1.3.2 Definition

PCDs are large-tonnage, generally low-grade metal deposits formed by large hydrothermal systems that show a physical-geochemical continuum from late-magmatic, mesothermal temperatures, to ‘conventional’ hydrothermal conditions (temperatures between 350° and 650°C). The grade of primary mineralization in a typical PCD is up to 0.8 wt % Cu and 0.02 wt % Mo, and the orebody is always related to a porphyritic igneous intrusion of intermediate composition which is passively emplaced and subsequently cooled at shallow crustal levels (depths of 2 to 8 km). The primary sulfide mineralization comprises of significant amounts of pyrite and chalcopyrite, with minor amounts of molybdenite and bornite. Other elements such as Pb, Zn, Au, and Ag may eventually have economically important concentrations. The mineralization may occur as disseminations, stockworks, and breccias and may be confined to the inferred source plutons and/or in their immediate wall rocks.

The deposits are generally large, on the scale of several hundred to a few thousand meters across, relatively homogeneous and commonly roughly equidimensional. The plutons to which the mineralization is related are commonly small - ½ to 1 km in diameter – but the effect of their emplacement produces hydrothermal solutions, which originate the alteration, and mineralization that involve large volumes (many cubic kilometers) of host rocks. The evolutionary path of the hydrothermal process is dominated by cooling and results in the precipitation and zoning, in roughly concentric patterns, of both alteration mineral assemblages and ore minerals. The composition and patterns of alteration and mineral distribution, however, are strongly controlled by the wall-rock composition.

1.3.3 Tectonic setting

The tectonic setting for PCDs corresponds to arc systems associated with subduction processes on destructive plate boundaries dominated by a compressional tectonic regime with high rates of uplift and exhumation during intrusion and mineralization. Worldwide, most deposits occur in linear calc-alkaline volcano-plutonic arcs of present or former orogenic belts, they are emplaced on the overriding continental crust, above the Benioff zone, along convergent plate margins (Fig. 1-1). In fact, more than half of the known deposits occur in two west-facing continental arc systems, the Andes, beneath which subduction continues today, and the inactive arcs of the Western Cordillera in North America. A smaller number of deposits are also present in orogens that have developed into continent-continent collisions.

In general, their distribution is apparently controlled by factors such as distance from the trench, distribution of faults transverse to the orogenic belts, total thickness of the crust, and the chance results of erosion or burial.

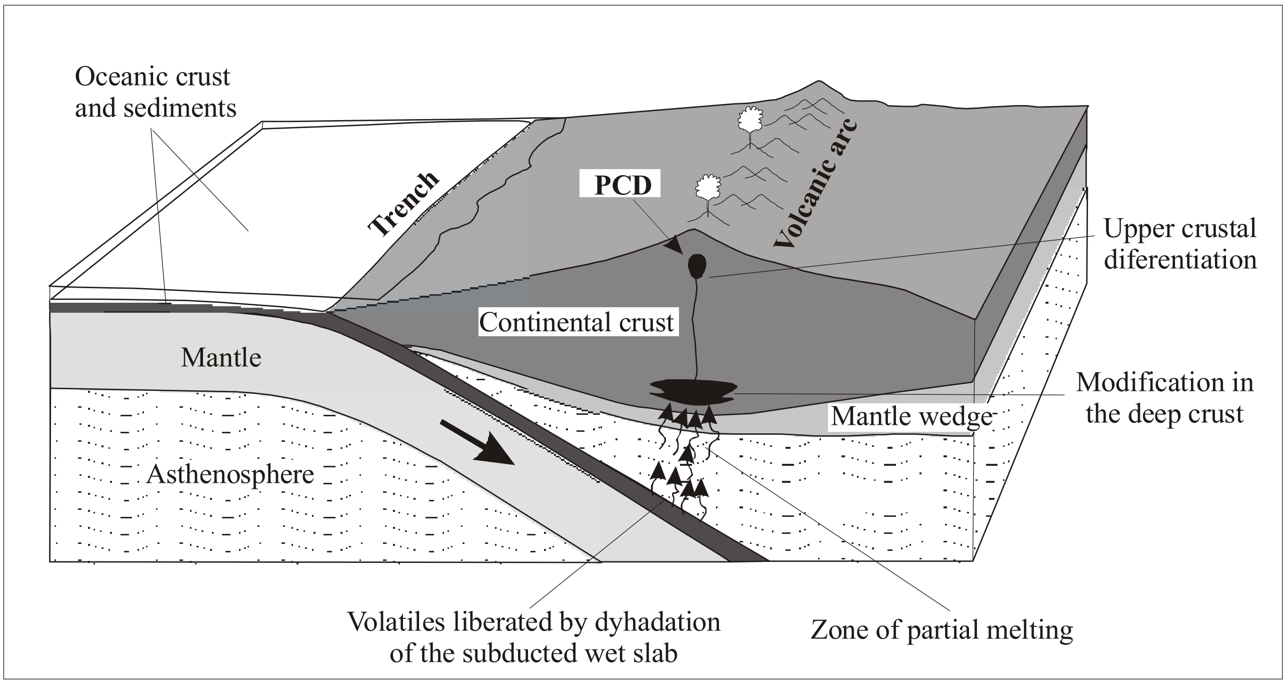

Figure 1-1 Tectonic setting of porphyry copper deposits. Modified after Davidson et al. (1991).

1.3.4 Global and temporal distribution

PCDs occur principally within Mesozoic and Cenozoic terrains, less commonly in pre-Mesozoic mountain belts or their eroded roots (Fig. 1-2), becoming increasingly rare with age (Fig. 1-3). Mesozoic and younger PCDs occur mostly around the Pacific Rim, displaying an episodic age distribution, which coincides with variations in the intensity of magmatism along this belt. An important episode of PCD generation took place from 74 to 48 Ma ago in the Cordillera of North America (Fig. 1-3). In the Andean Province of South America, the age for most of the deposits ranges from ca. 50 to 3.0 Ma. The youngest episode of PCDs mineralization took place in the southwestern Pacific Island arcs (Fig. 1-3).

Within the Late-Paleozoic/Mesozoic mountain belts, these deposits are found in the northern Appalachian orogen from Maine to Quebec, with deposits of Cambrian-Ordovician and Devonian-Carboniferous ages. This orogen is a continuation of the Caledonian Province of the British Islands where this type of mineralization has been found in North Wales (Cambro-Ordovician) and Scotland (Devonian). Paleozoic deposits are also recognized in the Tasman belt of eastern Australia, in Kazakhstan, the Caucasus, Uzbekistan and the Batenevski range in Siberia. The majority of the latter deposits show peak abundance during the Carboniferous.

PCDs seem to be less frequent in the Early Paleozoic and Precambrian belts, perhaps because of diminishing chances of survival due to destruction by erosion or concealment by burial. However, a more fundamental cause for the seeming lack of really old deposits may be due to changes in the mechanism of plate tectonics. PCDs are formed at convergent boundaries during plate tectonics. The evidence for relative plate motions in the Archean and Early Proterozoic areas is not clear and it seems likely that planetary mechanisms were different then in degree or kind. As a consequence, if PCDs did form in the Precambrian, they may have been essentially different because of different tectonic regimes. Although survival in a recognizable form would be low because of the likelihood of their being subjected to strong deformation and metamorphism, their existence therefore is a matter of conjecture.

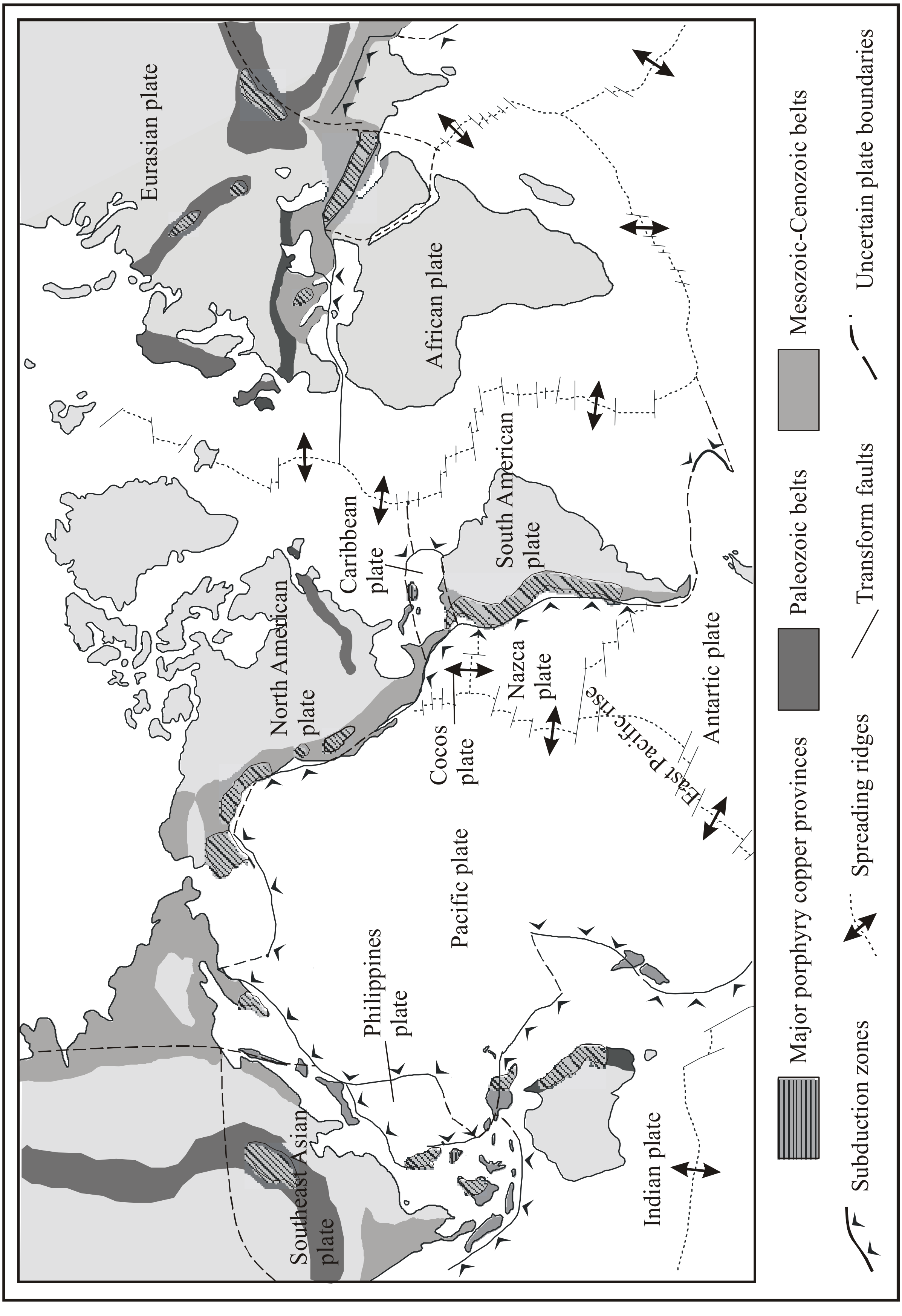

Figure 1-2. Global distribution of porphyry copper provinces and related mountain belts. Modified after Sawkins (1984).

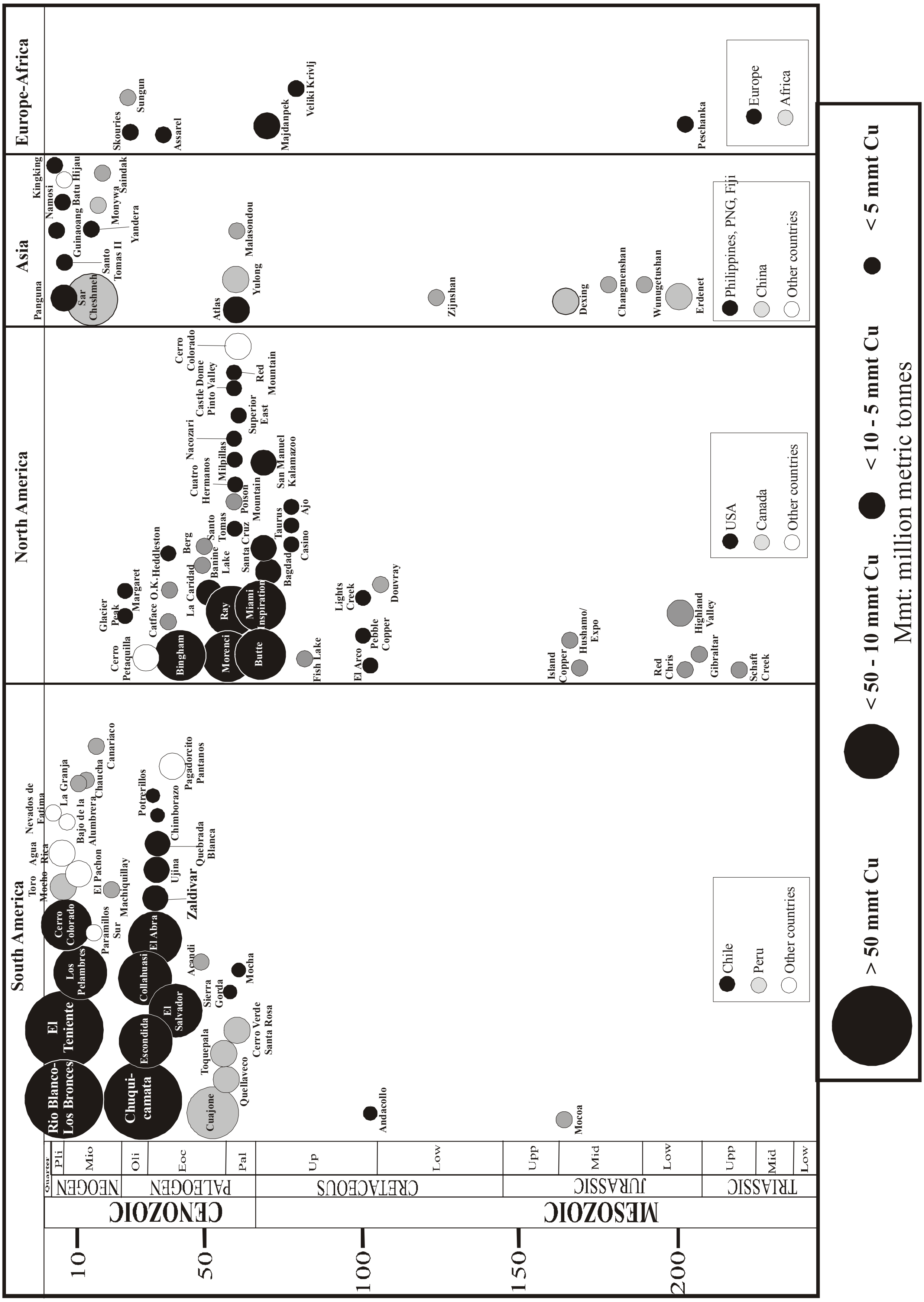

Figure 1-3. Age distribution and tonnage (million metric tons of copper) of porphyry copper deposits around the world. Modified after Einaudi (1997).

1.3.5 Geological setting

The PCDs occur in areas displaying a complex geological evolution that includes multiple episodes of faulting, deformation and uplifting, as well as many intrusive events. Despite the complexity of the regions in which these deposits occur, regional studies have revealed that PCDs around the world share many common characteristics like similar tectonic and geological settings, and corresponding evolutionary histories.

1.3.5.1 Host rocks

The spatial and temporal association of mineralization with intrusions is indicated mainly by the distribution of alteration and mineralization, which is centered, either symmetrically or asymmetrically, on porphyry intrusions or their contacts. A major problem in determining the primary rock composition in the intrusive units associated with PCDs results from the strong and widespread hydrothermal and supergene alterations that mask the composition of these rocks. Nevertheless, it has been stated that hypabyssal epizonal igneous centers, to which the copper mineralization is genetically related to, do not necessarily exhibit a simple or typical rock composition. The intrusion centers may range from small (less than 1 km in diameter) to large (more than 5 km in diameter). As they increase in size, there is a tendency to consist of multiple intrusive events that may comprise a broad compositional range and textural variation from coarse phaneritic to distinctly porphyritic.

Most frequently, the porphyritic-textured stock is genetically linked to the copper mineralization and is commonly the host for a significant proportion of the ore. This stock is inferred to grade downwards into stockwork mineralization and potassic alteration hosted in a phaneritic intrusive, which in turn is transitional downwards to an essentially unaltered pluton of similar composition and of considerably larger dimensions than the stock. Therefore the porphyritic stock may be linked to cupola-like projections on the upper surface of large plutons, which is emplaced in a subvolcanic environment, closely associated with subaerial calc-alkaline volcanism. The stock usually appears to be passively rather than forcefully emplaced at relatively shallow crustal levels (2 to 8 km in depth).

PCDs are associated to rocks of different compositions, each one typical for a given tectonic setting. The calcic-diorite seems typical of island-arc magmatic systems developed on oceanic crust. Calc-alkaline and alkali-calcic granodiorite to quartz monzonite systems develop in conventional magmatic arcs over subduction zones in continental margin settings. The source of these plutonic rocks is most probably the subjacent mantle, and their generation is closely tied to the subduction process.

1.3.5.2 Wall-rock petrology

The mineralized stock is normally emplaced on or above an older, but probably genetically related larger pluton, sometimes of batholith size. When the stock is emplaced outside of the major intrusive body, it also may at different levels be in contact with much older, genetically unrelated formations comprising a variety of wall rocks of different composition.

The pre-intrusion host rocks include a wide variety of lithologies, from coeval volcanics in some instances through older clastic or even crystalline basement rocks in others. Although the most common situation involves volcanic rocks slightly older than the intrusive, some of the older deposits may show an association with Precambrian metamorphic and intrusive rocks. Contacts with the pre-intrusion host rocks are generally sharp with little structural disturbance and abundant dykes and sills often project outward from the stock.

1.3.5.3 Structures

The emplacement of a PCD occurs in an open system with large-scale introduction of both magmas and hydrothermal solutions along structural breaks resulting from the stress applied both by regional forces and localized magmatic forces into the host rock. This does not necessarily imply that mineralized fluids are vented to the surface during early mineralization stages.

Major zones of fracturing generated by regional forces seem to have been strongly important in controlling the location and shape of igneous intrusions, suggesting that plutons penetrate continental crust along deep fractures; in fact several deposits are developed at the intersection of marked lineaments. Some of these fractures may correspond to reactivated older faults, while others were possibly initiated during subduction by strike-slip movements that are parallel to the trench.

The formation of characteristic porphyry crackled breccia, radial-concentric veins and micro-veins that usually form the stockwork mineralization is evidence of magmatic forces produced especially during retrograde boiling of residual liquids in the largely consolidated igneous rock.

Porphyry style mineralization is also associated with collapse breccia and hydrothermal breccia structures that form irregular bodies of “pebble” dikes and well-defined tourmaline breccia pipes.

The shifting location of intrusive centers and major zones of fracture permeability during the evolution of hydrothermal activity is the major factor controlling whether the resultant mineralization-alteration is concentric or asymmetric.

1.3.5.4 Hydrothermal alteration

Hydrothermal alteration in PCDs results from water rock interaction between the hydrothermal fluids and the host rocks, resulting in different types of alteration assemblage depending on the extent and chemical character of the metasomatism. Major differences of the mineral assemblage in different deposits will also relate primarily to differences in host-rock composition. The metasomatic alteration may range from selective (replacement of specific minerals), to pervasive (complete conversion of all primary minerals).

Open fractures, by which the hydrothermal solutions will move through a mass of rock, are of primary importance to the alteration process. In PCD systems, fractures are widespread and occur at all scales. They seem to begin forming at a very early stage of pluton cooling, and continue to be produced intermittently at various times and places during the life of the hydrothermal system, as is indicated by sets of intersecting cracks, of which successive generations commonly results in different alteration assemblages.

Models of PCD zoning illustrate the dominant tendency for concentric cylindrical shells of alteration in alumino-silicate rocks, the porphyritic intrusion generally being the controlling feature for the alteration pattern (Fig. 1-4).

The hydrothermal alteration zoning comprises a central potassic zone located in or near the porphyritic intrusion (Fig. 1-4), which is caused by K metasomatism and the leaching of Ca and Na from all aluminosilicate minerals. The K-feldspar-biotite-quartz mineral assemblage characterizes the potassic zone and the minerals can either be secondary or stable primary phases. Accessory minerals are albite, sericite, anhydrite, carbonates and apatite. K-feldspar always occurs with quartz-filling veinlets and/or replacing primary alkali feldspars to varying degrees. Primary biotites generally altered to a more magnesian variety and sericite is scarce and usually does not replace secondary K-feldspar or biotite.

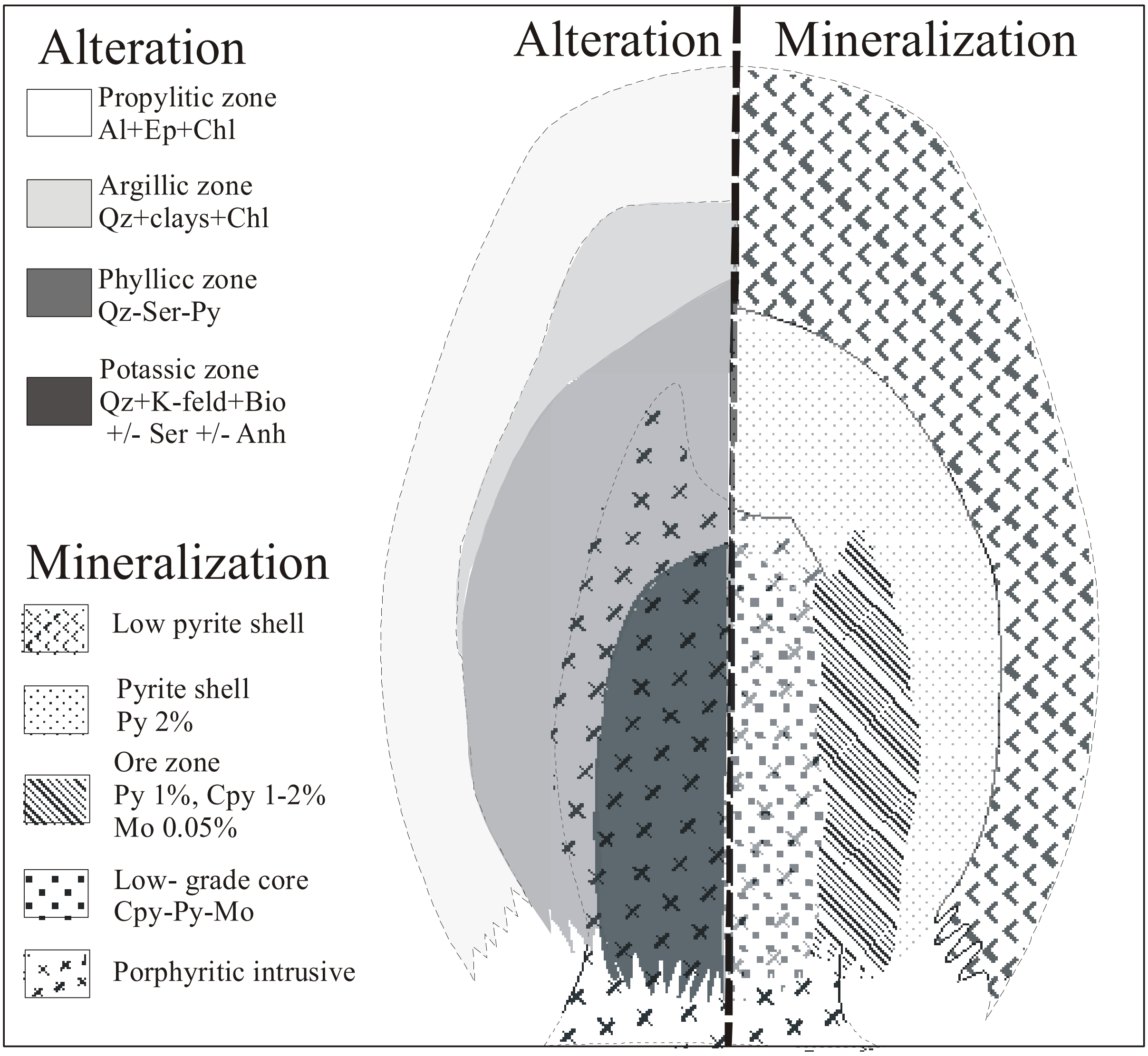

Figure 1-4. Schematic illustration of mineralization and alteration zones in a generalized model of a classic-type porphyry copper deposit. After Lowell and Guilbert (1970), and Bean and Titley (1981). Al: albite, Ep: epidote, Chl: chlorite, Qz: quartz, Ser: sericite, Biot: biotite, Ahn: anhydrite, K-feld: K-feldspar, Py: pyrite, Cpy: Chalcopyrite, Mo: molybdenite.

The potassic core is surrounded and to some extent overlapped by a peripheral halo of phyllic or quartz-sericitic alteration (Fig. 1-4). This alteration zone results from a strong leaching of Ca, Mg, and Na from primary aluminosilicate minerals, while K can be introduced or derived from the alteration of primary feldspar and is limited to sericite. The characteristic mineral assemblage is quartz-sericite-pyrite, with chlorite, rutile and apatite as accessory minerals. Typically in the phyllic zone, a mixture of fine-grained sericite and quartz replaces all silicates except quartz, while primary quartz is generally overgrown. Sericite predominates in the inner phyllic zone, and clay minerals in the outer margins, which may grade to the argillic zone.

The contact between the phyllic and the argillic alteration zones is poorly defined (Fig. 1-4). The latter zone is characterized by the formation of a clay mineral assemblage in aluminosilicate minerals by the circulation of acid solutions that produce an extensive to complete leaching of all alkali cations. The alteration mineral assemblage includes montmorillonite, illite, and chlorite with or without kaolinite.

The outermost halo of the hydrothermal alteration zoning corresponds to a broad aureole of propylitic alteration (Fig. 1-4) resulting from the heating of the wallrock by the hydrothermal fluid, accompanied by addition of H_2O and CO_2, and recrystallization without strong leaching of bases. The typical mineral assemblage includes chlorite-epidote-calcite-albite; montmorillonite, sericite, quartz, and pyrite are locally present. Accessory minerals include apatite, anhydrite, ankerite, and hematite. Chlorite, epidote, and calcite are formed by alteration of mafic minerals and the anortitic component of plagioclase. K released by chloritization of biotite appears as nonessential sericite, and the albite component of the original plagioclase is generally conserved.

Silicification appears in the form of quartz veins and as cryptocrystalline varieties such as jasper or chalcedony. In contrast to the formation of quartz in association with other silicate minerals typical of phyllic and argillic alteration, silicification requires coupled Si metasomatism and cation leaching of sufficient extent to remove not only alkalis but also Al.

Studies of alteration in PCDs at various levels of detail throughout the world have documented numerous localities in which the proposed zoning does not correspond with this model. The variations might be due to geological factors such as type of wallrock, fluid and intrusion compositions, levels of exposure, and structural controls on intrusion and mineralization.

If the porphyritic intrusion is emplaced in or near carbonatic rocks, extensive contact metamorphism and metasomatic effects will extend into carbonate wallrock well beyond a zone reasonably attributed to thermal metamorphism producing a skarn or calc-silicate alteration.

1.3.5.5 Mineralization

Primary or hypogene sulfide mineralization is also closely related to the hydrothermal activity. The ore may be found completely within the stock, partially in the stock and partially within the wallrock or in the wallrock only. In the porphyry host, common control of alteration and sulfides by veinlets indicates that much of the copper was introduced after consolidation of the exposed intrusive.

Hypogene sulfide mineralization commonly consists of chalcopyrite and bornite accompanied by variable amounts of pyrite; molybdenite is a common accessory. The sulfides occur commonly with quartz in veinlets and in the wallrock adjacent to the fractures, where the sulfides replace the original ferromagnesian minerals.. In a large proportion of well-studied deposits the hypogene sulfides frequently show a general pattern of lateral and possibly vertical zoning consistent with the hydrothermal alteration zoning (Fig. 1-4). In those deposits in which this relationship is not clear, the pattern seems to fit if the various permutations of multiple stages of mineralization, retreating source, and supergene alteration are added.

The zoning of hypogene sulfides comprises a barren or low-grade nucleus that coincides with the potassic zone (Fig. 1-4). The most common opaque minerals in this zone include magnetite, chalcopyrite and pyrite, showing a pyrite/chalcopyrite ratio of 1:2 and a generally low copper content. Within this zone, chalcopyrite commonly occurs in and adjacent to small veins containing orthoclase or with orthoclase-rich or biotite-rich alteration halos, this texture indicates the coexistence and the probable contemporaneity of at least some of the copper sulfides with the potassic alteration. Molybdenite and bornite, if present, are typically most abundant in this central zone.

The core grades into the ore zone with the highest primary Cu content, this zone contains moderate amounts of sulfides with dominant chalcopyrite and lies mainly in the interface potassic-phyllic zone, extending a short distance out into the phyllic zone (Fig. 1-4). The average Cu grade is 0.7 wt %, mainly as chalcopyrite, with a pyrite/chalcopyrite ratio of about 2:1. This zone may constitute primary ore if enough sulfides are present.

Outside of the ore zone there is a halo that largely coincides with the phyllic zone (Fig. 1-4) in which pyrite is the dominant sulfide (6 to 20 wt %) whereas chalcopyrite normally shows variable contents. The Cu grade is only around 0.03 %, indicating a pyrite/chalcopyrite ratio of about 100. In the pervasive phyllic-altered material, pyrite forms veinlets and generally granular disseminations, and the pyrite-rich veins exhibit the same textural relation observed in the chalcopyrite mineralization in the potassic zone. The major sulfide present within the argillic alteration zone is pyrite, although chalcopyrite and, less often, bornite may also occur. The strongly pyritized zone in the phyllic zone fades outward into the propylitic halo which contains minor amounts to traces of pyrite and rare economic concentrations of chalcopyrite (Fig. 1-4).

Supergene enrichment is very important in PCDs, especially in continental margin deposits. Percolating groundwater commonly leaches the upper part of the deposits to form a barren leached zone, sometimes more than 100 m thick underlain along sharp contacts by a zone of supergene enrichment related to the surface of the water table. Below the leached zone, precipitation of copper results in a supergene blanket up to many tens of meters thick in which the grade of the original protore may have increased by a factor of more than four. Secondary mineralization consists of oxides, carbonates, sulfates, and silicates of copper as surface coatings, or minor replacements of silicates minerals, and as supergene sulfides, chiefly chalcocite, which replace hypogene sulfides.

1.3.6 Fluids

Stable and radiogenic isotope studies in PCDs indicate that the upper and interior portions of the ore deposit were formed by hydrothermal fluids showing an unmistakable magmatic isotopic signature, whereas further out from the intrusion, there is a cooler hydrothermal fluid dominated by meteoric groundwater and/or connate waters. The simultaneous presence of these two different fluids, early in the history of the deposit, implies that two, non-related hydrothermal convective circulation systems are established in and around the porphyry intrusion.

The inner convective hydrothermal cell originates from magmatic dominated water exsolved during the late stages of magma crystallization. This solution will react with the porphyry and to a varying extent with the surrounding country rocks developing the central core of potassic alteration. The introduction of much of the metals and sulfur probably accompanies this stage. The magmatic system usually will show a normal evolution from high temperature and lithostatic pressure to lower temperature and hydrostatic pressure.

The external convective circulation is set up by the thermal gradient in the country rocks, and is responsible for the development of phyllic, argillic and propylitic alteration assemblage. This convective system will persist even after the internal cell fades away; in fact, when the intrusive cools down, the internal magmatic system will die down, then the external system will likely collapse inwards and downwards into the hydrothermally altered rocks formed by the magmatic system. The argillic and quartz-sericitic alteration zones will then be locally superimposed on the outer part of the potassic core, or upon the fresh intrusive, particularly replacing K-feldspar and biotite.

The major locus of ore mineral deposition tends to occur along the interface between these two different types of hydrothermal systems, probably due to the gradients in pH, temperatures and salinity.

1.3.7 Origin of metals

Even after decades of exhaustive worldwide research on PCDs, the origin, transport and deposition of copper still remain controversial. There are several models intending to find the most probable answer to these questions.

a) **Convection of ambient water model (e.g. Norton and Knight, 1977; Norton, 1978).** The convective circulation of groundwater is initiated and sustained by the heat from the intrusion. Trace elements from the neighboring rocks are leached out and concentrated by a circulating convective system of non-magmatic aqueous fluids. Metals are later precipitated during hydrothermal alteration, peripheral to the igneous protolith.

b) **Convection of ambient water with boiling model (Cathles, 1977).** A variety of the former model, in this case the convective water boils near the pluton, reconciling the high salinity of fluid inclusions with the lower salinity of groundwater.
c) **The orthomagmatic model (e.g. Fournier, 1967; Rose, 1970).** The intrusion is the primary source of metals and volatile, suggesting that mineralization is associated with natural processes of pluton emplacement and crystallization of silicic melts. The main mineralization process occurs during the magmatic/hydrothermal transition from a magmatic to a high-temperature, hydrothermal system in response to decreasing pressure (first boiling) and crystallization (second boiling) as the magma approaches the surface. These last two factors will reduce the capacity of the magma to contain dissolved water, and chlorine-rich aqueous fluid will be exsolve to the hydrothermal system, removing the copper from the melt. Repeated episodes of fluid expulsion from the magma will also provide the mechanical energy required to fracture the confining rocks producing the extensive fracture systems characteristic of productive PCDs.
d) **The vapor plume model (e.g. Henley and McNabb, 1978; Eastoe, 1978).** During crystallization of the intrusive, the exsolution of volatiles gives rise to large amounts of vapor bearing a few percent of NaCl. The vapor will form a plume above the intrusive, eventually mixing with groundwater. On cooling at temperatures at which the solubility of NaCl in the vapor is at its minimum, the vapor must condense to some salt-rich aqueous fluid. The salt-rich liquid could deposit magma-derived copper, provided the concentrations of copper and other components in the vapor were sufficient.

Each of these models may play an important role, and contribute to different degrees to the origin and transport of copper, so that the problem focuses on identifying which feature of a deposit might correspond to the dominant processes, rather than the right or wrong alternatives.

Isotopic evidence for direct derivation of the bulk of mineralizing fluids supports a common source with the parental intrusive for the S, Cu, and other heavy metals found in these deposits. A stream of researchers favor the extraction of metals and other elements from the continental crust, either at the site of partial melting, or by magma contamination resulting from assimilation of older ore bodies, or as a consequence of scavenging by circulating hydrothermal fluids. Others instead support a subcrustal source for Cu, in which the subducted oceanic crust and pelagic sediments play a pre-eminent role, whereas the continental crust only provides a site for fractional crystallization of magmas, not contributing with a significant proportion of PCD components.

For some authors the mineralization in a PCD is integrally related to the magmatic evolution of the intrusive rocks. In the magma chamber, copper would be extracted not only from apical portions of the porphyry host, but also from deeper parts of the parent copper-bearing calc-alkaline intrusion. The mechanisms by which copper is enriched during differentiation of these types of magmas would be the incompatible behavior of copper early in the development of the magmatic system, and the number of octahedral sites available in the crystallizing magma, because the Cu^{2+} ion in a silicate melt will be preferentially partitioned into octahedral rather than tetrahedral co-ordination sites. Magmas with more octahedral sites, calc-alkaline type, would tend therefore to partition a greater proportion of copper into the residual magmatic hydrothermal phase as the crystallization progresses, and eventually may give rise to a PCD.

For other authors, most factors in the magma genesis are not critical in the formation of PCDs, but the history of volatile evolution during the rise of magmas through the crust. Therefore only melts which avoid separation of the predominantly CO_2-rich fluid phase may reach shallow crustal reservoirs with enough sulfur and accompanying metals to produce eventually significant concentrations of copper in cupola areas.

1.4 Porphyry copper deposits in Chile

In the year 2001, copper production in Chile was at about 4.500 million metric tons, representing near 28 % of the world's total production, and this has made Chile the world's leading copper producer. Nearly 80 % of the copper was recovered from 12 PCDs in production today, including four of the world's richest and largest orebodies, Escondida, Rio Blanco-Los Bronces, El Teniente and Chuquicamata (Fig. 1-5). In addition to the working mines, more than 60 porphyry copper prospects are known, ranking Chile as the leading country of world's copper reserves.

All PCDs in Chile occur in the domains of the Andean range and are genetically and spatially related to Lower and Upper Tertiary intrusive porphyritic stocks, which range in composition from diorite to quartz monzonite. The porphyries are normally much younger than their host rocks and are emplaced in igneous and/or metamorphic rocks Paleozoic to Tertiary in age.

The Mesozoic evolution of the continental margin in northern Chile is the consequence of the subduction of Nazca oceanic plate beneath the South American continental plate. This evolution involves the alternation of transtensional regimes characterized by extensional and strike slip faults associated with essentially effusive magmatism, and transpressive regimes dominated by folding, reverse and strike slip faulting and basically plutonic magmatism. The magmatism show a eastward migration in time originating four distinct continental magmatic arcs, each has an associated system of strike slip faults parallel to their longitudinal axes, also each associate to a characteristic metallogenic province (Espinoza et al., 1996).

The greatest known concentration of the world's largest PCDs occur in or close to a major dextral shear zone related to the Late Eocene-Early Oligocene structural belt, the West Fissure Zone or Domeyko fault system that extends for over 1.000 km and includes the giant deposits Chuquicamata and Escondida (Fig. 1-5) (Sillitoe, 1988; Cornejo et al., 1997). The spatial distribution of this numerous PCDs gives form to a metallogenic copper province that has been called the Chilean Porphyry Copper Belt, situated north of 36° S, and at heights between 1.000 to 4.500 m a.s.l., which corresponds to a discontinuous longitudinal belt, 20 to 45 km wide, and about 2.400 km long, having a marked parallelism with the axis of the Peru-Chile trench.

Within this copper belt, at least four Meso-Cenozoic narrow sub-belts of PCDs can be distinguished, each emplaced during a discrete time interval, Late Cretaceous (90-73 Ma), Paleocene (67-54 Ma), Late Eocene-Early Oligocene (41-29 Ma) and Middle-Late Miocene (16-5 Ma). The sub-belts migrated progressively eastwards with time from the Pacific coast, and are geometrically comparable with belts of Pliocene and more recent andesitic volcanoes in the high Andes, and appear not to have overlapped one another.

PCDs are not present in the older (Jurassic) plutonic rocks adjacent to the coast where possible earlier most ore bodies may have been removed by erosion. Upper Tertiary or Quaternary post-mineral volcanic and sedimentary rocks cover an important area in the PCDs belt possibly covering yet undiscovered deposits.

Supergene sulfide enrichment processes occurring during the Miocene affected the Andean porphyry systems located under arid to semi-arid conditions and modified most of the primary characteristics of these deposits. In some PCDs the supergene enrichment has caused copper grades to more than double in the enriched sulfide zone.

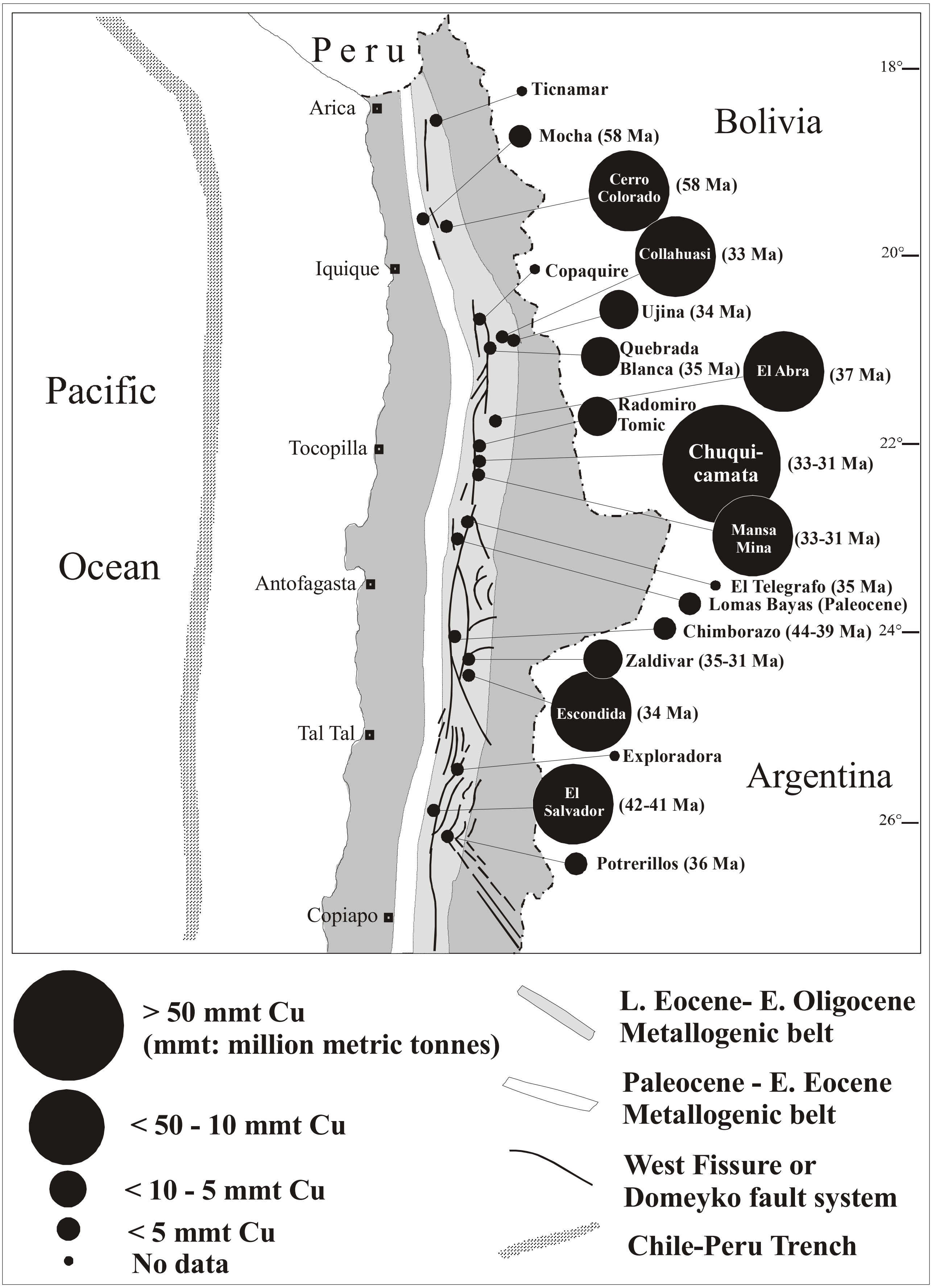

Figure 1-5. Distribution of porphyry copper deposits from northern Chile and their relation to the West Fissure. Modified from Clark et al. (1998).

Chapter 2

The Zaldívar Deposit

2.1 Introduction

The Zaldívar deposit is genetically related to a shallow porphyritic intrusive of Late Eocene age that is part of a large Tertiary porphyry copper complex that also includes the Escondida PCD. The complex is placed within the West Fissure structural system, a major regional feature that controls the emplacement of some of the largest PCDs in northern Chile (e.g. Espinoza et al., 1996).

2.2 Location and access

The Zaldívar mine is a typical porphyry copper deposit located in the Atacama desert of northern Chile (24°12'30" Lat. S and 69°04'00" Long. W) (Fig 2-1). The deposit lies approximately 1400 km north of Santiago, and 180 km east of the port of Antofagasta, only 5 km north of the Escondida mega-deposit. The Zaldívar site is accessible by highway from the city of Antofagasta, and is also served by the Antofagasta-Salta railway.

Geomorphologically, the Zaldívar deposit lies in the western Andean foothills forming the occidental margin of the Cordillera de Domeyko. At the northern margin of the deposit, the topography discloses several isolated hills, with a maximum elevation of 3,500 m (a.s.l.) is the Zaldívar peak. On the western limits of the mine, small ranges surrounded by alluvial plains represent the lowest altitude of about 3,200 m (a.s.l.). Slopes in the area fluctuate between a maximum of about 30° on the flanks of the Zaldívar peak, progressively flattening towards the south and west to less than 5°.

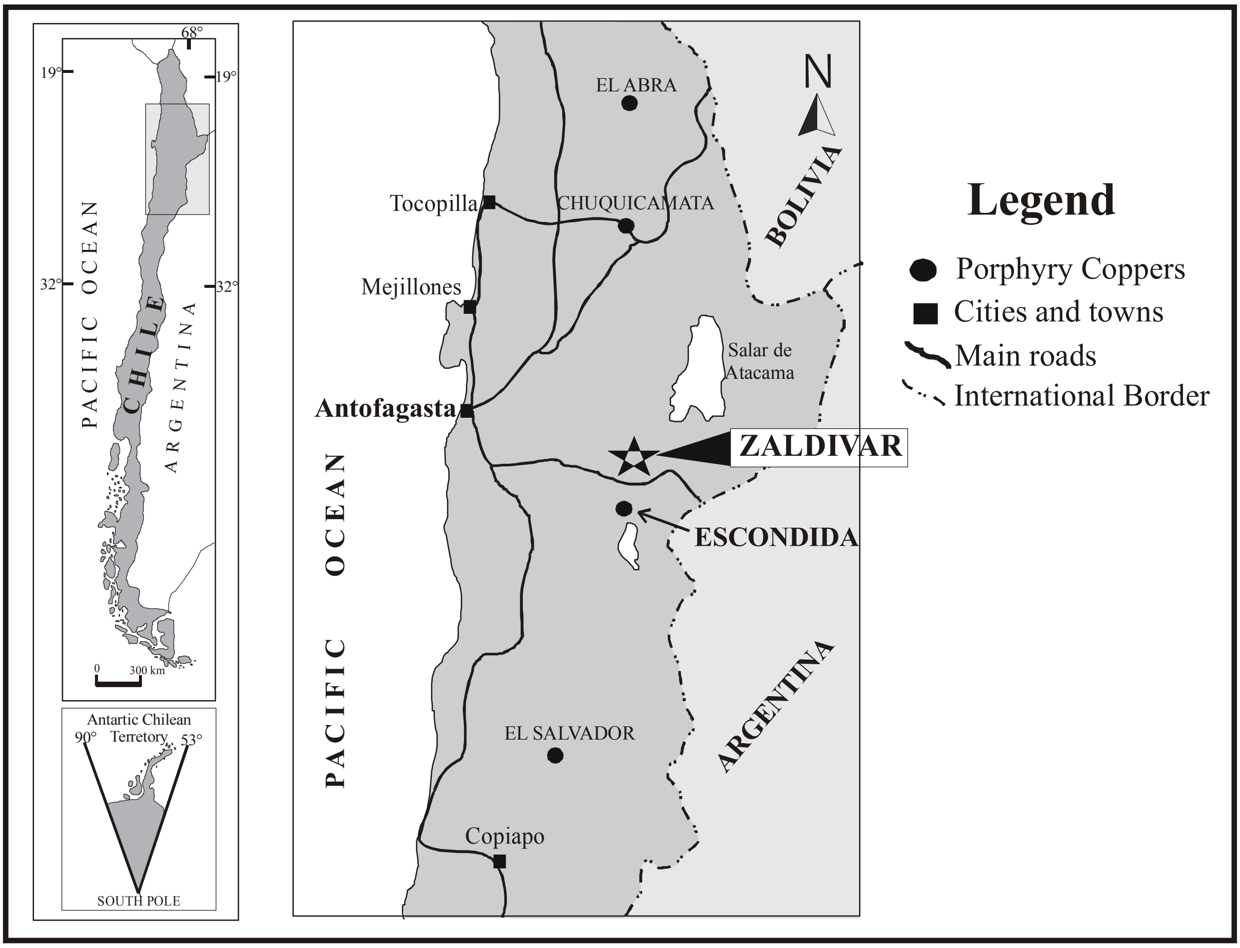

Figure 2-1. Location map of the Zaldívar deposit

2.3 Mining overview

The mineable ore reserves (including proven and probable reserves) are 4.9 million metric tonnes (mmt) of copper in 315.7 mmt of ore grading 0.89 % TCu (total copper) and 0.34 % ASCu (acid soluble copper). The reserves can be broken down into 246.4 mmt of heap leach ore grading 1.02 % TCu and 0.37 % ASCu, 69.3 mmt of dump leach ore grading 0.41 % TCu and 0.24 % ASCu, and 868.3 mmt of waste.

The mine is exploited by a conventional open pit method, with an estimated mine life of 21 years. The copper production is estimated to be 1.9 mmt of cathode copper obtained by sulfide heap leach ore, oxide heap leach ore and dump leach ore that will contribute 49 %, 45% and 6% of the copper production, respectively.

2.4 Regional geology

2.4.1 Stratified Units

The oldest stratified unit outcropping around the Zaldívar site (Fig. 2-2) is a mostly siliceous volcanic sequence exposed along the eastern and western margins of the Zaldívar mine in a non-continuous belt, essentially consisting of rhyolites, tuff, and andesitic lava flows assigned to the La Tabla formation (Garcia, 1967, in Marinovic et al., 1995). This unit overlies along an angular unconformity the Argomedo strata (Devonian to Lower Carboniferous) (no outcrops in figure 2-2), and west of Zaldívar contacts Mesozoic volcano-sedimentary rocks along an angular and erosional unconformity. K-Ar dating on rhyolites from La Tabla Formation yield ages between 291 and 239 Ma, (Marinovic et al., 1995).

The Mesozoic lithological record begins with rocks from the El Profeta formation (Chong, 1973, in Marinovic et al., 1995), a thick marine sedimentary sequence, probably deposited on the eastern margin of a back-arc basin (Palma, 1993, in Marinovic et al., 1995). This unit forms a N-S trending belt, outcropping west of Zaldívar comprising of sandstones, conglomerates, andesitic volcanic intercalations, acidic tuff layers, limestones, shales and calcareous sandstones. The age of this formation, based upon fossiliferous fauna, is Upper Triassic to Kidmmeridgian. On the upper levels, the El Profeta formation shows a transitional contact with the Santa Ana formation.

The Santa Ana formation (Naranjo y Puig, 1984, in Marinovic et al 1995) outcrops west of the Zaldívar mine and correspond to a marine-continental clastic sequence, with volcanic intercalations. The lower levels of this unit correspond to pelites with Trigonia-bearing calcareous bioclastic intercalations, whereas on upper levels sandstones and shales prevail. Southwest of the Zaldívar mine, on the Cerro Bayo hill, thick beds of andesitic lavas, breccias and tuff are intercalated. The fossil fauna of this formation gives an age between Upper Jurassic to Neocomian (Marinovic et al., 1995).

Overlying the Santa Ana formation along an angular unconformity, outcrops the Augusta Victoria formation (Garcia, 1967, in Marinovic et al., 1995). This unit corresponds to a volcanic complex consisting of andesitic lava flows, rhyolites, and tuffs, frequently intruded by sub volcanic dacitic domes and small stocks of a variable composition, from gabbros to quarziferous porphyries. The sequence also includes sandstone and volcanic breccias and conglomerates, some of these related to a caldera development. The age of the Augusta Victoria formation has been defined by K-Ar dating between 66.6 +/- 2.2 and 41.2 +/- 2.2 Ma (Marinovic et al., 1995).

Several continental gravel deposits, including mainly conglomerates and breccias settled during and alluvial and piedmont desertic environment, outcrop in the area, are assigned to the Pampa de Mulas formation (Chong, 1973, in Marinovic et al., 1995). The overlying colluvial and alluvial Miocene-Pliocene deposits give the minimum age for these deposits, confirmed by K-Ar dating on an ash intercalation of 5.4 +/- 1.6 Ma. (Marinovic et al., 1995), and because they overlie along an unconformity rocks from the Augusta Victoria Formation, the maximum age must be post-Eocene.

2.4.2 Unconsolidated deposits

The unconsolidated colluvial and alluvial sedimentary deposits are widely distributed in the whole area. They consist of gravel and sand of variable composition, polymictic (alluvial) and monomictic (colluvial), with angular to subangular clasts up to 10 cm in diameter. Sands and clays are fairly consolidated, not well stratified and with variable granulometry. These deposits contain intercalations of volcanic ashes, some of these have been dated and yield K-Ar ages between 1.9 and 1.5 Ma (Marinovic et al., 1995). The thickness of these deposits varies from a few centimeters to several meters.

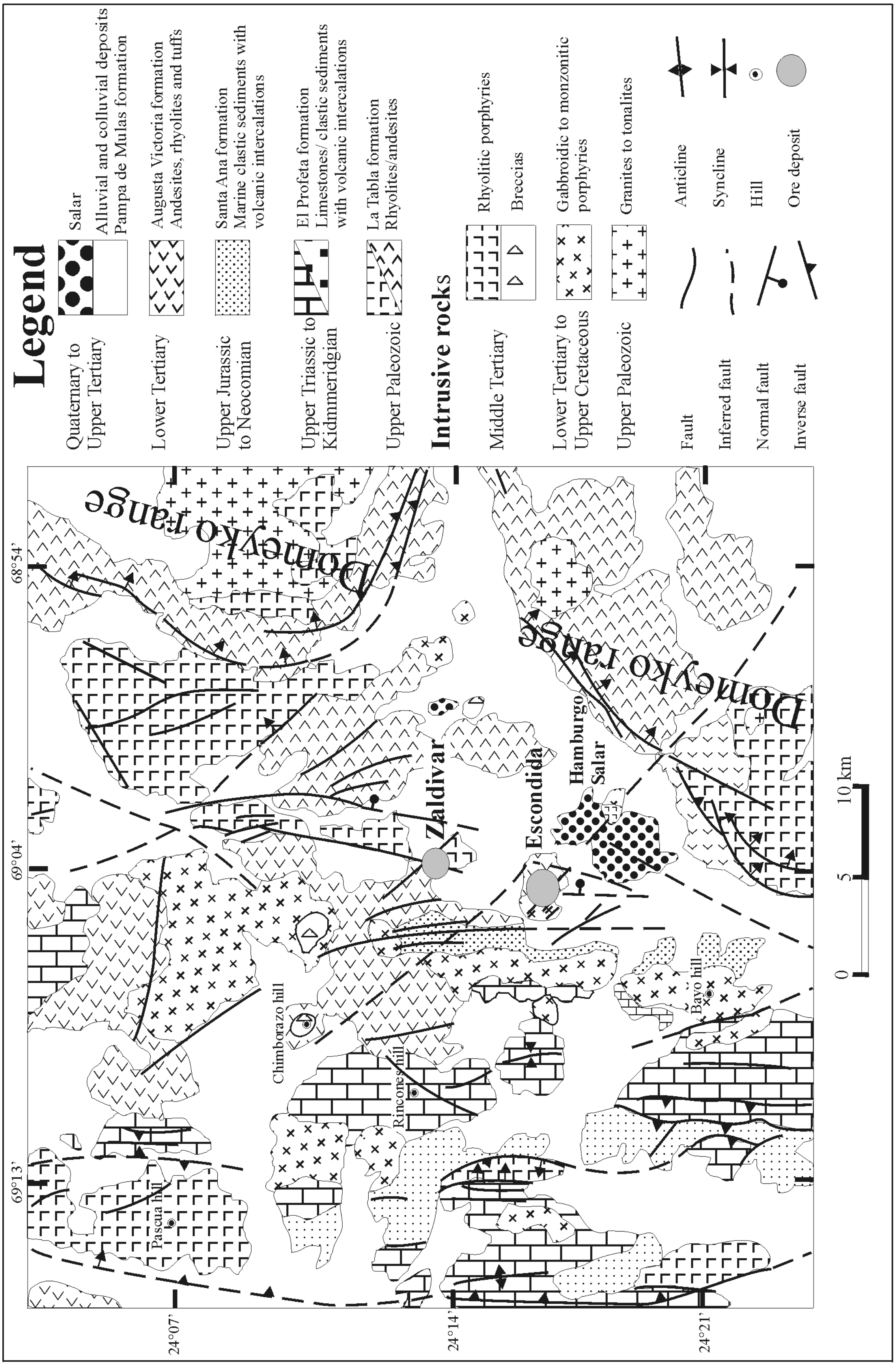

Figure 2-2. Simplified regional geological map with the location of Zaldívar deposit. After Maturana and Zaric, (1991)

2.4.3 Intrusive rocks

2.4.3.1 Paleozoic intrusives

Partially covered by the Mesozoic volcano-sedimentary sequences, several coarse-grained, calc-alkaline hypabyssal intrusives outcrop in the area. These intrusives are porphyries in which two lithologic types are recognized: red rhyolitic porphyries and greenish-gray rhyolitic to dacitic porphyries, both showing similar mineralogy and texture, differing basically in their granulometry. In the red rhyolitic porphyries the groundmass and the phenocrysts show a coarser grain. The age of these intrusives, defined by a K-Ar dating, is 277 +/- 8 Ma (Marinovic et al., 1995).

2.4.3.2 Upper Cretaceous - Eocene intrusives.

A number of stocks intrude most Mesozoic volcanic and sedimentary rocks, and are overlain by Oligocene-Miocene gravels. These intrusives are genetically related with the andesites from the Augusta Victoria formation (Marinovic et al., 1995).

The compositional variation of these intrusives is wide and includes rhyolitic to gabbro porphyries, the most abundant being the diorite and monzodiorite porphyries. The contact relations between the different facies are gradational, indicating several intrusive pulses. According to the differences in composition, five main lithologic associations can be recognized among these intrusives.

- Diorites and to a lesser extent monzodiorites and gabbros cover the largest area, and outcrop in a discontinuous belt between the Bayo and Pascua hills. The plutons are generally elongated, and correspond to quartz-diorites and quartz-monzodiorites with a high contents of pyroxenes. Less abundant are pyroxene gabbros and hornblende monzogabbros.
- Monzonitic porphyries, monzodiorites and monzogranites are exposed between the Bayo and Rincones hills, west of Zaldívar. This unit is closely related with the preceding unit.
- Granodiorites outcrop northeast of Zaldívar mine.
- Granites and gabbros occur south of the Zaldívar mine.
- Andesitic porphyries and aplitic intrusives are small subvolcanic bodies outcropping in the whole area.

Several radiometric ages have been done on these rocks, showing a distribution between 79 and 41 Ma. Within this range of ages it is possible to define three different groups, probably indicating three magmatic pulses (Marinovic et al., 1995). The oldest groups (79 to 74 Ma) represented by intrusions of diorites and gabbros, outcrops southeast of the Zaldívar area. The middle stage (67 to 52 Ma), is a series of rhyolitic and dioritic stocks outcropping southeast of Zaldívar. Finally several intrusives located in areas near the alteration zone of the Escondida PCD define the third set of ages (49-41 Ma).

2.4.4 Oligocene porphyries

The intermediate to acid hypabyssal intrusive complex are usually intruding rocks from the Augusta Victoria formation, generating the extended hydrothermal alteration and mineralization at the Zaldívar and Escondida mines, both deposits are part of the Escondida porphyry copper complex. At the Escondida mine, the complex is composed of three main intrusive bodies: Escondida, Colorado Grande and Rhyolitic porphyries. The first two are considered to be responsible for the mineralization, while the third shows no hypogene mineralization. Dacitic-latitic dykes and hydrothermal breccias were setting at a late hydrothermal stage. At Zaldívar, the intrusives comprise of early rhyolitic porphyries, and a later phase of granodioritic to rhyolitic porphyries to which the mineralization and strong hypogene alteration is associate.

At the Escondida deposit, the synmineralization Escondida porphyry yield a crystallization age of 37.9 ± 1.1 Ma (Richards et al., 1999). Furthermore, 33.7 and 32.8 Ma ages have been obtained for the hypogene mineralization associated with the Colorado Grande and Escondida porphyries (Alpers and Brimhall 1988), also, values of 31.6 to 31 Ma (Marinovic et al., 1995) were obtained on the rhyolitic porphyries and late dykes in the system. All the age yielded at the Escondida mine, defines an Oligocene age for all intrusive in the area.

2.5 Geology of the mining district

The following section regarding the geology of the Zaldívar deposit is based on the information provided by the staff geologists of the Zaldívar mine and my own observations. The majority of the database concerning the geology of this ore deposit is contained in unpublished internal reports.

2.5.1 Lithology

Three petrographic units are recognized within the Zaldívar deposit: the Zaldívar porphyry, the andesite unit, and the Llamo porphyry. The ore body itself displays a NNE elongation, 2 km long (N-S) by 1 km wide (E-W), generally centered on the Llamo porphyry (Fig 2-3).

The Zaldívar porphyry is the oldest, 290 ± 4 Ma (Richards et al, 1999) and the most extensive intrusive unit observed in the mine (Fig 2-3), and it outcrops only on the eastern side of the Portezuelo fault. This rock unit typically consists of gray rhyolitic feldspar-quartz porphyry, presenting a well-developed coarse porphyritic texture. The phenocrysts are of small to medium size (0.2-0.7 cm) and correspond to plagioclase, K-feldspar and quartz. The groundmass is an aggregate of very fine-grained quartz, variable quantities of hydrothermally formed sericite, primary alkali feldspar, ferromagnesian minerals, and scarce rutile, zircon and calcite. The groundmass and the phenocrysts (except quartz) are strongly altered to sericite, quartz and clay minerals.

The andesite unit correlates with the Augusta Victoria Formation (between 66.6 +/- 2.2 and 41.2 +/- 2.2 Ma; Marinovic et al., 1995) and is the dominant lithology west of the Portezuelo fault, showing a straight structural contact with the Zaldívar porphyry along this structure (Fig 2-3). Rocks are of greenish-gray to dark-gray color. They are usually fine-grained to aphanitic and less commonly show a fine-grained porphyritic texture. If the porphyritic texture is present, it normally contains plagioclase phenocrysts, 0.1 to 0.2 cm in size, dispersed in a fine-grained, greenish- to brownish-gray groundmass. The groundmass consists of plagioclase, quartz, and mafic minerals. The hydrothermal alteration affecting the groundmass consists mainly of chlorite-magnetite patches with colloidal silica, whereas the phenocrysts are slightly to strongly altered to sericite, sericite-chlorite, clays and quartz.

The Llamo porphyry is the most recent intrusive event in the area; the crystallization age for this intrusive has been defined by U/Pb in zircon and yield 37.4 ± 0.18 Ma (Richards et al, 1999). The Llamo porphyry trends roughly NE-SW across the deposit, it outcrops on either side of the Portezuelo fault intruding the andesites and the Zaldívar porphyry, and is exposed as an irregularly shaped dyke, intrusive plug or stock, 50 to 200 m wide (Fig 2-3). This rock unit typically consists of a light-gray/green, fine-grained feldspar-biotite-quartz porphyry. The phenocrysts correspond to plagioclase, biotite, K-feldspar and rounded quartz crystals (smaller than 2 mm). Zircon and apatite are also present as minor phases. The groundmass is fine-grained to aphanitic, composed of feldspar, quartz and biotite. The hydrothermal alteration is characterized by secondary biotite and K-feldspar, evidence of phyllic alteration (quartz-sericite) with secondary chlorite are found locally in the deposit overprinting the potassic alteration. Biotite is commonly altered to supergene kaolinite.

Closely associated with some major structures, for example the Portezuelo fault, several hydrothermal and tectonic breccia bodies have been recognized in the mine area. There is often an overprinting in these breccias of different hydrothermal and mineralization processes, forming somehow different types of breccias. Frequently they show a non-continuous development and angular clasts predominate over the matrix, the clasts having the same composition as the surrounding rocks.

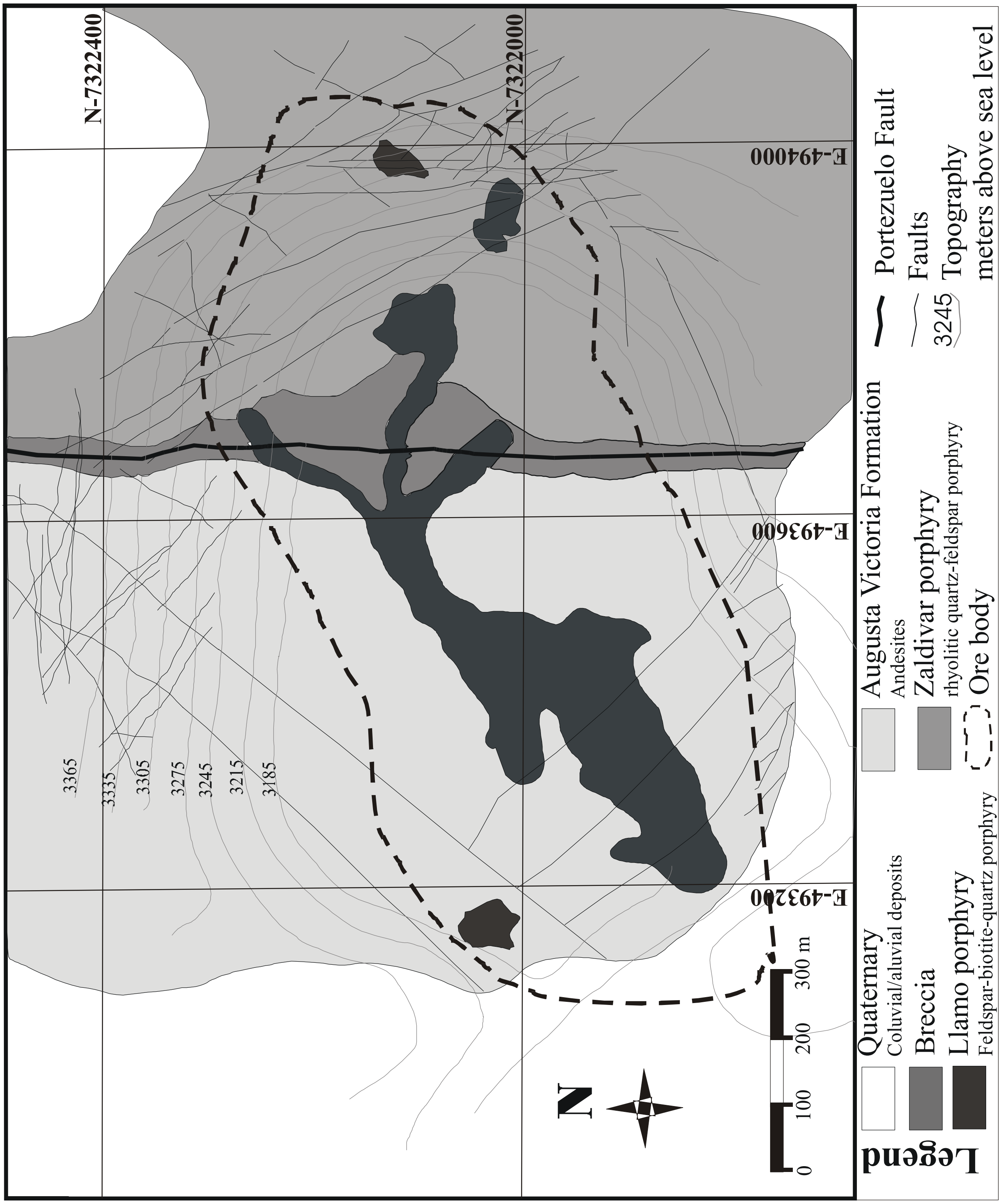

Figure 2-3. Geological map of the Zaldívar deposit showing the distribution of rock units and faults.

Much of the lower slopes and valleys floors in the area are covered with thick Quaternary alluvial/colluvial deposits, which are typically more than 2 m thick in the SW and central portion of the mine, and which generally thicken towards the SW. These deposits have been derived by weathering from the local bedrock and generally consist of dry, loose to dense, well-graded silt, sand and gravel. Coarse sand and gravel components tend to be very angular, friable, strongly weathered or altered andesite to rhyolite fragments.

Pockets of eolian silt and fine sand, probably derived from winnowing of the colluvial soils, are also present in the area. The deposits commonly show some stratification, and occasional bands of volcanic ash can be observed. In some areas, these sediments are cemented with sulfate salts (gypsum), silica, calcite, limonite, or copper oxide minerals.

2.5.2 Structures

The Zaldívar PCD is at the intersection of three major sets of faults striking NS, NW-SE and NE-SW (Fig 2-3). This structural complex apparently has strongly controlled the emplacement of the intrusives and the hypogene mineralization, as well as the processes of leaching and secondary enrichment.

The most prominent discontinuities strike NS to NW-SE, and dip moderately to steeply NE to SW, they define the strongest fault population, and correspond to the major structures observed in the mine. The NS structures are apparently pre-intrusive and presumably controlled the regional emplacement of the porphyries. The faults have a regional character that parallels a major regional structural trend, the West Fissure or the Domeyko fault system, which is approximately 10 km wide, and consists of an arrangement of steeply dipping, NS trending structures with numerous associated parallel and sub-parallel fractures zones. Breccias zones 1 to 5 m wide are commonly associated to this fault set. The Portezuelo fault belongs to this set.

The NW-SE set is later than the NS one and also parallels a secondary structural trend that is continuous on a regional scale. It contains zones with fractured and argillaceous rocks, faults breccias and quartz-filled fissures. The intersection of NW-SE and NS fault sets presents the most interesting concentrations of copper. The relative age relationship between these two regional fault subsets is unclear, but the NW-SE faults may represent splays off the primary NS faults, or they may pre-date them.

A second fault set strikes NE-SW and dips rather steeply to the NW-SE and is weakly to moderately developed. It represents the westernmost branches of the Domeyko fault system, and is closely associated with the Zaldívar deposit. It could have controlled the emplacement of it, since these structures are sub-parallel to the trend of the Llamo porphyry.

The third fault set is weakly developed, and strikes NE-SW dipping moderately to the SE, and it may be a subset of the NE-SW set.

Only one fault striking EW and dipping moderately to the S has been recognized.

There is a corresponding set of joints related to each of the principal fault set described above.

2.5.3 Hypogene alteration and mineralization

All rock types and ore zones in Zaldívar PCD have been subjected to hypogene hydrothermal alteration to varying degrees. Characteristically in the hypogene zone potassic alteration in the form of secondary biotite and local K-feldspar is most prominent in the Llamo porphyry, this intrusive can also be locally affected by phyllic alteration. Propylitic alteration dominates in the andesites, while phyllic alteration and silicification are well developed in the Zaldívar porphyry.

The Zaldívar mine represents a typical PCD in which the hypogene mineralization is closely related to the Llamo intrusive. In this ore deposit the combination of primary and secondary Cu enrichment processes have produced several mineralized zones, occurring as supergene blankets in all rock units present in the mine (Fig. 2-4).

The hypogene zone contains sub-ore grade mineralization (0.2 to 0.3 % Cu) consisting of pyrite, chalcopyrite, molybdenite and scarce bornite. Pyrite is the most abundant primary sulfide showing concentrations between 5 to 15 wt %. The mineralization occurs mainly disseminated in the intrusives and in the volcanic rocks, less commonly in veins that are relatively scarce in the deposit. The sulfides were deposited by hydrothermal fluids migrating upwards along fractures and permeating the rock mass. The main primary mineralizing events are closely related to an extensive and sometimes very strong hydrothermal alteration related to the Llamo porphyry.

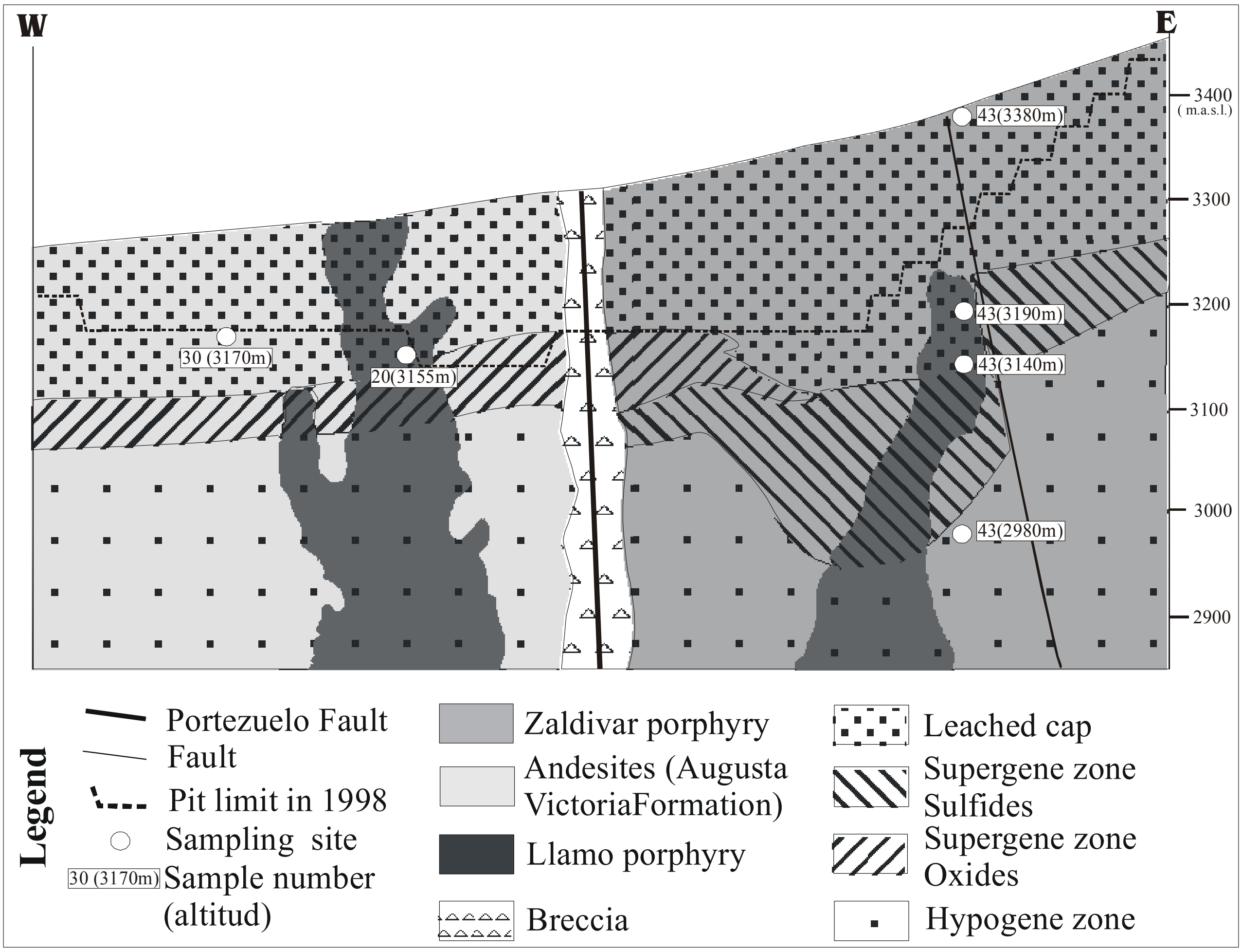

Figure 2-4. Schematic cross section through the Zaldívar ore deposit showing the distribution of the rock units and the different mineralized zones at depth. Also showing the sampling site that falls in this cross section.

2.5.4 Supergene leaching and secondary enrichment

Supergene alteration is closely related to the principal faults in the area, usually strongly overprints the hypogene alteration assemblage and is dominated by argillic alteration (kaolinite) with secondary chloritization and minor silicification. On the western margins of Portezuelo fault, in the andesites, argillization, limonitization and chloritization are most prominent, whereas, on the eastern margin, in the Zaldívar porphyry, argillization and limonitization predominates.

The majority of the copper occurs at the bottom of a leached zone in a secondary enriched blanket which overly a deeper primary sulfide mineralization of lower grade. The leached cap extends to a depth of about 150 m, which contains relicts of sulfide minerals, and scarce copper sulfate (brochantite), as well as limonite, associated to argillic alteration.

The economically important mineralization is distributed in the supergene-enriched blanket that resulted from a complex history of leaching of the hypogene sulfides, secondary enrichment (supergene), and partial oxidation of the secondary ore. In the enriched blanket the mineralization types are secondary sulfides, oxides and a mixed mineralization that combines oxidic and sulfide copper minerals.

The oxidic ore, consisting of several isolated bodies with a thickness between 20 and 60 m made of brochantite, chrysocolla, antlerite, malachite, and cuprite. Brochantite is the most important ore mineral in this zone, followed in significance by chrysocolla.

The sulfide zone shows a NE elongation, (1.600 m long and 500 m wide) with a variable thickness between 100 and 150 m. The main sulfides present in this ore zone are pyrite, chalcocite, less covellite and chalcopyrite. Chalcocite (including chalcocite *sensu stricto*, djulerite, and digenite) is the most important copper sulfide, it normally occurs coating on primary pyrite and chalcopyrite.

These zones appear to be essentially subhorizontal, however, variations in thickness and distribution do occur. The blanket of supergene enriched ore may not be present in all areas in the mine, in general, secondary oxidic ore predominates in the andesite, and secondary sulfide ore predominates in the Zaldívar porphyry. The greater thickness of these zones is related to the intersection of faults.

Chapter 3

Sampling and methods of investigation

3.1 Introduction

The sample preparation and all experimental and analytical work were carried out in the Faculty of Earth Sciences and Physics and Astronomy division of the Faculty of Sciences, both at the Vrije Universiteit Amsterdam (VUA), The Netherlands.

The present study was focused only on quartz phenocrysts since they show no signs of hydrothermal alteration and therefore represent the best chance to preserve magmatic remnants. Microscopic and electron-microprobe (EMP) investigations have shown that K-feldspar, biotite and plagioclase mineral inclusions in quartz phenocrysts appear to be shielded from the effects of hydrothermal alteration. In contrast, mineral phenocrysts other that quartz and the groundmass are both strongly altered.

The quartz phenocrysts are usually between 1 to 2.5 mm in size. They show subidiomorphic shapes of high-temperature β-quartz (hexagonal dipyramids), as well as corrosion embayments, which clearly indicate an early magmatic origin.

3.2 Location of the investigated samples

To achieve a representative sampling of all rock units, hydrothermal alteration, and mineralization features at the Zaldívar deposit, 89 samples were collected in the main pit. 25 of these samples were taken from benches 3170 and 3140 (the lowest bench at the time of sampling) (Fig. 3-1). In order to have also a good coverage of the ore body at depth, 23 diamond drill cores were sampled at their upper, middle and lower levels, totaling 64 samples. From the total number of samples, 29 correspond to the Zaldívar porphyry, 38 to the Llamo porphyry, 15 to the andesites, and 7 are from the breccia bodies.

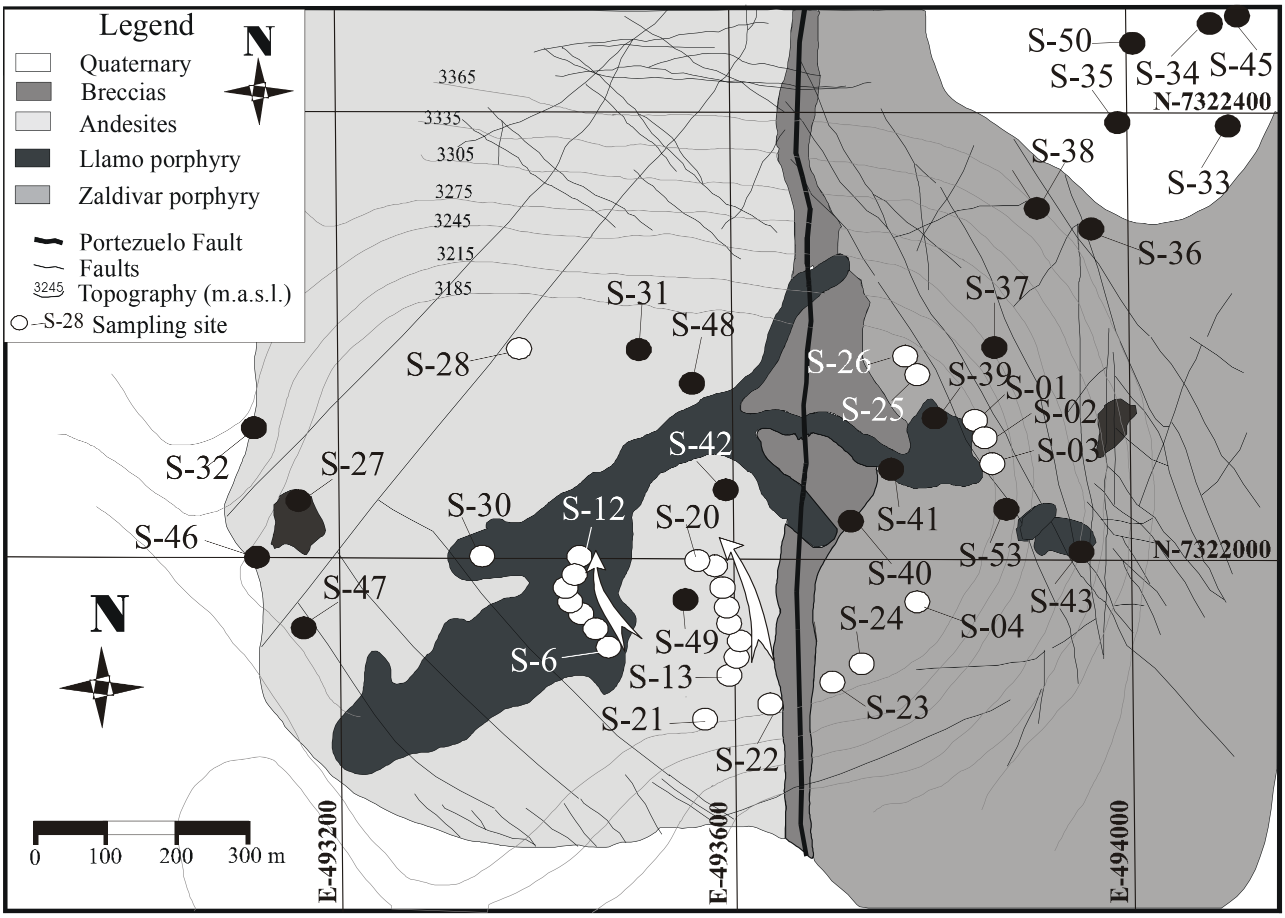

Figure 3-1. Geological map of the Zaldívar deposit indicating the sampling sites. Open circles are surface samples; filled circles are samples from drill cores.

3.3 Sample preparation

For the study of melt and fluid inclusions, quartz phenocrysts where collected in samples from the Llamo and Zaldívar porphyries. Samples were crushed in a steel jaw crusher, pulverized in a disc mill, sieved to a size between 2 and 0.5 mm, washed to remove the fines, and finally dried. Subsequently, handpicking under a binocular microscope resulted in around 100 single quartz grains that were mounted on EPOXY resin following the procedure described below (Fig. 3-2).

Single quartz grains were placed over a double-sided adhesive tape attached to a glass, within an area of about 3 cm in diameter, then the grains were embedded in EPOXY resin using a plastic mold of around 3.5 cm in diameter. After a hardening period of 24 hrs, the resin block was remove from the mold and the grains were polished on both sides at a thickness of about 300 μm in the way described by Shepherd et al. (1985). For analytical procedures individual, doubly-polished grains were taken off from the resin and then thoroughly cleaned with acetone and alcohol to remove all the resin.

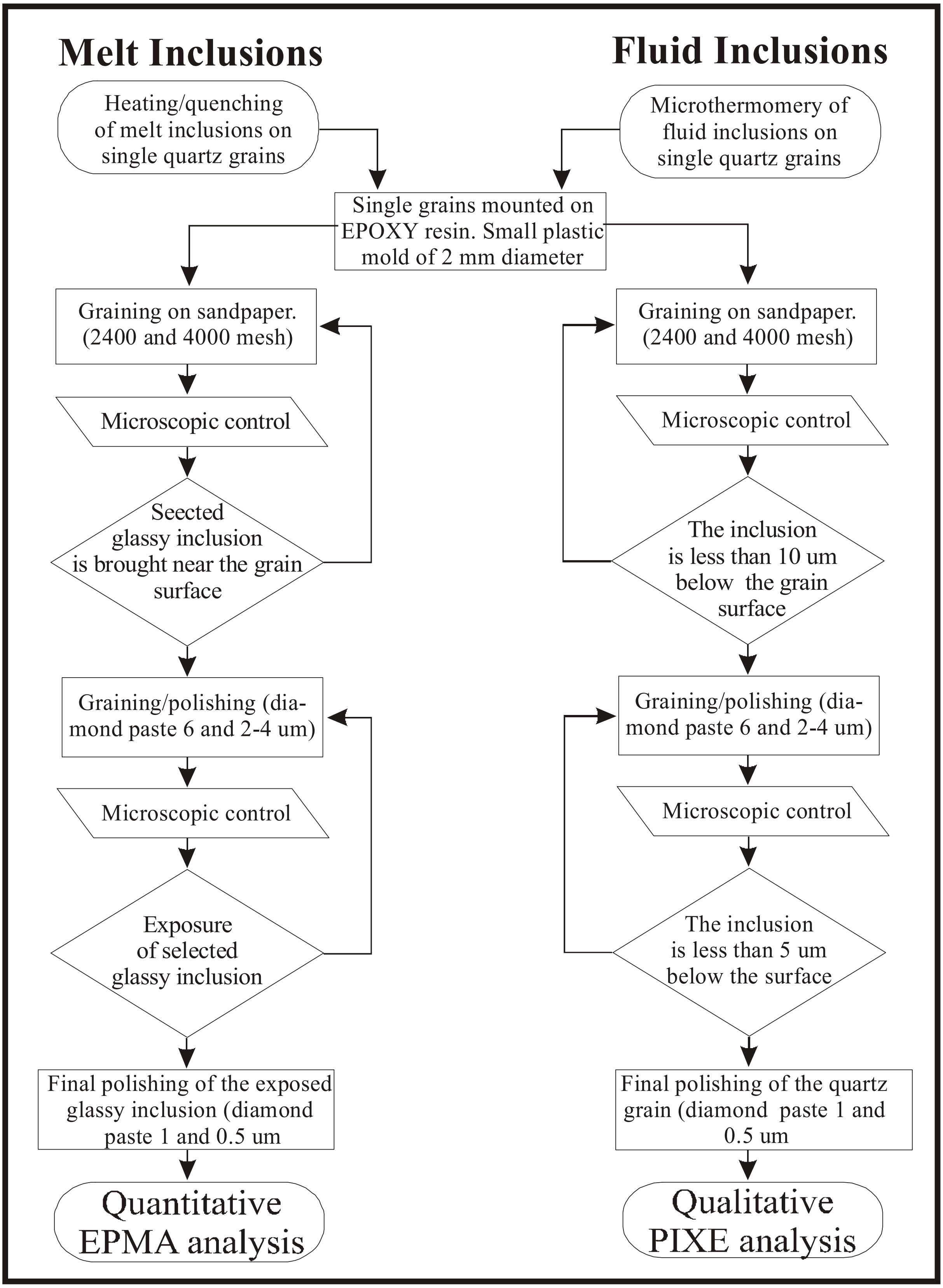

Figure 3-2. Sample preparation procedures of single quartz grains containing melt and fluid inclusions for EMP and PIXE analysis, respectively.

After microthermometry and heating/quenching procedures, a number of fluid inclusions and quenched glass inclusions were selected for further PIXE and EMP microanalysis, respectively. However, because the sensitivity of the PIXE is strongly influenced by the absorption of the induced X-rays by the enclosing mineral, the selected fluid inclusions had to be brought to less than 10 µm from the surface. Also in the case of quenched glasses, they have to be exposed at the surface to be analyzed by EMP. To safely bring the fluid inclusions to the surface, and expose the quenched glass, a hand polishing procedure was applied.

For the hand polishing, selected host grains were individually embedded in EPOXY resin using small plastic molds of 0.5 mm diameter, further on the grains were ground on silicon carbide paper (#2400 and #4000) and polished with diamond polishing compounds (6 µm, 2 µm, and 1 µm). This procedure was carried out with repeated microscope control (Fig. 3-2). The EPOXY molds have to be less than 20 mm in height to allow the wheel target holder of the PIXE to turn freely inside the microbeam chamber (see description of the PIXE).

3.4 Fluid/melt inclusion studies in mineral phenocrysts: some general considerations.

Especially in high-temperature microthermometric research (above 600°C), the traditional technique for fluid/melt inclusion studies is tedious, time consuming and usually, measurements can only be performed on a small number of inclusions. A constant problem is then the representativity of the relatively few inclusions that can be investigated in detail, against the very large number of inclusions occurring in natural samples.

As described in a number of publications, the basic procedure to minimize this problem is to define "Fluid Inclusion Assemblage" (FIA) (e.g. Goldstein and Reynolds, 1994; Ulrich et al., 2001). FIA will correspond to closely associated groups or trails of inclusions supposed to share a number of identical features such as constant composition (visually identical phase ratios) and similar shape (Goldstein and Reynolds, 1994).

This definition implies, that inclusions occurring in small number (single or few individuals) should be neglected, as they lack the counterpart to test the group homogeneity. But it must also be remembered that many inclusions may have suffered some kind of “post-trapping evolution” after initial formation (Roedder, 1984). In most, if not all cases, these post-trapping changes modify the fluid density, as well as the inclusion shape, but much less the fluid composition. This indicates that all criteria used for the definition of a FIA as described above have not the same value: synchronicity and fluid composition are much more important than fluid density, whose homogeneity requires to be tested separately.

For these reasons, the procedure developed in the Vrije Universiteit Amsterdam gives the greatest importance to inclusion chronology, under the concept of "Groups of Synchronous Inclusions" (GSI) (Touret, 2001). The location of each measured inclusion is carefully recorded, through elaborate drawing procedure, in order to be able to come back at any time to a given inclusion and eventually modify a former interpretation in light of additional data (e.g. Fonarev et al., 1998; Fu, 2002). In the present study, this general procedure had to be adapted to the specific character of inclusions hosted in quartz phenocrysts that occurs in small domains (typically few mm in size), in which two fundamentally different groups of inclusions may be present:

- Very abundant hydrothermal fluid inclusions (homogenization temperatures below 600°C). These inclusions are well known in Cu-porphyry systems (e.g. Roedder, 1971; Moore and Nash, 1974), and they can be treated according to the general fluid inclusion procedure (Chapter 10).
- High-temperature inclusions, either highly saline fluids (MS-type) or melt, which homogenize at temperature up to ca. 1000°C (Chapters 8 and 9 respectively) are rare, occurring as few individuals in not all studied phenocryst. The highly saline fluid inclusions, especially, occur typically as single or groups of very few inclusions, in an almost inclusion-free domain. But their microthermometric behavior is quite constant and repetitive in different phenocrysts, and as a whole

they constitute a perfectly defined inclusion group, despite their small number in a single phenocryst.

3.5 The instruments to study melt and fluid inclusions

3.5.1 Heating/quenching stage

For all those microthermometric measurements that required temperatures above 500°C, notably melt inclusions, heating runs were conducted on a high-temperature heating/quenching stage (upper heating limit 1500°C) developed by A. B. Slutsky and A. V. Sobolev (Sobolev et al., 1980) (Fig. 3-3-A). The application of this particular type of heating stage to the study of PCDs can be of great help to reveal the occurrence of metals in the magmatic environment, and to constrain the timing of the magmatic exsolution of volatiles and metals. It may also be very useful to unravel the chemistry of magmatic aqueous ore fluids and how the evolution of these fluids is related to mineralization before its transformation into hydrothermal solutions, bridging the gap between silicate melts and fluids in hydrothermal ore deposits.

The heating/quenching stage consists of a gas-tight sealed body cooled by running water, a heating element, and a metallic sample holder. A screwed lid with a quartz glass window covers the top of the stage body. The basic outfit of the stage corresponds to the platinum-alloy heating element that has a cylindrical shape (2 mm in diameter), free of ceramic insulation (Fig. 3-3-B). A ring-shaped metallic sample holder is set within the heating element at the middle of this height. On this stage the temperature is measured with a $Pt\text{-}Pt_{90}Rh_{10}$ thermocouple (accuracy +/- 5^oC) calibrated with the melting point of gold (99.9 % purity). The wires of the thermocouple are welded to the sample holder, very close to the sample to be measured. A millivolt display is used to measure the temperature.

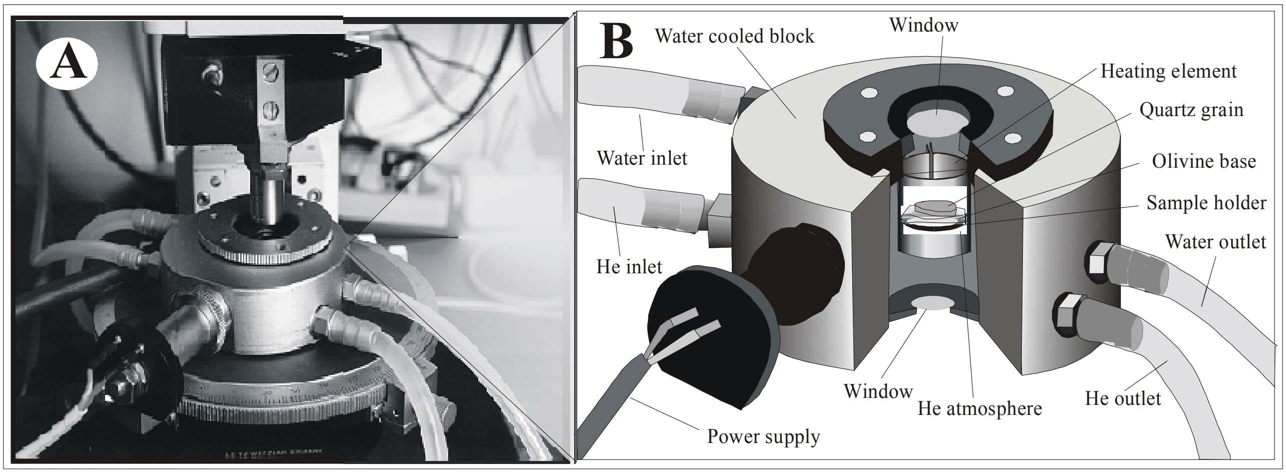

Figure 3-3. A) The heating/quenching stage. B) Detail of the heating element

The operational procedure is as follows: A double-sided polished mineral grain, or a sample chip not larger than 1.5 mm in diameter is loaded inside the heating element, on a thin transparent base in the sample holder, in this case is also a double-sided olivine crystal of 0.3 mm thickness. Then the stage is closed, and after one minute (needed to establish the He atmosphere), the temperature is increased at a rate of between 30 and 60°C/min, until the first crystal begins to dissolve within the inclusion. Further heating is done at a rate of about 5°C/min, until the crystal dissolution or total homogenization is reached. During heating runs, phase transitions were monitored by a video camera and a monitor.

All heating runs are performed in a He-atmosphere, with the He being purified by a 700°C Ti filter. The measuring procedure on this stage is described in detail by Sobolev and Danyushevsky, (1994).

On this stage quenching is achieved by switching off the power supply. Due to the low thermal inertia of the heating system the average cooling rate from maximal temperature to 900°C is about 500°/sec. This procedure allows for obtaining ideally quenched glasses.

3.5.2 Electron microprobe

Concentration of major elements of quenched glasses (melt inclusions) were analyzed using a JEOL JXA-8800 instrument, equipped with four crystal spectrometers, at the following conditions: acceleration potential of 15 kV, beam current of 10 nA, probe diameter between 3 and 10 µm. Natural minerals, synthetic oxides, and MORB glass (JDF-D2#2, Lamont-Doherty Earth observatory of Columbia University) were used as standards.

It was also possible to use, when necessary, an energy-dispersive X-ray analysis system (EDS) attached to the EMPA.

During each measuring run, we took the greatest care to minimize analytical “wall” effects, which are directly related to the small size of the inclusions and the integration of part of the host crystal during the analysis. Therefore, the spot size of the electron beam was always set in the center of the quenched melt inclusion. Moreover, the spot size was always smaller than the diameter of the inclusion exposed on the surface. Also, we analyzed selected inclusions several times, polishing down between each new measurement, always with consistent results, which were within the limits of the analytical error.

3.5.3 Heating/freezing stage

Conventional heating/freezing procedures on fluid inclusions were carried out with a Linkam TP/91-THMS 600, nitrogen-cooled stage (working temperature range: –200° to 600°C), assembled on an Olympus microscope. A video camera and a monitor followed the measured phase transitions. Several experimental runs were also recorded in a VHS video recorder (Fig. 3-4).

During the cooling procedure, all inclusions were first cooled down to almost –190°C, to observe the occurrence of species nucleating at temperatures below zero, and thereafter heated to define the temperatures of first melting (Te) and final ice melting (T_{IM}). After the cooling procedure, inclusions were heated in order to obtain the dissolution temperature of halite (Ts_h) and sylvite (Ts_s) when appropriate, and the homogenization to liquid (T_{HL}) or vapor (T_{HV}).

Temperature measurements were calibrated at low temperature using natural fluid inclusion samples (Calanda, Western Alps) with known phase transitions at –56.6°C (triple point of CO_2), and at 0.0 °C (triple point of pure H_2O). Freezing rates varied between 50° and 30°C/min. The precision of temperature measurements was obtained by replicate measurements and was within ± 5°C on the heating runs (between 30° and 500°C), and ± 0.2° C in the freezing runs (between -60° and 30°C).

Re-measurement of a number of homogenization temperatures (T_H) after freezing reproduced the initial results, indicating that the inclusions did not stretch.

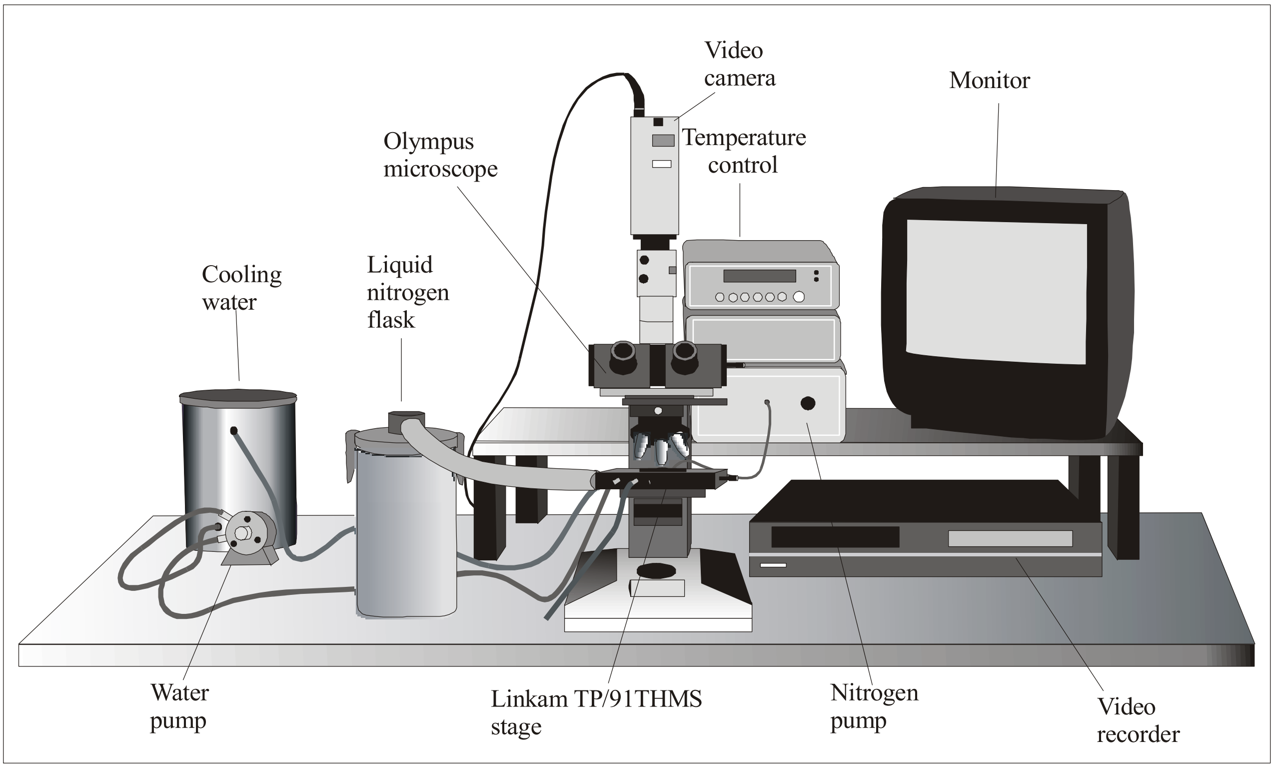

Figure 3-4. Setting of the Linkam stage at the VUA

3.5.4 Proton-induced X-ray emission (PIXE)

On the nuclear microprobe installed at the VUA, the production of the PIXE micro-beam begins with the generation of protons in the alphatross ion source (Fig. 3-5) (Vis et al., 1993). The protons are negatively charged by passing through a channel filled with rubidium gas, and then the negative ions are accelerated through a 30 kV voltage, and focused into a proton beam that will enter the accelerator.

The acceleration of particles is done in a 5-SDH-2 NEC tandem pelletron accelerator using a maximum terminal voltage of 1.7 MV (Vis et al., 1993). After acceleration a set of quadrupole magnets focus the beam, which is then guided to the micro-beam line (Fig. 3-5-A and B). The micro-beam line consists of three high-precision slit systems, adjustable between 0 and 100 µm, followed by a high-precision magnetic quadrupole doublet system to focus the beam down to the final spot, (in the present case about 5 µm in diameter). Emitted X-rays are detected with a high-purity Ge detector (Ortec-Iglet) that is placed at an angle of 135° with respect to the incoming beam (Vis et al., 1993). To suppress the count rate of the Si X-rays from the host mineral, an aluminum filter (30 µm thick with a 1 mm hole) was placed in front of the detector.

Data acquisition is done in list mode and the recorded X-ray spectra are analyzed by means of the computer code GUPIX, which fits peaks to the calculated intensities. Spectra are recorded with a UNIX-based real-time data-acquisition system.

The target chamber (Fig. 3-6) contains several parts to facilitate the focusing of the beam and observing the target. To determine the beam and target position accurately, a mirror is used with a 1 mm hole in the center through which the beam passes. The focusing of the beam is accomplished by placing a quartz target that emits light when hit by the beam. There is also a long-working distance transmitted-light optical microscope with a maximum magnification of 200x, which allows indirect observation of the target positioning (Fig. 3-6). The illumination of the target inside the micro-beam chamber is carried out by means of a glass fiber connected to the Schott KL 1500 light source placed outside the chamber. A video camera mounted on the microscope allows the observation of the target on a monitor that makes it easy to search for previously selected inclusions in the target.

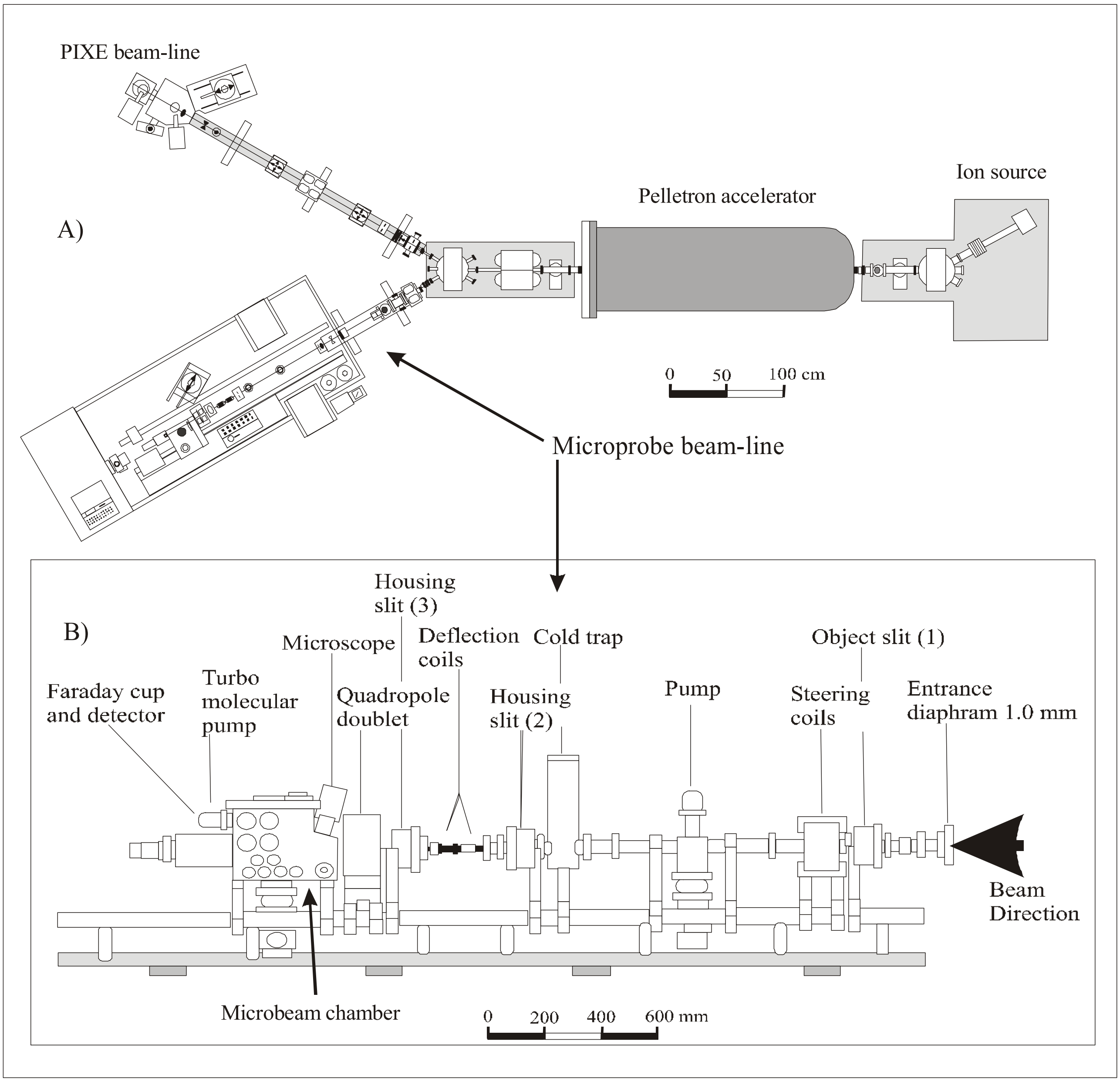

Figure 3-5. A general scheme of the micro-beam setup at the VUA (A), also showing an schematic drawing of the micro-beam chamber (B).

The targets (samples in EPOXY mold) are mounted on aluminum frames (Fig. 3-6) that are later placed in the target chamber on a target wheel that can accommodate eight targets. The target wheel is mounted on a high-precision motor-controlled XYZ-stage with a positional accuracy of 1 µm, this permits the target wheel to rotate remotely for 360° in 480 steps allowing the positioning of the selected target under the beam, and the focusing of the target.

All inclusions were analyzed using an irradiation time of 10 minutes. PIXE analyses were done on single inclusions already studied by microthermometry.

For further description of the PIXE at the VUA, see Damman et al. (1996), and Vis et al. (1993).

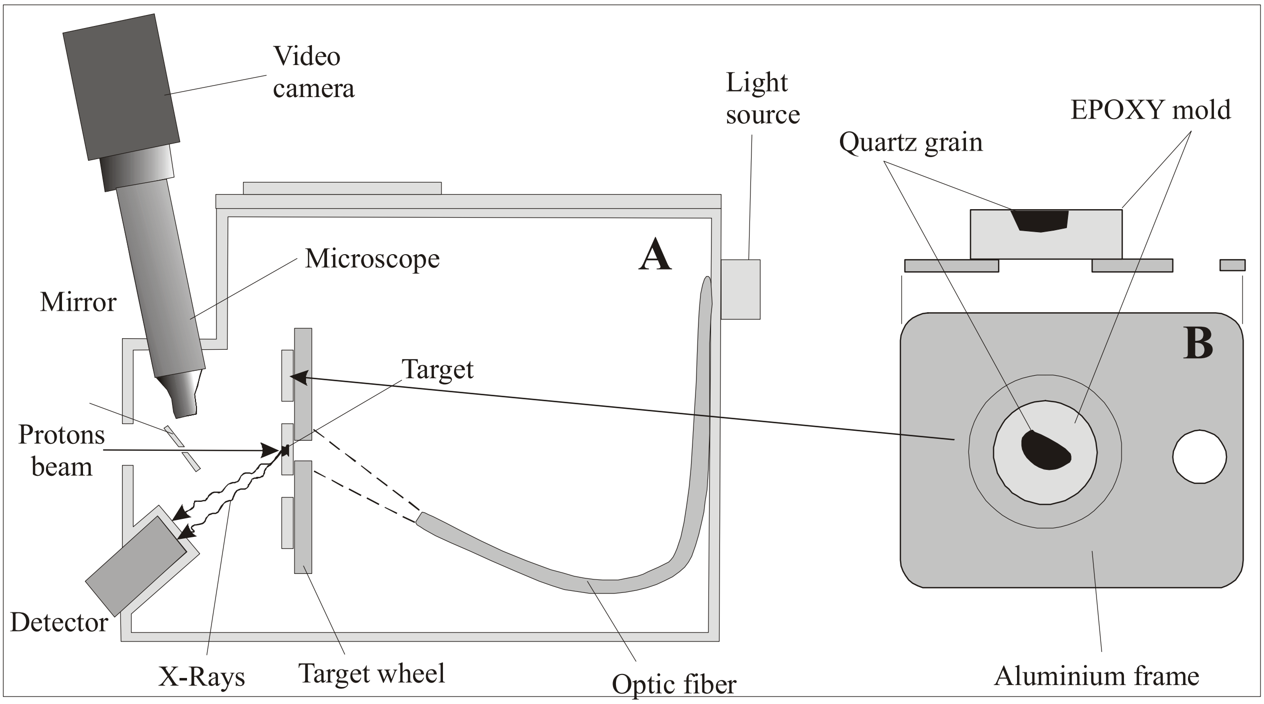

Figure 3-6. Diagram showing the target chamber (A) and the aluminum frame containing the mounting of the plastic mold with the quartz grain (B).

3.5.5 Raman analysis

The Raman microspectrometer installed at the VUA is a multi-channel Microdil-28 of Dilor S.A. For the analysis of fluid inclusions, an Olympus research-grade microscope has been coupled to the instrument.

Raman analyses were carried out on several fluid inclusions to identify Raman-active daughter minerals, polyatomic gases or polynuclear species in solution.

3.6 ^{40}Ar/^{39}Ar geochronology

Laser step heating and spot fusion experiments were carried out at the argon laser probe facility in the Laboratory of Isotopic Geology, Vrije Universiteit Amsterdam. The instrument consists of a 24W CW argon ion laser, a low volume UHV gas inlet system and a MAP 215-50 noble gas mass spectrometer. All isotopes are measured using a Johnston MM1 secondary electron multiplier (SEM) collector operated at gain 5×10^3. For a detailed description of the argon laser probe see Wijbrans et al. (1995)

For spot fusion experiments the laser beam is focused to an appropriately small diameter to deliver sufficient energy to the sample to produce melt spots ca. 50 µm in diameter. Then the sample is exposed to several laser pulses of approximately 0.1-second duration.

During incremental heating, argon extraction was performed by using a defocused continuous laser beam with a spot size of ca 3 mm, sufficient to cover the whole sample holder and ensure uniform heating of the grains. On every single gas extraction, samples were heated on six 1-minute steps in laser power settings between 0.3 W and 1.4 W, the next step was the final fusion of the micas. Each spot fusion or heating step experiment was analyzed after four minutes of clean-up time. The evolved gas was admitted into the mass spectrometer where simple expansion ensures transfer of more than 90 % of the argon for isotopic measurement. The gas was measured isotopically by stepping the magnet current at half mass intensity from 40 to 35.5 argon masses.

Blanks intensities were measured routinely every four measurements, providing 6 blank analysis for one measuring day, allowing a good evaluation of argon blank intensities and reproducibility.

Chapter 4

Petrography and Geochemistry

4.1 Petrography

4.1.1 The Zaldívar porphyry

All samples from the Zaldívar porphyry have rather similar textural features; however, major differences are observed when considering the type and degree of hydrothermal alteration affecting the phenocrysts and the groundmass (Fig. 4-1). Petrographic descriptions of 21 samples from the Zaldívar porphyry are presented in Appendix 1 (Table 4-1).

On the basis of an overall petrographic description, this intrusive unit is characterized by a coarse to medium porphyritic texture, with phenocrysts representing between 20 to 50 % of the rock (most commonly 30%). Out of this percentage, less than 10 % corresponds to quartz phenocrysts. Because of the strong hydrothermal alteration affecting the plagioclase and K-feldspar phenocrysts, only a rough approximation can be made of their relative abundance based on the occurrence of ghost crystals, which is between 60 to 80 % (Fig. 4-1). Evidence of ferromagnesian minerals has not been observed in all the studied samples.

The groundmass is in general very fine-grained, consisting apparently of feldspar and quartz, representing up to 70 % of the rock. The primary mineral composition of the groundmass is normally obliterated by the hydrothermal alteration, which can vary from weak replacement by clay minerals to complete obliteration by pervasive phyllic and/or argillic alteration (Fig. 4-1).

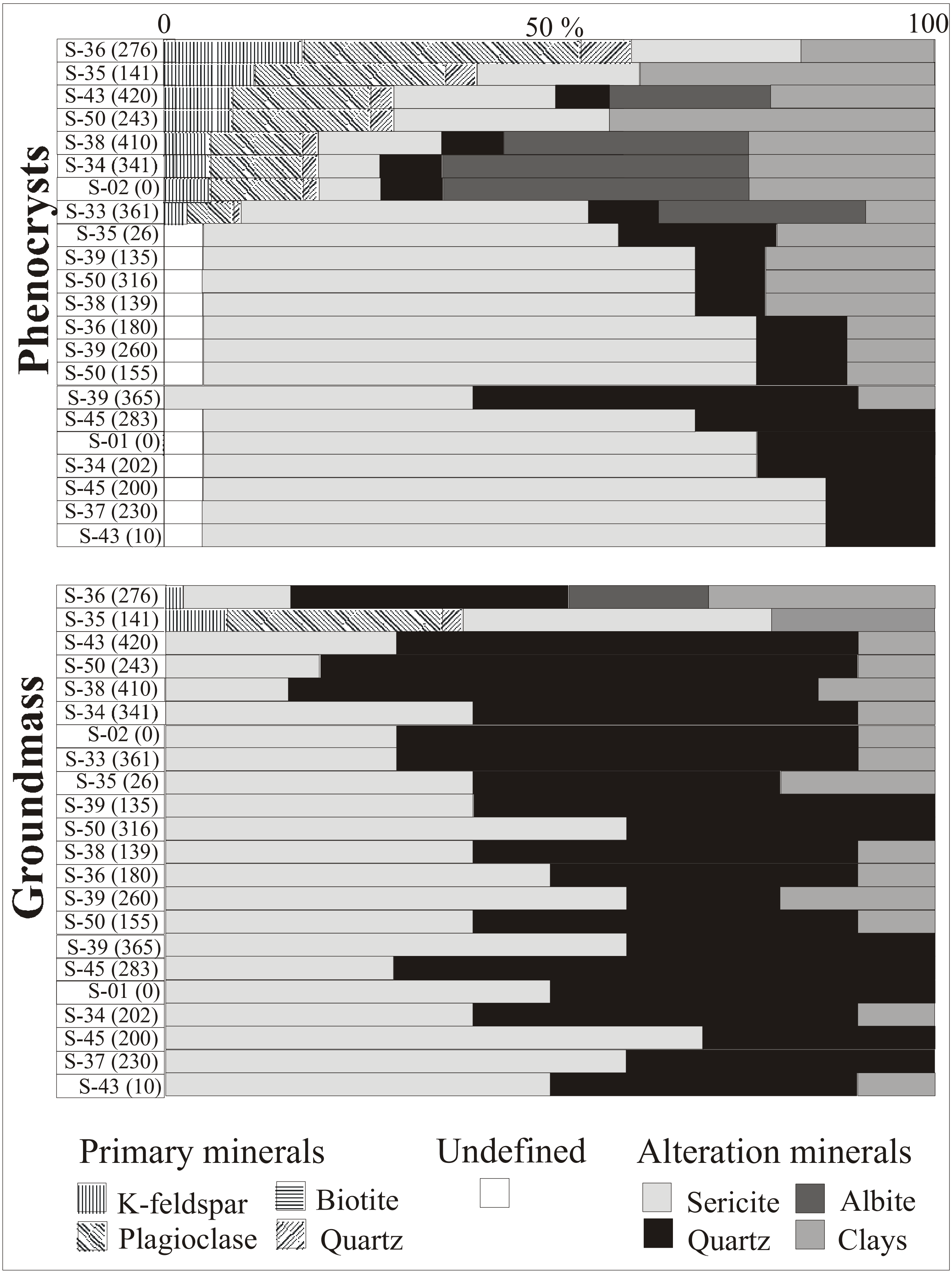

Figure 4-1. Relative abundances of primary and secondary minerals in the samples from the Zaldívar porphyry. For more details on the petrographic description, see Appendix 1, Table 4-1.

4.1.1.1 Plagioclase

Plagioclase phenocrysts are the most abundant in all studied samples, they usually occur as tabular idiomorphic to subidiomorphic crystals up to 4 mm in size. These phenocrysts are most sensitive to the effects of hydrothermal alteration, which can modify their primary mineral composition to different degrees. In general the alteration may vary from weak argillization with minor sericite, to strong pervasive phyllic alteration (Fig. 4-1 and 4-2).

Despite the effects of hydrothermal alteration, remnants of primary features of plagioclase crystals can be observed, such as the tabular shape and the characteristic polysynthetic twinning (Fig. 4-2-A). However, when the hydrothermal alteration is stronger, no relic of the primary mineralogical composition can be found and most grains occur as ghost crystals filled up with fine-grained secondary sericite-quartz, or clay minerals assemblages (Fig. 4-2-B, and -D).

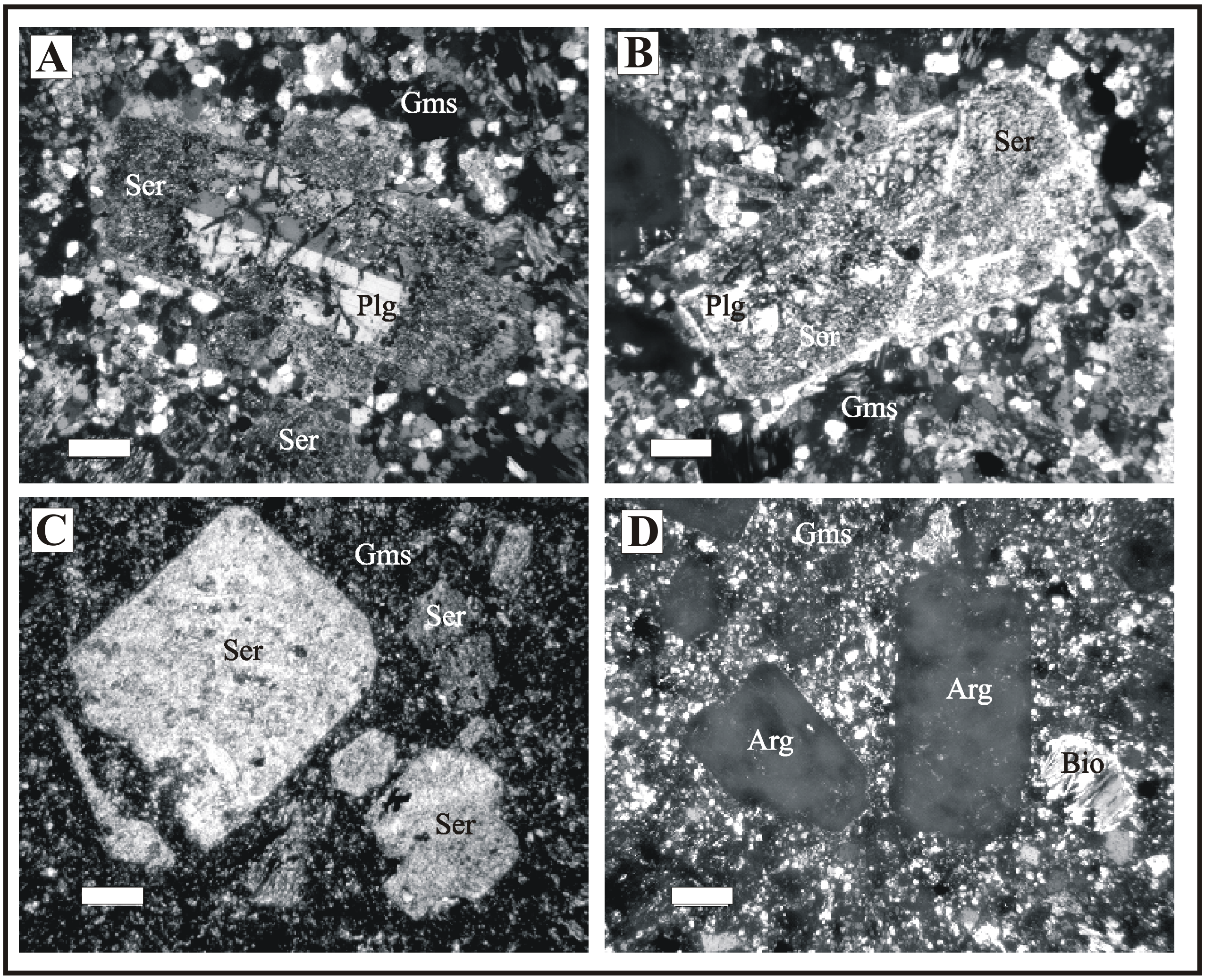

Figure 4-2. Plagioclase phenocrysts showing different degrees of sericitization by hydrothermal alteration from medium (A), strong (B) to a complete replacement (C). The groundmass corresponds to a fine-grained quartz-sericite assemblage. Also shown are former plagioclase phenocrysts completely altered to clay minerals (D). Plg: plagioclase; Ser: sericite; Kao: kaolinite; Bio: biotite; Gms: groundmass. Scale bar 200 µm.

4.1.1.2 K-feldspar

K-feldspar phenocrysts are the second most abundant in all samples, they may occur as single isolated grains or intergrown with plagioclase and/or other K-feldspar phenocrysts. Idiomorphic to subidiomorphic, usually K-feldspar crystals are smaller than 5 mm.

Despite the relative abundance of K-feldspar phenocrysts, remnants of the original composition of the mineral can be seen only in few samples (Fig. 4-1). In most cases the strong hydrothermal alteration completely transformed the composition of the grains (Fig. 4-2-C).

Hydrothermal alteration of K-feldspar varies from a weak argillization to strong sericitization (most samples) (Fig. 4-1). In the most strongly altered samples, the K-feldspar crystals have been completely replaced by sericite or clay minerals, leaving a ghost crystal as the only evidence of the primary mineral (Fig. 4-2-C). In the strongly altered samples the occurrence and abundance of K-feldspar phenocrysts can only be estimated by means of the shape of the ghost phenocrysts, namely subquadrangular. Furthermore, the occurrence of these phenocrysts can also be estimated by the composition of alteration minerals. Usually K-feldspar have show a higher concentration of sericite than plagioclase.

4.1.1.3 Quartz phenocrysts

Most quartz phenocrysts occur as single crystals, usually showing idiomorphic to subidiomorphic, or well-rounded grain shape (Fig. 4-3-A and –C), always smaller than 5 mm. In nearly all these phenocrysts, the crystal boundaries are strongly corroded and show embayments or corrosion gulfs (Fig. 4-3-A-B and -C), features that indicate magmatic corrosion.

Quartz phenocrysts frequently exhibit a marked undulatory extinction, some are also broken or cross-cut by microfractures (Fig 4-3-B). Frequently these microfractures are filled-up with sericite or fine-grained secondary quartz.

All quartz phenocrysts are crowded with inclusions, most of these correspond to fluid inclusions, but it is also possible to find opaque minerals as well as sericite inclusions. The latter may correspond to a sericite filling of microfractures in the host crystal. Also frequently observed in quartz phenocrysts are rounded to elongate inclusions of altered material, which may correspond to former melt inclusions (Fig. 4-3-A and -B).

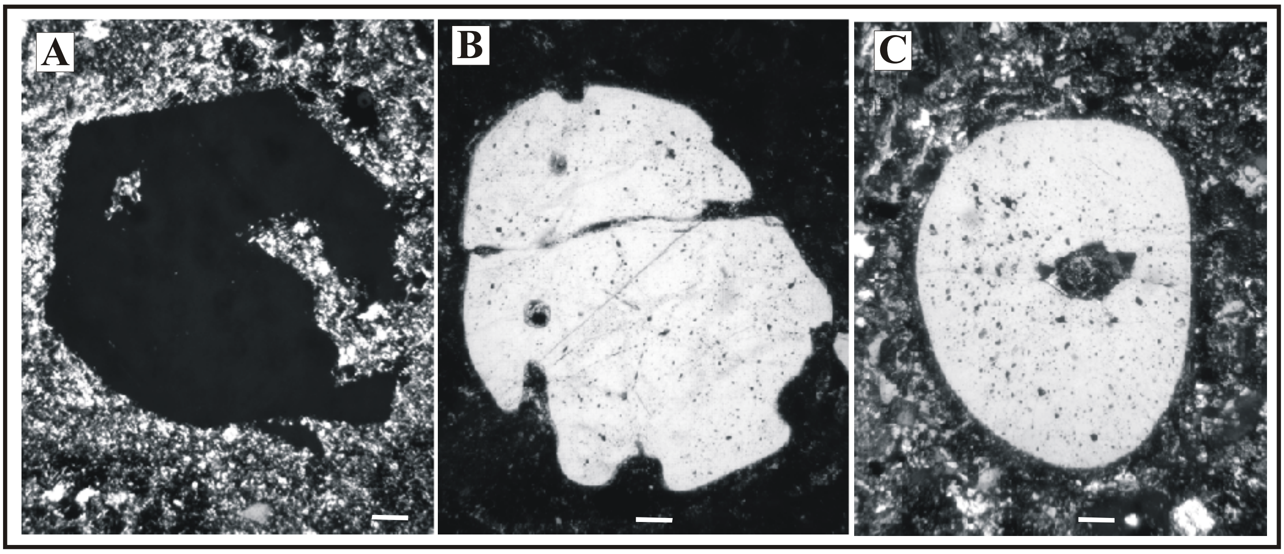

Figure 4-3. Different shapes of quartz phenocrysts, nearly idiomorphic (A) to well rounded (C). Corrosions gulfs are a normal feature in most igneous quartz phenocrysts (A, B and C). Scale bar 200 µm.

4.1.1.4 Other phases

Rutile, zircon and apatite are normally present as accessory minerals.

4.1.2 Andesites

Rocks from the Andesite unit have an aphanitic to fine-grained porphyritic texture and are greenish-gray to dark-gray in color. When the porphyritic texture is present, the rock normally contains less than 25 % of phenocrysts corresponding mainly to plagioclase and less K-feldspar. The phenocrysts are always smaller than 2 mm in length. A few dark-green phenocrysts smaller than 1 mm are also present, they show a quadratic to rounded shape, and may correspond to biotite. The petrographic description of the Andesites is presented in Appendix 1, Table 4-2.

The phenocrysts are presented within a very fine-grained groundmass that is mainly made up of plagioclase crystals representing about 70 % of the sample. Within the groundmass, K-feldspar is not easily recognized since it is strongly albitized and later altered to secondary clays and quartz, with also small amounts of sericite (Fig. 4-4). Also all primary micas (most likely biotite) are completely altered to chlorite and clay minerals.

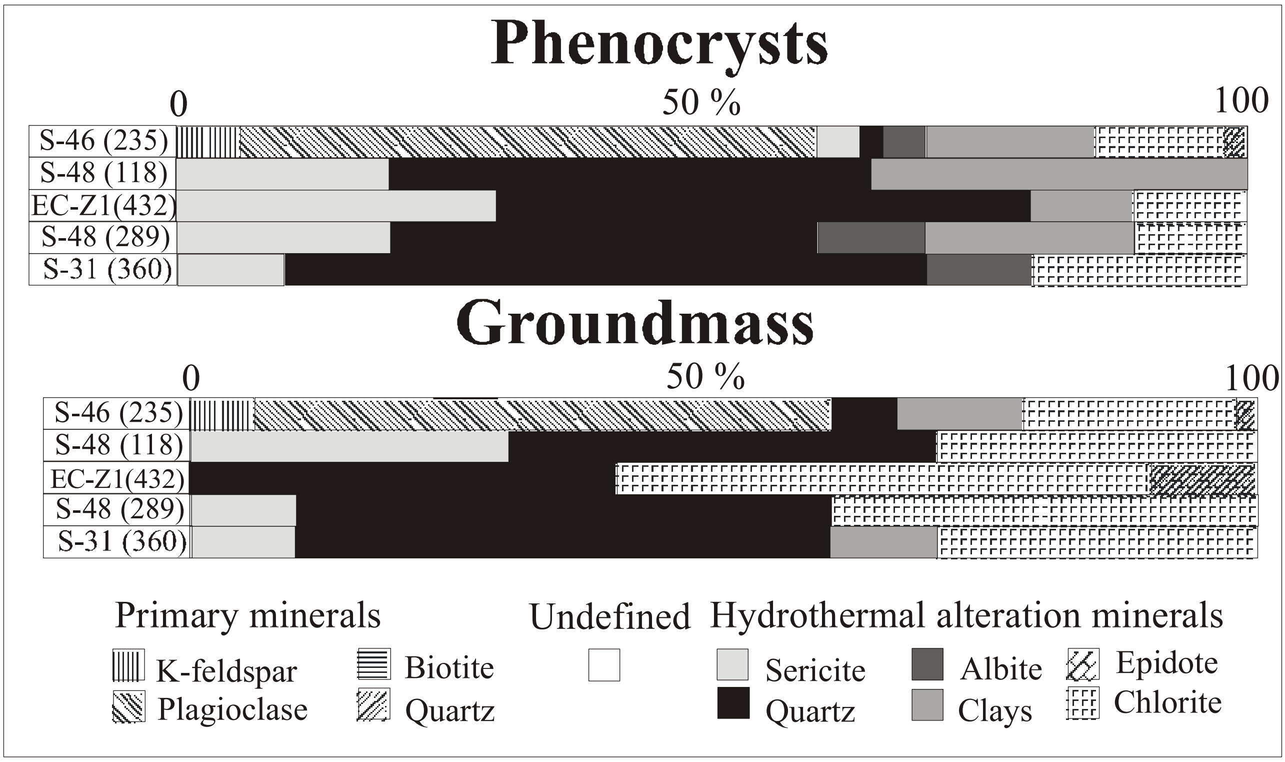

Figure 4-4. Relative abundances of primary and alteration minerals in samples from the Andesites unit. For more details on the petrographic description, see Table 4-2 in Appendix 1.

4.1.2.1 Plagioclase

Plagioclase phenocrysts are the most abundant in the sample, they usually show a euhedral rectangular to quadratic shape and also well-defined polysynthetic twinning. The size of these phenocrysts varies from 0.4 up to 2.0 mm, most commonly around 1 mm, and they may occur as isolated phenocrysts or intergrown with several grains.

4.1.2.2 K-feldspar

K-feldspar phenocrysts are less abundant than plagioclase and not larger than 2.0 mm in length. They show a strong replacement by albite, clays and sericite. Few relics of the original composition have been observed, in most cases only the shape of ghost crystals and the level of alteration allows the identification of these phenocrysts.

4.1.2.3 Biotite

Biotite forms the least abundant phenocrysts in the sample. They are strongly altered to chlorite and clays, in fact the only way to recognize a former biotite phenocryst is by its complete transformation to massive chlorite and opaque minerals produced by the hydrothermal alteration.

4.1.2.4 Other phases

Zircon and apatite are minor magmatic phases that occur disseminated in the groundmass.

4.1.3 The Llamo porphyry

The petrographic description of 24 samples from the Llamo porphyry unit has shown that all these samples share similar primary magmatic features and compositional characteristics, the main differences among them being the type and intensity of hydrothermal alteration (Appendix 1, Table 4-3). The alteration varies from selective potassic hydrothermal alteration, in which most primary features are slightly modified, to a strongly pervasive argillic supergene alteration completely replacing the primary components and textures by a massive assemblage of kaolinite with minor sericite and quartz.

The following general petrographic description is based on three of the least altered samples from the Llamo porphyry unit. They exhibit a coarse to medium-grained porphyritic texture, in which the phenocrysts, always smaller than 6 mm, represent between 60 to 40 % of the total rock. The most abundant phenocrysts are plagioclase and K-feldspar, between 60 to 70% and 30 to 20 % in total respectively. Biotite and quartz phenocrysts represent less than 10 % of the total rock, quartz usually being less abundant than biotite. The phenocrysts are in a crystalline groundmass representing between 60 to 40 % of the total rock mass, this groundmass is made up of a fine-grained mixture of plagioclase, K-feldspar, quartz and biotite. In most samples the groundmass is intensively altered (Fig. 4-5).

4.1.3.1 Plagioclase

In all studied samples, plagioclase represents the most abundant and the largest phenocrysts, which occur as tabular to quadratic idiomorphic crystals up to 6 mm in size, usually showing a characteristic polysynthetic twinning. These phenocrysts may occur as isolated grains or intergrown with several feldspar crystals.

The effects of hydrothermal, alteration modified to different extents the primary composition of the plagioclase phenocrysts, and it is stronger in the smallest grains. These phenocrysts may be weakly or not at all affected by potassic alteration (Fig. 4-5); the main transformation corresponds to the albitization of the anorthitic component and cannot be precisely quantified. The albitization of plagioclase may affect only the rims of some phenocrysts or produce a complete transformation of the anorthitic component of the mineral. Argillic alteration involves a weak to strong argillization with minor sericite that normally progresses through microfractures. In a number of samples the argillic alteration strongly affects the composition of plagioclase phenocrysts, in most cases completely replacing the original mineralogy so that the phenocrysts occur as ghost crystals filled up with fine-grained sericite and secondary quartz (Fig. 4-2-B).

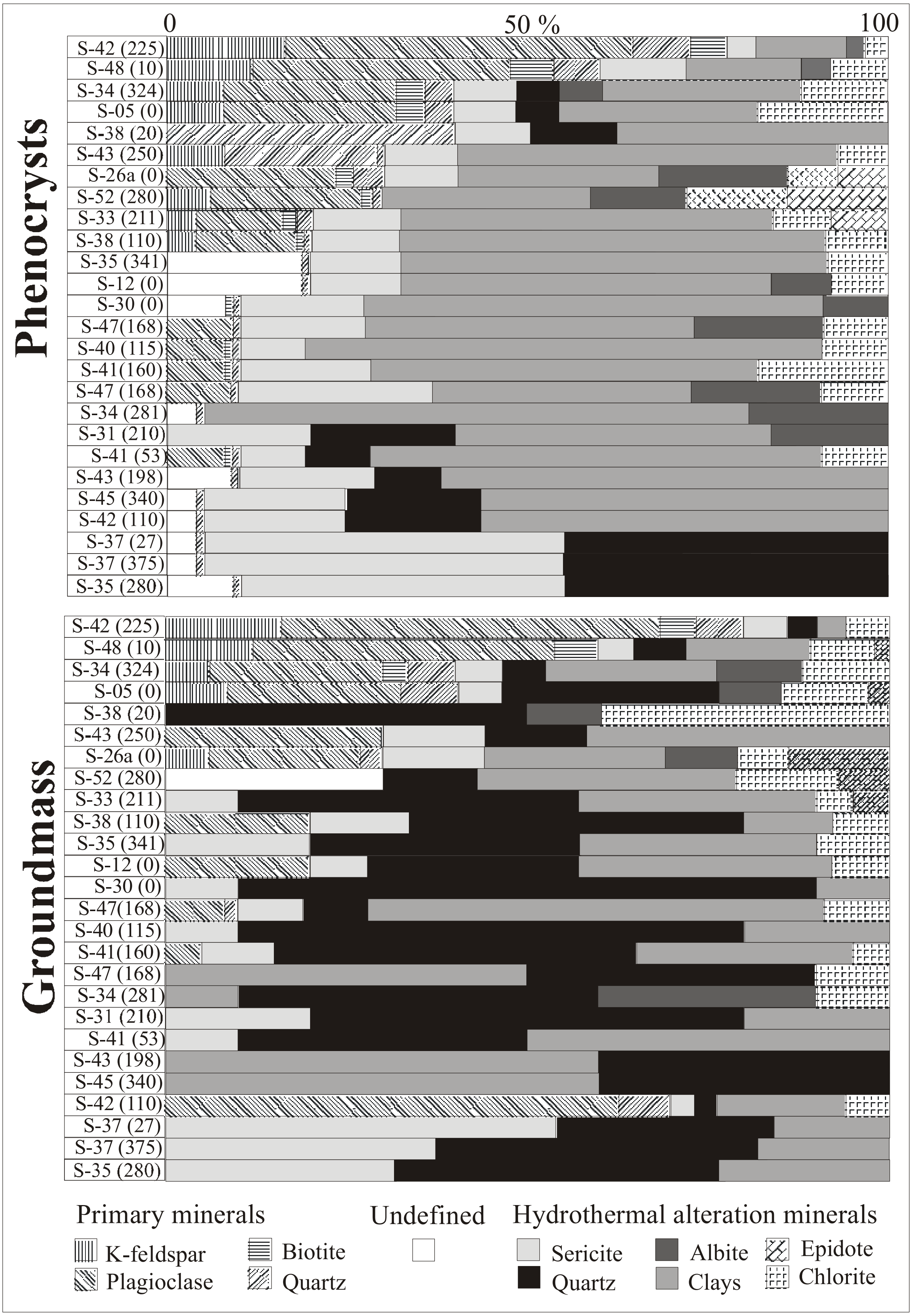

Figure 4-5. Relative abundance of primary and alteration minerals in the samples from Llamo porphyry. For more details on the petrographic description see tables in Appendix 1, Table 4-3.

Fresh plagioclase grains are normally present as mineral inclusions within quartz phenocrysts in which plagioclase is shielded from the hydrothermal fluids. The EMP analysis of these mineral inclusions indicates that the composition of the fresh plagioclase varies from oligoclase to andesine (An24 to An45) whereas the composition K-feldspar is closely similar to the orthoclase type (ca. 6 to 22 % albite, (see Chapter 5) (see Appendix 2, Table 4-4).

4.1.3.2 K-feldspar

K-feldspar phenocrysts are the second most abundant in all samples. These crystals are usually idiomorphic to sub-idiomorphic, smaller than 5 mm, and may occur as single isolated grains or intergrown with plagioclase and/or other K-feldspar phenocrysts.

In several samples primary K-feldspar phenocrysts appear to be unaffected by hydrothermal alteration indicating that they were in the stability field of potassic alteration, whereas in others, kaolinite severely transforms the primary composition of the mineral and only relics of their original composition can be observed. When the primary mineralogical composition of K-feldspar phenocrysts has been strongly argilized, their occurrence and relative abundance can only be estimated by the presence of ghost phenocrysts.

Dominant phyllic alteration has been observed only in few of the analyzed samples, sericite usually occurs as a minor component in the alteration of K-feldspar.

The chemical composition of primary K-feldspar can be obtained from mineral inclusions hosted in quartz phenocrysts that may occur as isolated grains, or associated with plagioclase crystals. The composition of these inclusions corresponds to pure K-feldspar or mixtures of K-feldspar$_{80}$-Albite$_{20}$ (see Appendix 2, Table 4-5). The high silica content in some of the EMP analyses can be explained as a wall effect, in which part of the host (quartz) is incorporated accidentally into the analysis of the K-feldspar.

4.1.3.3 Quartz phenocrysts

Quartz phenocrysts are less than 2 mm in size with a relative abundance of about 5%, being therefore always the smallest and the least abundant of all phenocrysts in a given sample. They occur frequently as round-shaped single crystals, rarely subidiomorphic to idiomorphic, in which the boundaries are strongly corroded, and frequently showing corrosion gulfs as a rather common feature that would indicate perturbations during growth in a magmatic stage.

Microfractures and undulatory extinction are also characteristic features for the quartz phenocrysts usually most evident on the biggest grains. These features are the reflection of the permanent tectonic activity occurring at the mine site.

These quartz phenocrysts frequently contain mineral inclusions such as K-feldspar, plagioclase, apatite, and zircon. The feldspar and biotite inclusions in particular seem to be shielded by the surrounding quartz from the effects of hydrothermal alteration.

Fluid inclusions are always present in these phenocrysts, most of these representing the typical association brine/gas–rich type. Although they may be abundant, they are not so frequent as in the phenocrysts from Zaldívar porphyry.

4.1.3.4 Biotite

Biotite phenocrysts are the third most abundant phenocrysts in the sample, they are idiomorphic to subidiomorphic and smaller than 5 mm.

In all studied samples, biotite crystals are the most sensitive for transformation caused by hydrothermal alteration. In samples affected by propylitic and argillic alteration, they are readily altered to greenish chlorite or clay minerals (Fig. 4-6-B). In the mildly and strongly argillic-altered samples, they are totally replaced by fine-grained kaolinite and minor sericite. Despite the high susceptibility for being altered, in a few samples it was still possible to find grains that contain a relatively fresh core (Fig. 4-6-A).

Completely fresh grains of biotite can easily be found as mineral inclusions hosted in quartz phenocrysts (Fig. 4-6-C). These grains are well preserved, being completely shielded from the effects of hydrothermal alteration (see Appendix 2, Table 4-6).

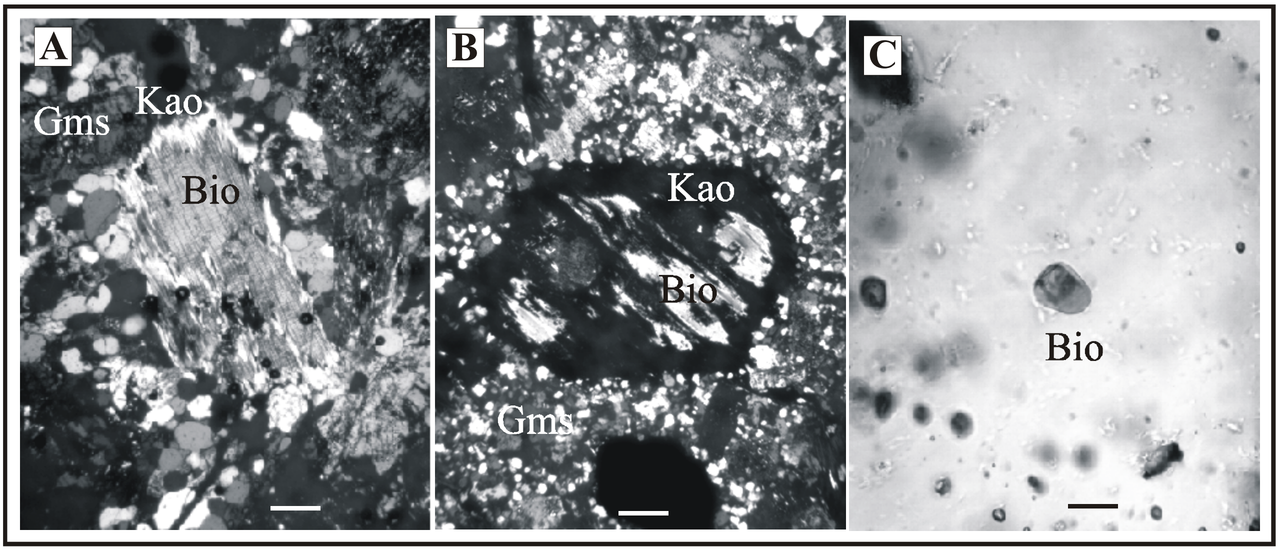

Figure 4-6. Biotite phenocrysts showing weak (A) and strong argillic (B) alteration, phenocrysts are in a fine-grained groundmass made of secondary quartz and sericite. Also shown is a biotite inclusion hosted in quartz phenocrysts (C). Bio: biotite, Kao: kaolinite, Gms: groundmass. Scale bar A and B: 200 µm; C: 50 µm.

4.1.3.5 Other phases

Minor magmatic phases include zircon and apatite, these minerals normally occur disseminated in the groundmass or as inclusions in quartz and biotite phenocrysts.

4.2 Bulk rock geochemistry

Chemical analyses of the major elements of samples from the Andesite unit, the Zaldívar porphyry and the Llamo porphyry were carried out by the Outokumpu mining services (Zaldívar internal report) by X-ray fluorescence (XRF) (Appendix 3, Table 4-7). However, since it is almost impossible to obtain completely fresh rocks, the analyses of these geochemical data must always consider the perturbations due to the effects of hydrothermal alteration.

As indicated from the petrographic studies, pervasive phyllic alteration is the most widespread alteration in all rocks units from the Zaldívar PCD. Conversely a good estimation of the degree of alteration of the samples analyzed by XRF can be made from the degree of sericitization (sericitization index = SI) (MacLean and Hoy, 1991) (Fig. 4-7). In this diagram, the Zaldívar porphyry appears to be most intensively affected by the alteration in comparison with the rocks from the regional magmatism. Slightly less altered are the samples from the Llamo porphyry, and the least altered are samples from the Andesite unit. These results perfectly agree with the petrographic observations.

All analyzed samples from the Zaldívar mine are within the field of the subalkaline series which is also characteristic for an important group of igneous rocks from regional magmatism (Fig.

4-8). All samples are also slightly depleted in total alkalis with respect to other igneous rocks found at a regional scale.

The available geochemical data show that in an AFM diagram, the Llamo porphyry and the Andesite unit are within the calc-alkaline trend, while most samples from the Zaldívar porphyry are on, or near the boundary between the tholeiitic and cal-alkaline fields (Fig. 4-9). Once again, the distribution of the samples from the Zaldívar deposit nearly coincides with the calc-alkaline trend defined by the igneous rocks found elsewhere in the regional magmatism.

Finally on a Harker type K_2O vs. SiO_2 variation diagram all the samples fall in the high-K calc-alkaline series (Fig. 4-10), with the Zaldívar samples being slightly depleted in K_2O compared with the most evolved igneous rocks of the regional magmatism.

Most classification schemes available for intermediate to acid igneous rocks are based upon silica and alkalis contents (e.g., TAS diagram $Si0_2$ vs. Na_2O+K_2O). However, these diagrams are not recommended for rocks that have been altered, since the original alkalis and silica contents may be strongly modified (enriched or depleted) by the hydrothermal alteration. To avoid as much as possible the effects of hydrothermal alteration on the geochemical classification based on major elements composition, the cation percentages of Al, (Fe+Ti) and Mg, were plotted on a Jensen ternary diagram (Fig. 4-11). These elements are more suitable since they are relatively immobile during phyllic alteration (MacLean and Hoy, 1991). According to this classification scheme, all analyzed samples from the Zaldívar porphyry are within the rhyolitic field, the Andesite units are between the andesitic (one sample) and the dacitic field (six samples), whereas samples from the Llamo porphyry are near the dacitic-rhyolitic boundary (Fig. 3-11).

If the samples are plotted on a TAS diagram (Le Bas et al., 1992) (Fig. 4-8), a slightly similar behavior is observed for the Andesite unit, the Llamo samples are clearly within the dacite field and the rhyolites show a strong enrichment in silica, most probably due to hydrothermal alteration.

The Harker variation diagrams (Fig. 4-12) for the three petrological units in the Zaldívar mine indicate a negative correlation between SiO_2 and TiO_2, Al_2O_3, FeO, MgO, CaO, and P_2O_5, and positive for K_2O in the Llamo porphyry and the Andesite unit. These geochemical features are similar to the ones observed by Marinovic et al. (1995) for the igneous rocks that form the regional background of the Zaldívar mine.

A major difference between the geochemistry of the regional magmatism and the samples from the Zaldívar PCD would be the correlation between SiO_2 and Na_2O. This correlation is constant for the regional igneous rocks (Marinovic et al., 1995), negative for the Llamo porphyry, positive for Zaldívar porphyry and non-variant for the Andesite unit.

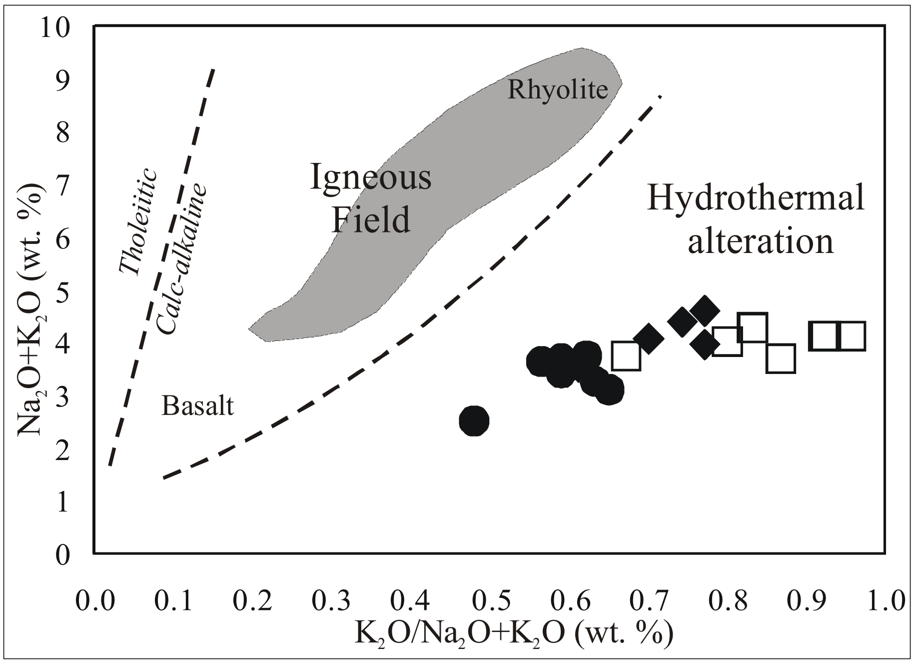

Figure 4-7. Sericitization index (SI) diagram (MacLean and Hoy, 1991; and references therein). Andesite unit (filled circles), Llamo porphyry (filled diamonds), Zaldívar porphyry (open squares)

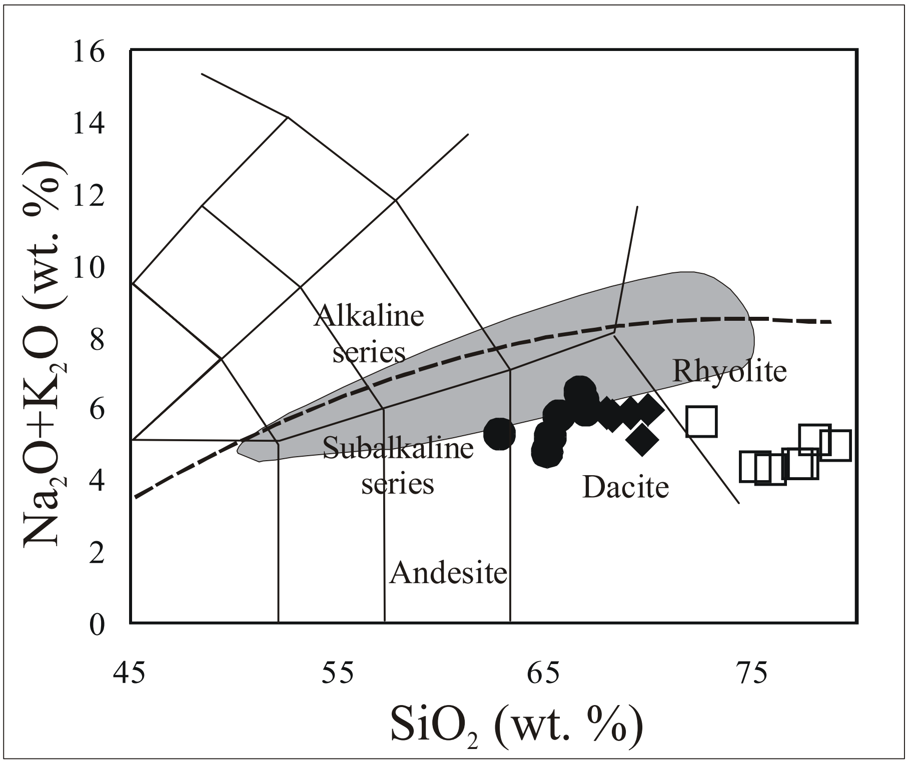

Figure 4-8. Total alkalis versus silica diagram, showing also the fields for TAS rock classification diagram from Le Bas et al. (1992). Alkaline-subalkaline boundary from Irvine and Baragar, 1971 *in* Rollinson, 1993. Symbols as in figure 4-7.

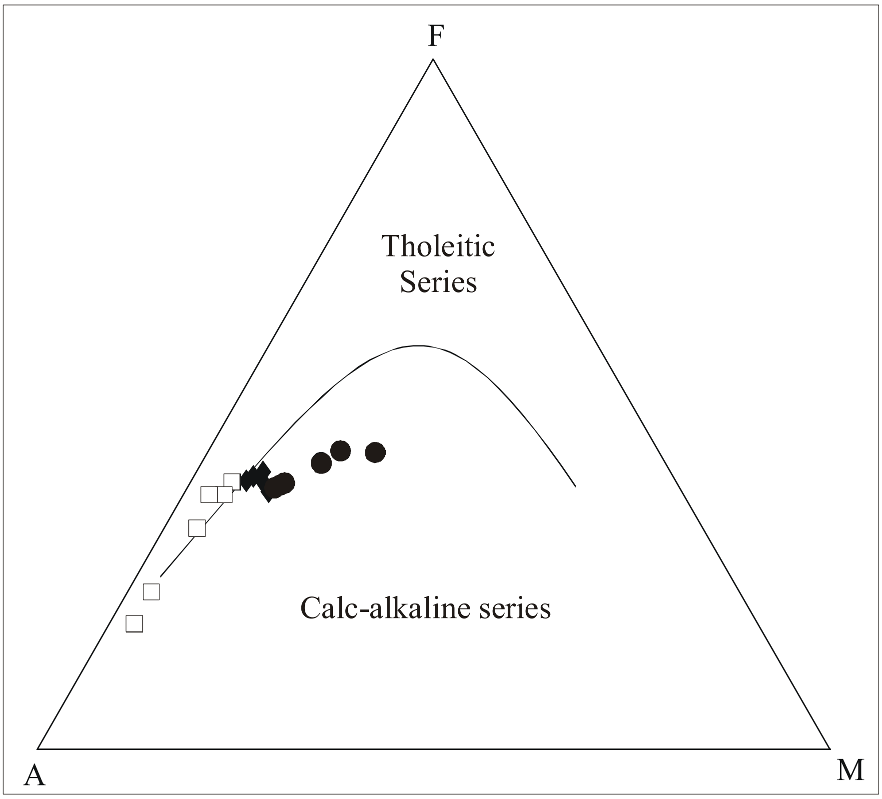

Figure 4-9. AFM triangular diagram. Symbols as in figure 4-7.

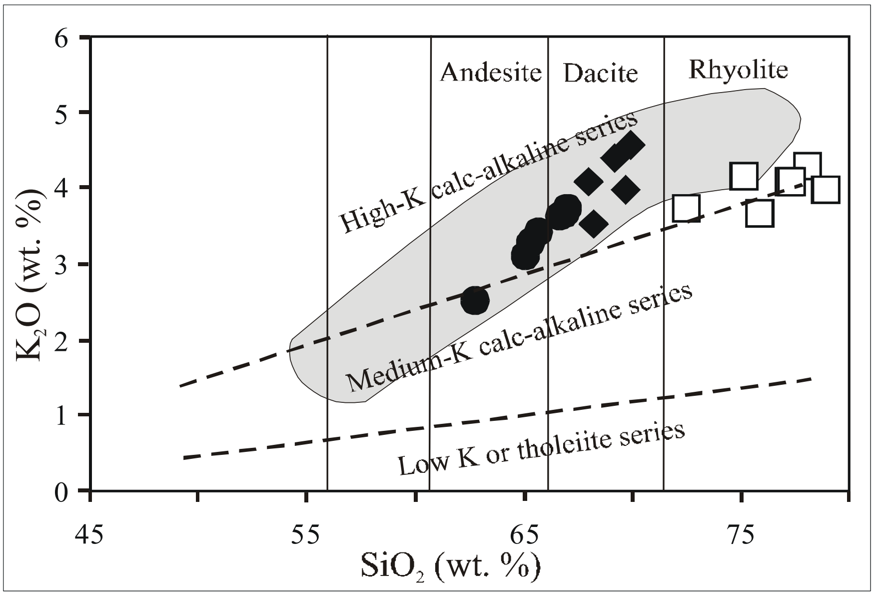

Figure 4-10. Harker type K_2O vs. SiO_2 variation diagram showing the division into tholeiitic and calc-alkaline series (Rollinson, 1993; and references therein) as well as the division into different rock types(van Soest, 2000; and references therein). Symbols as in figure 4-7.

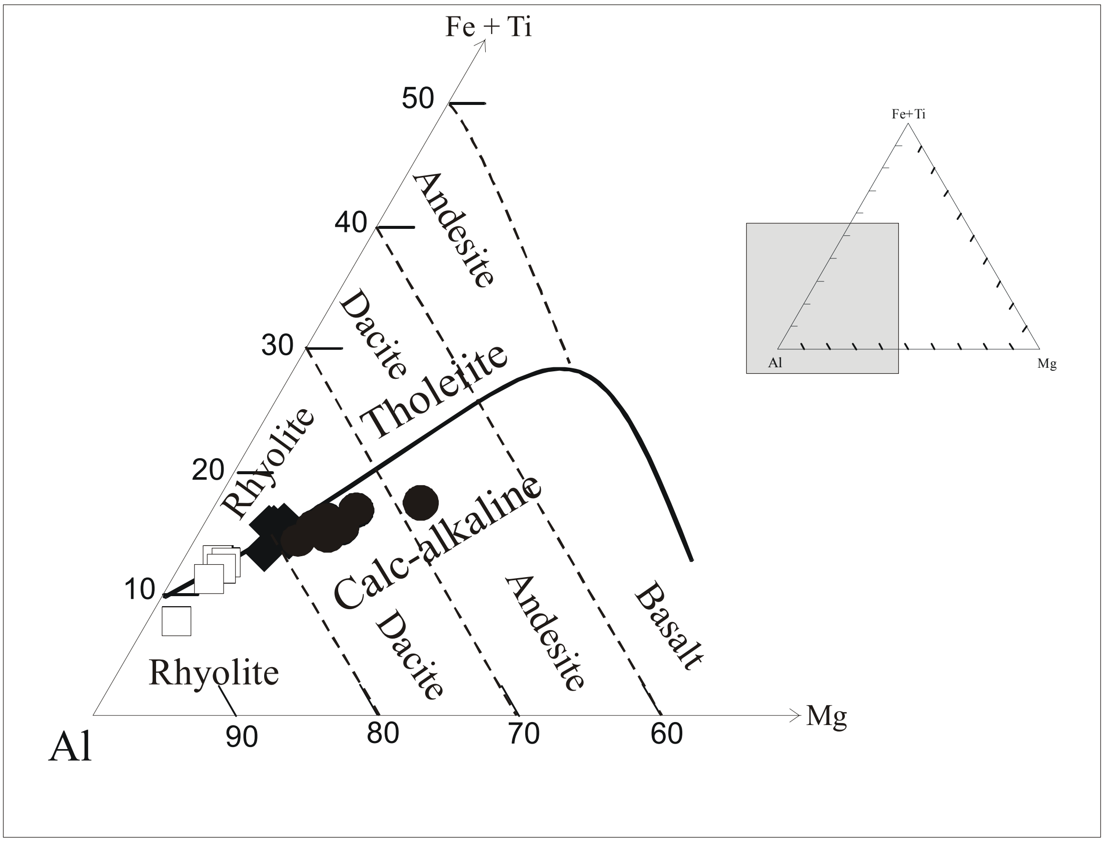

Figure 4-11. Jensen ternary diagram based on the cation percentage of Al, (Fe + Ti) and Mg (Rollinson, 1993; and references therein). Symbols as in figure 4-7.

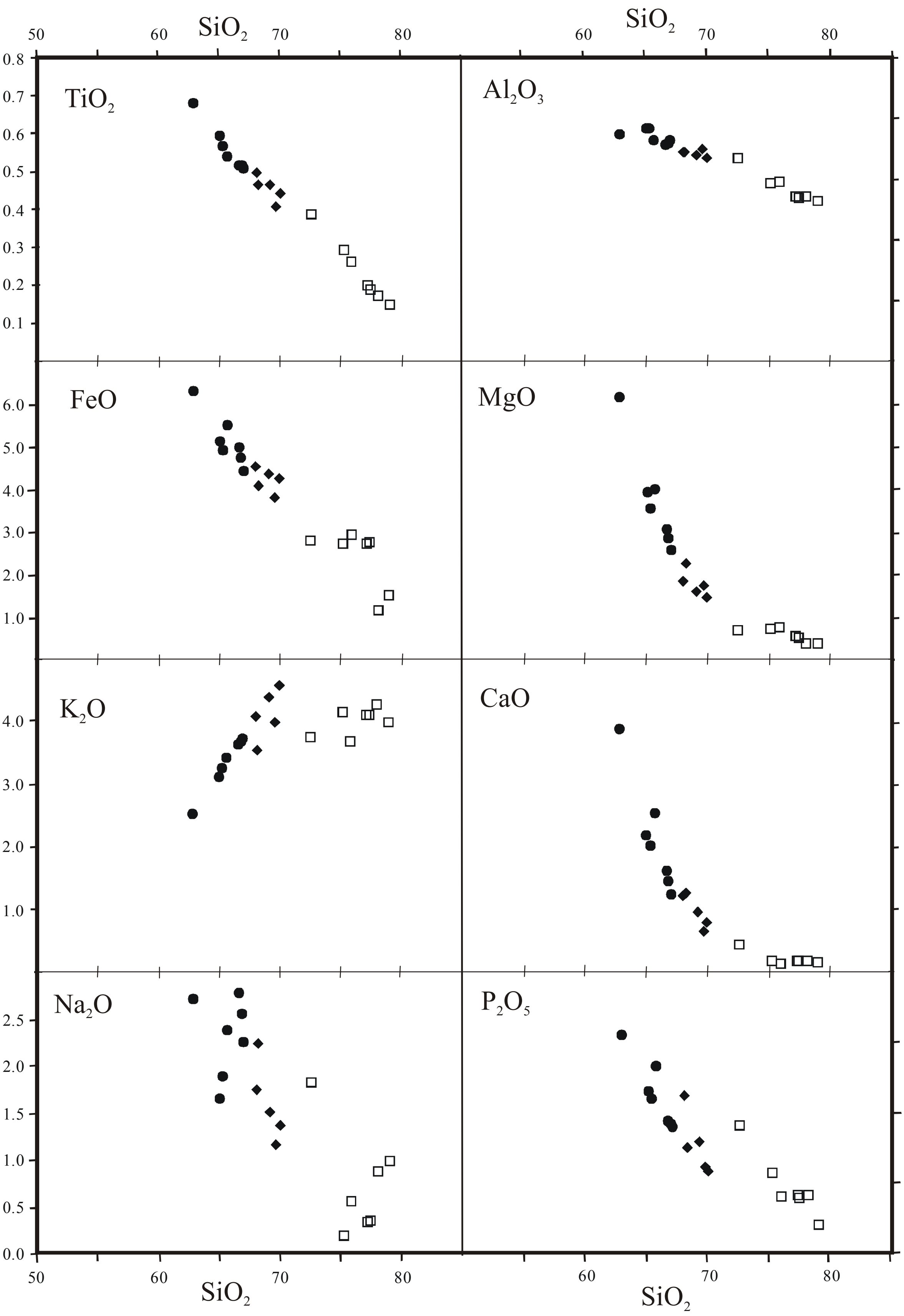

Figure 4-12. Harker differentiation diagram. Symbols as in figure 4-7

Chapter 5

Mineral inclusions in quartz phenocrysts

5.1 Introduction

The characterization of petrography and bulk chemistry of parental intrusives in porphyry copper systems has been strongly restricted because of the pronounced and widespread metasomatism and leaching effects that accompanied the processes of mineralization and secondary enrichment. These chemical modifications are usually produced by the combination of multiple and complex events of hydrothermal alteration and strong weathering that develop in and around the parental intrusive.

The degree to which the combined overprinting effects of alteration and weathering processes modify the chemistry and mineralogy of the original rocks is strongly controlled by the composition of the parental intrusive as well as by the nature and character of the hydrothermal solutions. Normally in rocks of intermediate to felsic calc-alkaline composition, like the ones found in the Zaldívar deposit, the transformation effects generate profound modifications to the chemical composition in nearly all primary magmatic rock-forming minerals, making it nearly impossible to find any fresh remnants of the parental intrusive. Furthermore, if primary minerals may have apparently survived the alteration processes, there is never a certainty to what degree its composition may have been modified (e.g., primary K-feldspar or biotite in the potassic alteration zone).

Among all rock-forming minerals found in calc-alkaline rocks, quartz represents an important exception because it usually remains compositionally unchanged under conditions occurring in most events of hydrothermal alteration and weathering. As quartz grains are resistant to hydrothermal alteration and weathering, then it can be expected that any mineral trapped within magmatic quartz phenocrysts during magma crystallization will be completely isolated from all post-magmatic events, unless the quartz phenocrysts are strongly fractured. As a consequence, mineral inclusions accidentally trapped within quartz phenocrysts have the potential of representing well-preserved magmatic remnants, and they represent an important source of information and the best chance to study and characterize the chemical composition of unaltered primary magmatic minerals.

Crystal grains of different mineralogical compositions were trapped as mineral inclusions in igneous quartz phenocrysts from the Llamo and Zaldívar porphyries, they represent a set of accessory and rock-forming minerals characteristic for calc-alkaline silicate rocks. These magmatic remnants are common in phenocrysts from the Llamo porphyry, but less abundant in the Zaldívar porphyry.

5.2 Characterization

Mineral inclusions are most commonly found randomly distributed near the rims of the magmatic phenocrysts. They may occur isolated or in groups of several inclusions, showing a variety of mineralogical compositions. The size of mineral inclusions can be up to several tens of micrometers, but they are normally smaller than 20 μm.

Mineral inclusions containing silicate minerals can easily be mistaken for homogeneous glassy melt inclusions, therefore a careful observation and characterization under the microscope is fundamental to avoid misinterpretation during melt inclusion studies

Although most mineral inclusions are too small to be fully identified under the microscope, the recognition of a few distinctive physical and optical properties allows the identification of six different minerals trapped as inclusions in quartz phenocrysts: K-feldspar, plagioclase, biotite, iron oxides (magnetite and/or ilmenite), zircon, and apatite.

- The K-feldspar and plagioclase crystals are both colorless and transparent, usually they occur as quadratic to round-shaped grains, or in irregular shapes (Fig. 5-1-C and -D). Under the microscope, no clear differences could be seen between these two minerals.
- Biotite grains show different physical characteristics depending on the thickness of the mineral grain. They usually are transparent, colorless to slightly greenish when occurring in thin flakes, or semitransparent to opaque dark-brown in thicker grains. The shape of individual biotite inclusions varies from tabular to well rounded (Fig. 5-1-C and -D). Occasionally opaques (magnetite and/or ilmenite) are closely associated to biotite mineral inclusions.
- Zircon grains are colorless to pale brown, easily recognized because they occur as euhedral, short elongated prisms terminated by pyramid faces (Fig. 5-1-A), clearly reflecting their ditetragonal dipyramidal crystal habit.
- Apatite crystals occur as colorless, semitransparent long-prismatic idiomorphic grains that show a well-defined hexagonal dipyramidal crystal habit (Fig. 5-1-A, B).

Most mineral inclusions correspond to single mineral crystal phases; occasionally they may show a multimineral association normally consisting of two grains of different mineral composition such as K-feldspar and plagioclase, zircon and apatite (Fig. 5-1-A) or biotite and iron oxides (magnetite and/or ilmenite) (Fig. 5-1-F).

In samples from the Zaldívar porphyry only inclusions of K-feldspar and plagioclase has been identified.

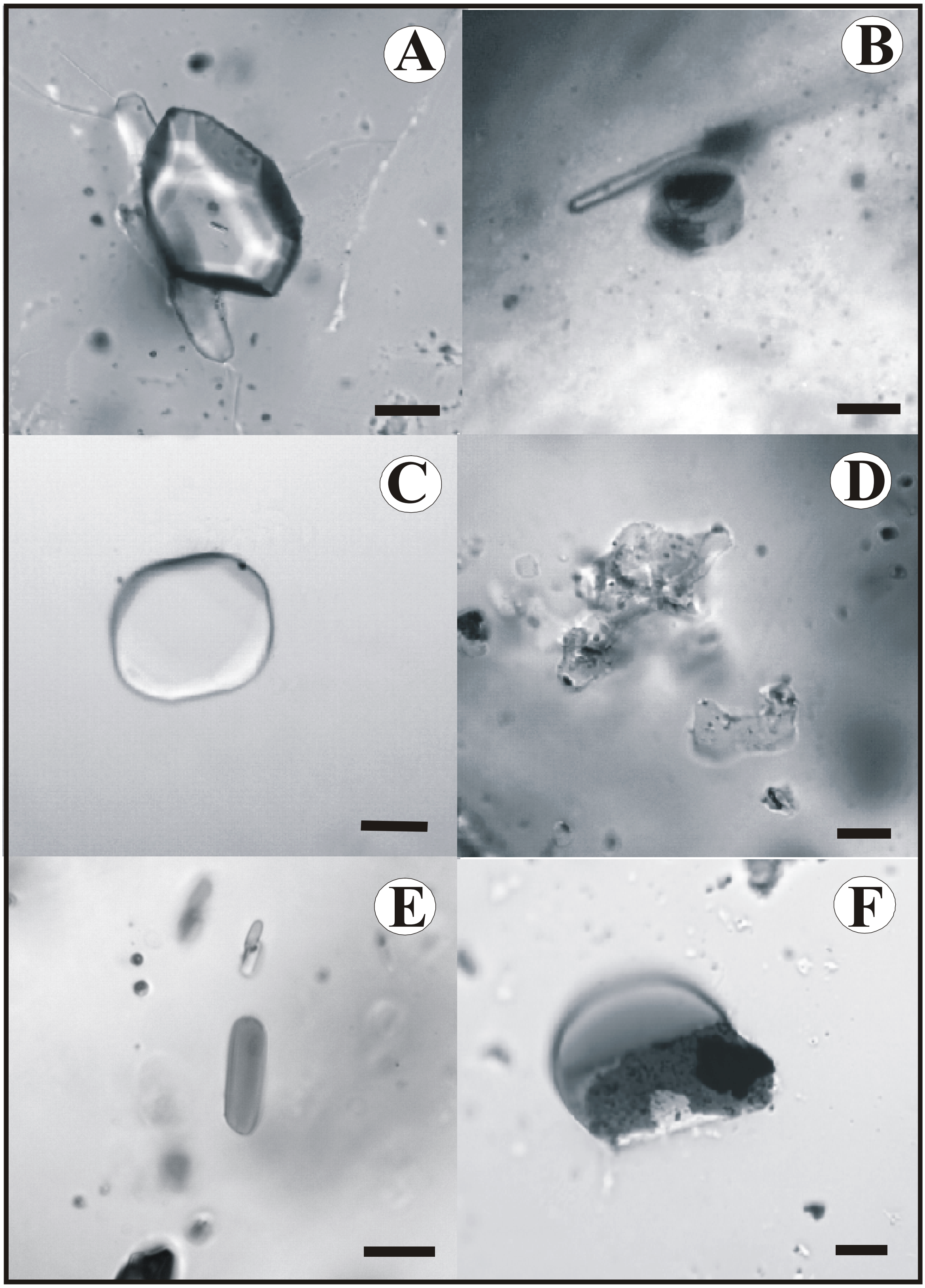

Figure 5-1. Different types of mineral inclusions hosted in igneous quartz phenocrysts. A: euhedral crystal of zircon associated with an elongated apatite grain; B: long prismatic grain of apatite close to a biotite crystal; C: isometric to rounded crystal of feldspar, probably K-feldspar; D: feldspar grains showing an irregular shape; E: several biotite crystals showing a tabular shape; F: iron oxide grain grown within a round-shaped biotite crystal. Scale bar 20 µm.

5.3 Chemical composition

The chemical composition of mineral inclusions as analyzed by electron microprobe (Table 5-1) has confirmed the occurrence of rock-forming minerals such as K-feldspar, plagioclase and biotite and accessory minerals such as apatite and zircon.

The chemical analysis of K-feldspar mineral inclusions shows a composition closely similar to the orthoclase type (ca. 6 to 22 % albite, (Deer et al., 2001), whereas the composition of plagioclase varies from oligoclase to andesine (An24 to An45) (Deer et al., 2001).

The chemical compositions of all minerals phases that occur as mineral inclusions show no sign of metasomatism or leaching, furthermore, those minerals that are usually very susceptible to be altered, such as feldspar or biotite, are not affected by hydrothermal alteration. In the contrary, the groundmass and most mineral phenocrysts other than quartz are strongly altered. In consequence, the mineral phases trapped as mineral inclusions appear to have been shielded from the effects of post-magmatic, hydrothermal alteration.

Table 5-1. Composition of mineral inclusions from Llamo porphyry measured by EMPA.

Sample	Inclusion	SiO_2	TiO_2	Al_2O_3	FeO	MnO	MgO	CuO	CaO	SrO	Na_2O	K_2O	P_2O_5	SO_3	F	Cl	Total
K-feldspar																	
S-30 (0)	10f	63.34	0.02	18.64	0.04	0.01	0.00	0.00	0.04		1.18	14.87	0.00	0.00	0.04	0.08	98.25
S-37 (27)	c19-3	65.50	0.03	18.38	0.00	0.00	0.00	0.02	0.22		1.12	12.25	1.12	0.00	0.00	0.02	98.66
S-37 (27)	c37-1	66.21	0.00	18.88	0.34	0.27	0.06	0.07	1.15		0.40	12.38	0.00	0.00	0.00	0.00	99.75
S-43 (420)	c63-2	66.18	0.00	18.75	0.02	0.00	0.01	0.01	0.02	0.02	0.32	14.30	0.26	0.00	0.02	0.00	99.90
S-43 (420)	c62-1	66.38	0.03	19.01	0.43	0.06	0.06	0.00	0.90	0.00	2.09	10.99	0.00	0.00	0.04	0.01	99.99
S-41 (53)	c87-1	62.79	0.03	18.01	0.14	0.00	0.00	0.00	0.02	0.13	1.66	13.96	0.01	0.01	0.00	0.01	96.75
S-43 (420)	c62-1	64.51	0.01	18.20	0.37	0.05	0.05	0.03	1.07	0.01	2.00	13.65	0.00	0.00	0.00	0.01	99.96
S-30 (0)	c9-2	64.86	0.03	18.98	0.07	0.00	0.00	0.01	0.12	0.13	2.25	12.48	0.00	0.00	0.00	0.00	98.92
Biotite																	
S-30 (0)	14c	39.14	2.44	14.61	13.97	0.21	16.36	0.01	0.00		0.13	9.75	0.00	0.02	1.22	0.29	98.15
S-30 (0)	16a	37.54	3.61	14.63	12.84	0.21	16.29	0.00	0.00		0.23	8.94	0.00	0.04	0.56	0.10	94.98
S-41 (53)	c85-1	39.39	1.25	13.76	12.82	0.36	18.70	0.01	0.02	0.02	0.19	8.80	0.00	0.02	0.33	0.23	95.88
Plagioclase																	
S-30 (0)	16c	65.68	0.04	20.83	0.05	0.00	0.00	0.00	1.93		10.50	0.23	0.00	0.00	0.01	0.00	99.28
S-30 (0)	10e	59.64	0.00	25.04	0.02	0.01	0.00	0.03	7.99		7.02	0.17	0.00	0.01	0.00	0.05	99.98
S-37 (27)	c41-2	57.56	0.03	26.87	0.14	0.00	0.01	0.00	8.57	0.13	6.43	0.20	0.00	0.00	0.04	0.00	99.99
S-30 (0)	c9-3	67.05	0.00	21.06	0.12	0.01	0.00	0.00	4.98	0.11	6.37	0.26	0.00	0.02	0.00	0.00	99.98
S-41 (53)	c80-1	62.69	0.00	23.82	0.18	0.01	0.00	0.02	5.61	0.08	7.36	0.14	0.00	0.01	0.05	0.00	99.95
S-11 (0)	c109-1	66.70	0.01	20.67	0.00	0.00	0.00	0.00	1.88	0.10	9.45	0.13	0.00	0.01	0.00	0.00	98.96

5.4 Fluids associated with the mineral inclusions

Most mineral inclusions appear closely associated with high-salinity fluids that may occur partially or fully surrounding the crystal grain, as fluid inclusions within the mineral inclusion or, as a corona of minute inclusions around the mineral inclusion's cavity.

5.4.1 Fluids enveloping margins of mineral inclusions

When the silicate phase does not occupy the entire volume of a mineral inclusion, the remaining volume of the cavity is usually filled up with a combination of aqueous and gaseous phases and/a semitransparent crystal of halite (Fig. 5-2). The identification of the halite crystal is seldom certain and is based mainly on physical and optical properties such as the isotropic character, the colorless look and the characteristic sharp cubic crystal form. The amount of aqueous phase within the mineral inclusion cavity is highly variable (between 90 to 10 %). When the gaseous phase represents more than 70 %, no halite crystal has been observed. In some inclusions opaque minerals, tentatively identified as hematite, have also been observed.

Microthermometry studies where carried out on several mineral inclusions that contain well-defined cavities filled with high-salinity aqueous phase. The results indicate that all trapped fluids homogenize by bubble disappearance at temperatures between 230° and 300°C. The halite daughter crystal, which is not clearly visible in all mineral inclusions, dissolves within a temperature range of 250° to 350°C (Table 5-2). Since the dissolution temperature for halite is directly related to the wt % of NaCl in solution, if referred to a simple NaCl-H_2O saturated system (Shepherd and Rankin, 1985; Bodnar and Vityk 1994), then the dissolution temperature of halite would indicate a total salinity between 32 and 35 wt % NaCl equiv.

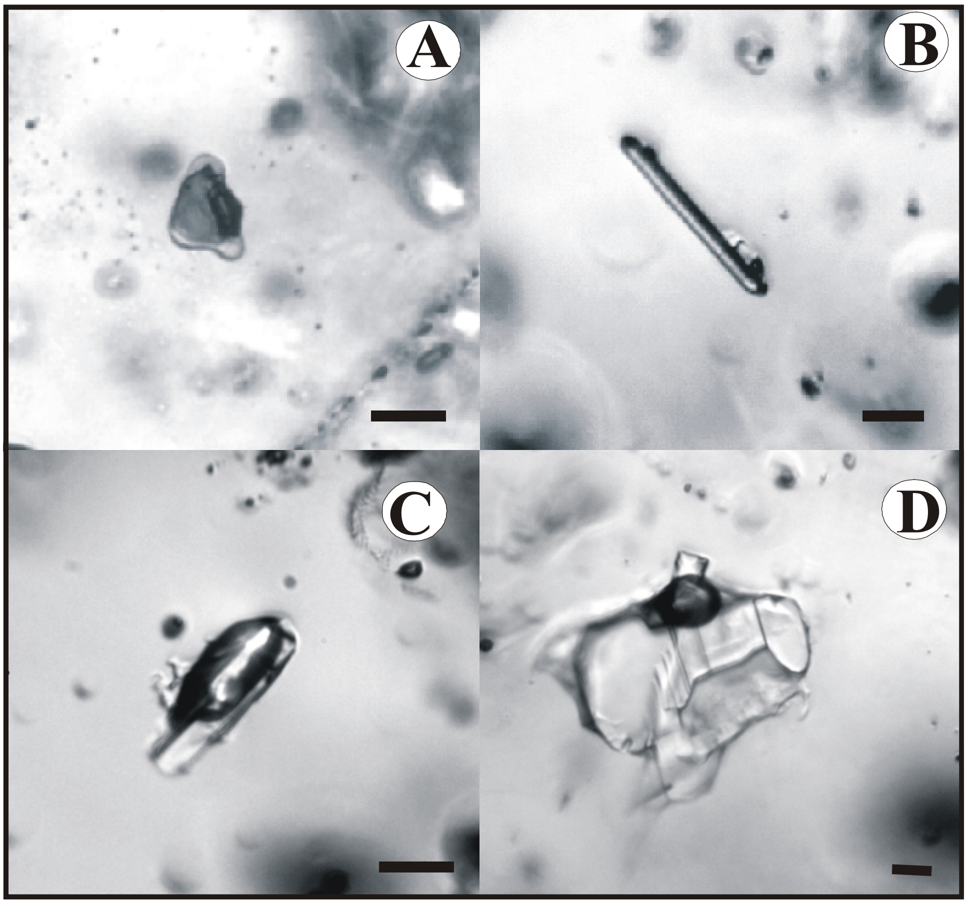

Figure 5-2. Fluids partially enveloping crystals within mineral inclusions. A: biotite crystal enveloped by a gaseous and a fluid phase; the halite crystal is below the gas bubble. B: in the lower end of the apatite crystal, a cavity associated with the crystal contains an aqueous phase, a gas bubble and a halite crystal. C: apatite crystal partially surrounded by a gas bubble and an aqueous fluid. D: mineral inclusion containing a feldspar crystal and a high-salinity fluid. Scale bar 20 µm.

5.4.2 Coronas

Some mineral inclusions, mostly biotite and K-feldspar, show a number of minute fluid inclusions distributed in the host mineral in a more or less radial pattern surrounding the solid inclusions. This arrangement of inclusions may extend several tens of micrometers into the host crystal. The inclusions that make up the corona around the mineral inclusion normally correspond to halite-bearing aqueous inclusions (Fig. 5-3-A), however in a few grains they also are gas-rich, containing no visible aqueous phase and showing a rounded shape (Fig. 5-3-B). The association of both types around a single mineral inclusion has not been observed.

The high-salinity aqueous inclusions show a more or less constant phase ratio in which the aqueous phase represents about 60 % of the total inclusion volume, the bubble about 20 % and the halite crystal around 20 % of the cavity. These inclusions show a regular morphology, normally round to elongated, and always tending towards a negative crystal shape; their size varies from several micrometers up to 10 µm.

Microthermometry studies on these fluid inclusions show that the bubble disappears within a rather narrow temperature range (between 230° and 300°C) (Table 5-2), and all inclusions homogenize by halite disappearance. However, to avoid the risk of decrepitation of the studied inclusions, they were heated only ten degrees beyond the temperature at which the bubble homogenizes, although this was not enough to fully dissolve the halite crystal. Therefore the maximum temperature at which the inclusions were heated (260°C) was taken to estimate a minimum value for the total salinity of these inclusions (> 42.3 wt % NaCl equiv.).

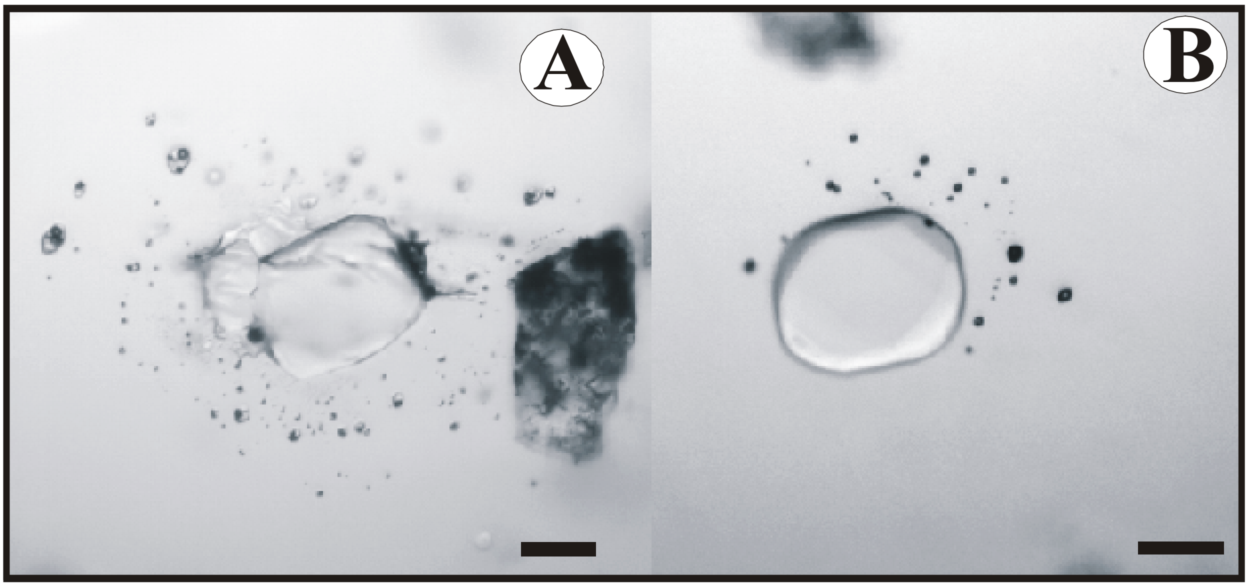

Figure 5-3. A: corona of minute, halite-bearing fluid inclusions around a feldspar crystal; B: gas-rich inclusions around a feldspar mineral inclusion. Scale bar 10 µm.

5.4.3 Fluid inclusions hosted by mineral inclusions

Mineral inclusions of apatite and zircon hosted in quartz phenocrysts often contain multiphase high-salinity fluid inclusions (Fig. 5-4). Usually they are minute inclusions not larger than 10 µm, showing a rounded or tabular shape, and they contain an aqueous fluid, a bubble and a soluble solid crystal, most likely halite.

Because of their small size and difficulties to find well-defined examples, only a few of these fluid inclusions have been studied by microthermometry. Upon heating, halite dissolves in a narrow temperature range, 230° to 240°C. In a saturated NaCl system these temperatures would indicate a salinity of 33.1 to 33.6 wt % NaCl equiv. In all the studied inclusions homogenization occurs by bubble disappearance within a temperature range of 355° to 430°C (Table 5-2).

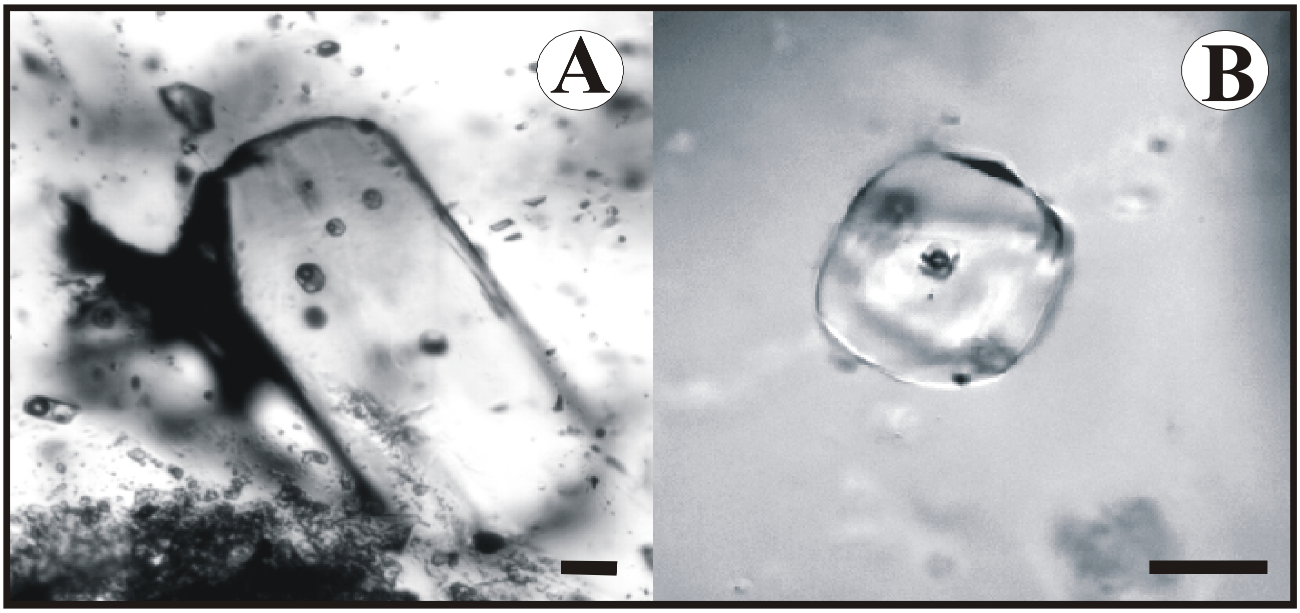

Figure 5-4. High-salinity fluid inclusions hosted within apatite inclusions in quartz . Scale bar 20 µm.

Table 5-2. Microthermometry of different types of fluids associated with mineral inclusions. The final homogenization temperature range is indicated in italics.

Related mineral inclusion	Halite dissolution	Bubble disappearance	Salinity (wt % NaCl equiv.)
Biotite, K-feldspar, plagioclase	*269° - 317° C*	200° - 300°C	35.4 - 38.8
Corona	*> 260°C*	215° - 250°C	> 42.3
Apatite, Zircon, Anhydrite	230° - 240°C	*355° - 430° C*	33.1 - 33.6

5.5 Conclusions

Mineral grains of different composition, mostly K-feldspar, plagioclase and biotite, were accidentally trapped during the late growing stage of quartz phenocrysts from Llamo porphyry. In quartz phenocrysts from Zaldívar porphyry only K-feldspar and plagioclase has been observed.

The EMP analyses of a number of mineral inclusions show a normal chemical composition and no evidence of metasomatism or leaching. This fact indicates that the trapped minerals were shielded from the effects of hydrothermal alteration. A major consequence of this shielding effect is that other magmatic remnants, such as melt inclusions, are also well preserved from post-magmatic chemical modifications.

The high salinity fluids that surround some mineral inclusions indicate that these have been enclosed in the host quartz at a relatively late magmatic stage, when fluids had already been exsolved from the crystallizing melt (Yang and Bodnar, 1994). As most mineral inclusions (K-feldspar, plagioclase and biotite) crystallize at the liquidus of the magmatic system, this also indicates a relatively early fluid exsolution, at submagmatic temperatures, as later demonstrated by the occurrence of high temperature, magmatic fluid inclusions (MS-type, see chapter 7).

Chapter 6

Melt inclusions

6.1 Introduction

In the field of melt inclusions research, much work is done on basic rocks (primitive melts in mantle-derived basalts), in fact these studies have become an essential aspect of the petrology of basic and ultrabasic rocks (Sobolev, 1996). However, for years relatively little attention was given to melt inclusions hosted in acid rocks, although they are present in most shallow intrusions (Touret and Frezzotti, 1993; Audédat, et al., 2000).

Remnants of melt inclusions were briefly mentioned in several PCDs (Pintea, 1993; Yang and Bodnar, 1994), but they were not studied thoroughly. Instrumental difficulties, mainly the lack of an adequate heating stage, have also been an important limitation to the study of melt remnants in PCDs. This situation has drastically change in the past few years with an increasing number of papers devoted to the study of silica melt inclusion in PCDs systems (e.g. Kamenestky, et al., 1999; Audédat, et al., 2000; Campos et al., 2001), and the application of new analytical techniques (Halter, et al., 2002).

The study of melt inclusions can be very helpful for the understanding of the early magmatic origin of these deposits, in particular, how the evolution of magmatic components relates to mineralization before their transformation into hydrothermal solutions. They can also characterize the chemistry of magmatic aqueous ore fluids in a magmatic environment, and their subsequent transport at this early evolutionary stage (Hedenquist and Lowenstern, 1994), and consequently bridge the gap between silicate melts and fluids on hydrothermal ore deposits. Furthermore, melt inclusions may preserve direct evidence of immiscibility phenomena (Kamenesky, et al., 1999; Audédat, et al., 2000), constrain the timing of the magmatic exsolution of volatiles and metals, and provide essential data on liquid evolutionary paths at an early magmatic stage evolution.

The PCDs have been intensively studied during the last two decades, however still remain conflicting ideas concerning their early magmatic evolution, mainly because nearly all PCDs lack well-preserved primary magmatic features that may shed some light onto this problem. As indicated in Chapter 1, PCDs are hydrothermal mineral deposits in which close spatial and genetic links exist between a sub-volcanic porphyry intrusive complex and broadly disperse magmatic-hydrothermal alteration and mineralization. This magmatic/hydrothermal association will have a significant effect on the preservation of features related to the early magmatic evolution of the deposit, mainly because of the substantial changes occurring during the hydrothermal stages (i.e., metasomatism, extensive fracturing) (see Chapter 1). The circulation of hydrothermal solutions usually strongly modify the primary composition of the porphyritic complex and the host rock, one of the most evident and widespread transformations will be the rather strong metasomatism of most rock-forming minerals notably plagioclase, biotite, and K-feldspar.

The post-magmatic events mentioned above may also impose severe post-entrapment modifications to primary melt inclusions, such as loss of volatile and a complete change in chemical composition; these factors may question the potential significance of melt remnants as their information would be only reliable if the inclusions remained unmodified since the time of trapping (Roedder, 1984, Touret and Frezzotti, 1993). However, most of the fears of post-entrapment modifications are largely exaggerated and they can easily be overcome by the correct selection of host minerals in which melt inclusions are going to be studied.

In the present case, despite the strong hydrothermal alteration observed in samples from the Zaldívar deposit, detailed microscopic and electron microprobe investigations of quartz phenocrysts have shown that K-feldspar, biotite and plagioclase mineral inclusions hosted in these phenocrysts show a normal primary chemical composition with no sign of alteration. As a consequence, we assume that other magmatic remnants such as melt inclusions are also well preserved in the phenocrysts, completely shielded from the enclosing magma and the effects of post-magmatic hydrothermal alteration after their entrapment. A major consequence of this finding is that a detailed study of melt inclusions can provide important information that may be helpful for unravelling the early magmatic evolution of the Zaldívar deposit in particular, and other PCDs in general.

6.2 Characterization and distribution

Melt inclusions at Zaldívar are relatively rare, less than 40 µm in size, and rounded to ellipsoidal in shape. Filled with a partly or fully microcrystalline solid aggregate, they show no visible gas bubble or liquid phase at room temperature (Fig. 6-1-A). All types of melt inclusions typically show a random distribution in relatively inclusion free areas of the host mineral. Either isolated or in clusters, they are apparently unrelated to the numerous fluid and mineral inclusions (namely K-feldspar, plagioclase and biotite) coexisting in the same phenocryst.

If melt inclusions are hardly recognizable as such at room temperature, they become most evident after quenching from high-temperature heating (900° - 1100°C), when a dull, microcrystalline aggregate becomes completely homogeneous and glassy with or without a bubble (Fig. 6-1-B).

6.3 Microthermometry

For heating/quenching experiments in melt inclusions, the preparation of single, double-sided polished quartz phenocrysts (see Chapter 3), were made on seven selected samples from the Llamo porphyry and two from the Zaldívar porphyry (Table 6-1). For each heating run, single quartz grains were removed from the resin mold, thoroughly cleaned and placed into the furnace of the high-temperature heating stage (Fig. 3-2, Chapter 3).

On progressive heating, melt inclusions typically show the sudden appearance of a gas bubble during melting of the daughter minerals. This bubble will readily homogenize in some inclusions at temperatures around 1000°C, in other inclusions total homogenization of the bubble is not possible, even after overheating up to 1200°C, and the bubble will persist after quenching (Fig. 6-2-C).

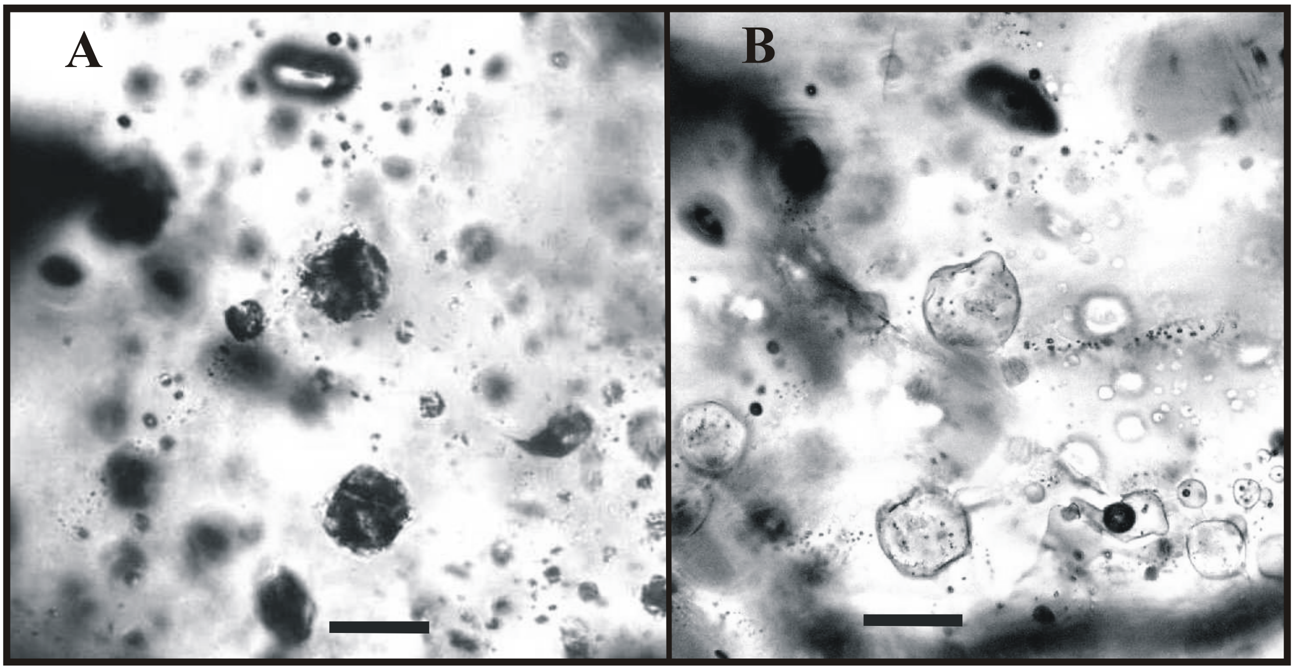

Figure 6-1. Melt inclusions at room temperature before (A) and after (B) heating/quenching experiments. Normally melt inclusions are difficult to identify unambiguously before heating. Scale bar 40 µm.

The microcrystalline aggregates in all melt inclusions will be transformed to a completely homogeneous semitransparent glass after quenching from high-temperature heating (900° - 1100°C). Three subtypes of melt inclusions can be characterized after quenching, based on their appearance at room temperature, the M_1-, M_2- and M_3-subtypes, (Fig. 6-2-B, -C, and –D, respectively).

In M_1-type inclusions, melting of the microcrystalline aggregates starts at 850° - 915°C, at the same time a sharper definition of the bubble of relatively constant size (about 10 % volume total) is observed. Complete melting of the microcrystalline aggregates occurs in the 915° - 1020°C temperature range, resulting in inclusions that will show a clean liquid (melt) and a gas bubble. Most inclusions completely homogenize by disappearance of the bubble between 900° - 1050°C, some only after 0.5-1 hour heating. Quenching of these inclusions results in the formation of a clean glass.

In M_2-subtype inclusions the last daughter crystal disappears between 900° and 1030°C, at this temperature the inclusion contains a clear, transparent glass and a large bubble of variable size (more than 40 % of volume total). Total homogenization is not possible; the volume of the bubble does not change appreciably even if heated up to 1200°C.

M_3-subtype quenched glasses have a typical feature that has only been found in samples from the Llamo porphyry. In this particular type of melt inclusions, melting of daughter crystals begins at 800°C, also accompanied by the sharp definition of the bubble (about 20 % volume total), and distinct movements of the enclosed microcrystals. Both disappear progressively, and total homogenization by bubble disappearance occurs between 950º and 1030°C. During melting of the daughter minerals, micrometer-sized black dots are evident in the melt. Quenching results in the formation of a translucent glass with several micrometer-sized black dots dispersed in the inclusion, which show no change in size or shape upon cooling to room temperature.

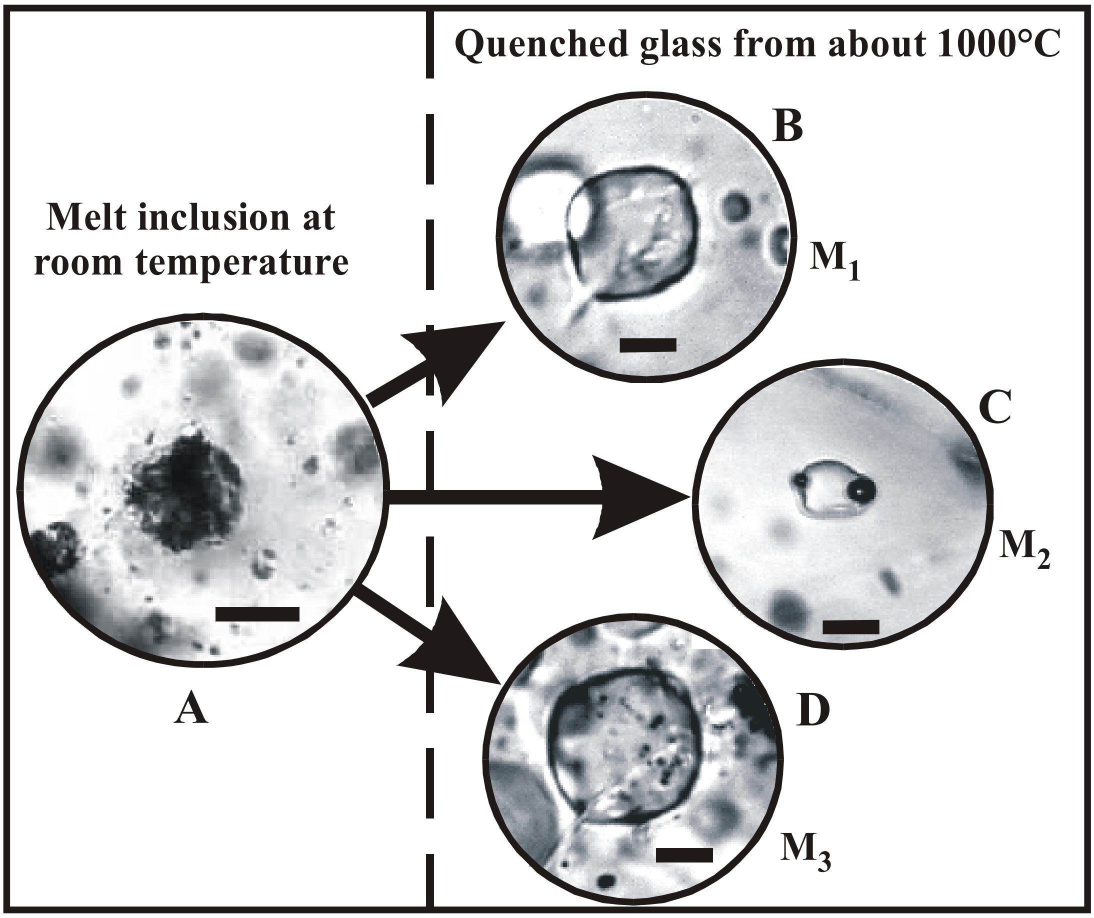

Figure 6-2. After the heating/quenching procedure, two types of quenched glasses can be recognized: the M_1-type that corresponds to a completely homogeneous semitransparent glass, and the M_2-type that shows a semitransparent glass always with a bubble. A third type (M_3-type), only recognized in samples from the Llamo porphyry, this typically is a semitransparent glass with several black-dot inclusions with no bubble. Scale bar 20 µm.

6.4 Chemical composition of melt inclusions

High-temperature microthermometry was carried out on a number of single quartz phenocrysts, however most heated grains failed to show the existence of quenched glass inclusions appropriate to estimate the contents of major elements (essentially inclusions larger than 10 µm). After careful selection and preparation under the microscope, fifty-six quenched glasses (39 from Llamo and 17 from Zaldívar porphyries) (Table 6-1) were successfully exposed at the grain's surface and then analyzed with the electron microprobe (Appendix 4, Tables 6-2 and 6-3).

The concentrations of major elements in all analyzed quenched glasses are rather similar, in fact no major compositional variations have been observed among inclusions hosted in the Llamo or Zaldívar porphyries (Appendix 4 Tables 6-1 and 6-2). All quenched glasses are characterized by a continuous compositional variation between relatively high silica contents (70.02 to 77.00 wt % SiO_2), with contents of TiO_2 lower than 0.33 wt %, MgO (< 0.40 wt %), MnO (< 0.10 wt %) and P_2O_5 (< 0.12 wt %). The concentration of CaO represents a major difference among both intrusives, it is high in the glasses in the Llamo porphyry (up to 2.5 wt %), and low for those in the Zaldívar porphyry (< 0.3 wt %).

Table 6-1. List of melt inclusions analyzed by EMP from Llamo and Zaldívar porphyries.

Llamo porphyry					
Sample	Quartz grain	Inclusion	Sample	Quartz grain	Inclusion
S-37 (27)	C-24	C24-7	S-30		15c
		C24-7b		C-3	C3-9
	C-32	C32-1		C-95	C95-1
		C32-1	S-45 (238)	C-15	C15-4
		C32-2	S-37 (27)	C-21	C21b-1
		C32-2b			C21b-3
		C32-1d	S-41 (53)	C77	C77-2
		C32-6d		C78	C78-4
	C-43	C43-18e		C76	C76a-4
		C43-18d		C81	C81-1
		C43-6			C81-2
		C43-19d			C81-3
		C43-7		C83	C83-4
		C43-7b		C84	C84-1
		C43-6b			C84-3
	C39	C39-4	S-35 (26)	C-122	C-122b
	C44	C44-10b		C-96	C96-1
	C45	C45-5b		C-99	C99-2
				C-100	C100-1
			S-11	C110	C110-1

Zaldívar porphyry		
Sample	Quartz grain	Inclusion
S-43 (420)	C61	C61-1
		C61-2a
		C61-2b
		C61-7
		C61-9
	C63	C63-5
	C65	C65-1
		C65-1b
	C67	C67-1b
		C67-1c
		C67-2
	C72	C72-2
		C72-3
		C72-4
	C74	C74-3
		C74-4
		C74-11

Some of the analyzed glasses show SiO_2 content higher than about 79.00 wt %, this high silica content could be related to the re-melting procedure of the melt inclusion needed to restore the homogenization of the enclosed glass. During heating at high temperatures, the glass could have interacted with the host mineral (quartz) by melting part of the host boundary layer (SiO_2 gain). Perturbations that arise from this procedure are abundantly described in the specialized literature (Roedder, 1984). Another possible cause for silica enrichment could be the integration of part of the host crystal during microprobe analyses due to the small size of the inclusions. Although the greatest care was taken to minimize analytical "wall" effects, either by placing the microprobe beam always at the core of the glassy inclusion and by keeping the size of the beam at all times smaller than the area of the inclusion exposed at the surface. However, the small size and/or thickness of some glass inclusions could incorporate part of the host into the total glass analysis.

A most important result in the composition of quenched glasses is that Cu has been clearly detected in M_1- and M_2-type glasses hosted by the Llamo intrusive (Appendix 4, Table 6-1). These quenched glasses contain amounts of copper in the order of 0.04 to 0.57 wt %, with an average concentration of 0.10 wt % (detection limit for copper is 0.03 wt %). The Cu values are at least one order of magnitude higher than those expected for normal calc-alkaline magmas (Einaudi, 1997). The highest Cu concentrations (0.5 to 1.5 wt %) are always related to the M_3-type quenched glasses.

In the Cu vs Cl and Cu vs K_2O differentiation diagrams (Fig. 6-3-A and -B) there is a clear positive correlation between Cu and Cl and K_2O, whereas in the Cu vs Na_2O differentiation diagram the higher Cu values are related to the lower most values of Na_2O (ca. < 2.0 wt% Na_2O) (Fig. 6-3-C). A negative correlation is observed between Cu and SiO_2 (Fig. 6-3-D).

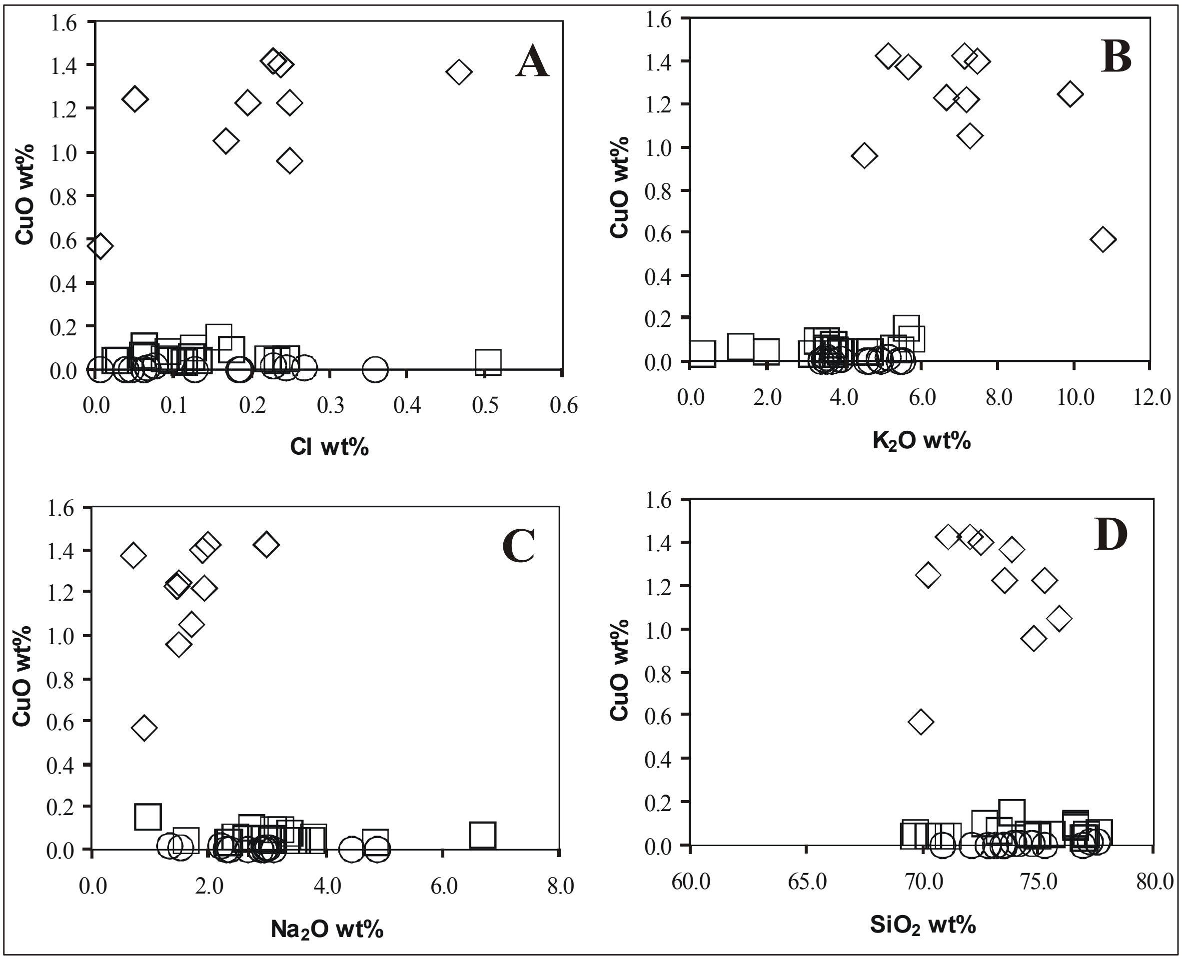

Figure 6-3. Differentiation diagrams showing the relation between copper and Cl (A), K_2O (B), Na_2O (C) and SiO_2 (D) in quenched glasses from the Llamo porphyry. Diamonds: M_3-type copper rich glasses (> 0.5 wt % Cu); squares, M_1- and M_2-type copper rich glasses (0.3 to 0.5 wt % Cu); circles: quenched glasses with no copper.

Although most analyzed quenched glasses from the Llamo porphyry appear to be enriched in copper, a major compositional difference between the different types of melt inclusions would be the higher copper content measured in M_3-subtype (> 0.5 up to 1.23 wt %). The highest copper values are always present in those M_3-subtype glasses on which the defocused spot during EMP analysis includes the black-dots. In fact, EMP analysis performed in dot-free areas from M_3-type glasses, give similar major element compositions as in M_1- and M_3-type glasses with similar copper values (lower than 0.10 wt %).

To define the composition of the black dots and understand their contribution to the high copper contents in the M_3-type glasses, the droplets where analyzed by energy-dispersive X-ray analysis (EDS) during SEM analysis (Fig. 6-4). All analytical results have consistently indicated a Cu-Cl composition, which indicates that the black dots most likely represent immiscible Cu-Cl rich drops trapped together with the melt during the crystallization of the parental magma (the Llamo intrusive). Even if at first sight the black appearance could suggest the possible occurrence of ores (notably sulfides), no trace of sulfur has been detected in any analysis.

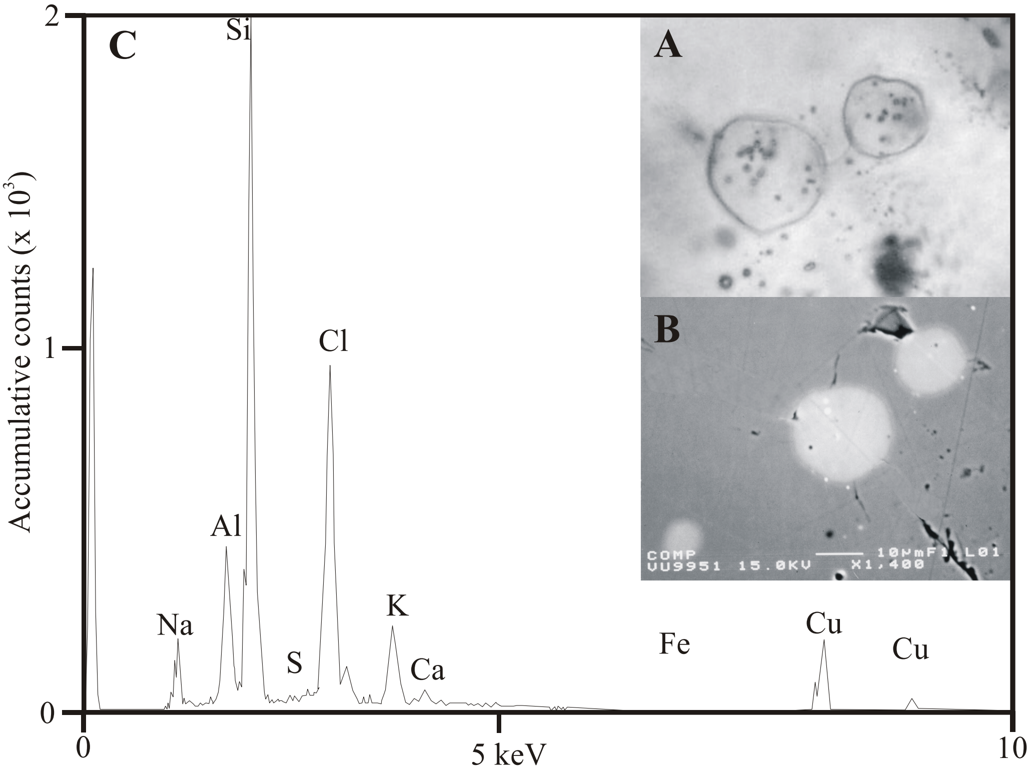

Figure 6-4. A: Quenched M_2-type melt inclusions showing the distribution of black-dots. B: Back-scattered image of the same inclusions, brighter points correspond to the black-dots. C) X-ray spectra of the black-dots by EDX.

6.5 Comparison between melt inclusion, host rock and regional magma compositions

Comparing the major-element concentrations measured in whole-rock samples from the Llamo porphyry and in glasses hosted in the same rock units (Appendix 3 Table 4-7 and Appendix 4 Table 6-1, respectively), the former show higher contents of TiO_2, FeO, MgO, and P_2O_5, rather similar Al_2O_3, and lower Na_2O and CaO (Fig. 6-5). In the case of the Zaldívar porphyry, the concentration of major elements in the host rock with respect to the glass inclusions are also higher for FeO, rather similar for TiO_2, Al_2O_3 CaO, MgO, MnO and P_2O_5 and lower for Na_2O and K_2O (Fig. 6-5).

The volcanic and intrusive rock units that represent the regional magmatism within which the Zaldívar deposit is emplaced show the same tendency in the Harker diagrams, but the volcanic rocks are more disperse (Marinovic et al., 1995). The SiO_2 positively correlated with K_2O (Fig. 6-5), and negatively with Al_2O_3, TiO_2, CaO, FeO, MgO, and P_2O_5. Na_2O tends to be constant with increasing SiO_2 (Fig. 6-5) The only difference among both rock units is that the volcanic rocks are more alkali-rich (4-10 wt %) than the intrusives (4-8 wt %) (Marinovic et. al, 1995).

The Harker differentiation diagrams for glasses hosted in the Llamo and Zaldívar porphyries show a negative correlation between SiO_2 and Al_2O_3, however there is no apparent correlation for any of the other major elements (Fig 6-5).

On a TAS diagram (Le Bas et al., 1992) all melt inclusion compositions from the Llamo and Zaldívar porphyries plot within the rhyolitic field, overlapping with the most evolved rhyolitic phases found elsewhere in the regional magmatism that surrounds the Zaldívar deposit (Fig. 6-6-A). The rhyolite can be further subdivided as peraluminous rhyolite since they show an AI (alkaline index) between 0.35 and 0.9 (Le Maitre et al., 1989), and have a ISA index (Zen, 1986) between 1.0 to 2.0 (Fig. 6-6-B).

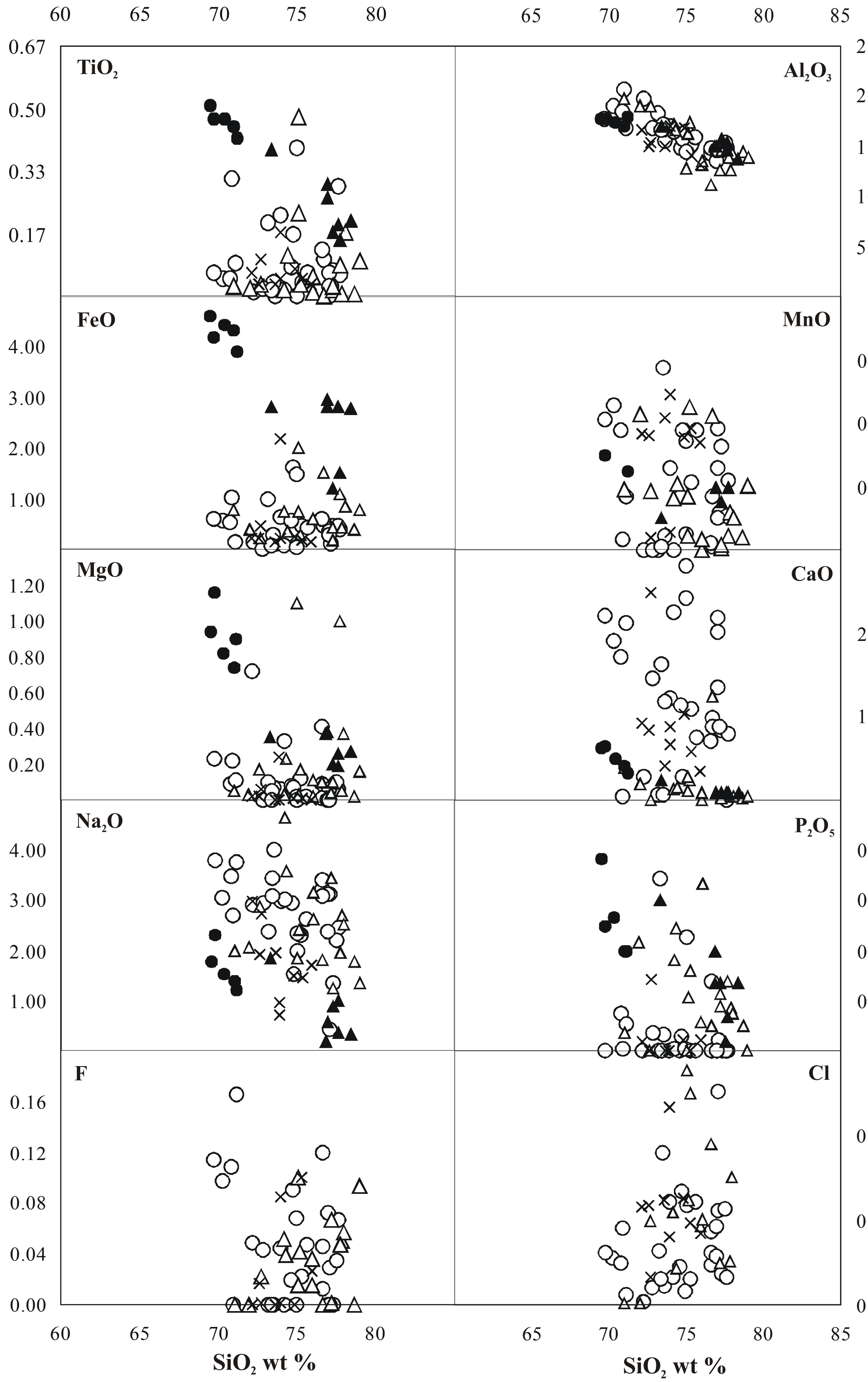

Figure 6-5. Harker differentiation diagram for major elements. Open circles (quenched glasses hosted in the Llamo porphyry), black circles (whole-rock composition of the Llamo porphyry), open triangles (quenched glasses hosted in the Zaldívar porphyry), black triangles (whole-rock composition of the Zaldívar porphyry); crosses (copper-rich quenched glasses, Cu > 0.5 wt %, in Llamo porphyry).

All studied glasses are within the subalkaline field defined in the TAS diagram (Rollinson, 1993 and references there in) (Fig. 6-6-A). The subalcaline composition can be further subdivided in a plot of K_2O vs. SiO_2 concentrations (Fig. 6-7). This variation diagram indicates that all glasses can be put into a medium-K to high-K series (Le Maitre et al., 1989), or the high-K calc-alkaline to calc-alkaline series (Peccerillo and Taylor, 1976).

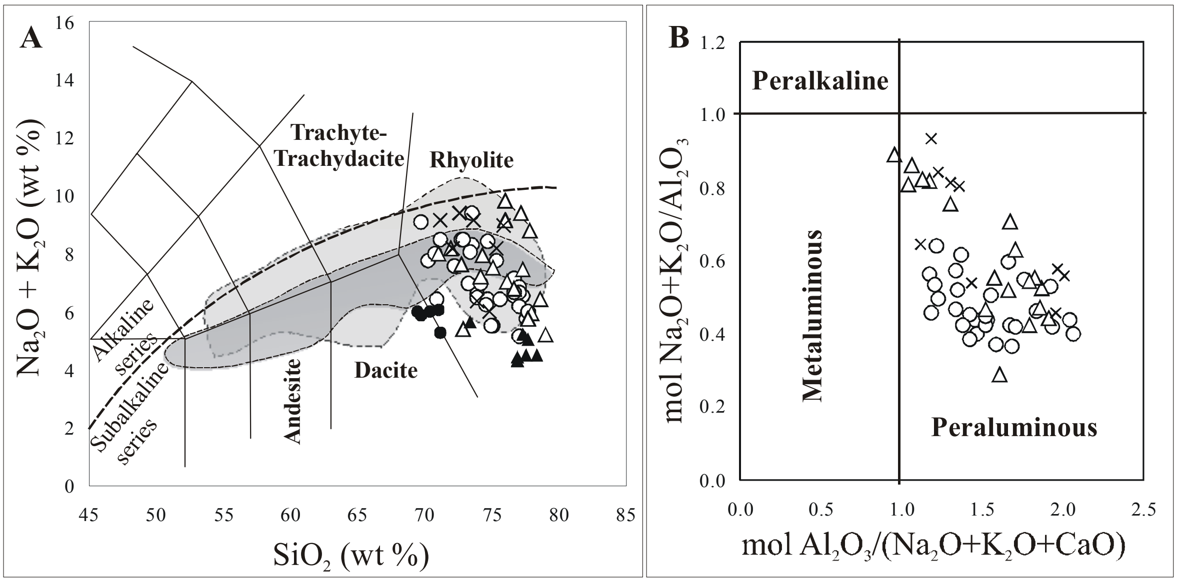

Figure 6-6. A) Silica vs total alkalis diagram (Le Bas et al., 1992) showing the distribution of quenched glasses within the intrusives (dark shaded area) and volcanic rocks (light shaded area) found elsewhere in the regional magmatism. Symbols as in Fig. 6-3. B) Alkaline index vs ASI index diagram showing the peraluminous character of the quenched glasses. Symbols as in figure 6-5.

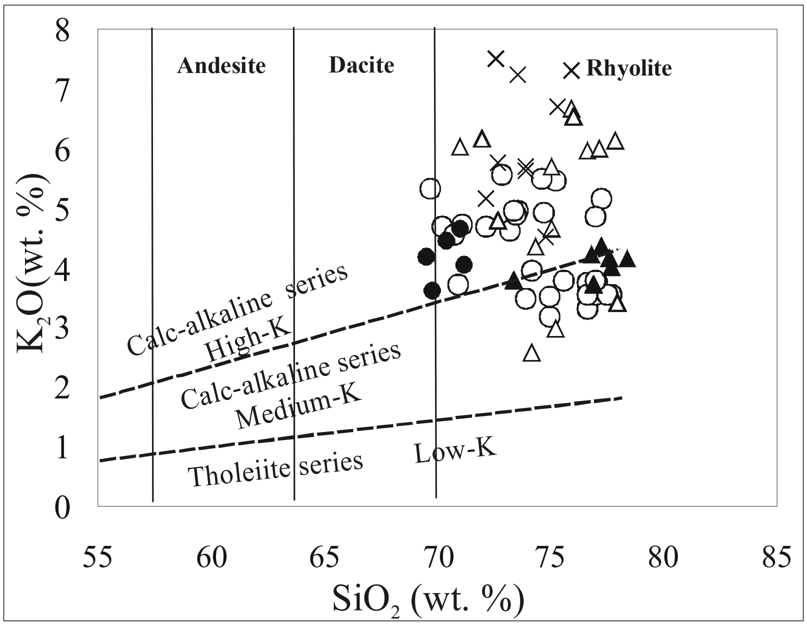

Figure 6-7. A Harker type differentiation diagram of K_2O vs. SiO_2 showing the division between tholeiitic and cal-alkaline magma series (Peccerillo and Taylor, 1976) and low-, medium- and high-K series (Le Maitre et al., 1989) as well as the division into different rock types (Wilson, 1989). Symbols as in figure 6-5.

6.6 Concluding remarks

Quartz phenocrysts from Llamo and Zaldívar porphyries contain well-preserved magmatic remnants in the form of melt inclusions that are best visible only after high-temperature re-heating.

Melt inclusions homogenize between 900° and 1050°C, these values should correspond, or at least be very close, to the trapping temperature. The homogenization temperatures would indicate that the quartz phenocrysts have started to grow at temperatures at around 1000°C, during an early crystallization stage of the porphyries, near the liquidus of the magmatic system in a possibly overheated magma. The temperature range is well above the final crystallization of most acid magmas (about 850°C).

The compositions of quenched glasses represent highly evolved silica-rich rhyolitic melts, comparable to the most evolved acidic rhyolitic end member found elsewhere in the regional magmatism.

Copper enrichment appears to be a general feature for most melt inclusions hosted in the Llamo porphyry, their compositions are characterised by high copper content (usually higher than 0.05 wt %), at least one order of magnitude higher that expected for calc-alkaline plutons in general. The Cu content is independent of other chemical elements, except possibly for a correlation with Sr and K_2O. Furthermore, the total of major elements on these inclusions equals 100 %, indicating a practical absence or very small amount of volatiles

Chapter 7

Magmatic multisolid MS-type fluid inclusions

7.1 Introduction

Nearly all of the extensive literature and large amount of data generated by the study of fluid inclusions in PCDs are related to the moderate to low-temperature range (less than 600°C). A major limiting factor in this fluid inclusion research, is the temperature limit which can be reached by most used, economically available heating-freezing stages: Chaixmeca and Linkam (600°C), and somewhat higher for the USGS/Reynolds (700°C). These maximum values are still far below possible magmatic temperatures, leaving an important temperature field in which very few data are presently available.

During the study of fluid/melt inclusions hosted in igneous quartz phenocrysts from the Zaldívar PCD, a distinct type of multisolid, highly saline fluid inclusions have been found in the Llamo porphyry that homogenize at magmatic temperatures, up to 1000°C. At room temperature these fluid inclusions contains a gas bubble and a multisolid aggregate, for that reason they have been labeled the MS-type (for multisolid).

Fluid inclusions showing high T_H (> 650°C) and an extremely saline composition (> 65 % NaCl equiv.) probably are rather common features in magma-related ore deposits (Roedder, 1971). They have been studied in several PCDs worldwide, such as Bingham, U.S.A; Apuseni Mountains, Romania; Panguna, Papua New Guinea; and Granisle, Canada; and Bajo de la Alumbrera, Argentine (Roedder, 1971; Pintea, 1995; Eastoe and Eadington, 1986; Wilson et all, 1980, Ulrich et al., 2001, respectively). However, despite the widespread occurrence, their attribute as a potential source for key information about the formation of PCDs (Roedder, 1971), not much research is found in the current literature concerning this type of inclusions (e.g. Ulrich et al., 2001; Campos et al., 2001), therefore their knowledge remains insufficient compared to the wealth of data available for lower-temperature, immiscible aqueous/vapor and brine inclusions (boiling fluids), by far the most abundant inclusions in PCDs.

The current comprehensive investigation intends to provide microthermometric and qualitative compositional data on the MS-type inclusions, and to discuss their significance in the evolution of the Zaldívar porphyry copper, with special attention to the origin of metals.

For the study of MS-type fluid inclusions, several non-destructive techniques have been employed to estimate the composition of the trapped fluids such as high- and low-temperature microthermometry (heating/quenching and heating/freezing stages respectively, see chapter 3), Raman spectrometric microanalysis, and PIXE (Particles-induced X-ray emission microanalysis).

Complementarily, selected inclusions were opened and the residual solid phases within the cavity were analyzed by SEM (scanning electron microscope) and EDX (energy dispersive X-ray analysis).

7.2 Description and distribution of MS-type inclusions

At room temperature, MS-type inclusions are easily distinguished from the coexisting and more abundant liquid-rich brine inclusions mainly because of the small proportion of liquid, squeezed gas bubble and multiple daughter minerals that they typically contain, commonly no less than three. These inclusions are always smaller than 35 μm, showing a characteristic rounded to drop-like shape (Fig. 7-1-A to -D). Their relative abundance varies from sample to sample, but usually they are very scarce and restricted to inclusion-free domains in the crystal host. They are randomly distributed in the quartz phenocrysts, either isolated (Fig. 7-1-C and D) or in clusters of a few inclusions, or more rarely in trails (Fig. 7-1-A and -B).

No direct coexistence or association has been observed for MS-type inclusions with melt inclusions or other types of aqueous inclusions that are quite abundant in the quartz phenocrysts. Also, no definitive criteria were observed that could distinguish primary and secondary inclusions (e.g. inclusions within growth zones or trapped along fracture planes). Nevertheless, MS-type inclusions are interpreted as the earliest inclusions as they occur within the host mineral in areas that show no evidence of coexistence or spatial association with other aqueous inclusion types that are related to subsequent hydrothermal stages.

At room temperature MS-type inclusions characteristically contain extremely dense saline brines that almost lack any aqueous phase (the liquid represents less than 5 % of the inclusion total volume) (Fig. 7-1). In this respect they resemble the hydrosaline melts described by Roedder (1971), or the “liquid-absent” inclusions studied by Schiffries (1990) in the Bushveld Complex, although the nature of the mineral content in the Bushveld case is very different.

The various daughter minerals observed in the MS-type inclusions at room temperature show a very consistent volume ratio amounting to about 60% by volume. This typical multiple solid arrangement consists of at least three translucent solids easily recognized with the petrographic microscope. A small opaque grain may also be present in this inclusion type (Fig. 7-1). The translucent solids are all soluble salts (see microthermometry) and they can be classified as follows:

- A first and largest solid phase has been identified as halite (NaCl), it occurs as an isotropic colorless crystal normally showing idiomorphic sharp cubic shape (Fig. 7-1-A, B and D).
- The second solid most probably corresponds to sylvite (KCl) which can be recognized as being colorless and showing an isotropic behavior, a somewhat rounded crystal, a relief slightly lower than halite and high solubility (see microthermometry) (Fig. 7-1-A and B).
- The third semitransparent unknown solid typically shows a greenish-blue color with a high-order birefringence and high positive relief. It always occurs as anhedral grains

filling the space between the gas bubble, the halite and sylvite crystals (Fig. 7-1-A, B and D). This solid phase is always the first to dissolve upon heating (see below).

The vapor bubble shows a more-or-less constant size of approximately 30% of the total cavity volume, and is normally compressed and deformed by the daughter minerals (Fig. 7-1-A to –B)

Within the Zaldívar deposit, all studied MS-type inclusions were observed in quartz phenocrysts from the Llamo porphyry. These inclusions are absent in the Zaldívar porphyry and in the Andesite unit.

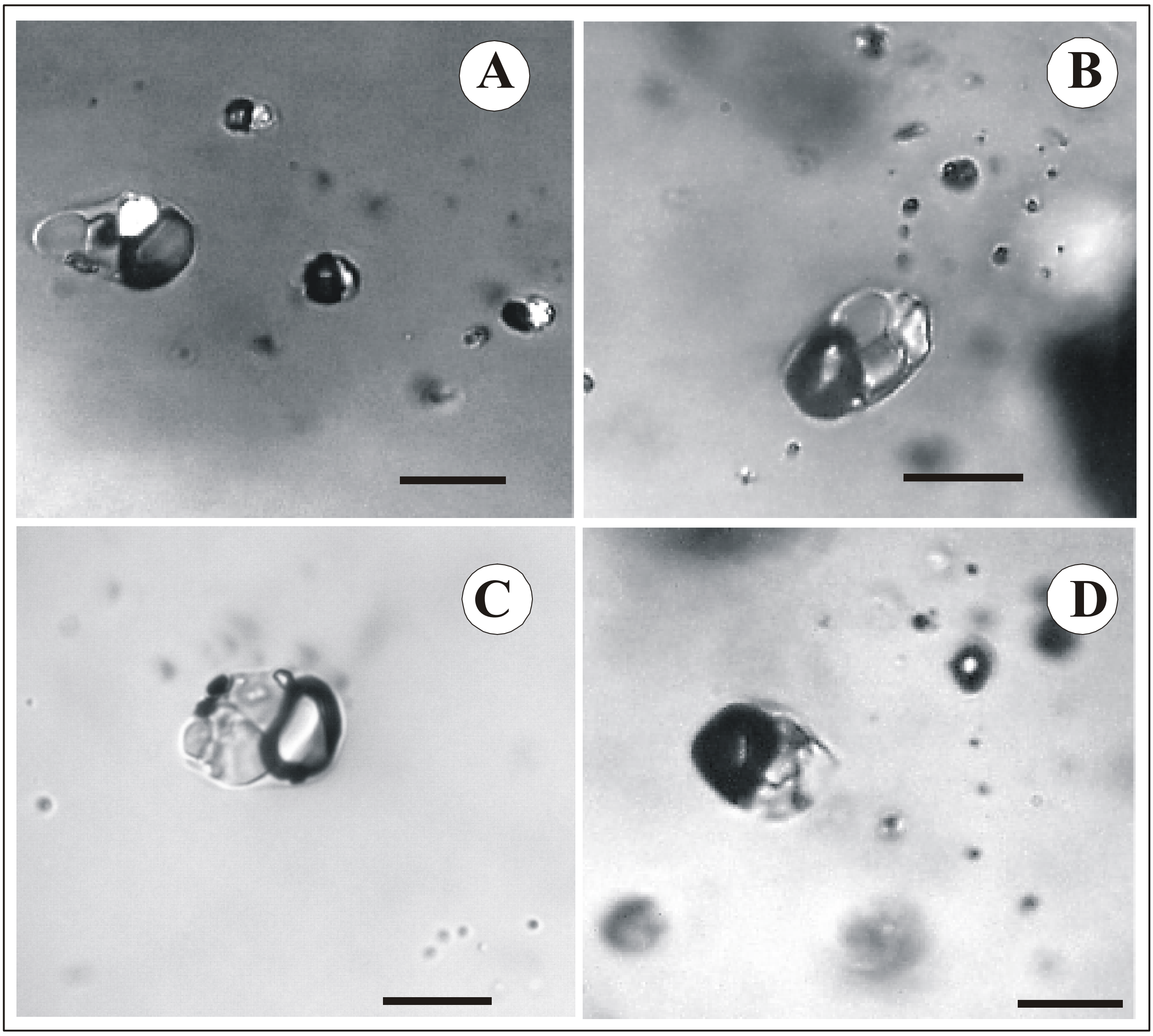

Figure 7-1. A set of microphotographs showing general features of MS-type inclusions such as shape, size and multi-solid content. Scale bar 20 µm.

7.3 Microthermometry

Conventional heating/freezing procedures on MS-type inclusions were carried out with a nitrogen-cooled Linkam TP/91-THMS 600 stage. Fluid inclusion data were obtained by first freezing to almost -190°C, to test for the existence of any gaseous phase different from H_2O (e.g., CO_2, CH_4 or N_2). However, no phase transitions that would indicate the presence of any of these gases were observed, if these gases are present at all, they are so to a minor degree. Upon cooling, there were no indications for the nucleation of chloride hydrated compounds at temperatures below zero. This could be due to the scarcity of the aqueous phase present in the cavity, the impossibility to observe phase transitions owing to the small size of the inclusions, or more likely a combination of both.

During sequential heating from room temperature to the homogenization temperature, all MS-type inclusions show systematically the same behavior (Fig. 7-2): The first, translucent crystal dissolves between 100° and 160°C, at this point the borders of the cavity become clearer. Sylvite, the second daughter crystal, dissolves next between 250° - 350°C. On further heating the last translucent crystal of halite dissolves within the 350° to 500°C temperature interval (Appendix 5, Table 7-1). At this point, the fluid inclusion contains two phases (liquid and vapor), with the size of the gas bubble making up to about 30% of the total inclusion volume.

Similar behavior upon heating has already been described in porphyry copper deposits from the Apuseni Mountain, Romania (Pintea, 1993), Panguna, Bouganville, Papua New Guinea (Eastoe and Eadington, 1986) and Bajo de la Alumbrera, Argentine (Ulrich et al., 2001).

Complete homogenization of MS-type inclusions was only possible by using the high-temperature atmosphere-controlled heating stage (Fig. 3-3). Total homogenization, always by disappearance of the vapor bubble into the liquid phase, occurs at temperatures between 750° and 1030°C (Fig. 7-2, Appendix 5 Table 7-1). The opaque grain, when present, does not dissolve even after the bubble homogenization.

Cooling of the inclusions after total homogenization will provoke the vapor bubble to reappear at 10° to 30°C below the homogenization temperature, then the renucleation in reverse order for all dissolved solid phases will occur. The first solid phase will be halite, followed by sylvite and finally, at temperatures below 100°C, the phase with the lowest melting temperature will crystallize in the free space left by the early nucleated solids. At room temperature, all the initial phases are again present in the inclusion.

All microthemometric measurements were repeated at least twice for each inclusion, with very consistent and reproducible results. No changes in the original shape of the cavity were observed so it is assumed that the inclusion did not stretch upon heating.

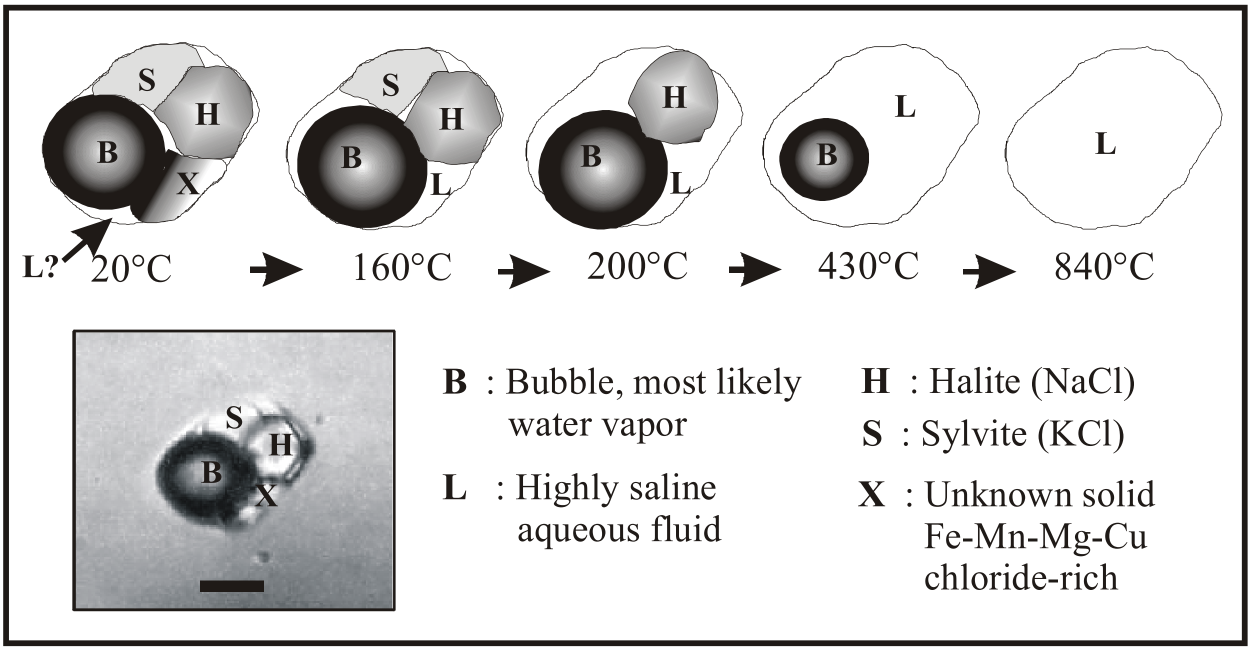

Figure 7-2. Sequential heating from room temperature to homogenization temperature of MS-type fluid inclusions. Scale bar 20 µm.

7.4 PIXE microanalysis

Since a PIXE microbeam has a penetration depth of several tens of micrometers, it turns out to be a valuable non-destructive technique to analyze fluid inclusions within the host (Damman et al., 1996), leaving the inclusion intact for subsequent, and complementary studies and observations.

Fluid inclusions hosted in quartz represent the most suitable case, since this mineral is optically transparent and contains very low concentrations of nearly all elements of interest that might be present in the cavity. The major disadvantage of the PIXE technique is that it is not suitable for detection of elements with $Z \leq 10$ (Anderson et al., 1989), which is compensated by the high sensitivity that the technique has for many havier elements (20-50 ppm).

The present PIXE study will provide only qualitative information on the fluid inclusion composition as the quantitative interpretation of PIXE spectra requires complex analyses (e.g. Rayn et al., 1991; Heinrich et al., 1992), which are beyond the scope of this research.

The typical X-ray emission spectra (K- and L- lines) obtained by PIXE microanalyses on selected MS-type inclusions can be characterized by the spectrum shown in figure 7-3, which shows a strong Fe peak, followed by lower intensities of neighboring Mn, Cu, and Zn (Appendix 6, Table 7-2). The occurrence of strong Cl and K peaks would be expected from the occurrence of sylvite as a daughter mineral, however Cl and K intensities are low and their intensities are strongly dependent on the depth of the inclusions, due to the absorption of the overlying quartz. Moreover, the presence of a halite daughter mineral shows that these inclusions contain high concentrations of sodium that cannot be detected by PIXE because the overlying quartz produces a strong X-ray attenuation for this element. In fact, during the present investigation it was not possible to detect elements lighter than S.

A “near-surface” MS-type inclusion was selected to perform an X-Y scan using the PIXE microbeam to investigate the distribution of the metals within the cavity. The experimental results indicate that Fe, Cu, Mn, and Zn occur closely related (Fig 7-4), it also indicates that the quartz host completely lacks these elements, so any possible contamination from the crystal host can be ignored.

During PIXE microanalysis, the heat generated by the proton bombardment is sufficient to provoke the dissolution of at least one of the solid phases. This melting effect can clearly be demonstrated by the change in the arrangement of the solid phases after the inclusion has been irradiated (Fig. 7-5-A and B). The complete re-crystallization of the dissolved solid may take several weeks after the PIXE experimental procedure (Fig. 7-5-C).

All MS-type inclusions that have being exposed to the PIXE microbeam show that one of the solid phases as well as the enclosing liquid change from colorless to pale yellow brown, and the color did not disappear upon heating as indicated by Heinrich et al. (1992). The coloring effect could be due to oxidation of Fe^{+2} by protons to form ferric chloride (Anderson et al., 1989).

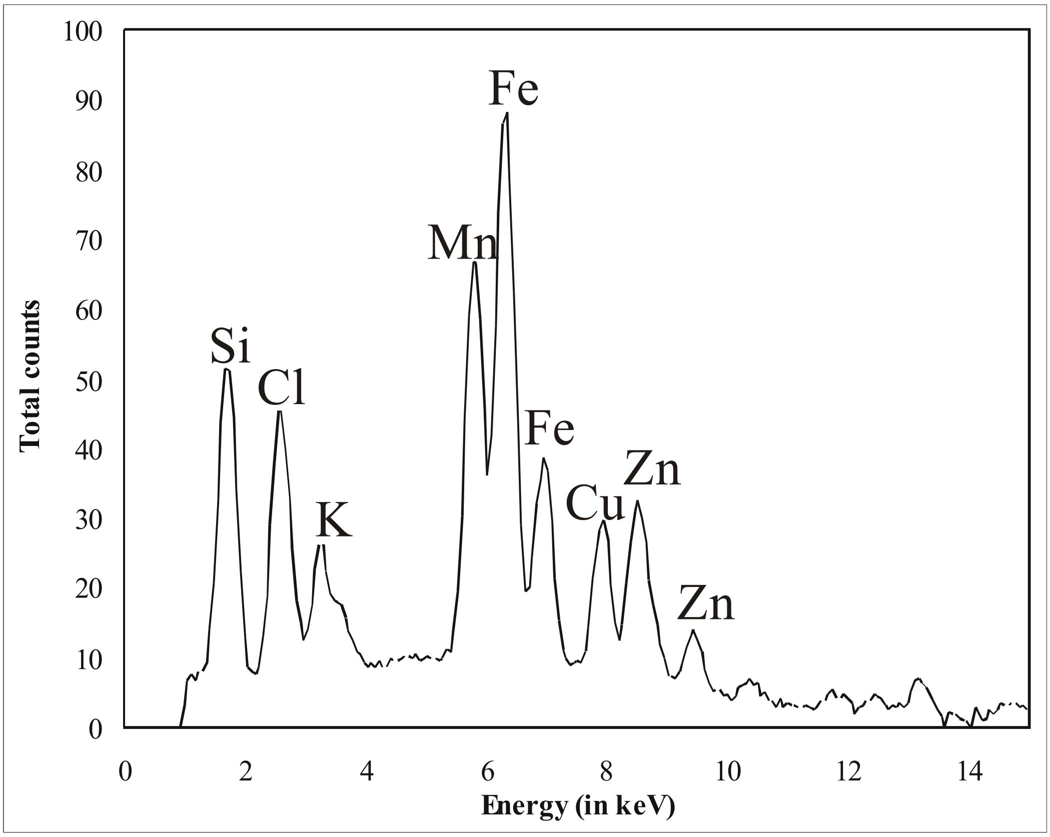

Figure 7-3. Typical PIXE spectra from MS-type fluid inclusions.

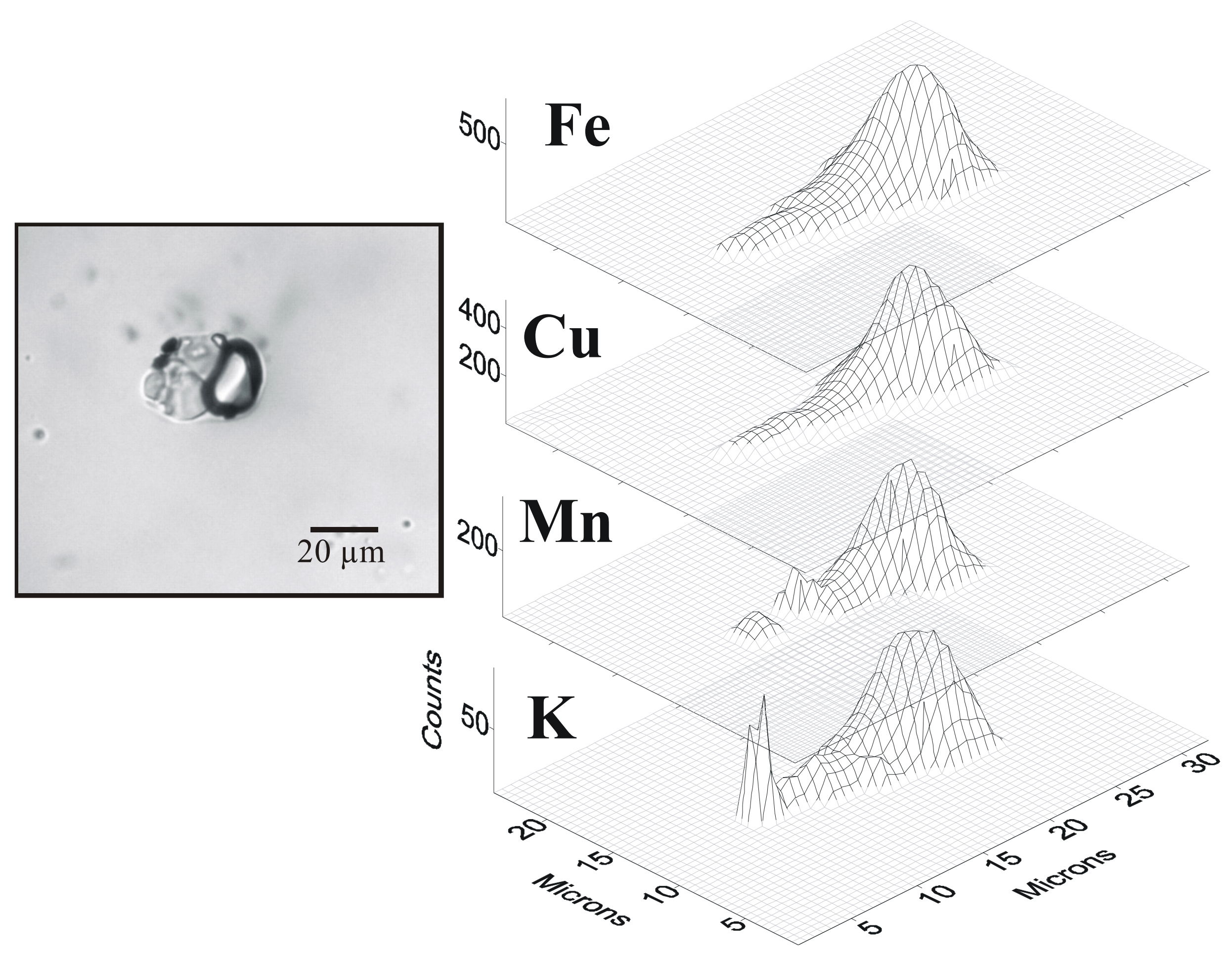

Figure 7-4. X-Y scanning of an MS-type fluid inclusion showing the distribution of metals.

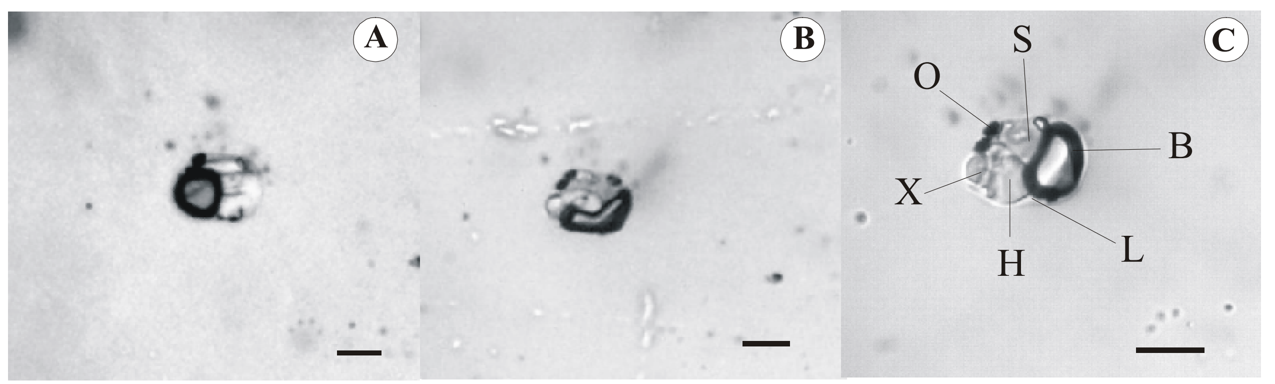

Figure 7-5. MS-type fluid inclusions before PIXE analysis (A), a week after (B) and three months after (C) respectively. O: opaque; other symbols as in figure 7-2. Scale bar 20 µM.

7.5 Raman microanalysis

All studied MS-type inclusions fail to indicate the presence of any Raman-active daughter mineral, polynuclear species or in particular polyatomic gas, therefore it is believed that the bubble corresponds mostly to H_2O.

During the experimental procedure, the dissolution of at least two of the solids with the lower dissolution temperatures occurs every time the laser beam hit the inclusions. The increasing temperature that provokes the dissolution within the inclusions may be explained as a phenomenon of energy absorption by the iron-rich fluid and/or solid (Burke, pers. comm.).

7.6 SEM analysis

Several selected MS-type inclusions were opened by careful hand-polishing to prevent the dissolution of daughter minerals, following the same technique described for the melt inclusions (Chapter 6). The aim of this experimental procedure was to identify the solids contained within the inclusions. With this technique it was possible to confirm the occurrence of halite and sylvite crystals (Fig. 7-6), however the other crystalline phase could not be detected.

If halite and sylvite crystals were found after the opening procedure, then we assume that the other solid phase observed in unopened inclusions is probably a highly hydrous phase or a gel-like compound that will easily be lost during the opening or carbon-coating procedure needed for the SEM analyses. In consequence, the unknown mineral would correspond most likely to a hydrous Fe-Mn-Cu chloride-rich compound.

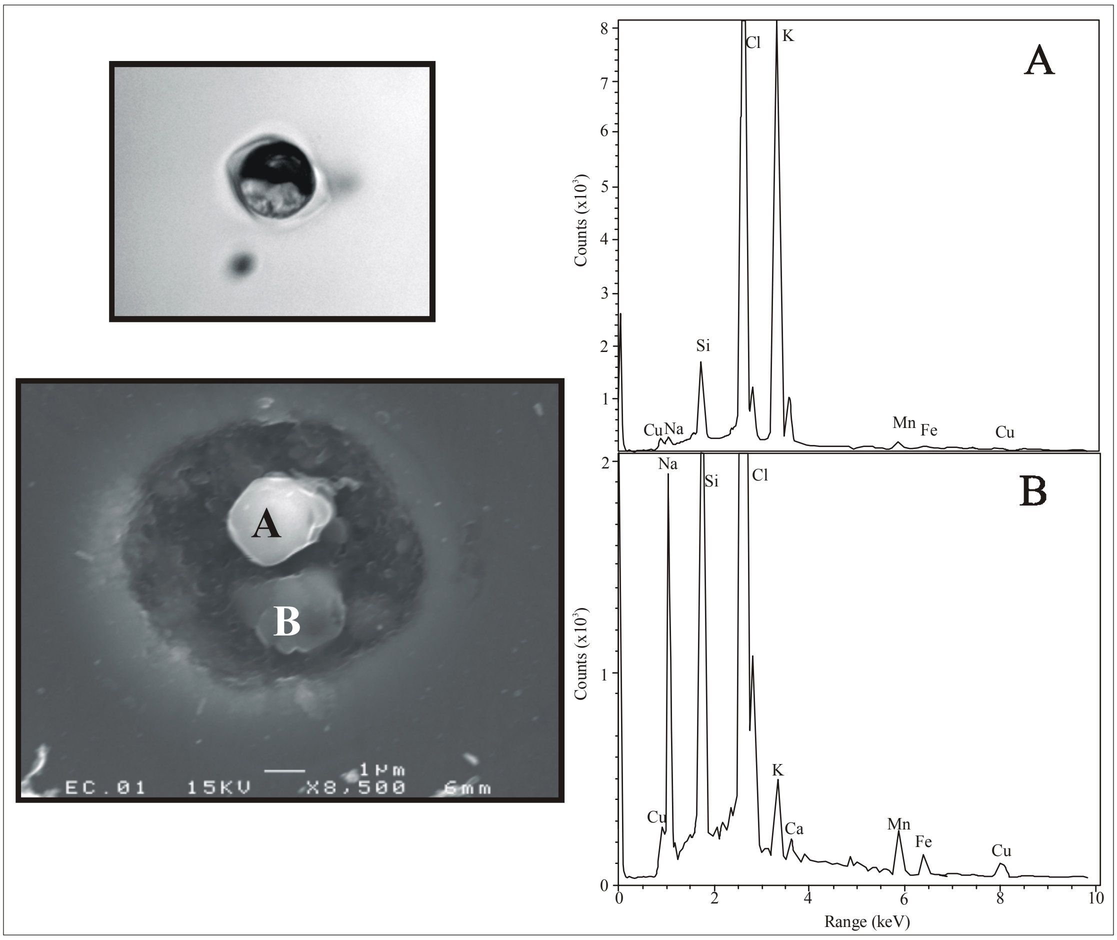

Figure. 7-6. EDS spectra on a opened MS-type inclusions

7.7 Conclusions

Total homogenization in MS-type inclusions occurs at extremely high temperatures (700° to 1030°C), which certainly lie within the magmatic temperature range, well above the typical "boiling" fluids that characterize the late-magmatic and main hydrothermal stage in porphyry copper systems (Fig. 7-7)

Non destructive, in situ analyses of individual MS-type inclusions, in particular PIXE microanalysis and microthermometry, in combination with the characterization of daughter minerals done by the EDX technique, provide a good qualitative approach to the overall composition of the trapped fluids and solids. The analytical results indicate that this early magmatic fluid has a highly complex chlorine-rich chemical composition, which most likely corresponds to the Na-K-Fe-Cu-Mn-Zn-Cl-H_2O system. Unfortunately, experimental data for such a system are scattered and insufficient and therefore phase equilibrium for systems containing these components are unknown. The best approximation of the bulk salinity of this fluid can be estimated by considering the dissolution temperature of halite and sylvite and the H_2O-NaCl-KCl system, in this case the real salinity would be between 60 and 80 wt. % NaCl equiv.

A major difference between the inclusions described from Panguna (Easton and Eadington 1986), Apusei Mountains (Pintea, 1995), Granisle (Wilson et all, 1980), and Bajo de la Alumbrera, (Ulrich et al., 2001) with the MS-type inclusion from the Zaldívar PCD, is that the MS-type inclusions do not coexist with vapor-rich inclusions. This observation indicates that MS-type inclusions represent the first magmatic, homogeneous aqueous fluid, exsolved during the crystallization of the host magma, and they cannot be interpreted as resulting from heterogeneous trapping as observed in the Granisle PCD (Wilson et al., 1980).

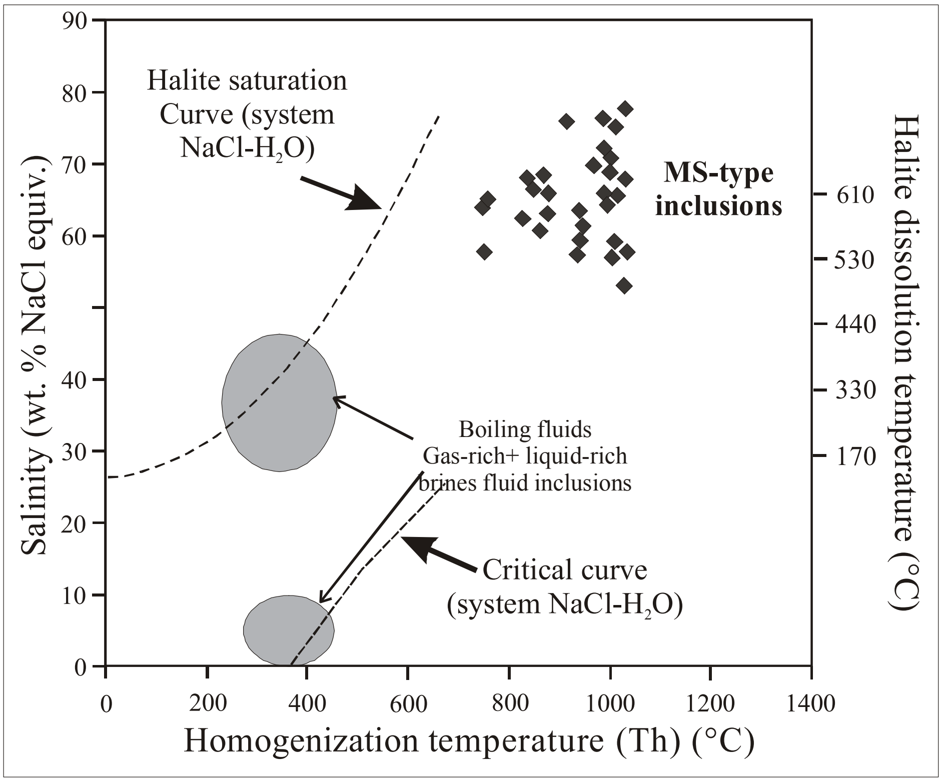

Figure 7-7. In the salinity vs. homogenization temperature plot, MS-type inclusions (filled diamonds) define a field markedly different from the most abundant "boiling" hydrothermal fluids (coexisting liquid-rich brines and vapor-rich inclusions) (shaded areas).

Chapter 8

Hydrothermal Fluid Inclusions

8.1 Introduction

As fluid inclusions are a potential source of information on the pressure, temperature and composition of the trapped fluids, they directly provide a unique possibility to study the physicochemical conditions at a specific stage of the fluid evolution. However, this premise is valid only on the condition that they are not affected by post-entrapment phenomena such as those described by Roedder (1971).

Because they constitute sealed samples, fluid inclusions have repeatedly demonstrated to be one of the most significant sources of geochemical information regarding the nature of mineralizing fluids and the processes by which mineral deposits were formed in hydrothermal systems (metal transport, mineralization and hydrothermal alteration), therefore they have long been a central topic of study in porphyry copper deposits (e. g. Roedder, 1984; Heinrich et al., 1999).

Roedder (1971), Nash and Theodore (1971), Moore and Nash (1974), and Bodnar and Beane (1980) have meticulously demonstrated the widespread occurrence of high-temperature (~400° - ~800°C), highly saline solutions (brines with about ~35 to > 60 wt % NaCl equivalent) in PCDs. These solutions are closely related to the concentric hydrothermal alteration pattern, particularly to the potassic and phyllic zones with which the primary ore is associated (Lowell and Guilbert, 1970). Another typical feature of fluid inclusions in porphyry copper deposits is that quartz phenocrysts contain coexisting vapor-rich and salt-bearing liquid-rich fluid inclusions (Nash, 1976; Beane and Bodnar, 1995), a feature that is also evidence for a shallow level of emplacement (Yang and Bodnar, 1994). Furthermore, the widespread coexistence of both types of inclusions that homogenize at nearly the same temperature would mean that they were generated along the immiscibility surface of the overall system (Pichavant et al., 1982), a clear indication of a boiling system. As a concluding result, fluid inclusion studies have convincingly shown that fluids of magmatic origin are responsible for transporting copper in the hydrothermal system (Heinrich et al., 1999).

The aim of this chapter is to present microthermometric and geochemical characterizations of the fluid inclusions hosted in quartz phenocrysts from the Llamo and Zaldívar porphyries, and by the interpretation of the obtained data to reach a better understanding of the complex evolution of hydrothermal fluids at various stages between the post-magmatic and late hydrothermal stages in the Zaldívar porphyry copper deposit.

The basics and principles of fluid inclusion techniques and terminology have been comprehensively reviewed elsewhere by Roedder (1984), Nash and Theodore (1971), Sheperd et al. (1985), therefore no further details concerning these topics will be given here.

8.2 Description

Emulating a recognized common feature in nearly all porphyry copper systems, quartz phenocrysts from the Llamo and Zaldívar porphyries are crowded with different types of aqueous fluid inclusions that are intimately associated on a microscopic scale (Fig. 8-1). A meticulous microscopic examination of aqueous-rich and vapor-rich fluid inclusions hosted in quartz phenocrysts was done on double-sided polished wafers 0.3-0.05 mm thick. This study indicated three main types of fluid inclusions on the basis of their phase assemblage at room temperature: B-type inclusions are dense salt-bearing liquid-rich inclusions, G–type inclusions correspond to low-density vapor-rich inclusions, and W-type inclusions represent brines of low to moderate salinity liquid-rich inclusions. These types of inclusions have been reported as being typical for porphyry copper deposits (Nash, 1976).

The most abundant types of inclusions correspond to salt-bearing aqueous-rich (B) and vapor-rich (G) inclusions, however the relative abundance and the spatial distribution of each type of inclusion is highly variable among phenocrysts from the same sample.

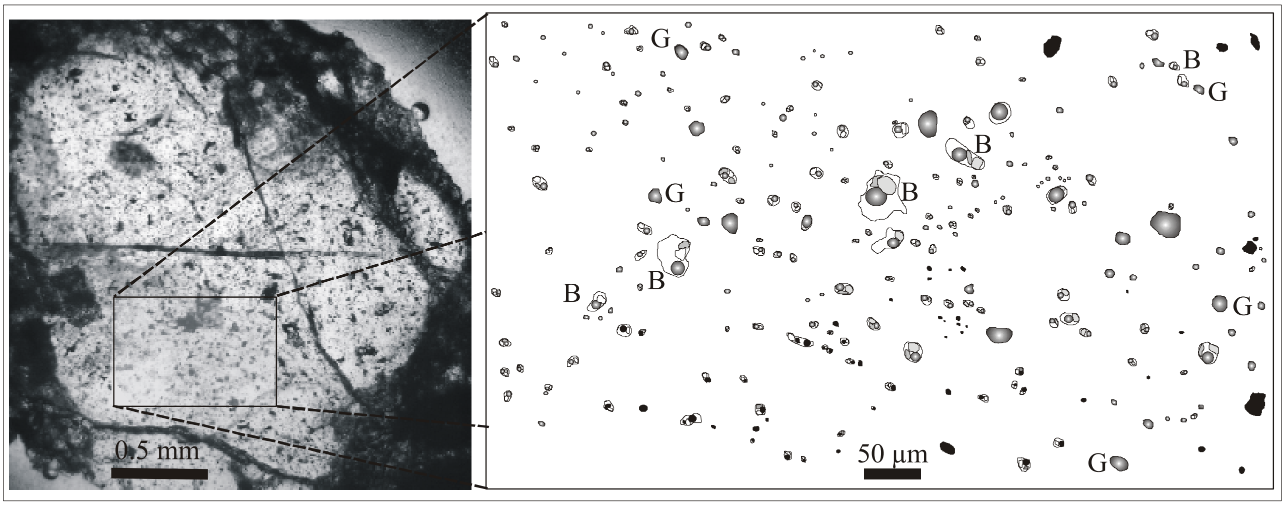

Figure 8-1. Quartz phenocrysts from the Llamo and Zaldívar porphyries show a dense concentration of aqueous and gaseous fluid inclusions. B: high-salinity inclusions, G: gaseous-rich inclusions.

8.2.1 B-type: salt-bearing aqueous-rich inclusions

For a general classification, all B-type inclusions are grouped together, even though their physical or chemical properties may differ.

A B-type inclusion shows a regular morphology, normally round to elongated, always tending to a negative crystal shape, their size varies from a few micrometers up to 50 μm, but most frequently smaller than 30 μm. These inclusions occur randomly or are distributed along possible growth faces in the host crystal. They appear to be primary as they are unrelated to visible healed fractures, however the distinction between primary and secondary fluid inclusions is never absolute (Roedder, 1967), and is particularly problematic in high-temperature deposits with a complex evolutionary history (Nash and Theodore, 1971), as observed in all studied host phenocrysts.

The B-type inclusions typically contain an aqueous fluid as the most abundant phase at room temperature, representing about 30 to 50 % of the cavity total volume; the vapor bubble is relatively small and occupies about 20 % of the inclusion. Raman analysis indicates that only traces of CO_2 are present in the bubble, therefore it is believed that it contains mostly low-density H_2O.

As mentioned above, one of the most distinguishing features in porphyry copper deposits in general and for the Zaldívar mine is the occurrence of highly saline fluid inclusions containing multiple daughter minerals. Daughter minerals have crystallized from the enclosed saturated liquid phase on cooling after trapping as the fluids reach saturation for a particular phase (Roedder, 1971; Sheperd et al., 1985), therefore the presence and correct identification of these solid phases can provide important data on the fluid chemistry at a specific moment during the hydrothermal evolution (Roedder, 1971; Nash and Theodore, 1971).

Daughter crystals altogether can occupy between 20 to 50 % of the cavity total volume, they were identified with a petrographic microscope. A few selected inclusions were also studied by SEM microanalysis to verify the correct identification of some crystals.

Three different colorless, semitransparent daughter minerals have been identified with relative certainty by their physic and optical properties.

- Halite (NaCl) is always the largest, easy to recognize and the most common solid phase in all B-type inclusions. It generally occurs as an isotropic well-formed cubic crystal, rarely as rounded grains (Fig. 8-2-A and B).
- Sylvite (KCl) was identified with less confidence; it occurs as an isotropic crystal usually showing a rounded shape and a lower refractive index than halite. Closely associated with halite, sylvite appears always as the second largest daughter mineral (Fig. 8-2-A).
- Anhydrite ($CaSO_4$). An elongated or rectangular prismatic grain is inferred to be anhydrite, based on the shape, parallel extinction and moderate birefringence. This daughter crystal corresponds to the smallest semitransparent solid phase and is not always clearly visible (Fig. 8-2-A).

Opaque minerals are ubiquitous in the B-type inclusions, in fact this inclusion type may contain up to two opaque grains (Fig. 8-2-A and -B). One of the opaque minerals is inferred to be hematite on the basis of its color in thin flakes (red to yellow or orange-yellow), although when the hematite grains are thicker or equant, they will appear as opaque grains. The second opaque mineral appears always as a black grain, there is no evidence that may help to identify the composition of this grain; its response to a strong magnet was not tested. Other solid phases of unknown composition may also occur.

The B-type inclusions can be further split into at least two subtypes according to the number of solid phases that they contain at room temperature. The B_1-subtype typically contains three semitransparent daughter minerals, halite, sylvite and anhydrite plus two opaques (Fig. 8-2-A), representing the most common assemblage of solid phases in fluid inclusions from porphyry copper deposits (Roedder, 1984). The B_2-subtype is characterized by the presence of a single semitransparent crystal and one opaque (Fig. 8-2-B). Most probably there is a continuous compositional transition between the B_1-subtype with a rather complex fluid composition to the simpler B_2-subtype.

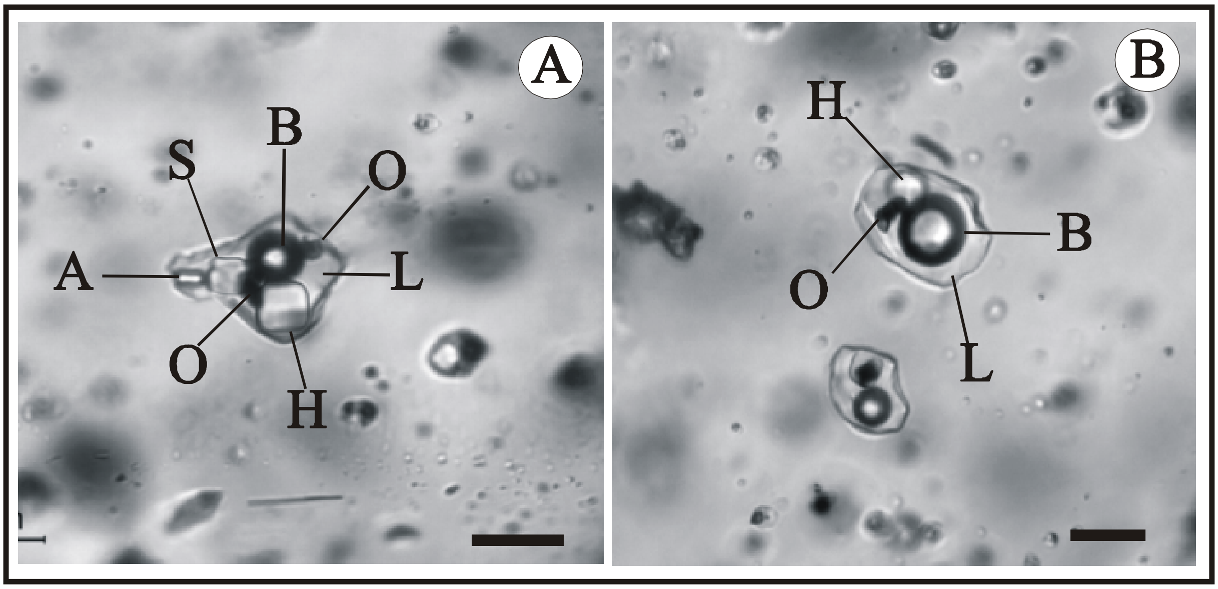

Figure 8-2. High salinity B_1-type (A) and B_2-type (B) fluid inclusions hosted in quartz phenocrysts from the Llamo and Zaldívar porphyries. L: aqueous fluid, B: bubble, H: halite, S: sylvite, A: anhydrite, O: opaque mineral. Scale bar 20 µm.

8.2.2 G-type: vapor-rich inclusions

G-type corresponds to low-density, vapor-rich inclusions, in which the vapor bubble comprises more than 70% of the total inclusion volume. The gas is believed to be mostly water-rich as Raman analysis shows that only a few inclusions contain CO_2, however in negligible amounts (less than 1%).

The size of these inclusions varies from a maximum of 50 µm to less than 1 µm, and in most cases their shape approximates a negative quartz crystal. Elongated to irregularly shaped inclusions may also be present. They are randomly distributed within the host crystal or aligned along probably recrystallized microfractures.

In G-type inclusions a liquid rim frequently occurs around the bubble, it can range from very thin and hardly visible (Fig. 8-3-A) to relatively wide, occasionally containing halite, anhydrite or an opaque mineral as daughter minerals (Fig. 8-3-B) (for identification of solid phases see above). The wide liquid rims with daughter minerals may result from the trapping of a little high-salinity liquid with the predominant vapor or by necking down of B-type inclusions (Roedder, 1971; Eastoe, 1978).

8.2.3 W-Type: liquid-rich inclusions

W-type inclusions are liquid-rich, low-salinity inclusions, which contain two fluid phases, a liquid amounting to about 60 to 80 % of the total cavity volume plus a vapor bubble that occupies the remaining 20 to 40 %. The bubble is considered to be essentially H_2O vapor as there is no indication of CO_2 contents from Raman analysis or microthermometry.

Based on their shape, size of the bubble and solid contents, the W-type has been subdivided into the following three subtypes:

W_1-type inclusions usually contain a reddish-brown hematite daughter crystal that in some inclusions may not be present or visible, they are also characterized by having a vapor bubble larger than in the other subtypes (W_2 and W_3), and showing a rather regular shape (Fig. 8-4-A and -B).

W_2-type inclusions occur randomly distributed in the host crystal, isolated or in healed fractures, their shape is always regular trending to a negative crystal shape (Fig. 8-4-C).

W_3-type inclusions are irregular in shape and aligned along microfractures, they also correspond to the largest inclusions hosted in the quartz phenocrysts, up to 100 µm. (Fig. 8-5-D).

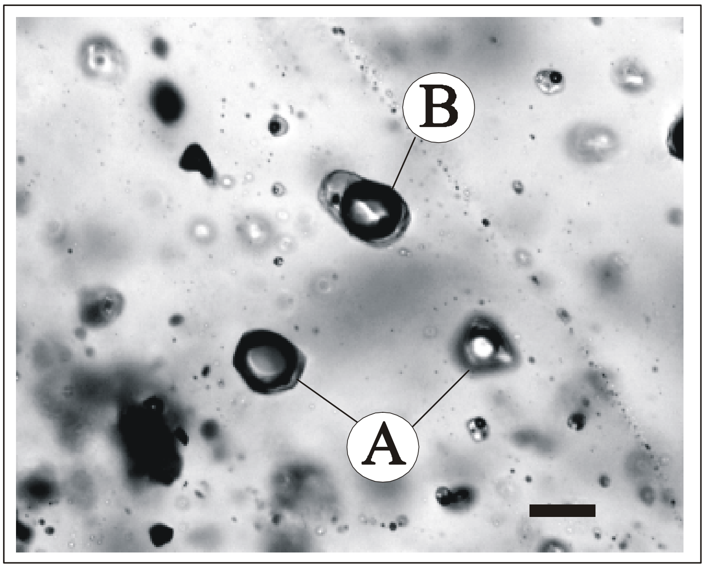

Figure 8-3. Most of the inclusions disseminated in the host mineral correspond to the G-type, in the picture two types of gas-rich inclusions are shown, one showing a narrow rim of liquid (A) and the other a greater volume of liquid plus an opaque grain (B). Scale bar 30 µm.

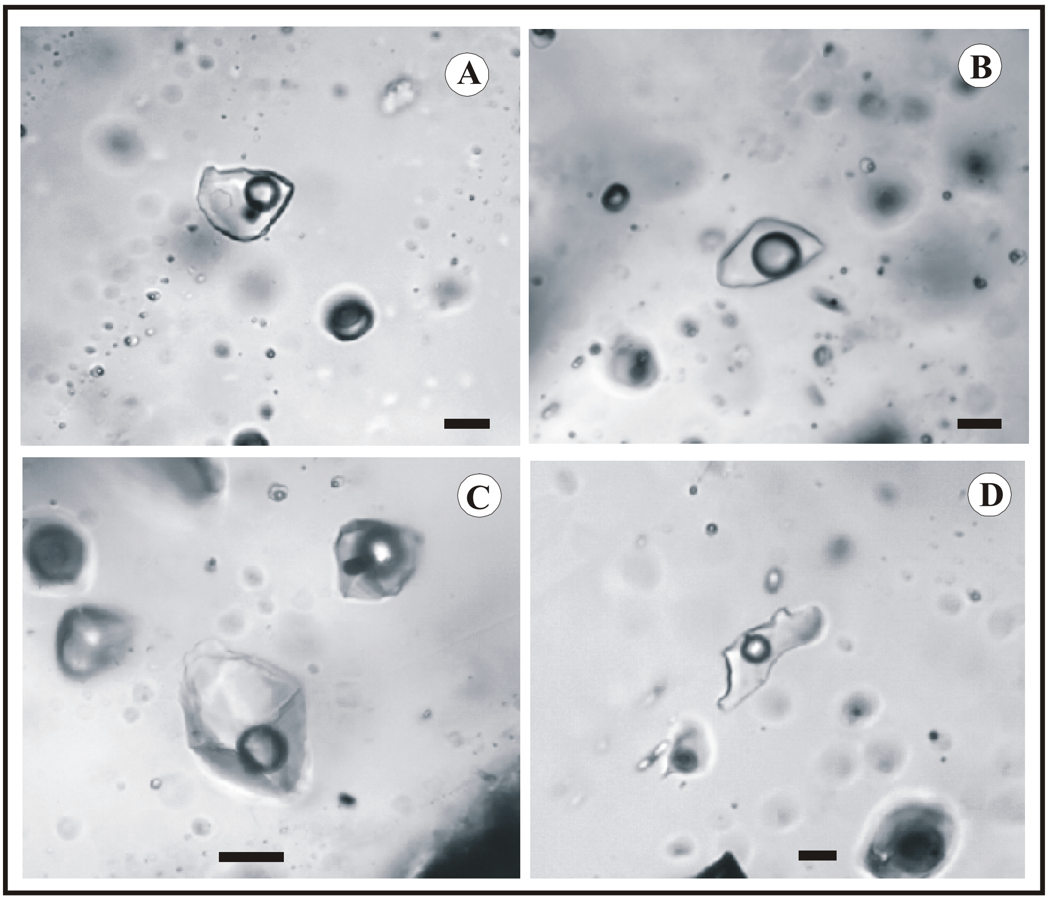

Figure 8-4. W-type fluid inclusions, A: W_1-type inclusion containing a small opaque, most likely hematite; B: W_1-type inclusion; C: Low-salinity W_2-type inclusion; D: Low salinity, secondary W_3-type inclusion. Scale bar 10 µm.

8.3 Distribution

The distinction between primary and secondary fluid inclusions is extremely difficult to establish in higher-temperature deposits such as porphyry copper (Roedder, 1971; Ahmad and Rose, 1980; Nash and Theodore, 1971), in fact this type of environment would yield mostly secondary inclusions, whereas primary inclusions are rare (Roedder, 1992). In the studied quartz phenocrysts those fluid inclusions that appear isolated, not occurring in any sort of linear array except along traces of growth planes are usually classified as primary, however they most probably are secondary inclusions that migrate out of the fracture planes (Audétat and Günther, 1999). Furthermore, widely spaced inclusions showing a linear arrangement without any trace of a fracture plane most probably have formed in older fractures that later become completely healed (Fig. 8-5-A), so they are actually secondary or pseudosecondary in origin.

In all studied samples W-type inclusions represent less than 20 % of all observed inclusions. The W_1-type occurs randomly distributed or aligned in healed fractures, usually closely associated with B_2-type inclusions. The distribution of W_2-type is random and not apparently associated with any of the other type of inclusions in the quartz host. Only W_3-type inclusions are most commonly found aligned along well-defined microfractures that frequently cut across the host crystal. Because of their morphology and distribution, they are undoubtedly secondary.

The spatial distribution and relative ages of the different B-subtypes and the G-type inclusions are difficult to determine because their distribution patterns are highly complex. Nearly all quartz phenocrysts are densely crowded with these inclusions and generally there are no structural criteria to correlate the multiple generations of healed fractures that crisscrossed the host mineral with the different inclusions types. In fact, almost any imaginable plane can be defined containing inclusions of contrasting composition.

The accurate recognition of healed fractures containing cogenetic inclusions is especially problematic, and only possible in rather sparse clear areas of the phenocryst that contain only a few inclusions (Fig. 8-5-A).

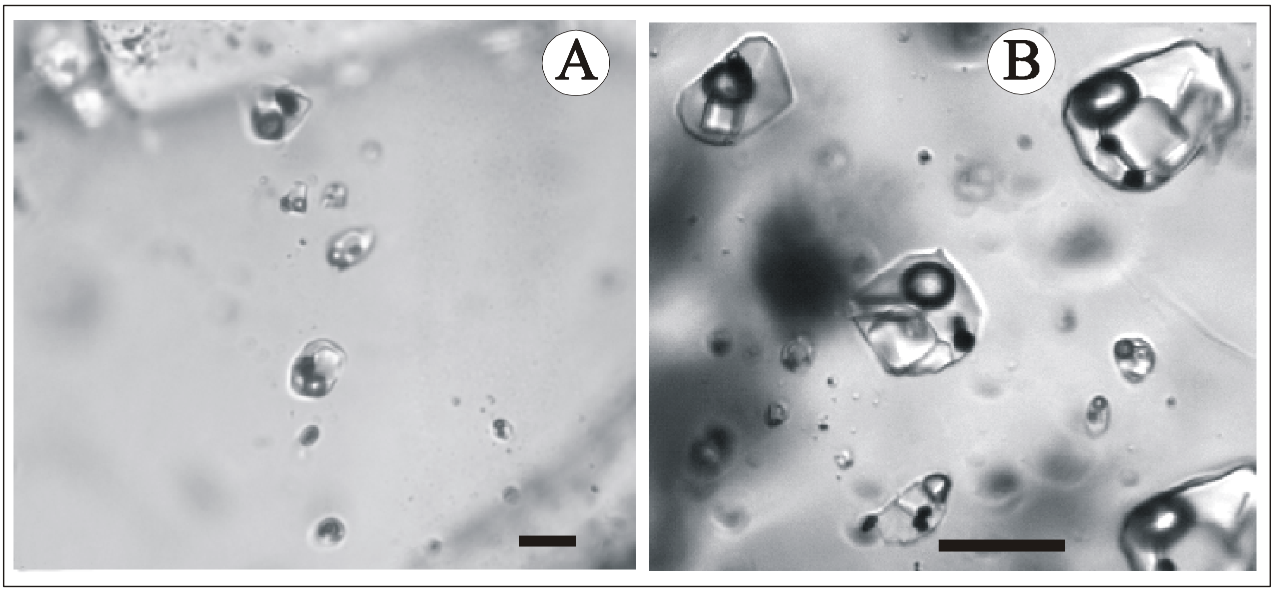

Figure 8-5. A) B1-type inclusions aligned along a possible healed fracture; note that the composition of all the aligned inclusions is similar. B) Co-genetic B_1-type inclusions showing similar composition. Scale bar 20 µm.

When a group of cogenetic inclusions can be recognized, their composition along any given plane is uniform and is usually distinctly different from the inclusions occurring along adjacent healed fractures (Fig. 8-5-B).

Some B-type inclusions may occur closely associated and apparently coexist with G-type inclusions, suggesting aqueous fluid immiscibility (Fig. 8-6), however the genetic relationship between them cannot always be established with certainty.

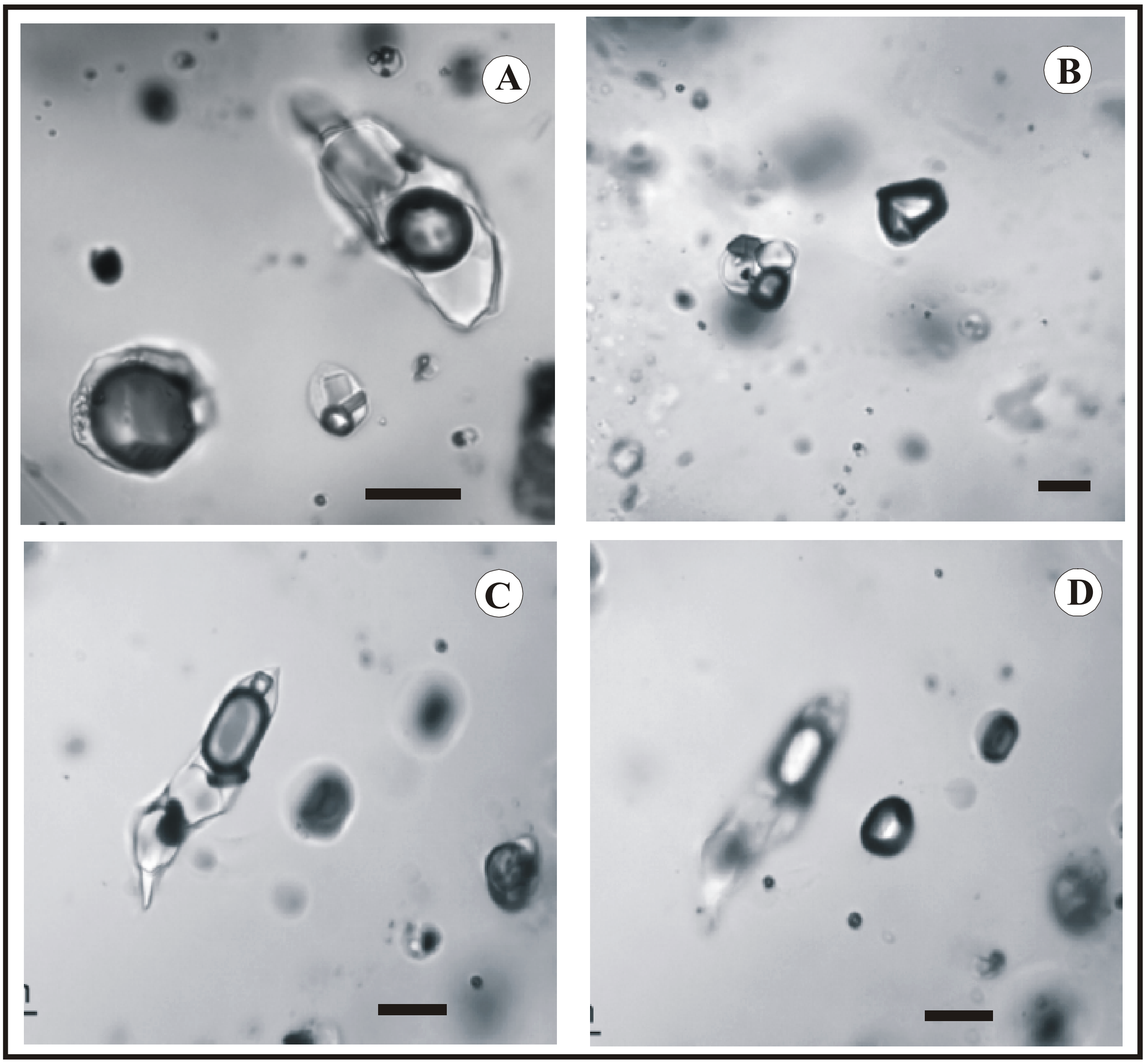

Figure 8-6. B- and G-type fluid inclusions usually show a very close coexistence within the host mineral. A and B coexisting inclusions in the same horizontal plane; C and D coexisting inclusions in a nearly vertical plane. Scale bar 20 µm.

8.4 Microthermometry

In heating experiments, the temperature at which the vapor and liquid phases disappear into the remaining fluid is called the filling temperature; it does not necessarily mean total homogenization (Ahmad and Rose, 1980). There is a difference between filling and homogenization temperatures because in many studied fluid inclusions solid phases such as halite may commonly dissolve above the filling temperature, or such as hematite and anhydrite which do not dissolve at all.

Petrography and microthermometry indicate considerable variability in fluid inclusion composition, reflecting the complex chemistry of fluids trapped in the inclusions. Efforts were therefore made to interpret the complex microthermometry data in the simplest possible way. Freezing and heating measurements were performed on each inclusion, however as the phase changes during the freezing of multiphase inclusions are generally complex and not possible to interpret (Roedder, 1971), the freezing data of those highly saline B-type inclusions was excluded.

8.4.1 B-type

8.4.1.1 B_1-subtype

No major differences can be established among the data resulting from heating experiments in B_1-subtype fluid inclusions hosted in the Llamo and Zaldívar porphyries, therefore in the discussion of the results no separation will be made between fluid inclusions hosted in either rock unit.

Upon heating from room temperature B_1-subtype inclusions, the dissolution of sylvite (T_{sKCl}) occurs at temperatures ranging from 62° to 225°C, upon further heating halite gradually becomes round and dissolves (T_{sNaCl}) at temperatures between 200° and 500°C (Table 8-1). In about half of all measured inclusions halite dissolution occurs after reaching the filling temperature that always occurs by disappearance of the gas bubble within the 225°- 550°C temperature range (Table 8-1 and Fig. 8-7-A). Hematite and anhydrite did not dissolve during heating.

The compositional complexity of B_1-subtype inclusions is such that the measurements of T_{sNaCl} would only indicate a relative salinity, therefore the dissolution temperature of sylvite is also required to better approximate the real composition of the fluid in the ternary system NaCl-KCl-H_2O. Using the paired T_{sNaCl} and T_{sKCl} obtained for 89 fluid inclusions from the Llamo porphyry and 56 from the Zaldívar porphyry, and the method described by Roedder (1971), the weight percents of NaCl and KCl for each inclusion can be estimated by referring to the NaCl-KCl-H_2O ternary system. The concentration of NaCl and KCl varies between 19 to 56 and 9 to 38 wt % respectively (Table 8-1).

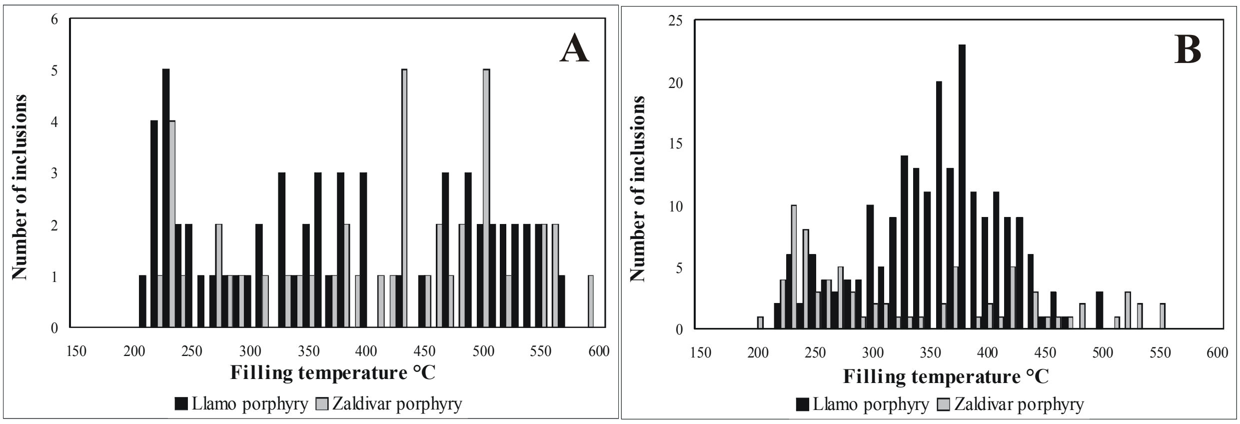

Figure 8-7. Frequency-filling temperature histogram for B_1-type (A) and B_2-type (B) fluid inclusions from Llamo and Zaldívar porphyries.

8.4.1.2 B_2-subtype

During the heating procedure of B_2-subtype inclusions, the bubble slowly decreases in size and finally fades away into the fluid phase. The filling temperatures measured in 180 inclusions from the Llamo porphyry and 62 from the Zaldívar porphyry define a wide temperature range of 200°-550°C (Fig. 8-7-B). The halite dissolution can occur before or after the filling temperature, in either case the T_{sNaCl} would be between 170° and 550°C. Halite dissolution before the filling temperature occurred in about 2/3 of the measured inclusions.

Assuming that all the salts in the B_2-subtype inclusions are pure NaCl, then the T_{sNaCl} values measured on these inclusions would define salinities between 30 and 56 wt % NaCl equiv (Table 8.1) for the system NaCl-H_2O (Sourirajan and Kennedy, 1962).

Table 8.1. Quantitative data for B-type fluid inclusions in quartz phenocrysts from the Llamo and Zaldívar porphyries. (*) Final homogenization occurs by halite dissolution.

Sample	Inclusion type	Dissolution temp, °C KCl / NaCl	Salinity (wt %) KCl / NaCl	Filling temp °C
Llamo				
181197-11	B_1-type	180 – 170 / 330 – 370	24 – 25 / 29 – 34	250 – 270
Z-111-27	B_1-type	110 – 150 / 320 – 435	17 – 22 / 30 – 45	225 – 570
108-315	B_1-type	65 – 225 / 200 – 425	9 – 38 / 19 – 42	275 – 392
181197-11	B_2-type (*)	/ 260 – 435	/ 35 – 49	220 – 380
108-315	B_2-type(*)	/ 262 – 500	/ 35 – 56	221 – 390
Zi-115	B_2-type (*)	/ 173 – 478	/ 30 – 54	226 – 431
181197-11	B_2-type	/ 170 – 380	/ 30 – 44	300 – 435
108-315	B_2-type	/ 214 – 378	/ 32 – 44	246 – 405
Zi-115	B_2-type	/ 356 – 495	/ 42 – 56	335 – 500
Zaldívar				
Z-121-420	B_1-type	62 – 170 / 230 – 389	10 – 28 / 21 – 42	307 – 409
Z-120-10	B_1-type	70 – 195 / 220 – 487	10 – 24 / 27 – 53	225 – 500
171197-01	B_1-type	86 – 225 / 328 – 500	12 – 20 / 33 – 56	368 – 600
Z-108-26	B_1-type	125 – 175 / 241 – 283	22 – 29 / 22 – 26	324 – 350
Z-121-420	B_2-type (*)	/ 200 – 380	/ 32 – 45	200 – 380
Z-120-10	B_2-type (*)	/ 261 – 550	/ 35 – 49	215 – 362
171197-01	B_2-type (*)	/ 296 – 435	/ 37 – 49	239 – 414
Z-121-420	B_2-type	/ 200 – 220	/ 35 – 56	295 – 360
Z-120-10	B_2-type	/ 176 – 535	/ 33 – 51	267 – 550
171197-01	B_2-type	/ 211 – 460	/ 32 – 52	289 – 550

8.4.2 G-type

Cooling procedures on G-type inclusions have no effect on the size or appearance of the gas bubble, and because of the small amount of liquid, it was difficult to observe any changes in the aqueous phase.

In the G_1-type inclusions freezing typically occurs with a sudden darkening of the aqueous phase at temperatures lower than -45°C, down to –75°C. On slow heating, these inclusions show the melting of several solid phases that occur at successive steps. The first melting episode occurs in the temperature range -56.8° to -36.9°C, then a second one between –28.5° to –18°C, the final ice melting occurs between -23.4° to - 5.6°C which correspond to salinities of 19.4 to 9.1 wt % NaCl equiv., respectively (Table 8-2). This behavior upon cooling strongly suggests the occurrence of ions other than Na^+ (notably Fe^{++}, Mg^{++}, K^+) in the aqueous phase. In some inclusions a solid phase remains above 0°C, which melts between 3° and 26°C, this solid may be halite and this would indicate that in these inclusions, the aqueous fluid is highly saline, close to NaCl saturation.

In G_2-type inclusions, the rim containing the aqueous phase freezes around -30°C, on subsequent heating, final ice melting occurs within the temperature range of -6.5° and -0.0°C, indicating salinities of 9.9 to 0.0 % NaCl equiv (Table 8-2).

In all G-type fluid inclusions, the aqueous phase gradually evaporates into the vapor bubble upon heating, and as the amount of liquid is progressively reduced, optical difficulties arise in determining the point at which the vapor phase completely fills the cavity, therefore, the filling temperature cannot be defined with accuracy; however, all measurements fall within a narrow range between 290° and 463°C (Table 8-2). The few inclusions that show significantly higher filling temperatures, in the vicinity of 500°C, most probably represent either inclusions in which part of the fluid has leaked out before or during the experiment or inclusions in which necking down has occurred; both phenomena will increase the filling temperature (Roedder, 1971).

The filling temperatures and salinity values of G-type inclusions measured on samples from the Llamo and Zaldívar porphyries show a complete overlap (Fig. 8-8 and Fig. 8-9), and no temperature differences can be established among inclusions hosted on either of the two intrusives.

In G_1-type inclusions from Llamo and Zaldívar porphyries, the filling temperature increases with the salinity (Fig. 8-9), however this feature does not necessarily relate to a evolutionary path, more likely it will be explained by the amount of high salinity fluid coexisting with the gas bubble; for the bigger the amount of aqueous fluid, the higher the filling temperature and salinity.

Table 8-2. Microthermometry and salinity data for all studied G-type fluid inclusions hosted in quartz phenocrysts.

Sample	Inclusion type	$T_{M\text{-ice}}$ °C	T_H °C	Salinity (NaCl wt % equiv)
Llamo				
Z-111-27	G_1-type	-10.0 – -21.0	308 – 410	13.9 – 18.6
108-315	G_1-type	-5.6 – -19.5	317 – 490	9.1 – 22.0
Zi-115	G_1-type	-8.4 – -23.4	410 – 520	12.2 – 19.4
Z-111-27	G_2-type	-1.5 – -6.5	290 – 450	2.6 – 9.9
108-315	G_2-type	-1.6 – -4.5	400 – 450	3.1 – 7.2
Zi-115	G_2-type	-0.4 – -4.3	350 – 441	0.7 – 6.8
Zaldivar				
Z-120-10	G_1-type	-5.8 – -19.9	370 – 500	8.9 – 22.3
Z-121-420	G_1-type	-7.5 – -16.7	350 – 415	11.1 – 20.0
Z-121-10	G_2-type	0.0 – -6.0	217 – 463	0.0 – 9.2

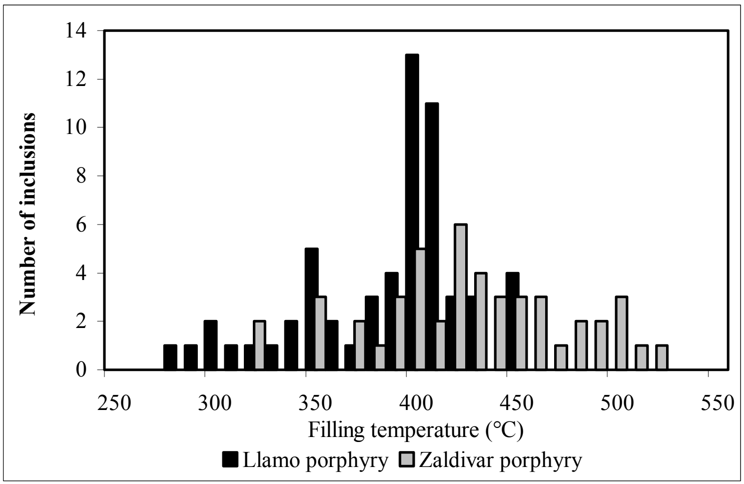

Figure 8-8. Histogram of filling temperatures in G_1-type (black bars) and G_2-type (shaded bars) fluid inclusions.

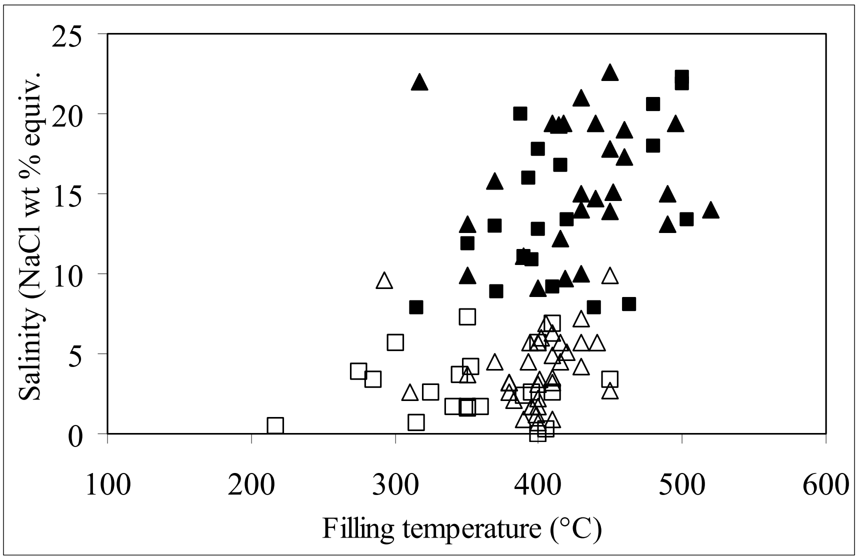

Figure 8-9. Filling temperatures versus salinities in G-type inclusions indicate that there are no major differences in the microthermometry data of inclusions from the Llamo and Zaldívar porphyries. The positive correlation between salinity and filling temperature in G_1-type inclusions is related to the amount of aqueous fluid present in a given inclusion. Black triangles: G_1-type from the Llamo porphyry; open triangles: G2-type from the Llamo porphyry; black squares: G1-type from the Zaldívar porphyry; open squares: G_2-type from the Zaldívar porphyry.

8.4.3 W-type

During cooling procedures, freezing of W-type inclusions occurs within two temperature ranges; -65° to -50°C, sometimes as low as -80°C (W_1-type inclusions) and between -30° to -41°C (W_2-type inclusions).

Freezing of the aqueous phase in the W_1-type inclusions is characterized by the formation of a brownish ice mass without an identifiable crystalline structure; in some cases it may became nearly opaque with further cooling, probably indicating the multinucleated growth of ice (Ahmad and Rose, 1980). The frozen aqueous phase in the W_2-type inclusions clearly shows the formation of a single ice crystal which is colorless and remains relatively transparent. Very often the ice crystal presses and deforms the bubble, a particularly useful phenomenon to obtain the freezing temperatures in some of these low-density inclusions.

Frozen inclusions were slowly heated at a rate of about 5°/min. During gradual warming, the W_1-type inclusions show simultaneously the appearance of the first liquid and the formation of several granular ice crystals at temperatures between -59° to -33°C. On further heating one frozen phase disappears between -41° and -10°C, at this point only a single crystal remains and it melts between -23° and -6.5°C. In many inclusions the last ice crystal only melts at temperatures between 2° and 20°C. Considering that the most common salt in all studied fluid inclusions from the Zaldívar deposit is NaCl, these values can be attributed to metastable melting of hydrohalite (NaCl-H_2O), a common phenomenon in low-salinity aqueous inclusions (Roedder, 1984).

The low initial melting temperature and the complex melting behavior observed in W_1-type inclusions indicate that the trapped fluids depart significantly from the pure NaCl-H_2O system, in fact a rather similar behavior is observed in the NaCl-$CaCl_2$-H_2O system (Vanko et al., 1992); however, compositional evidence indicates that Ca is rare or absent in fluid inclusions from the Zaldívar deposit compared to K and Na which are quite abundant, therefore it is most likely that the fluids trapped in these inclusions represent an aqueous solution containing Na, K, Fe, and perhaps Cu, and Mg.

The W_2-type inclusions show upon cooling a behavior consistent with the NaCl-H_2O system, the first liquid usually appears around –22°C, the eutectic point for the pure system. On further warming the ice crystal becomes rounded and small, and the final ice melting occurs between –0.2° and –6.5°C.

The concentration of salt dissolved in the fluid phase of aqueous inclusions can be estimated by using the relationship between salinity and freezing-point depression of aqueous sodium chloride (Potter et al., 1978). In the present case, salinities were calculated using the revised equation from Bodnar (1993). Considering the final ice melting temperature obtained in some W_1-type inclusions, the total salinity would be between 9.8 to 23.2 NaCl wt % equiv., and probably a little higher for those inclusions in which the solid phase persists above 0°C. However, the notion of NaCl wt % equivalent can only be considered as a rough approximation to the real salinity of the trapped fluids. The salinity estimated for the W_2-type inclusions is much lower, 0.1 to 9.2 wt % NaCl equiv.

On heating above room temperature, the bubble in all W-type inclusions fades away into the liquid phase. In the W_1-type inclusions, the filling temperature is between 228° and 520°C, showing a bimodal distribution with peaks at 325° and 450°C, and in the W_2-type it is between 221° and 417°C with a broad cluster between 250° and 400°C and a mode at 280°C (Table 8-3, Fig. 8-10).

Table 8-3. Quantitative data for W-type fluid inclusions from Llamo and Zaldívar porphyries. T_H, homogenization temperature, $T_{M\text{-}ice}$, final ice melting temperature.

Sample	Inclusion type	T_{Mice} °C	T_H °C	Salinity (NaCl wt % equiv)
Llamo				
Z-111-27	W_1-type	-10.0 – -21.0	308 – 410	13.9 – 18.6
108-315	W_1-type	-4.5 – -20.6	258 – 382	7.2 – 21.7
Zi-115	W_1-type	-4 – -21.3	295 – 501	6.4 – 21.7
181197-11	W_2-type	-0.5 – -1.5	228 – 267	0.9 – 2.6
Z-111-27	W_2-type	-0.1 – -1.8	224 – 384	0.2 – 3.1
108-315	W_2-type	-0.1 – -3.7	221 – 370	0.2 – 6.0
Zi-115	W_2-type	-0.3 – -6.0	236 – 417	0.5 – 9.2
Zi-115	W_3-type	-0.4 – -5.4	187 – 135	0.7 – 8.4
Zaldivar				
Z-120-10	W_1-type	-2.5 – -15.2	228 – 520	4.18 – 18.8
171197-01	W_1-type	-10 – -19	338 – 430	13.9 – 21.7
Z-121-420	W_1-type	-9.0 – -13.7	266 – 360	12.8 – 17.5
Z-121-10	W_2-type	0.0 – -6.0	242 – 390	0.2 – 9.2
Z-121-420	W_2-type	-0.2 – -6.5	186 – 364	0.4 – 9.7
171197-01	W_3-type	-0.2 – -3.5	143 – 154	0.4 – 5.7

A few well-developed fractures were found which contain aqueous inclusions corresponding to a W_3-subtype. These inclusions show a final ice melting temperature that occurs within the -0.2° to -3.5°C temperature range, indicating salinities between 0.4 to 5.7 wt % NaCl equivalent, and the homogenizing temperature is within the range of 143° - 154°C (Table 8-3). The low-salinity low-temperature W_3-type inclusions clearly reflect the simple NaCl-H_2O system, and they most probably represent the last hydrothermal event occurring in the Zaldívar ore deposit.

The microthermometry data of all the studied W-type fluid inclusions indicate that only minor differences can be observed among the inclusions hosted in either of the analyzed porphyrytic intrusives. In a filling temperature histogram (Fig. 8-10) and in a filling temperature versus salinity diagram (Fig. 8-11) there are no remarkable differences among the microthermometry data obtained for the Llamo and Zaldívar porphyries.

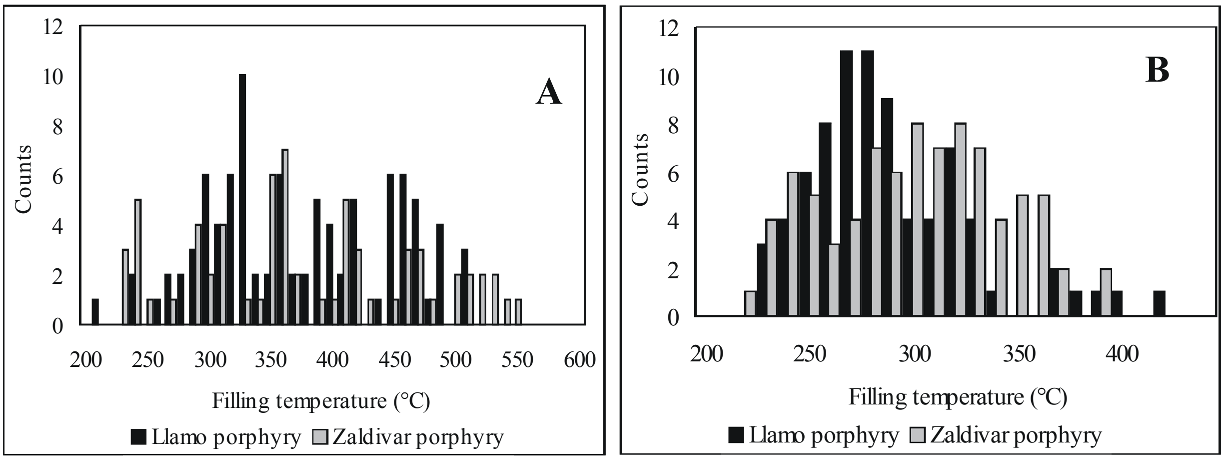

Figure 8-10. Histograms of filling temperatures in W_1-type (A) and W_2-type (B) fluid inclusions in samples from Llamo and Zaldívar porphyries.

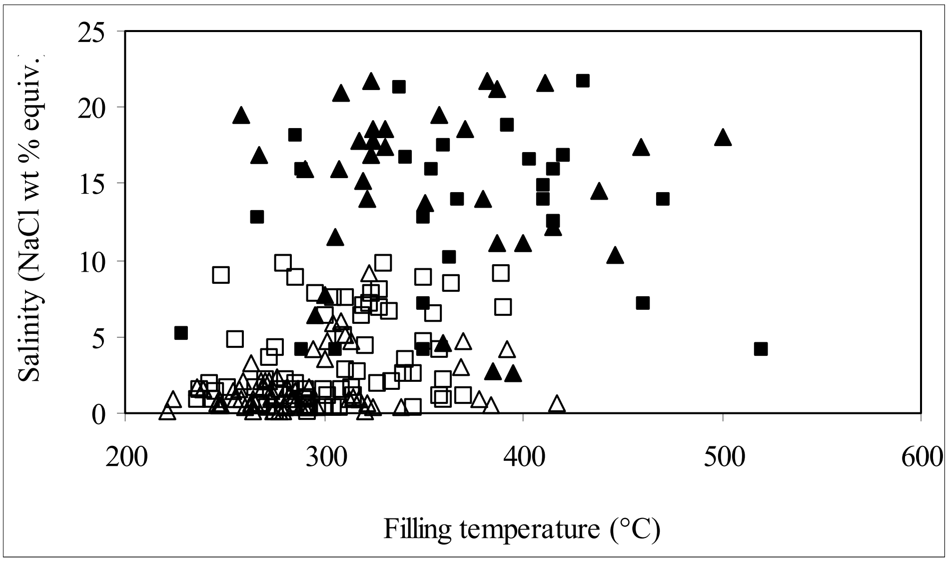

Figure 8-11. In a filling temperature versus salinity diagram the different subtypes of W-type fluid inclusions from the Llamo and Zaldívar porphyries are closely related. Triangles: samples from the Llamo porphyry; filled triangles: W_1-type inclusions, open triangles W_2-type. Squares: samples from the Zaldívar porphyry; filled squares: W_1-type inclusions, open squares: W_2-type inclusions.

8.5 Fluid pressure

The co-existence of B- and G-type inclusions mentioned in section 8.3 and the fact that the filling temperature in both types of inclusions (filling to liquid and vapor, respectively) occurs in a comparable temperature range (between 300° and 400°C) (Fig. 8-12), strongly suggest that these fluids were trapped along the immiscible surface of a boiling system (Pichavant et al., 1982). As fluids trapped in B- and G-type inclusions were at boiling conditions, then no pressure correction needs to be made, and the filling temperature is equal to the trapping temperature (Roedder, 1984).

If the G-type inclusions represent a steam phase of the boiling fluid, then knowledge of its composition and filling temperature can be used to estimate the pressure at which the fluid was boiling. Moreover, if the liquid phase found in most G-type inclusions condensed from the trapped steam, the total salinity of the inclusions obtained from the final ice melting temperature should be lower than 5 wt % NaCl equiv., at temperatures up to 500°C, according to the low-density region of the NaCl-H_2O system (Souririjan and Kennedy, 1962).

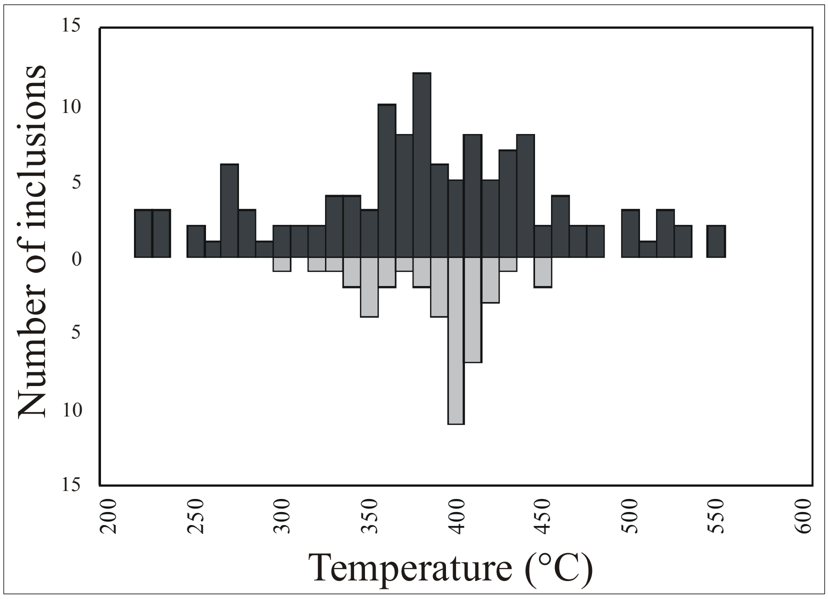

Figure 8-12. In a filling temperature histogram the values measured for the B_2-type inclusions (black bars) completely overlap with those of the G_2-type (shaded bars), indicating a major boiling event in the 350° - 450°C temperature range. For the B_2-type only those inclusions have been considered in which the filling temperature is higher than the halite dissolution, and for the G_2-type only those with salinities lower than 5 wt % NaCl equiv.

In the filling temperature-compositional diagram (Fig. 8-13), a number of G-type inclusions have high-salinity values (> 5 wt % NaCl equiv.) and plot above the critical curve for the NaCl-H_2O system in a field where they should homogenize to the liquid in a pure system (whereas they actually homogenize to the vapor). These high-salinity values are non-compatible with an origin of a trapped steam phase only, and they may not be truly representative of the steam phase, instead they will reflect some possible mixing between B- and G-type fluids where some high-salinity aqueous fluid must have been trapped together with the gas bubble, phenomena frequently reported in the literature (Roedder, 1971; Nash and Theodore, 1971; Eastoe 1978; Ahmad and Rose, 1980). The mixing phenomenon would be strong evidence supporting the coexistence of fluids of contrasting densities in a boiling system.

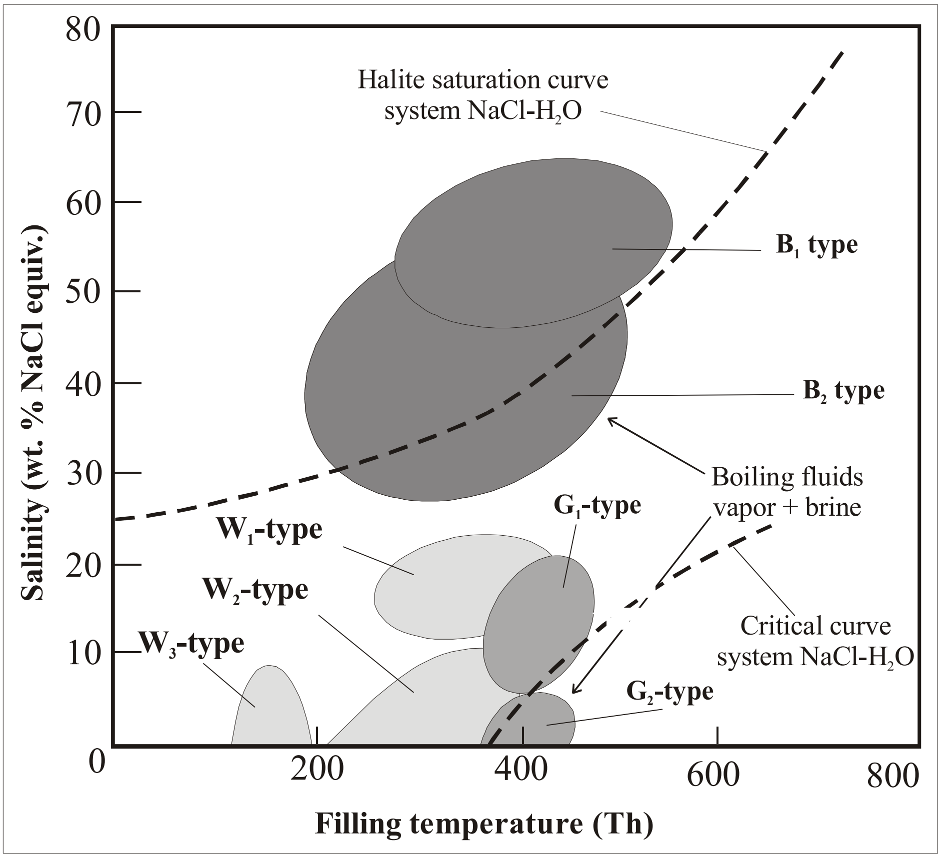

Figure 8-13. Filling temperature versus salinity diagram for all different subtypes of fluid inclusions from the Llamo and Zaldívar porphyries.

Taking into consideration the arguments given in the previous paragraph, only those G_2-type inclusions that present salinity values lower than 5 wt % NaCl equiv., and coexisting with B_2-type inclusions will be considered to estimate the fluid pressure at boiling condition.

Although our system is obviously more complex than $NaCl-H_2O$, as is usual for the study of fluid inclusions in porphyry copper deposits, this system can be taken as a first order approximation as it will not introduce major changes in the interpretation of P-T conditions of trapping B- and G-type fluid inclusions. However only G_2- and B_2-type pairs will be taken into consideration because they better approximate the pure $NaCl-H_2O$ system.

Considering the salinity values estimated for the G_2-type (between 0.88 and 3.23 wt % NaCl equiv.) and B_2-type (33.60 and 44.00 wt % NaCl equiv.) having similar filling temperatures between 390° and 460°C, the pressure at the immiscibility surface of the $NaCl-H_2O$ system will be between 200 and 350 bar (Sourirajan and Kennedy, 1962), corresponding to a depth of about 0.8 to 1.5 km on lithostatic conditions.

8.6 PIXE microanalysis

Representative PIXE X-ray emission spectrum for B_1- and B_2-type aqueous fluid inclusions (Fig. 8-14) show that in both inclusion types, Cl and Fe are the elements with the strongest peak, whereas the Mn and Zn peaks are much smaller.

The major difference observed in the spectra of these two types of inclusions would be that in the B_1-type, K and Cu peaks are easily recognized from the background, whereas for the B_2-type the same peaks are poorly defined. The well-defined K peak in the B_1-type inclusions is related to the occurrence of the sylvite daughter mineral that is absent from the B_2-type. In the case of the Cu peak, the feature observed in the PIXE spectrum will indicate that this element is present in the B_1-type inclusions, but nearly absent in the B_2-type.

As indicated for the MS-type inclusions, the presence of a halite daughter mineral in these inclusions would point to a high concentration of sodium, which cannot be detected due to a strong X-ray attenuation for this element.

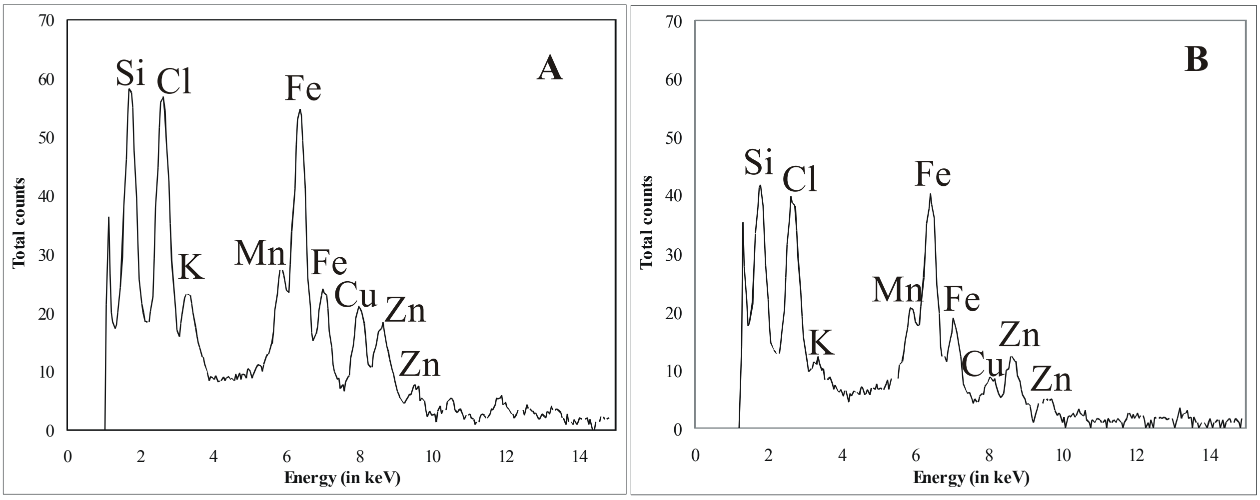

Figure 8-14. PIXE spectrum for B_1-type (A) and B_2-type (B) aqueous fluid inclusion.

8.7 Conclusions

Post-magmatic hydrothermal features preserved in igneous quartz phenocrysts from the Zaldívar deposit indicate that a complex evolution of aqueous fluids took place during the crystallization and cooling of the latest intrusive event. The fluid's chemical variability is demonstrated by the occurrence of several types of fluid inclusions showing contrasting composition and reflecting major changes in the chemistry of fluids, from a complex Na-K-Fe-Mn-Cl-H_2O system (B_1-type), probably at the end of the magmatic stage, to a more simple NaCl-H_2O dominated system (B_2-type).

The physical characteristics, microthermometry data and compositional variations of all different types of fluid inclusions recognized in igneous quartz phenocrysts (B-, G- and W-types), show no remarkable differences between samples from the Llamo and Zaldívar porphyries. A possible explanation for this resemblance is that the primary hydrothermal signature of the Zaldívar porphyry, if any, has been completely destroyed during the intrusion of the Llamo porphyry, and/or has been overprinted by the latest hydrothermal event associated with the Llamo intrusive. Consequently, it is assumed that all mentioned characteristics are representative for the latest hydrothermal event that is related to the intrusions of the Llamo porphyry, and therefore to the main mineralization event.

The low-temperature filling, low-salinity W_3-type fluids represent the latest hydrothermal event in the Zaldívar porphyry copper deposit. This fluid is related to a nearly pure H_2O system and most probably reflects the incoming of external non-magmatic aqueous fluids, probably meteoric water, into the vanishing hydrothermal system.

Chapter 9

Thermochronology

9.1 Introduction

The dating of mineral containing isotopic systems with different closure temperatures provides an excellent opportunity to study the cooling geochronology of intrusive bodies (Andriessen and Reutter, 1994). The same principle can be applied for timing the thermal evolution of ore deposits that are genetically related to intense hydrothermal activity such as the PCDs, regarding the selection of appropriated minerals whose isotopic system have not been modified by subsequent alteration events.

Geochronology data for the Zaldívar and Llamo porphyries have previously reported a crystallization age (U/Pb in zircon) for these intrusives of 290 ± 4 and 38.7 ± 1.3 Ma respectively (Richards et al., 1999). The same authors, from one sample collected at the synmineralization Llamo porphyry reported weighted mean ^{40}Ar/^{39}Ar plateau of 37.4 ± 0.2 Ma. Although these results are in agreement with data from other porphyry coppers in the neighboring area (Escodida and Chimborazo), it can only be considered preliminary, as the exact location of the sample within the deposit is unknown.

The present research is a more focused study aiming to further constrain the thermal history of the Zaldívar deposit during the period that follows the mineralizing hydrothermal event. The ceasing time of the main magma-related hydrothermal system would be defined by applying the ^{40}Ar/^{39}Ar isotope dating method on relatively unaltered igneous biotites phenocrysts (closure temperature of about 350°C) (Harrison et al., 1985). Furthermore, because fission tracks produced in zircons are only retained at lower temperature (below of ca. 250°C, Tagami et al., 1996), than those usually defined for the main hydrothermal event in porphyry copper systems (mostly above

300°C), the application of zircon fission-track dating method may shed some light on the time of cooling for the whole thermal event.

9.2 ^{40}Ar/^{39}Ar dating in biotites

The ^{40}Ar/^{39}Ar dating technique has derived from the conventional K-Ar radiometric method and is based on the decay of radioactive isotope ^{40}K over geological time producing the accumulation of radiogenic ^{40}Ar. The ^{40}Ar is indirectly measured by irradiating the sample with neutrons in a nuclear reactor, causing the stable ^{39}K to transmute into ^{39}Ar. The sample age is calculated by measuring both the ^{40}Ar and ^{39}Ar and knowing the ratio ^{40}K/^{39}K which is constant. However, because during the radiation of a sample the amount of ^{39}K to transmute into ^{39}Ar will depend on the neutron flux, the irradiation parameter J has to be added into the age calculation. The J value can be calculated by irradiating standards of known age, then:

$$J = \left(e^{\lambda T} - 1\right) \times \left(\frac{^{40}Ar^*}{^{39}Ar_K} \right)$$

λ = total decay constant of ^{40}K ($5.543 \mathrm{x} 10^{-10}$ yr^{-1})
T = age of the standard
$\left(\frac{^{40}Ar^*}{^{39}Ar_K} \right)$ = ratio for the mineral standard

By measuring the $\left(\frac{^{40}Ar^*}{^{39}Ar_K} \right)$ ratio of the unknown samples the age is calculated by:

$$t = \frac{1}{\lambda} \times \ln\left\{ 1 + J \times \left(\frac{^{40}Ar^*}{^{39}Ar_K} \right) \right\}$$

9.2.1 Location of the studied samples

The Llamo porphyry was selected as a target for the present dating study because of its relation to the mineralization and the presence of well-preserved igneous biotite phenocrysts, which makes it suited for dating by the ^{40}Ar/ ^{39}Ar technique.

Laser probe ^{40}Ar/^{39}Ar dating was conducted on seven selected samples collected on both sides of the Portezuelo fault. The porphyry contains relatively fresh clots of igneous biotite, usually smaller than 2.0-mm in diameter, dispersed and erratically distributed in a fine-grained groundmass. Samples S-03, S-05, S-06, S-11, S-16 and S-30 were all collected at the bottom of the pit at 3185 m a.s.l., the lowest bench at the time of sampling. Sample 40 was taken from a drill hole at a depth of 3115 m a.s.l. Samples location is shown in figure 9-1.

The general petrographic description presented in chapter 5 for the Llamo porphyry unit can be taken as representative for all studied samples as the samples selected for ^{40}Ar/ ^{39}Ar dating share similar primary magmatic features and similar mineralogical associations. However, because biotite phenocrysts are the object of this investigation, a more detailed characterization is given below, also the hydrothermal alteration related to the biotites is discussed in detail.

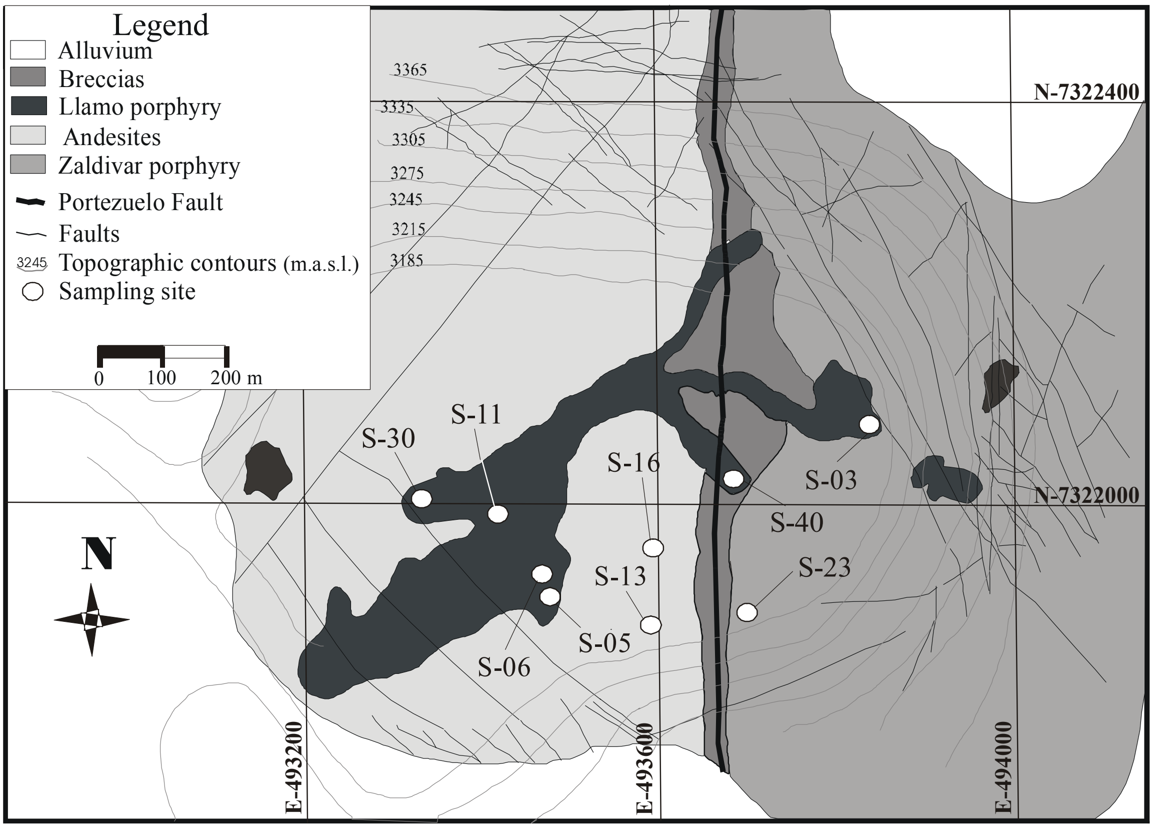

Figure 9-1 Geology and sample location.

9.2.2 Hydrothermal alteration

The presence of relatively fresh magmatic K-feldspar and biotite grains, would suggest that the rock has been in the stability zone of potassic alteration, as neither of these minerals would have survived the physicochemical conditions at the advanced argillic or pervasive phyllic alteration zone (Titley and Beane, 1981).

The hypogene potassic alteration appears usually strongly overprinted by argillic alteration that involves kaolinite with minor sericite and quartz. The intensity of argillic alteration may vary from weak to strongly pervasive, and usually is strongest in plagioclase and K-feldspar, whereas biotite crystals appear to be less affected. In several samples the argillic alteration completely replaced the original feldspar mineral assemblage with a fine-grained mixture of secondary minerals, in those cases the occurrence and relative abundance of primary minerals can only be estimated by the presence of ghost phenocrysts.

All selected samples contain coarse-grained relatively fresh-looking biotite grains, and because biotite is readily converted to chlorite and clay minerals during intermediate argillic alteration at hydrothermal temperatures, but can survive supergene alteration relatively unscathed (Einaudi, 1997), the strong argillic alteration most probably corresponds to supergene phenomena related to the secondary enrichment event in the Zaldívar deposit.

9.2.3 Characterization of biotite phenocrysts

Biotite phenocrysts occur mostly as dark-olive, hexagonal prisms or plates smaller than 6-mm in diameter. Mineral inclusions are usually abundant within the biotite grains and consist mostly of feldspars, quartz, apatite, and zircon. Only in sample S-03 are biotite grains smaller and dark brownish in color. In these biotites mineral inclusions are rare. In sample S-16 numerous micrometric inclusions of opaque minerals occur within the layers.

All biotite crystals show a parallel extinction, and most of them are strongly pleochroic from colorless to brown, showing strong birefringence with high interference colors and a mottled appearance between cross nicols. Biotites from sample S-03 show markedly different optical properties, the pleocroism is from pale brown to dark brown and the birefringence at cross nicols varies from dark-brown to olive-green.

Alteration of biotite grains to kaolinite commonly occurs, varying from mild (S-03) to strong (S-30). The alteration normally progresses inward or through microfractures as hairline veinlets interlaminated with the mica flakes (Fig. 9-2). Chlorite has been found only on samples S-05, S-06 and S-11 showing the same distribution of kaolinite. Hydrothermal alteration does not affect all biotite grains with the same intensity within any given sample, and it was possible to collect optically fresh grains for ^{40}Ar/^{39}Ar geochronology in all pre-selected samples.

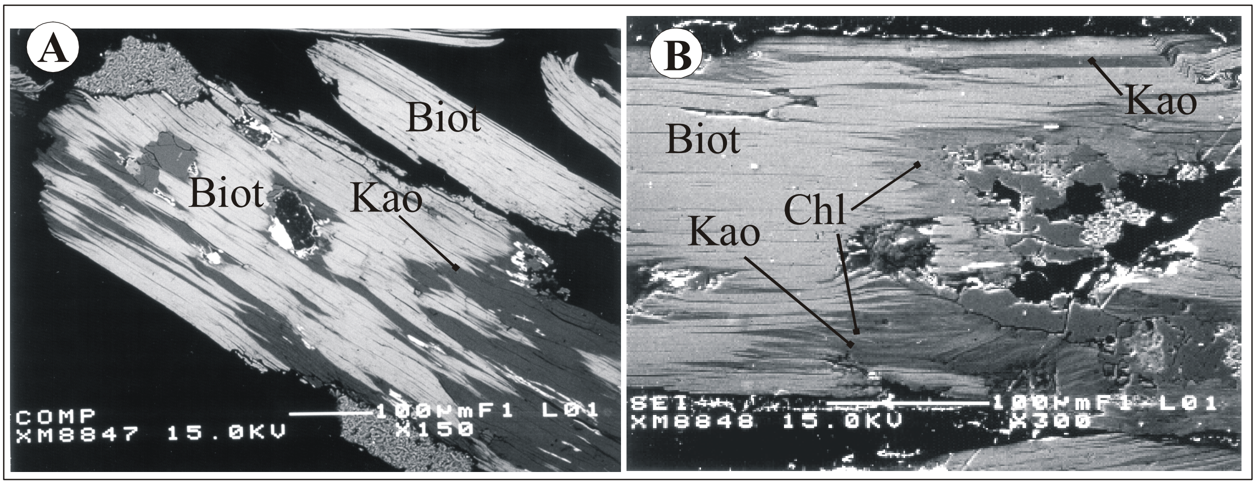

Figure 9-2. Scanning electron microscope image of biotite phenocrysts altered to kaolinite (A) and kaolinite and chlorite (B). Bio: biotite, Kao: kaolinite, Chl: chlorite.

Representative electron-microprobe analyses of selected biotite grains are listed in Table 9-1. The data set indicates that all analyzed biotites correspond to the phlogopite-enriched type. They contain between 8 and 10-wt % K_2O and have X_{mg} values between 0.61 and 0.71. Important differences can be found among the concentrations of some major elements which allows the division into three different groups of biotites:

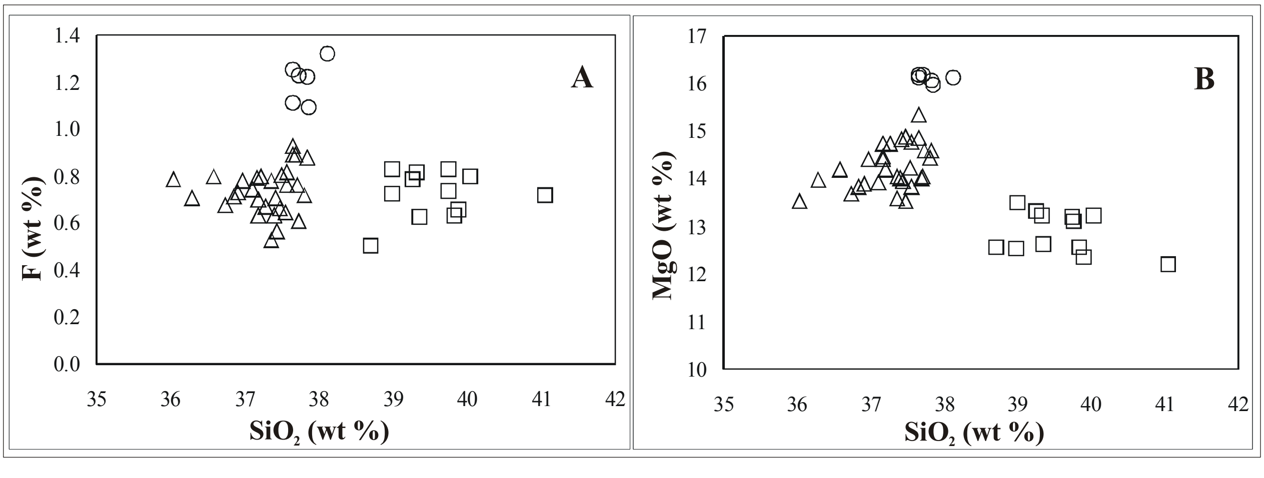

Figure 9-3. Diagrams showing some chemical differences among biotite grains from the studied samples: A) F vs. SiO_2, B) MgO v.s SiO_2. Open triangles: samples S-05, S-06, S-11 and S-40; open circles: sample S-16; open squares: samples S-03 and S-30.

Group 1 corresponds to biotites from samples S-05, S-06, S-11 and S-40 that share similar chemical compositions with only minor differences.

Group 2 is represented by sample S-16. These biotites are relatively similar to the group 1, but show lower TiO_2, FeO and higher Na_2O, Cl and F (Fig. 9-3-A).

Group 3 corresponds to samples S-03 and S-05, and shows major differences with biotites from group 1, characterized higher Si_2O and lowers FeO and MgO (Fig. 9-3-B), and a negative correlation between Al_2O and SiO_2.

Table 9-1. Representative electron microprobe analysis of biotite phenocrysts.

Sample	**S-03**	**S-05**	**S-06**	**S-11**	**S-16**	**S-30**	**S-40**
SiO_2	38.98	37.27	37.80	36.29	37.65	39.75	37.40
TiO_2	4.11	4.14	3.93	4.13	3.52	4.12	4.22
Al_2O_3	14.13	14.56	14.58	13.84	14.33	13.67	14.58
FeO	12.42	13.88	14.27	13.79	11.80	11.82	14.43
MgO	12.53	14.73	14.43	13.98	16.11	13.10	14.01
ZnO	0.00	0.02	0.00	0.00	0.05	0.01	0.00
CaO	0.08	0.03	0.00	0.02	0.00	0.09	0.02
Na_2O	1.24	0.19	0.21	0.23	0.46	0.12	0.20
K_2O	8.07	9.17	9.40	7.84	8.90	8.15	9.22
BaO	0.32	0.54	0.30	0.51	0.62	0.32	0.74
F	0.73	0.67	0.72	0.71	1.25	0.83	0.63
Cl	0.20	0.25	0.23	0.21	0.20	0.23	0.23
Total	92.80	95.45	95.87	91.55	94.90	92.20	95.68

9.2.4 Sample preparation

For spot fusion dating, disks of 20 mm in diameter and about 0.1 mm in thickness were prepared using a diamond drill. Sample wafers were placed in an aluminum sample holder of 25 mm diameter and then wrapped in aluminum foil and stacked vertically into a 11.5-cm long and 25 mm OD container. Flux monitors were placed between each sample package.

For incremental heating, the samples were crushed down to ca. 0.5 mm, then individual grains of biotite were handpicked. As in most porphyry copper deposits, biotite grains intergrow with other minerals, therefore all collected grains were meticulously washed in an ultrasonic bath for a 1-minute period to avoid incorporation of material attached to the grains surface, especially K-bearing minerals. Finally, two pieces of the freshest looking biotite grains from each sample were selected, and loaded onto a 3 mm thick, 20 mm diameter aluminum sample holder, which has 20 containers of 2 mm diameter and 2 mm deep. Four out of 20 positions in the sample holder are loaded with flux monitor (Wijbrans et al., 1995). Sample holder are then placed into a 11.5-cm long and 25 mm OD container and sent to the reactor

Samples where irradiated for 7 hours in the Cd-shielded position (CLICIT) at the TRIGA nuclear reactor at the Oregon State University at Corvallis. After irradiation, samples were mounted in the sample tray and placed inside a stainless steel chamber that is connected to an ultra high vacuum purification system. The sample chamber is positioned beneath a trinocular zoom microscope that is equipped with a video camera and a monitor that hallows a permanent observation of the sample.

9.2.5 Analytical results

9.2.5.1 Step heating

For sample S-03, a low age representing a typical feature of partial argon loss is observed in the first heating step and then a plateau is defined at 35.6 ± 0.7 Ma (Fig. 9-4-G). About 40 % of the gas is released in the last two heating steps.

Sample S-05 shows similar behavior as sample S-03 but the gas release indicates partial argon loss in the first two heating steps that represent about 15 % of total argon. The plateau is reached at 37.7 ± 0.4 Ma, and final fusion step contained more than 30 % of the gas (Fig. 9-4-A).

For sample S-06, partial argon loss is observed in the first two steps of the heating experiment, which contain about 30 % of the total gas, and then the plateau is reached at 37.1 ± 0.5 Ma. About 30 % of the gas is released during the fusion step (Fig. 9-4-B).

Sample S-11 shows a partial argon loss only in the first heating step corresponding to about 10 % the total gas released, then a well-defined plateau is reached at 36.5 ± 0.5 Ma. The fusion step accounts for about 30 % of the total gas (Fig. 9-4-E).

Sample S-16 produced little argon release during the first heating step (< 10 %), and then the plateau is reached at 36.0 ± 0.3 Ma. More than 40 % of the argon is released during the fusion step (Fig. 9-4-F).

For sample S-30, partial argon loss is not observed, a major distinctive feature with all the other studied samples is that most of the argon is released in the first two heating steps (about 70 %), and only 10 % during fusion of the biotite grains. The plateau for this sample containing seven steps is defined at 36.7 ± 0.9 Ma (Fig. 9-4-D).

Sample S-40 shows little argon released during the first heating step, then the plateau is reached at 36.6 ± 0.4 Ma, with more than 40 % of the argon been released during the fusion step (Fig.9-4-C).

9.2.5.2 Spot fusion

Sufficient argon for analysis from sample S-05 was extracted from eight out of twenty melt pit spots (Appendix 7), the age values obtained for each spot is characterized by a marked heterogeneity, with most of the data being much older or much younger that the ages defined by incremental heating on the same sample (Appendix 8, Fig 9-4-A).

In Sample S-30, ten out of twenty fusion spot liberates enough gas to be analyzed (Appendix 8). Within these analyses only six of them give ages that are comparable with those defined by incremental heating (Appendix 7, Fig. 9-4-D), however similar wide variation in ages observed in sample S-05 occurs in S-30.

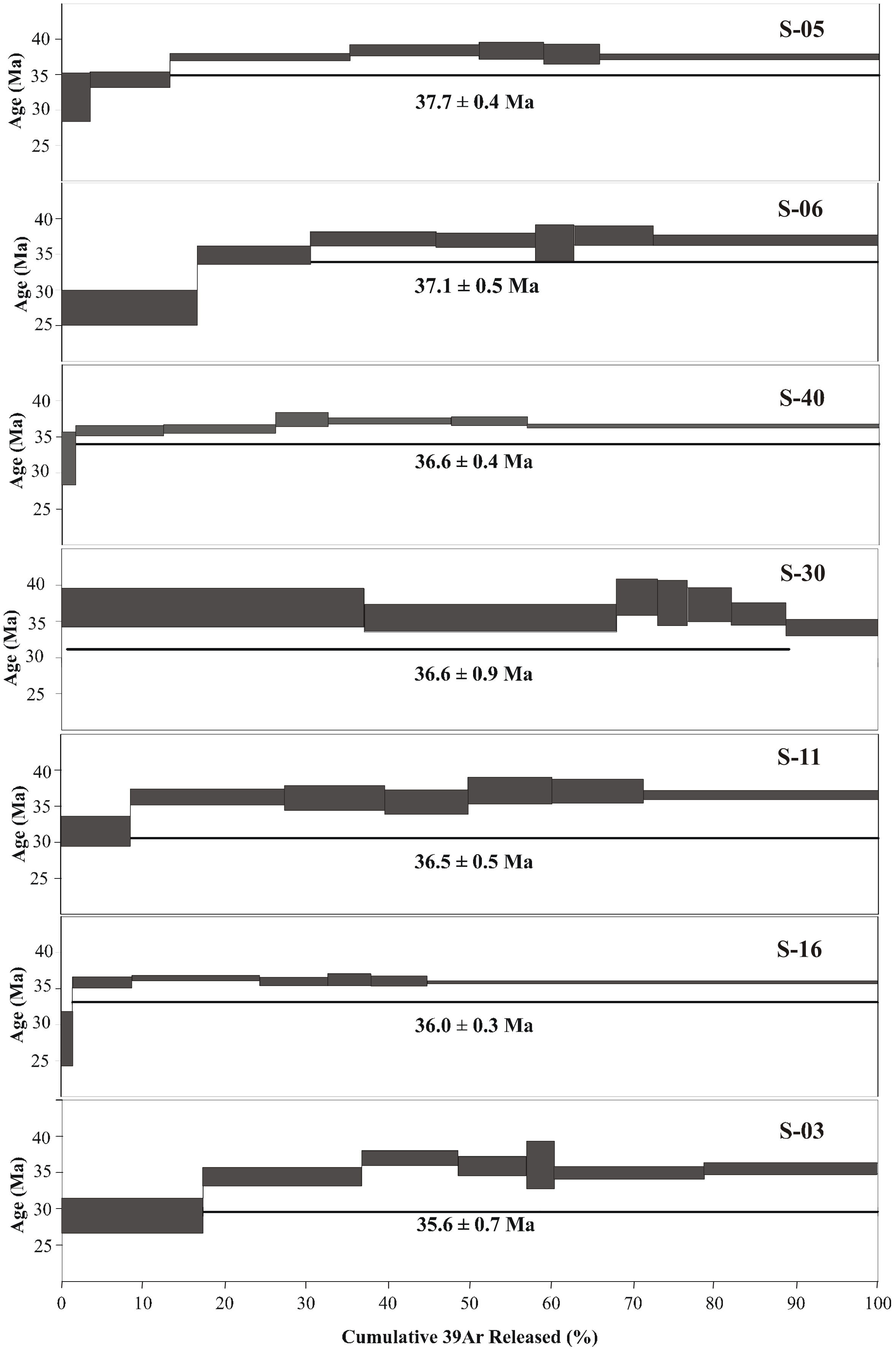

Figure 9-4. Incremental heating $^{40}Ar/^{39}Ar$ analyses of biotites from the Llamo porphyry. Data listed in Appendix 7

9.3 Zircon fission track

The principles and application of the fission track method has been comprehensively described by Dickin, (1997), Maksaev et al., (1988), Gallagher et al., (1998), Sanders, (1998), and de Bruijne, (2001), therefore only a general overview will be given in the following paragraph based on the work of the previously mention authors.

The fission track dating technique relies on the analysis of radiation damage features produced continuously through geological time due to the natural spontaneous fission of ^{238}U. The fission process will produce two fragments of roughly the same mass that are strongly propelled in opposite directions due to the liberation of about 200 MeV of energy that is mostly transferred as kinetic energy to the nuclides. The passage of the charged fission fragments through the crystalline structure will cause ionization of the neighboring atoms along its path due to the stripping of electrons. The ions produced along the trajectory of the fission fragments will be mutually repelled resulting in a single cylindrical damage zone in the crystal lattice a few tens of an angstrom wide and less than 20 microns long.

As the wideness of fission tracks is smaller than the smallest wavelength of visible light, they are invisible under an optical microscope. However, because the damage zone is more susceptible to chemical attack than the undamaged crystalline structure under certain conditions, the sample is abraded to expose an internal surface, and the fission tracks intersecting this surface can be preferentially dissolved and enlarged by appropriated chemical etching. The enlarged tracks can be observed using a high magnification optical microscope (500 x and higher).

The formation and stability of the fission tracks is temperature dependent and the tracks are only retained once the host grain cools below the effective closing temperature, ~ 250°C for fission tracks in zircons with cooling rates of ~ 10 to 100°C/m.y (Tagami et al., 1996). With increasing temperature the atomic movement also increases and displaced ionized atoms can be readily neutralized and go back to their original position in the crystalline structure producing the shortening or annealing of the tracks. The annealing process not only implies a reduction in the length of the tracks, but with a high enough temperature lead to complete erasing. Therefore fission track ages can be used to constrain the time at which a mineral cooled through its closure temperature and establish the cooling age of the host rock provided that they are emplaced near the surface and have not been subsequently deeply buried or reheated.

9.3.1 Dating procedure

The density of fission tracks in a given mineral will depend on the original uranium content and the time elapse since the tracks have been preserved, therefore the density of fission tracks intersecting a polished and etched surface will be the feature used for the age determination.

In this study the external detector method (EDM) (Fleischer et al., 1965) was applied for the fission track dating. A low-uranium mica sheet detector is placed in intimate contact with the etched surface of the zircon grains, and then the samples are irradiated in a nuclear reactor to create a set of induced tracks in both the zircons grains and in the mica. The induced tracks are produced by the fission of ^{235}U during the irradiation with thermal neutrons. After irradiation the external detector is removed from the sample and etched. The determination of spontaneous/induced tracks ratio for each grain on each sample yields single grain ages.

The uranium content of the sample is determined by counting the induced tracks in the detector, and the flux of thermal neutrons is monitored by two dosimeter glasses of known uranium content that are included in the same package which contains the samples to be irradiated.

The equation to calculate age from fission tracks according to Price and Walker (1963) and Naeser (1967) (*in* Sanders, 1998), is:

$$T = \frac{1}{\lambda}\ln\left[1+\frac{\rho_s\lambda_D\sigma I\phi g}{\rho_i\lambda_F}\right]$$

λ_D = total decay constant of ^{238}U (1.55125 x 10^{-10} years^{-1})

λ_F = decay constant for spontaneous fission of ^{238}U

I = ^{235}U/^{238}U; ratio of natural abundance of uranium, 7.2527 x 10^{3}

σ = Section for the fission of thermal neutrons for ^{235}U, 584.25 x 10^{-24} cm^{-2}

ϕ = Flux of thermal neutrons

N_s and ρ_s = number of spontaneous tracks and spontaneous track density (N_s*cm^2)

N_i and ρ_i = number of induced tracks and induced track density (N_i*cm^2)

N_d and ρ_d = number of tracks in the dosimeter and track density (N_d*cm^2) in the dosimeter

As the λ_D, σ and I values are known it will be only necessary to define the ρ_s/ρ_I ratio in the sample, measure the neutron flux and insert the λ_F value for calculating the age from the fission tracks. However, the λ_F value is not well defined and the determination of absolute values for neutron flux is complex and uncertain. To elude this problem an alternative empiric calibration defined as the zeta method is used. This method is a way of normalizing the spontaneous/induced tracks ratio to geological time by calibrating it against several age standards and by using a dosimeter (Hurford and Green, 1983) eliminating the uncertainty for the exact value of λ_F and the determination of the neutron flux. The fission track age is then calculated using the following equation derived by Hurford and Green, (1983):

$$Age = \frac{1}{\lambda_D}\ln\left[1+\lambda_D\zeta\rho_{ratio}\rho_d g\right]$$

Were $\rho_{ratio} = \frac{\rho_s}{\rho_i}$

And $\zeta = \frac{e^{\lambda_D T_{STD}}-1}{\lambda_D\left(\frac{\rho_s}{\rho_i}\right)_{STD}\rho_d g}$ for a single grain

g = geometry factor 0.5 for the EDM (Wagner and Van den Haute, 1992)

The fission track age for a single sample is defined as the central age that corresponds to the weighted mean of the single grain ages, providing a more robust central tendency for the single grain ages (de Bruijne, 2001). The central age is defined by:

$$T(\text{central age}) = \frac{1}{\lambda_D}\ln(1+\lambda_D\zeta\rho_d\frac{\eta_s}{\eta_i})$$

Where η correspond to the weighted mean average of the ratio N_s/N_i with weight *w:*

$$\eta = \frac{\sum w_j \left(\frac{N_s}{N_s + N_i} \right)_j}{\sum w_j}$$

Standard deviation for the central age is:

$$\sigma(T)_{central} = T \sqrt{\frac{1}{\eta^2 (1-\eta)^2 \sum w_j} + \frac{1}{N_d} + \left[\frac{\sigma(\zeta)}{\zeta} \right]^2}$$

9.3.2 Sample preparation

For fission track geochronology, five samples were collected at the lowest bench from the Zaldívar pit at an altitude of 3185 m a.s.l. Samples S-11 and S-30 are from the Llamo porphyry, and S-13 from the andesite unit, all were sampled west of the Portezuelo fault (Fig 9-1). Sample S-03 is from the Llamo porphyry and S-23 from the Zaldívar porphyry and they were taken east of the Portezuelo fault (Fig 9-1).

Samples were crushed, pulverized, washed to remove the fines, subsequently zircons grains were separated using heavy liquid following the separation procedure schematically described by de Bruijne (2001). After separation, zircon grains were embedded in a Teflon disk of about 20 mm diameter, and then the disc was mounted on a holder and polished. The polished grains were then etched in NaOH-KOH at 220°C for 96 hours in order to obtain similar tracks for all zircon grains.

After polishing and etching the zircon grains, the external detector (mica) was placed in close contact with the polished surface. The samples were irradiated for 3 hours in the low-flux reactor at Petten, The Netherlands.

9.3.3 Analytical results

To obtain the fission track age of each sample, between 20 to 25 grains were counted (Table 9-2). Individual grain fission track ages are graphically illustrated in the form of a radial plot in which the y-axis represents the standardized error, x-axis the precision, and the curved axis the age in Ma (Galbraith, 1990). The single grain age is read off by tracing a line from the origin through a given point and into the curved axis.

The calculated central ages for all samples are comparable and vary between 28.0 ± 1.5 (S-11) and 29.9 ± 1.8 Ma (S-23) (Table 9-3, and Fig. 9-13).

Graphically the central age is represented by a horizontal line that is extrapolated from the origin to the curved axis (Fig 9-13), with its standard error defined by two parallel lines at a distance of 2σ.

Table 9-2. Zircon fission track analytical results. Central ages were calculated using the Zeta-methods; ζ value for CN-2 glass (P. Andriessen) = 100.3 ± 2.99.

Sample	Rock unit	N (grains)	ρ_s (cm^{-2}) x10^6	N_s	ρ_i (cm^{-2}) x10^6	N_i	ρ_d (cm^{-2}) x10^6	N_d	P(χ^2)	Dispersion	Central age Ma ± 1σ
S-03	Llamo	20	4.63	1486	10.35	1661	0.66	13724	80.5	9	29.6 ± 1.8
S-11	Llamo	25	4.10	1839	9.70	2173	0.66	13724	99.9	5	28.0 ± 1.5
S-13	Andesite	21	2.94	1399	6.67	1588	0.66	13724	99.9	5	28.9 ± 1.8
S-23	Zaldívar	25	3.27	1189	7.23	1313	0.66	13724	31.1	12	29.9 ± 1.8

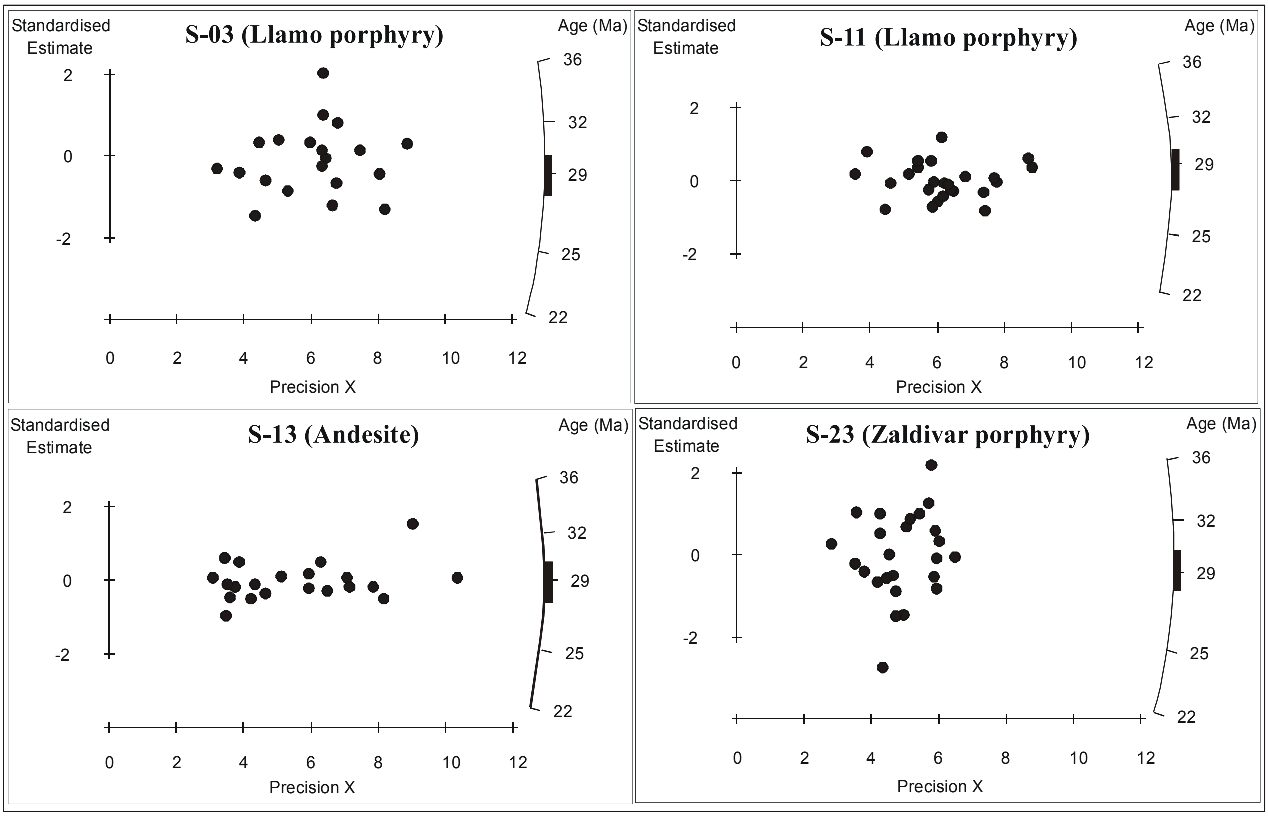

Figure 9-5. Radial plot of fission track single grain ages. In the curved axis the central age is indicated.

9.4 Data analysis

Although the selected targets for spot fusion and step heating in the $^{40}Ar/^{39}Ar$ method are coarse-grained phenocrysts that are less susceptible to alteration, and thus are more likely to preserve the least disturbed radiogenic $^{40}Ar/^{39}Ar$ signatures. The $^{40}Ar/^{39}Ar$ analyses in the spot fusion techniques are characterized by heterogeneous, hardly reproducible age values within a single grain. The contrasting age values obtained by spot fusion can be explained as a function of complex combination of effects described by Clark et al. (1998) and Koppers (1998).

a) Preferential degassing. Because in the spot fusion wafers, the biotite phenocrysts are surrounded by fine-grained, strongly altered groundmass, the incidence of the laser beam in the biotite during the spot fusion procedure will indirectly heat the groundmass around the biotite crystal producing a preferential degassing of K-bearing mineral phases that would have distinct argon signatures.

b) Hydrothermal alteration. For the step heating measurement, the less altered biotites could be chosen by handpicking, a process that cannot be done in the buffers. Because with spot fusion we can be dealing with heterogeneous alteration of a single biotite grain that could play a disturbing effect during the procedure of argon release.

c) The highly inconsistent data in the spot fusion could also be the result of the recoil effects acting on the argon system.

As a consequence, the ages defined by the spot fusion technique have no geological significance.

The data obtained by spot fusion markedly contrast with the good quality of mineral age determination performed by incremental heating. This is demonstrated by the comparable results obtained for most of the analyzed samples, which can be accepted as being geologically meaningful ages.

Because hydrothermal alteration events may disturb to varying degrees the $^{40}Ar/^{39}Ar$ systematics and so affect the final outcome of the ages, it is necessary to evaluate this potentially perturbing effect in light of the hydrothermal alteration observed in the analyzed samples.

All dated samples are within the potassic alteration zone, which is stable between 350° to 700° C (Titley, 1982), and are not affected by slightly lower temperature hydrothermal alteration such as phyllic or propylitic. Furthermore, the kaolinitization of biotites produced by supergene alteration is not stable at temperatures higher that 300°C (Hemley et al., 1971, *in* Moore and Nash, 1974). Considering that the closure temperature for the $^{40}Ar/^{39}Ar$ system in biotite, in a relatively fast cooling system (100° C/Ma) is around 345° C (Harrison et al, 1985), which is below the lower temperature range for potassic alteration, and is above the temperature of supergene alteration. The $^{40}Ar/^{39}Ar$ system should not be thermally disturb and only chemical perturbation of the system should be expected due to the supergene alteration.

Incremental-heating experiments in igneous biotites from the Llamo porphyry yield $^{40}Ar/^{39}Ar$ ages that vary from 37.7 ± 0.4 (sample S-05, Fig. 9-4-A) to 35.6 ± 0.7 Ma (sample S-03, Fig. 9-4-G). No major compositional or textural difference can be found between the older and younger biotites, except for biotites from sample S-03. These biotites show physical, optical and compositional properties markedly different from those found in igneous biotites from all other studied samples, and they are most likely of hydrothermal origin. Despite the different origin of biotites from sample S-03, the yielded age is indistinguishable from the igneous biotites; therefore not separation will be made on further interpretations.

To minimize the effect of outliers and to identify modes in the data that will lead to a better age determination, the ages were analyzed on a cumulative probability plot (Fig. 9-5). The plot for all the measured samples indicates that the most probable date for this set of samples is 36.5 Ma, similar to the weighted mean age of all samples 36.6 ± 0.2, and to the integrated age of samples S-30, S-11 and S-40 (Table 9-3).

All studied samples yield comparable zircon fission tracks ages of about 29 Ma, independently of the provenance of the sample or the host rock of the zircon grains (Andesites, Llamo porphyry or Zaldívar porphyry) (Fig. 9-7). In fact, sample S-03 taken east of the Portezuelo fault, the major structure in the site, and sample S-11 taken west of this fault, show comparable fission track ages, although they yield contrasting $^{40}Ar/^{39}Ar$ ages (Fig 9-7 and Table 9-3). The weighted mean age of all the analyzed samples is 29.08 ± 1.2 Ma.

Considering that fission tracks in zircon will only be stable below ~250°C, and that the zircon fission tracks ages are nearly the same despite the provenance of the sample, the yielded ages are most probably indicating that at about 29 Ma ago the thermal event in the Zaldívar area was uniformly cooled through ~250°C.

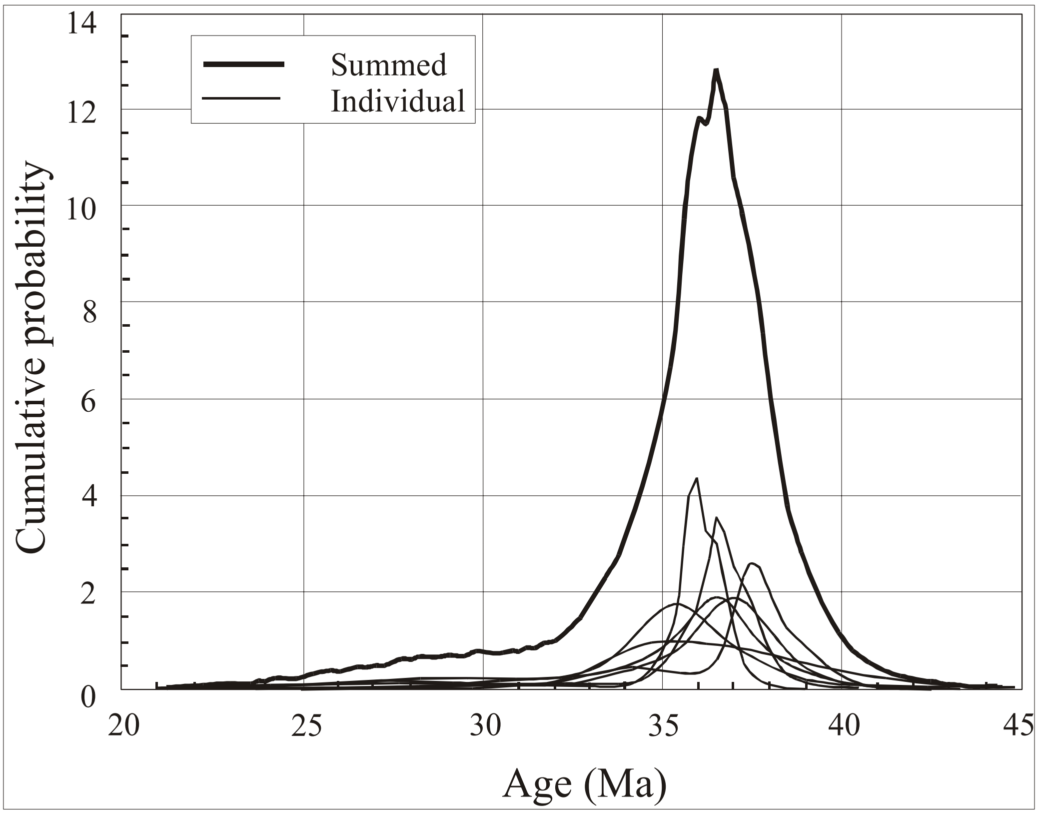

Figure. 9-6. Cumulative probability plot of step-heating $^{40}Ar/^{39}Ar$ ages in biotites from the Llamo porphyry. The enveloping curve is generated by summing the probability curves for each individual sample.

Table 9-3. Step-heating $^{40}Ar/^{39}Ar$ ages in biotites from Llamo porphyry with respect to alteration and texture. Pot: potassic alteration, Arg: argillic alteration, Sil: silicification.

Sample	Textural characteristic	Hydrothermal alteration	Mean $^{40}Ar/^{39}Ar$ plateau age (2σ)
05	Fine grained porphyritic	Pot, Arg	37.7 ± 0.4 Ma
06	Fine grained porphyritic	Pot-Arg	37.1 ± 0.5 Ma
11	Coarse-grained porphyritic	Pot-Arg	36.5 ± 0.5 Ma
40	Coarse-grained porphyritic	Pot-Arg	36.6 ± 0.4 Ma
30	Coarse-grained porphyritic	Pot-Arg	36.6 ± 0.9 Ma
16	Fine grained porphyritic	Pot-Sil	36.0 ± 0.3 Ma
03	Fine grained porphyritic	Pot-Sil	35.6 ± 0.7 Ma

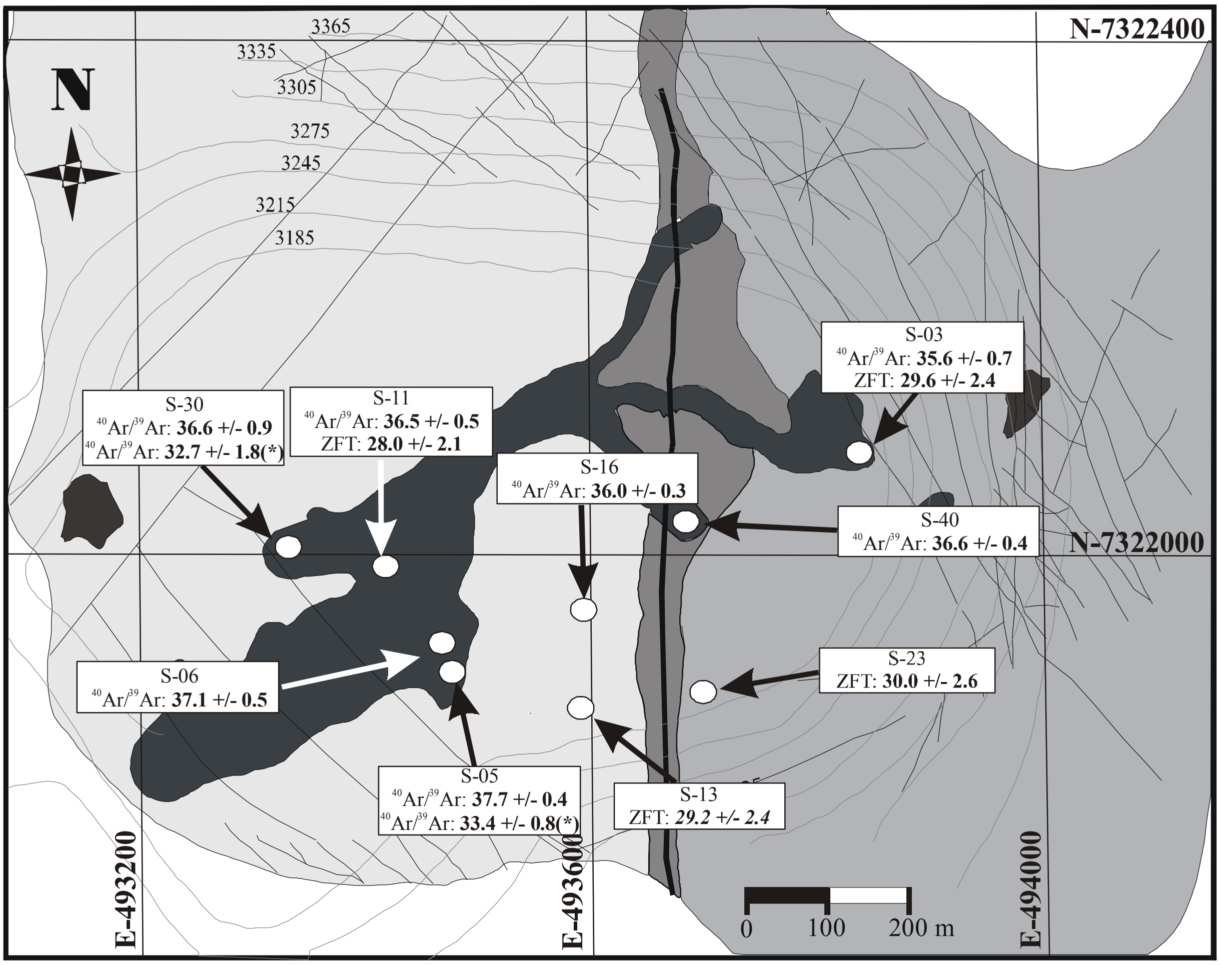

Figure 9-7. Geochronology data from $^{40}Ar/^{39}Ar$ in biotites and zircon fission track (ZFT). Legend as in figure 9-1. (*) spot fusion ages.

Chapter 10

Discussion of analytical results

10.1 Introduction

The origin of the Zaldívar PCD is related to the West Fissure, a NS-trending regional structure that controls the emplacement of nearly all-major porphyry copper deposits of northern Chile. Three petrographic units are recognized in the deposit, the quartz-feldspar Zaldívar porphyry (290 ± 4 Ma), the andesitic lavas from the Augusta Victoria formation (between 66.6 +/- 2.2 and 41.2 +/- 2.2 Ma), and the plagioclase-biotite-quartz Llamo porphyry (38.7 +/- 1.3 Ma). The andesites contact the Zaldívar porphyry throughout the NS-striking Portezuelo fault, whereas the Llamo porphyry intrudes the older units and outcrops on both sides of the same structure.

The mineralizing and alteration events clearly display the combined effects of hypogene and supergene processes. The primary sulfide mineralization is related to hypogene hydrothermal stages, whereas the main ore body corresponds to secondary enriched ore that resulted from the effects of supergene processes. The secondary ore overlies the deeper hypogene mineralization and occurs as a subhorizontal blanket that displays a NNE elongation, 2 km long by 1 km wide, generally centered in the Llamo porphyry.

Fairly fresh K-feldspar and biotite crystals often occur in samples from the Llamo porphyry, indicating that the intrusive was in the stability zone of potassic alteration, as neither of these minerals would have survived in the advanced argillic or phyllic alteration zones (Titley and Beane, 1981). These minerals may occur weakly or strongly alter to kaolinite with minor sericite and quartz, an indication that the potassic alteration has been overprinted by supergene, low-temperature alteration. The evidence for supergene alteration is based on the fact that the biotite is readily converted to chlorite and clay minerals during hypogene argillic alteration, but it can survive supergene argillic alteration relatively unscathed (Einaudi, 1997).

Because in the Zaldívar porphyry, magmatic and hydrothermal remnants are strongly overprinted by the intrusion of the Llamo porphyry and the subsequent related hydrothermal events, the following discussion will be centered only on the study of the synmineralization Llamo porphyry, unless otherwise stated.

10.2 Magmatic remnants and aqueous fluids evolution

10.2.1 Melt inclusions

Most melt inclusions are only visible after heating at high temperature when the microcrystalline aggregates re-melt and are transformed in clear transparent glass after quenching. During heating, most melt inclusions homogenize at temperatures between 900° and 1030° C, however, M_2-subtype inclusions show no indication of bubble size reduction on heating up to 1100° C, however no attempts to go higher were made in order to preserve the already homogenized inclusions.

The composition of the quenched glasses corresponds to high-silica rhyolite. The measured SiO_2 contents show a variation between 70.18 to 78.98 wt %, when recalculated on a volatile-free basis. The observed highest silica contents could be due to the fact that, in order to restore the homogenization of the enclosed glass, it was necessary to re-melt and quench the inclusions, it is then likely that, for these inclusions, part of the host boundary layer was re-melted and incorporated in the inclusion. Such contamination cannot be excluded for compositions lower in silica (less than 77 wt % SiO_2). However, it is likely that quartz contamination has been small or absent for these inclusions. Therefore they are considered to have a “normal” magmatic composition, which fall within a highly evolved rhyolitic field for all major elements. They are comparable to the most evolved acidic end member (rhyolitic) found elsewhere in the regional magmatism (Fig. 10-1).

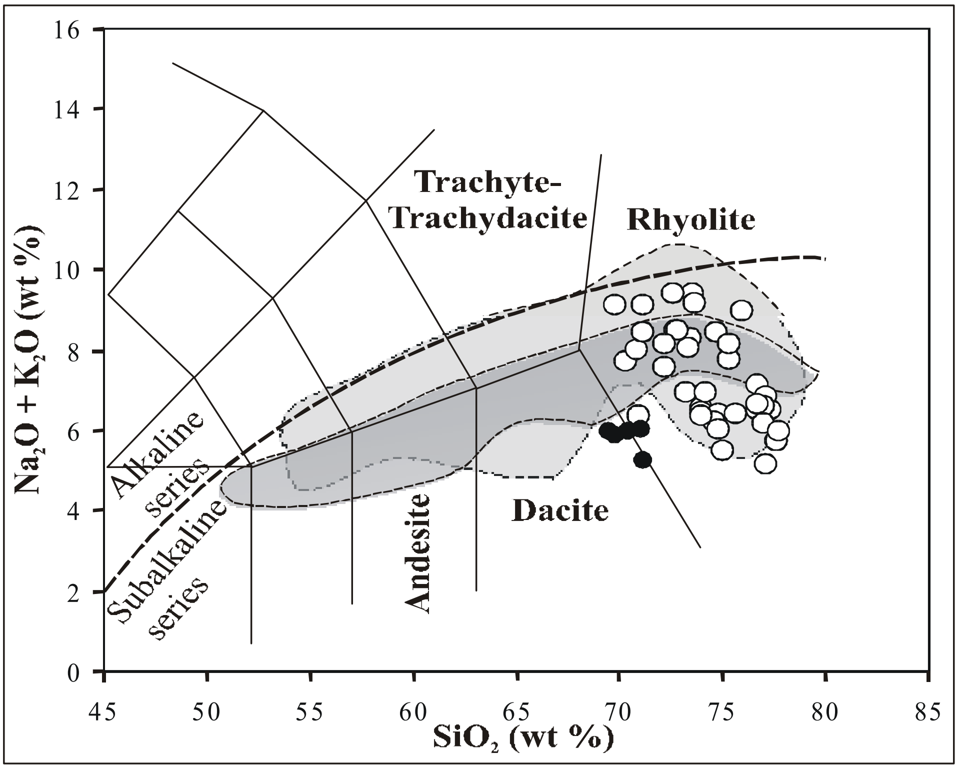

Figure 10-1. Total alkalis vs. silica diagram showing the distribution of melt inclusions (open circles) and the Llamo porphyry (host rock for the inclusions) (black circles) with respect to the evolutionary trend of regional magmatic rocks, volcanic (light-gray) and intrusive (dark-gray).

Most quenched glasses show copper concentrations in the order of 0.03 wt % to 0.57 wt %, with a mean of 0.10 wt %. These values are at least one order of magnitude higher than can be expected for calc-alkaline plutons in general (Einaudi, 1997).

10.2.2 Aqueous fluid: evolution from early magmatic to the late-hydrothermal stages

The earliest magmatic fluids involved in the genesis of the Zaldívar deposit correspond to the chlorine brines trapped in the MS-type inclusion, which are dominated by Na, K, Fe, Cu, Zn and Mn (Fig. 10-2). A coarse approximation of the bulk salinity of these dense brines would be 75 to 85 wt. % NaCl equiv., estimated from the dissolution temperatures of halite and sylvite. A rather similar complex chemical composition has been defined in fluid inclusions from the Granisle deposit with salinities in the order of 70 to 84 wt % of NaCl+KCl+$FeCl_2$, with $CaCl_2$ and $MnCl_2$ as minor components (Quan et al., 1987).

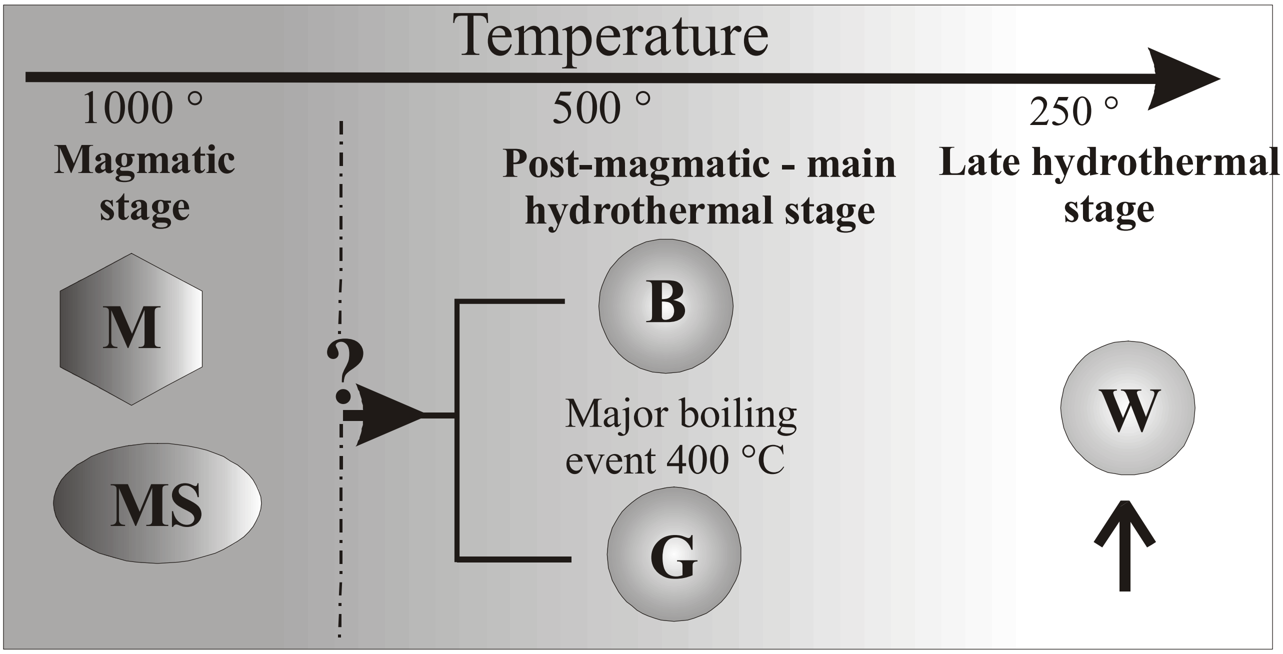

Figure 10-2. In the Zaldívar deposit the fluid evolution started at magmatic temperatures; the MS-type inclusions are the magmatic end member with homogenization temperatures between 1030 ° and 700 °C. A cooler post-magmatic hydrothermal event is marked by the occurrence of coexisting B- and G-type inclusions that homogenize in the range 600 ° to 250 °C, and a major boiling event occurred around 400 °C. A low-temperature (<250°C), low-salinity, groundwater-dominated fluid (W) is the final fluid influx into the system.

No evidence of immiscibility between vapor-rich and MS-type inclusions has been observed to explain the formation of this high-density fluid by boiling of a lower salinity fluid. As a matter of fact, at pressures higher than 2 kbar, the first aqueous fluid exsolved from a water-saturated melt would be stable as a single phase for all H_2O-NaCl compositions (Sourirajan and Kennedy, 1962); also at these pressures, the earliest fluid exsolved would be highly saline (Kilinc and Burnham, 1972). Furthermore, Cline and Bodnar (1991) and Cline (1995) provided quantitative support for the origin of high-salinity fluids in a porphyry copper system, they show that a granodioritic magma (porphyry copper type), crystallizing at pressures of about 2 kbar, exsolved very high-salinity fluids, which were homogeneous and copper-rich. Accordingly, the MS-type fluid represents these extremely dense metal-rich homogeneous brines exsolved during the early crystallization stage of the parental intrusive and did not form by boiling of a less saline fluid. The trapping of the MS-type fluid must have happened at a rather shallow depth at a pressure that was sufficient to prevent boiling of the exsolved fluid system and at elevated temperatures (700 to near 1000° C).

After the generation of the magmatic MS-type inclusions and during the cooling of the parental intrusive, the deposit was the site for an intense hydrothermal system (Fig. 10-2), which leads to widespread hydrothermal alteration and redistribution of metallic elements in the intrusion and surrounding host rocks.

The high-salinity fluids that surround the mineral inclusions correspond to late-magmatic fluids, and their origin can be easily explained if it is assumed that the mineral phases represent crystallized melt inclusions. In this context, the aqueous fluid would have been simultaneously trapped with the melt, or the fluid was exsolved from the melt during crystallization of the enclosed mineral (Yang and Bodnar, 1994). Either case would indicate that high-salinity aqueous fluids were exsolved from the crystallizing magma and that they were abundantly present during the last growing stage of magmatic quartz phenocrysts. However, if the solids only represent trapping sites for the aqueous inclusions, then the fluids will represent a later hydrothermal event (Yang and Bodnar, 1994). The latter possibility seems the least likely since mineral inclusions show no evidence of post-entrapment modifications, furthermore the trapping of high-salinity fluids within other magmatic phases such as zircon and apatite will also support the trapping of highly saline magmatic fluids.

The nearly constant phase ratio observed in the inclusions that form the coronas around mineral inclusions indicate that a homogeneous fluid was first trapped in the cavity together with the mineral. Subsequently, part of the fluid was expelled as an homogeneous aqueous phase through microcracks into the host mineral and reorganized as tiny secondary inclusions in a more or less radial pattern or decrepitation halo. This texture is commonly seen in shallow intrusives and is produced after trapping by microfracturing events, occurring when the melt in the inclusion becomes saturated in water as it is cooled and crystallized, the pressure inside the inclusion increases inside the cavity if a water-rich gas phase is produced ($P_{\text{external}} >> P_{\text{internal}}$) (Touret and Frezzotti, 1993; Yang and Bodnar, 1994; Lowenstern, 1995).

The decrepitation halo is produced either if the inclusion trapped water-unsaturated silicate melts or if the inclusion trapped a melt that was saturated in water (Yang and Bodnar, 1994). In either case, the aqueous fluid will be expelled as a homogeneous phase and the halite crystals will grow from the fluid on cooling after trapping of the secondary inclusions.

Aqueous fluids trapped in the B-, G- and W-type inclusions represent the main hydrothermal stage, their physical characteristics, microthermometry data and compositional variations, show no differences between the samples from the Llamo and Zaldívar porphyries. The reason for this resemblance is that all primary hydrothermal features of the Zaldívar porphyry, if any, have been completely destroyed during the intrusion of the Llamo porphyry, and/or have been overprinted by the latest hydrothermal event associated with the Llamo intrusive. As a consequence, all the observed characteristics of fluid inclusions are representative for the hydrothermal system related to the intrusion of the Llamo porphyry, and therefore to the main mineralization event.

Because B-, G- and W-type fluid inclusions reflect the chemistry of fluids occurring at given stages of the hydrothermal system, the identification of several inclusion subtypes will demonstrate the occurrence of at least two different fluids of contrasting compositions, from a complex Na-K-Fe-Mn-Cl-H_2O system to a more simple Na-Fe-Cl-H_2O system.

The temporal relation between the different fluid types during the evolution of the hydrothermal system is unclear, as the profusion in both number and generation of secondary fluid inclusions observed in nearly all studied phenocrysts makes it impossible to define temporal differences among the various inclusion subtypes. However, each subtype forms distinctive fields in a filling-temperature/composition diagram (Fig. 10-3), the fields are mostly dependent on the compositional variation and no major changes are observed in the filling-temperature range as they show a common peak around 350°C, throughout the whole compositional range.

The existence of multiple generations of secondary fluid inclusions having contrasting compositions (B_1- and B_2-subtypes, W_1- and W_2-subtypes) would indicate that the host mineral has been repeatedly and extensively fractured on a microscopic scale and repeatedly bathed and rehealed in the presence of fluids of different chemical composition during the evolution of the hydrothermal system. The occurrence of fluid inclusions showing different chemistry can be explained by the introduction of different magmatic-hydrothermal fluids, each corresponding to a different brine/vapor saturation event that occurs in an underlying magma chamber, (Hedenquist and Lowenstern, 1994).

The coexistence of B- and G-type inclusions in the studied samples indicates that they were trapped along the immiscible surface of a boiling system (Pichavant et al., 1982), between 390° and 460°C and at about 0.8 to 1.5 km depth. These temperature and pressure conditions closely match those defined for the brittle/plastic interface (Fournier, 1999). Therefore, the chemical variation of fluid inclusions can also be related to the contrasting conditions existing at the brittle/plastic transition. In the plastic domain, brines and vapor exsolved from the magma accumulate at lithostatic pressure, whereas in the brittle rock, hydrostatic pressure and meteoric fluids prevail. Furthermore, because the temperature and fluid pressure gradients across the plastic/brittle interface is very steep, episodic discharges of brines and or vapor pounded in the plastic domain are produced, accompanied by a sudden decompression from lithostatic to hydrostatic pressure conditions due to fracturing events, inducing the boiling of fluids, and abrupt changes in fluid composition.

On a NaCl-KCl-H_2O ternary diagram (Fig. 10-4), the estimated salinity values for MS-type inclusions plot close to those from Granisle (Wilson et al., 1980) being MS-type inclusions in general slightly less saline and richer in K, whereas the inclusions from Bingham (More and Nash, 1974) have a composition close to the B_2-subtype.

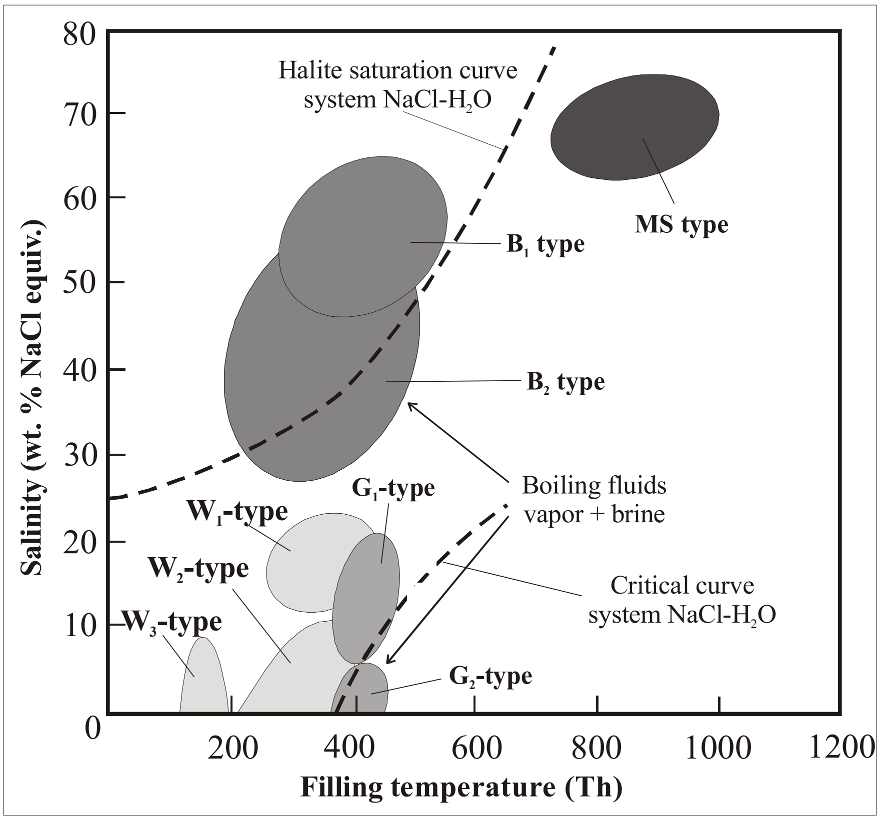

Figure 10-3. Filling-temperature/composition diagram showing the separated fields characterizing each different fluid-inclusion subtype.

The B-type fluid cannot be derived directly from the boiling of the MS fluid as the former has an lower overall salinity. One possibility would be a mixing of externally derived, low-salinity aqueous fluids, which would dilute MS fluids and produce the overall salinity balance between B and G fluids. A possible mechanism for the origin of a high-salinity fluid could be the boiling of a low-salinity liquid of magmatic origin. The boiling of this fluid can be related to the parental magma either as a nearby source of heat or high temperature vapor (Ahmad and Rose, 1980).

Low-temperature, low-salinity (nearly pure water) W_3-type fluid represents the latest hydrothermal event in the Zaldívar PCD, and most probably reflects the incoming of external non-magmatic aqueous fluids into the vanishing hydrothermal system (Fig. 10-2).

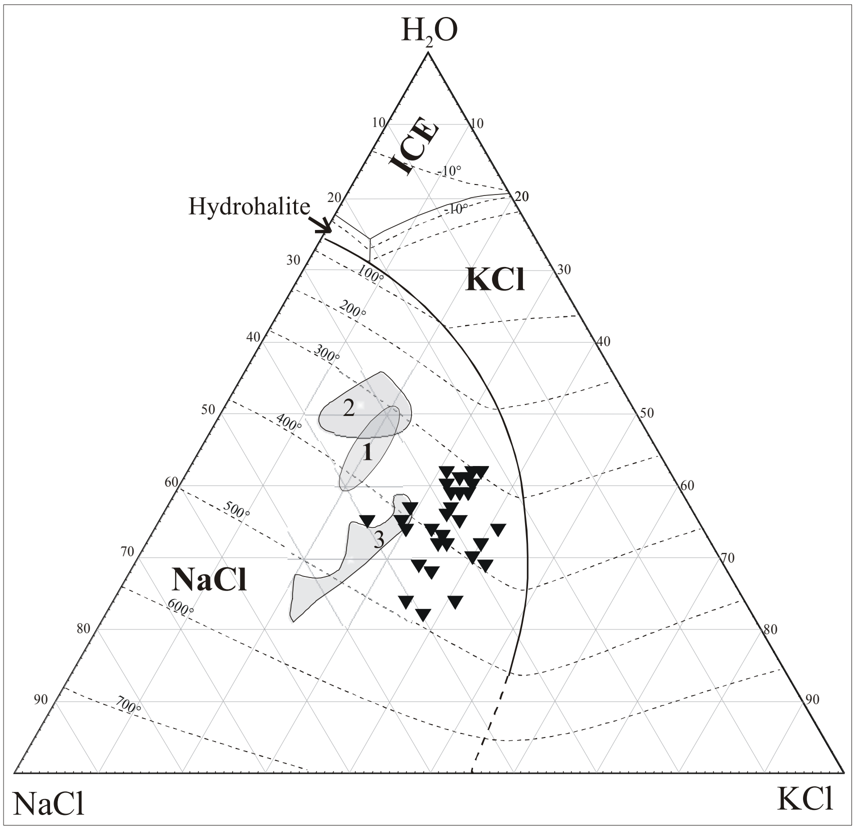

Figure 10-4. NaCl-KCl-H_2O ternary diagram; triangles: MS-type inclusions, shaded area 1: B_2-type fluid inclusions, shaded area 2: fluid inclusions from Bingham (Moore and Nash, 1974), shaded area 3: fluid inclusions from Granisle-Bell (Wilson et al., 1980)

10.3 Are high homogenization temperatures in melt and MS-type inclusions real or experimental artifacts?

As the homogenization temperatures measured in melt and MS-type inclusions are rather unexpected, around 1000°C, and as they are higher than the solidus temperature commonly accepted for granitic magmas (about 850° - 950°C, Tuttle and Bowen, 1958), they require a thorough evaluation and discussion.

The high homogenization temperatures measured in the melt inclusions can be explained by several factors:

a) Loss of volatiles through the host mineral, either during slow cooling at the time of intrusion, or during fracturing events (Lowenstern, 1995). This process is commonly seen in shallow intrusives (Touret and Frezzotti, 1993), evidenced id from a corona of minute fluid inclusions around the evolved melt remnants. Such figures, however, have never been seen in the Llamo intrusion. The quantity of volatiles must have been relatively low, as is indicated not only by the high remelting temperatures, but also because we could never observe any fluid phase during remelting, as for instance for the Monte Genis granite in Sardinia (Fig. 4 in Touret and Frezzotti, 1993).

b) The heterogeneous trapping of melt and a discrete vapor phase may occur if gas bubbles were present in the magma at the time of trapping. Total homogenization would then only occur at extremely high, unrealistic temperatures.

c) The kinetics of the melting process in the heating stage: Especially for acid magmas, equilibrium melting may require hours, sometimes days (Thomas et al., 1996). Even though the heating was performed slowly, and the final temperature maintained for several hours, we cannot exclude some disequilibrium melting, resulting in exceptionally high measured temperatures.

d) The partial re-melting of the mineral host during heating: If, during re-melting, some SiO_2 from the mineral host would be incorporated into the melt remnants, then the silica content and accordingly the re-melting temperature will increase. This possibility cannot be completely excluded given the high SiO_2 contents measured in some inclusions.

All these reasons indicate that the measured temperatures above 1100°C may be unrealistically high. However, in all types of melt inclusions, the final melting of daughter minerals occurs at temperatures between 915° and 1000°C, reinforcing the 900°-1050°C range as true trapping temperature for melt inclusions.

Furthermore the homogenization range found in most melt inclusions (900° to 1050°C) corresponds to the total homogenization temperatures of the earliest magmatic fluids (MS-type inclusions), which homogenize at magmatic temperatures (750° to near 1000° C), much higher than the typical “boiling” fluids that characterize the late-magmatic and main hydrothermal stages in Cu-porphyry systems.

The high homogenization temperatures measured in MS-type inclusions may seem unrealistic, and factors such as heterogeneous trapping, or post-entrapment modifications might explain the anomalous values. Although features indicating heterogeneous trapping are common in the M_3-type melt inclusions, no evidence for immiscibility has been observed in the MS-type inclusions. Therefore, in this last particular case, high homogenization temperatures cannot be interpreted as the result of heterogeneous trapping, as in the Panguna, Granisle and Apusei Mountain deposits (Eastoe and Eadington 1986; Wilson et al., 1980 and Pintea, 1995, respectively). Another feature supporting the validity of the homogenization temperatures measured in MS-type inclusions is the absence of post-entrapment features such as leaking or necking down, in fact all MS-type inclusions have a more or less consistent ratio among the different phases present in the cavity. Finally, the MS-type inclusions occur isolated in domains within the quartz phenocrysts showing no evidence of microfractures or coexistence with a latter generation of fluid inclusions that may have induced modification of their original composition.

All the arguments given above, support the validity of the high homogenization temperatures of MS-type inclusions, and as the MS fluid was trapped as a homogeneous fluid in a shallow intrusive, the measured values represent minimum trapping temperatures that will require only a minor pressure correction, not exceeding a few tens of degrees for these shallow intrusives. As a consequence, they will lead to a trapping temperature within the 750° to 1000°C range. The validity of the homogenization temperatures of MS-type inclusions is a major argument supporting the high homogenization temperatures measured in the melt inclusions.

In conclusion, the comparable homogenization temperatures measured both in melt and MS-type inclusions argue for the validity of the measured temperatures, therefore these magmatic features represent remnants of a magma trapped at temperatures around 1000°C. An important consequence of this finding is that quartz phenocrysts have started to grow well above the final crystallization of the intrusive, near the liquidus of the magmatic system in a possibly overheated magma. But this has happened at a rather shallow depth, after magma degassing at a pressure (probably of the order of 2 kbar) that was sufficient to prevent boiling of the fluid system.

10.4 Origin of the ore-bearing magma

During progressive subduction, a relatively shallow subduction angle favors the hydration of a cool mantle wedge by the incorporation of fluids associated with the subducted slab (Sillitoe, 1986, and ref. therein). Primary magmas can then be formed in the asthenospheric sub-arc mantle wedge, triggered by the dehydration of the subducted slab (Fig. 10-5-B). In the case of the Andes, isotopic and trace-element data (Sr/Nd isotopes, flat to LREE-depleted rare-element pattern) suggest that these primitive melts should not be too different from MORB (mid oceanic ridge basalt) (Davidson et al., 1991). The mantel-derived magma will be modified by large-scale interactions with the continental crust in magma reservoirs in the mantle–crust transition, in a zone of melting, assimilation, storage and homogenization (MASH) (Hildreth and Moorbath, 1988) (Fig. 10-5-B). Entrapment of the modified mantle-derived magma in the Middle Upper crust will result in the production of highly differentiated magmas caused by extensive magmatic differentiation in an intermediate magma chamber and magma-crust interaction due to a long residence time in the crust (Davidson et al., 1991) (Fig. 10-5-B).

The magma evolution described above, is combined with deformation peaks in which compression leads to crustal shortening and thickening over a shallow subducted slab (Kay et al., 1999). As a consequence, magmas intruded into a thickened crust in a compressional regime will not easily migrate upwards and therefore will evolve at depth (point 3, Fig. 10-5-B).

Present-day geophysical measurements identify a well-defined « low-velocity zone » (LVZ, Fig. 10-5-A) between 68 and 69°W, interpreted as a large-scale magmatic chamber at depth. This zone is situated within the lower crust of the South American plate, in contact with a wide « high conductivity Zone » (HCZ) slightly oblique to the crustal foliation.

The high-conductivity zone (HCZ) (Fig. 10-5-A) has been interpreted as being due either to disperse graphite particles or to the occurrence of interstitial brines (Touret and Marquis, 1994). However, as no trace of CO_2 (formed by oxidation of graphite during crustal assimilation) has been found in the Llamo porphyry, therefore the occurrence of interstitial brines is the most reasonable hypothesis. It provides a good explanation for the presence of high-salinity, magmatic brines, which appear to be so typical for the Llamo porphyry.

The extremely high magmatic temperatures are more in line with magmatic differentiation than with crustal assimilation. Anatexis (crustal rock melting) is a strongly endothermic process, which will buffer magmatic temperatures at values commonly encountered during crustal anatexis, about 750°C (Spear, 1993).

The rapid ascent of deep, hot magmas requires a favorable geodynamic environment, such as the West Fissure, that obviously will serve as a favorable pathway for providing a rapid ascent of deep hot magmas towards the surface, favoring the generation of the extremely high melt temperatures measured on melt inclusions.

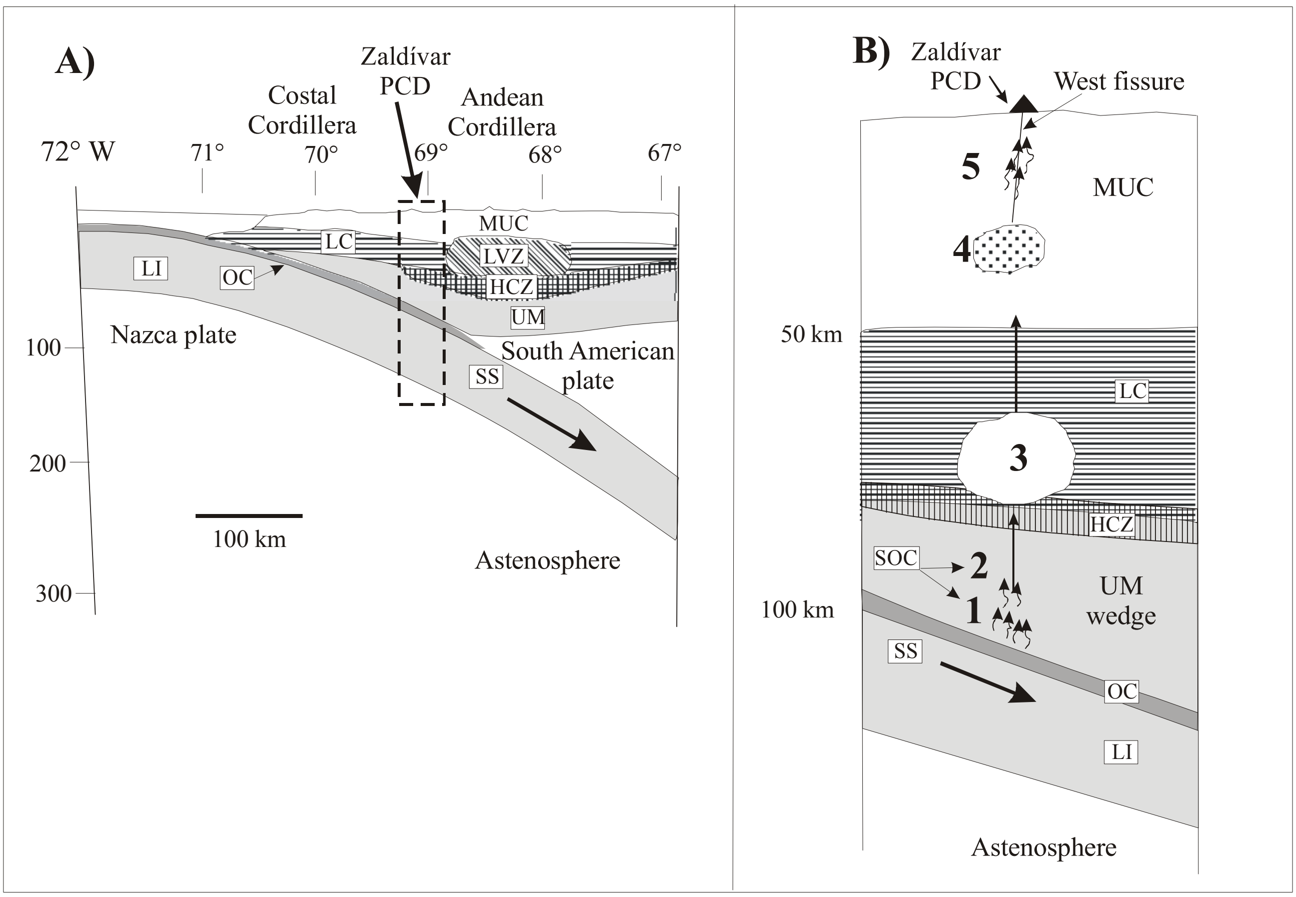

Figure 10-5. Model of the Oligocene magmatic evolution of the Llamo porphyry in Zaldívar PCD **A:** Interpretation of present-day geophysical cross section of the Andes in Northern Chile (from the work of Berlin-Potsdam groups, P. Giese and R. Emmermann, in Touret and Huizenga, 1999). OC: Oceanic crust, LI: Lithosphere, SS: Subducted slab (Nazca Plate), LC: Lower crust, granulite (horizontal foliation), MUC: Middle and Upper crust (in the South American plate), UM: Upper mantle, LVZ: Low-velocity zone (magma accumulation?), HCZ: High-conductivity zone at the LC/UM boundary but slightly oblique to major lithological structures (inferred to be caused by interstitial brines, see text). **B:** Evolution of the Oligocene magmatism (Llamo porphyry) in the Zaldívar PCD, adapted from Davidson et al., 1991. Same symbols as in A. Fluids released by dehydration of the subducted slab (1) induce the formation of primitive mantle melts (2) (MORB-like composition). These primitive melts differentiate in a lower crustal magmatic chamber (3), assumed to be the equivalent of the present-day LVZ. The end-product of the differentiation are acid magmas (Llamo porphyry), enriched in Cu (from SOC) and brines (from HCZ). Production of highly differentiated magmas will occur in the UC (4), magma then will ascend aided by local tectonic features (West fissure).

10.5 Provenance of Cu

Most quenched glasses from the Llamo porphyry show copper concentrations between 0.04 wt % to 1.50 wt %, the highest copper concentrations (> 1.5 wt %) are related to the black-dot-bearing M_3-subtype glasses, which show a normal major element composition if EMP analyses are performed on dot-free areas.

The EDS analyses of the black-dots indicate that they correspond to Cu-chloride micro inclusions, and hence they are the cause for the highly anomalous copper values yielded in the M_3-type quenched glasses. The black dots correspond to immiscible droplets of Cu-chloride that resulted from melt/copper-chloride immiscibility during the crystallization of the parental intrusive as chloride saturation was reached. The evidence of copper immiscibility support the idea that at the magmatic stage, chlorine has a strong capacity for metal transport, and the metals will be readily separated from the crystallizing magma mainly in the form of hydrosaline chloride-rich compounds.

Very striking is the lack of sulfur, which has not been detected by any of the analytical procedures, this fact further supports the idea that copper is separated in the form of chloride solutions during magma immiscibility.

The MS-type fluid would have played an important role in the separation of the metals from the crystallizing magma that will be later redistributed by post-magmatic hydrothermal fluids into the upper portions of the pluton were they could eventually be concentrated as a porphyry-type mineralization (Yang and Bodnar, 1994; Heinrich et al, 1999).

The metal contents in MS-type inclusions and the anomalous concentration of copper in melt inclusions provide strong support for the hypothesis that the metals present in the Zaldívar porphyry copper system were fundamentally derived from the crystallizing Llamo porphyry.

The origin of copper content in the Llamo porphyry would be related to magmatic differentiation of mantle-derived melt; copper can be further enriched by fluids and sediments associated with the subducted slab (Fig. 10-5-B). The continental crust will have a minor importance as a source of copper, it will only be important as the site for magma differentiation (Sillitoe, 1986, and ref. therein).

10.6 Thermochronology

U-Pb dating in zircons from the Llamo porphyry at the Zaldívar deposit and in the neighboring Escondida PCD deposit indicates that the crystallization of the synmineralization porphyritic magmatism in both deposits was coeval at ca. 38 Ma (Richards et al., 1999).

The weighted mean age for the ^{40}Ar/^{39}Ar ages in biotites from the Llamo porphyry yield 36.57±0.17 Ma and is in satisfactory agreement with, but more precise than, the 37.40 ± 1.8 Ma also measured in igneous biotites reported by Clark et al. (1998). Because the closure temperature for the ^{40}Ar/^{39}Ar system in biotites is about 350°C, the biotite ^{40}Ar/^{39}Ar age will constrain the time at which the samples were cooled below this temperature, furthermore the homogeneous plateau ages imply that reheating has never occurred. As the closure temperature for the ^{40}Ar/^{39}Ar system in biotite is closely similar to the lower temperature defined in the magma-related hydrothermal fluids (~350°C), the ^{40}Ar/^{39}Ar ages will represent the ceasing of the main mineralizing hydrothermal system.

The crystallization age defined for the Llamo porphyry, in combination with ^{40}Ar/^{39}Ar ages and fluid inclusions microthermometry data obtained in the present study, reinforce the concept that the time span between the crystallization of the porphyritic intrusives and the ceasing of the main mineralization-alteration event at the Zaldívar deposit is about 2 Ma, in agreement with the intrusive-mineralization-alteration timing defined for other PCDs of northern Chile by Reynolds, (1997), Clark et al., (1998) and references therein.

In the Escondida area, the magmatic activity continues long after the main mineralization event and is represented by a suite of dacitic dikes that yield ages as young as 31 Ma (K-Ar whole-rock) (Alpers and Brimhall, 1988). This value is comparable with the age defined by zircon fission tracks in the Zaldívar mine (29, 1±1.17 Ma). Although no direct evidence of post mineralization magmatic activity similar to the one observed in the Escondida area has been found in the Zaldívar deposit, the ZFT age is most probably dating the end of the magmatic activity in the Zaldívar-Escondida area, specifically signaling the time when the whole site became colder than about ~250°C.

10.7 Concluding remarks

Melt, mineral and fluid inclusions hosted in igneous quartz phenocrysts from the synmineralization Llamo porphyry occur as well-preserved features that record the entire evolution of the porphyry copper system at the Zaldívar deposit. These features provide substantial information to better constrain the evolution of the deposit that begins during the early magmatic crystallization and follows with the emplacement of a complex hydrothermal system associated with the late crystallization stages and cooling of the parental intrusive.

An exceptional characteristic of the magmatic remnants, namely melt and MS-type inclusions, is that the temperature of the magma at a few kilometers depth, during the time of the exsolution of dense metal-rich brines, was around 1000°C, well above the final crystallization temperature of most acid magmas.

Copper enrichment constitutes another remarkable characteristic of melt and MS-type inclusions that supports the hypothesis of a magmatic source of metals in this porphyry copper system, in line with the orthomagmatic model. These magmatic remnants also indicates that during the magmatic stage of the Zaldívar PCD, metals separate from the crystallizing magma as immiscible dense, highly saline fluids in equilibrium with the silicate melt, that are subsequently remobilized during the hydrothermal events as chlorine solutions.

The entire evolution of the hydrothermal system is marked by the presence of mainly two contrasting populations of fluid inclusions, high-salinity brines and low-salinity vapor-rich inclusions, that are interpreted to be contemporaneous and represent pristine samples of a boiling magmatic fluid trapped at temperatures ca., 400°C and about 1 km depth. The hydrothermal system was repeatedly recharged and the density of the trapped fluids has been progressively reset without any significant change in temperature.

The high-salinity fluids are in general complex chloride brines dominated by NaCl on which K, Fe, Mn, Cu and Mg are frequently present. The multi element composition indicates that these fluids have a strong capacity for transporting metals; this complexity is also reflected in the vapor-rich inclusions. The latest hydrothermal event is dominated by externally derived low-salinity almost pure water, and shows no relation with the mineralization.

The time span between the crystallization of the synmineralization intrusive and the ceasing of the main hydrothermal event was about 2 Ma, and the thermal activity in the area cooled off through the 250°C at about 29 Ma.

Chapter 11

Geodynamic evolution and metallogenetic model for the Zaldívar deposit

11.1 Geodynamic evolution of the Zaldívar area

The Central Andes of Northern Chile had experienced a very complicate evolution, from a non-arc-related rift basin during Upper Paleozoic times, to a complex arc-back-arc system during the Jurassic, and finally to a subduction-related continental magmatic arc from the Upper Cretaceous to the Present (e.g., Coira et al., 1982). The rocks outcropping in the Zaldívar deposit therefore have witnessed most major events related to this Andean geodynamic evolution at the latitude of the Zaldívar mine.

11.1.1 Pre-subduction regime: Upper Paleozoic magmatism

Prior to the Upper Paleozoic, the country rocks of the Zaldívar area formed part of the stable Gondwana super-continent. Before fragmentation and rifting at the end of the Paleozoic, the region was affected by intra-plate magmatism, here represented by the Permian Zaldívar intrusive (290 Ma). This petrographic unit, which corresponds to one of the earliest stages in the geodynamic history of the Central Andes in the area of the Zaldívar deposit (Fig. 11-1-A), is part of a volcano-plutonic belt of mainly rhyolites, dacites and cogenetic granitoids (Coira et al., 1982). The Gondwana continent appears to have been particularly stable from the Late Permian to the Middle

Triassic, in particular, no subduction took place at its western margin (Valencio and Villas, 1976, in Flint et al., 1993). The acidic rocks represented by the Zaldívar intrusive are typical intraplate magmatics (Breitkreuz et al., 1988) resulting from partial melting in the upper mantle (Flint et al., 1993), during an extensional phase in the final stages of the Gondwana orogenic cycle (Kay et al., 1989; Mpodozis and Kay, 1992).

11.1.2 From extension to compression: the Andean subduction

Since the beginning of the Mesozoic, a major change that is still active today, is observed in the tectonic regime of the central Andes of South America. The extensional regime has been replaced by the Andean Tectonic Cycle (Espinoza et al., 1996) characterized by the continuous convergence and subduction of oceanic plates beneath the South American continental plate (Fig. 11-1-B). This cycle shows alternating transpressional and transpressive regimes, and the active plutonism and volcanism is related to the subduction process (e.g., Davison et al., 1991).

- Cretaceous to Eocene

In the area of the Zaldívar deposit, a magmatic arc system was active from the Late Cretaceous to the Eocene (Marinovic et al., 1995). It created large volumes of andesitic lavas and pyroclastic flows, notably the andesites of the Augusta Victoria Formation. This magmatism is related to the generation of primitive melt produced by mantle melting (Fig. 11-1D), induced by the incorporation into the asthenospheric wedge of fluid released by dehydration of the subducted slab (Fig. 11-1-C). The primitive melt, similar to primitive mafic basaltic melts, is modified in the crust by the MASH process described by Hildreth and Moorbath (1988) (Fig. 11-1-C) and is finally erupted as andesites (Davison et al., 1991) (Fig. 11-1-E)

Figure 11-1. Next page. Geodynamic evolution of the Zaldívar mine area. Figure modified from Coira et al., 1982, and Kay et al., 1999. Interpretation at 38.7 Ma, pers. com. ANCORP'96, GFZ, Postdam, Germany. **A)** The Zaldívar area is stable during the Upper Paleozoic to Middle Triassic, and the region is affected by intra-plate magmatism represented by the Zaldívar intrusive (290 Ma). **B)** From the beginning of the Mesozoic the tectonic regime correspond to a continuous convergence and subduction of oceanic plates beneath the continental plate. From the Late Cretaceous to the Eocene a continental magmatic arc system was active in the area of the Zaldívar deposit. This magmatism is related to the generation of primitive melt produced by mantle melting, induced by the incorporation into the asthenospheric wedge of fluid released by dehydration of the subducted slab **(C)**. The primitive melt, similar to primitive mafic basaltic melts, is modified in the crust by the MASH process (Hildreth and Moorbath, 1988) **(D)** and erupted creating large volumes of andesitic lavas and pyroclastic flows, notably the andesites of the Augusta Victoria Formation **(E)**. During a shallow subduction regime **(F)**, fluids and volatiles produced by dehydration of the subducted slab are concentrated in the cooling mantle above the subducted slab. Crustal thickening and shallowing of the subducting slab is accompanied by continental lithospheric thinning and near elimination of the asthenospheric wedge. This phenomenon inhibits magmatism, but enhances mantle hydration and concentration of volatiles above the subducted slab **(G)**. Subsequent steepening of the subducting plate permits the development of a thicker asthenospheric wedge, which provides the heat leading to the melting of the overlying hydrated mantle and lower crust, causing the generation of fluid-rich magmas **(H)**. These magmas intrude into a thickened crust under a compressional regime, differentiate in lower crustal magmatic chambers producing highly differentiated acid magmas (Llamo porphyry) **(I)**. The West Fissure serves as a favorable pathway for a rapid ascent of deep hot magmas towards the surface into the Upper crust.

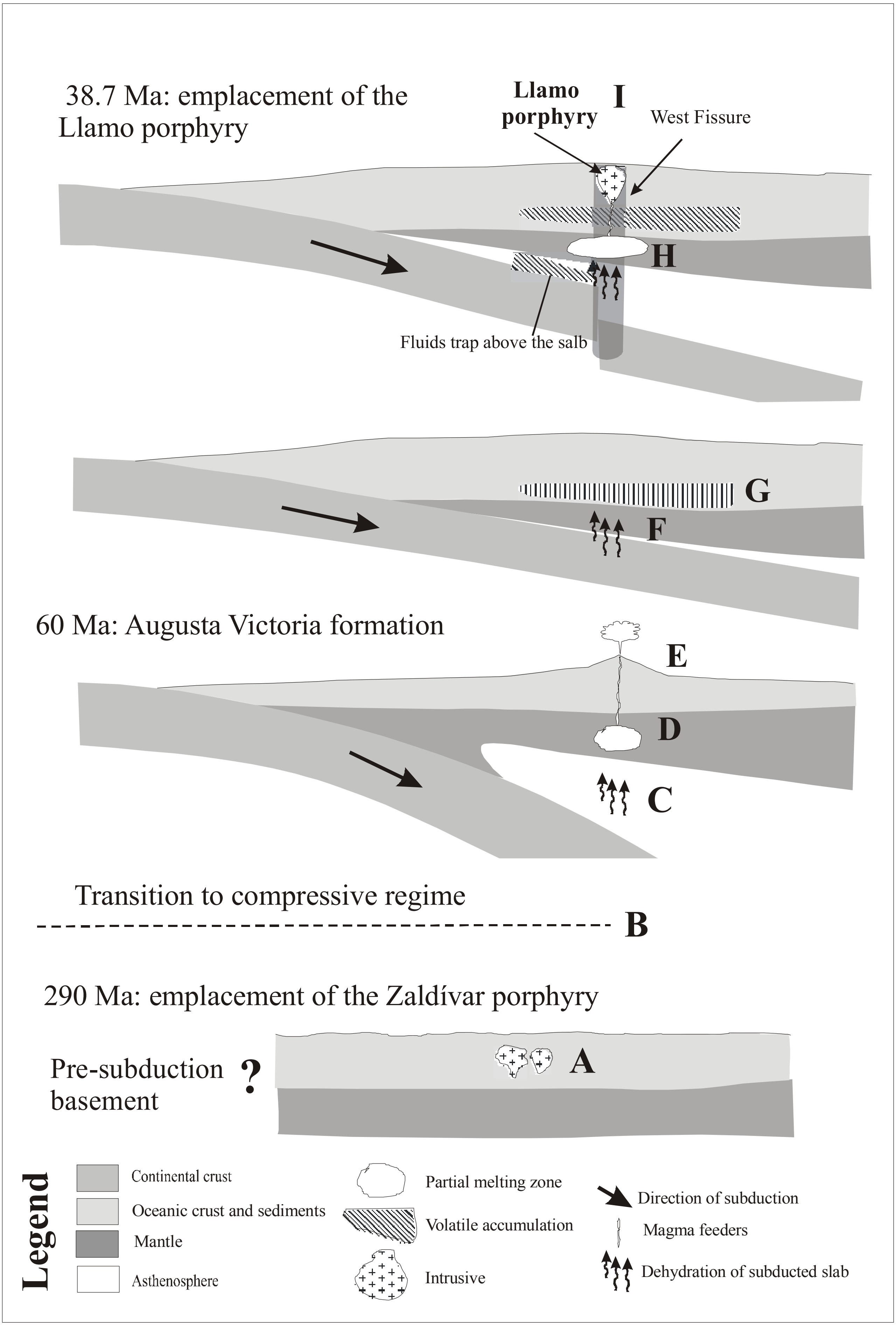
38.7 Ma: emplacement of the Llamo porphyry
Llamo porphyry
I
West Fissure
H
Fluids trap above the salb
G
F
60 Ma: Augusta Victoria formation
E
D
C
Transition to compressive regime
B
290 Ma: emplacement of the Zaldívar porphyry
Pre-subduction basement
?
A
Legend
Continental crust
Oceanic crust and sediments
Mantle
Asthenosphere
Partial melting zone
Volatile accumulation
Intrusive
Direction of subduction
Magma feeders
Dehydration of subducted slab

- Oligocene

During the Oligocene the volcanism almost ceased, and the magmatic activity was restricted to the emplacement of hypabyssal intrusives, notably those genetically relate to PCDs, such as the Llamo porphyry. The generation of these intrusives can be explained by the mechanism proposed by Kay et al. (1999): crustal thickening and shallowing of the subducting slab, accompanied by continental lithospheric thinning and near elimination of the asthenospheric wedge (Fig. 11-1-F). The thinned asthenospheric wedge inhibits arc magmatism, but enhances mantle hydration and concentration of volatiles above the subducted slab (Fig. G). Subsequent steepening of the subducting plate permits the development of a thicker asthenospheric wedge. The heat provided by the asthenospheric wedge leads to the melting of the overlying hydrated mantle and lower crust (Fig. 11-1-H). These magmas intrude into a thickened crust under a compressional regime. The primitive melts differentiate in a lower crustal magmatic chamber, being the end-product, highly differentiated acid magmas (Llamo porphyry), enriched in Cu and brines (Fig. 11-1-I)

Heating of the crust by mantle magmas leads to enhanced ductile deformation producing crustal thickening in response to regional compression. It may also facilitate the development of major deformation structures such as the West Fissure and the associated fault systems (Fig. 11-1-E) during the Eocene-Oligocene boundary. Magmas rapidly rise to shallow levels along this regional shear system.

11.2 Model of magmatic/post-magmatic evolution

As described above, the primitive magma related to the Llamo porphyry underwent upper crustal differentiation and became volatile-saturated as it intruded towards the surface. Copper was sequestered from the crystallizing magma by early exsolved brines as shown by melt and MS-type inclusions (Fig. 11-2-A). MS-type inclusions and the Cu+Cl black dots found in some melt inclusions indicate that copper and other base metals separated from the crystallizing magma as dense immiscible chloride and metal-rich brines in equilibrium with the silicate melt. This finding substantiates the hypothesis that chloride controls the partitioning of metals in igneous systems (Candela and Holland, 1984). Furthermore, copper enrichment constitutes a remarkable characteristic of magmatic remnants from the Llamo porphyry, supporting the hypothesis of a magmatic source of metals in this porphyry copper system.

Upon cooling at shallow depth, intensive degassing occurred in the form of brines, water vapor and other volatiles such as CO_2 and sulfur. Within a plastic rock regime, the exsolved brines and volatiles are pooled at the cupula of the cooling intrusive in an isolated, mechanically stable horizontal lens or fracture that has limited vertical interconnectivity (Fournier, 1999) (Fig. 11-2-B). The high-salinity fluids have a strong capacity for transporting metals and they correspond to complex chloride brines dominated by NaCl in which K, Fe, Mn, Cu and Mg are frequently present. During the degassing stage and the early hydrothermal events, metals are also transported as chlorine complexes.

In a crystallizing magma, sulfur behavior resembles that of chlorine and will be readily partitioned into the exsolved aqueous phase as SO_2 (vapor) in a high fO_2 environment that also favors fluid exsolution (Frei, 1996). In the early stages of magmatic immiscibility and high-temperature hydrothermal events, copper will be transported as chlorine complexes. However, as the temperature of the exsolved aqueous phase decreases, the fH_2S increases by hydrolyzation of SO_2, producing the precipitation of sulfides from the metal-chloride complexes (Cline, 1995; Frei, 1996).

The fluids produced by magma degassing of the cooling Llamo porphyry formed a complex hydrothermal system and its entire evolution is marked by the presence of mainly two contrasting populations of fluid inclusions, high-salinity brines and low-salinity vapor-rich inclusions, interpreted to be contemporaneous. These fluids represent pristine samples of a boiling magmatic fluid trapped at temperatures of ca. 400°C and about 1.5 km depth, closely similar to the pressure and temperature defined for the brittle-plastic interface. Boiling episodes were most probably related to a sudden pressure decrease during the transition from a lithostatic to a hydrostatic regime caused by episodical breaches of the self-sealed brittle-plastic transition (Fig. 11-2-C).

The hydrothermal system was repeatedly recharged and the density of the fluids progressively reset without any significant change in temperature.

The hydrothermal solutions react with the Llamo porphyry and to a varying extent with the surrounding country rocks. The water/rock interaction leads to extensive hydrothermal alteration that involves large volumes (many cubic kilometers) of host rocks. Potassic alteration occurs mainly in the Llamo porphyry, phyllic alteration in the Zaldívar porphyry, whereas propylitic alteration predominates in the Augusta Victoria andesites (Fig. 11-2-D). The introduction of much of the metals and sulfur probably accompanies this stage.

The time span between the crystallization of the syn-mineralization intrusive and the cessation of the main hydrothermal event was about 2 Ma, and the thermal activity in the area cooled through the 250°C isotherm at about 29 Ma.

The supergene argillic alteration strongly overprints the phyllic and potassic alterations (11-2-E), and is most probably related to the secondary enrichment processes.

At present day, the Zaldívar deposit is located at ca. 3400 m a.s.l. In order to bring the deposit at the surface, about 1.5 km of rocks were eroded by exhumation since ca. 37 Ma (main boiling event). This low rate of exhumation coincides with the 50 m/My rate defined by Maksaev and Zentilli (1999) for the uplift of the West fissure tectonic block since about 30 ma.

The low rates of exhumation, related to an arid environment, contribute to the generation and preservation of supergene-enriched zones in porphyry copper deposits. In fact, the ore mineralization at the Zaldívar deposit reproduces the effects of primary and secondary processes. From the surface and down to about 300 m depth, the primary sulfide ore has been leached and oxidized forming a blanket of a secondary enriched ore body (Fig. 11-3).

Figure 11-2. Next page. Schematic model for the metallogenetic evolution of the Zaldívar porphyry copper deposit. **A)** At a depth of about 6 km a dense saline metal-rich fluid phase start to exsolve from the crystallizing magma (MS-type inclusions). The Cu is sequestered from the magma by early exsolved chlorine solutions as shown by melt and MS-type inclusions. **B)** The Llamo porphyry is emplaced at shallow depth (2 km). Upon cooling intensive degassing occurs in the form of brines, water vapor and volatiles. Within a plastic rock regime, the exsolved brines and volatiles are pooled at the cupula of the cooling intrusive. **C)** Major boiling episodes occur at ca. 400°C and about 1.5 km depth, most probably related to a sudden pressure decrease during the transition from a lithostatic to a hydrostatic regime caused by intermittent breaches of the self-sealed brittle-plastic transition. This event initiates an inner convective hydrothermal cell dominated by magmatic water exsolved during the late stages of magma crystallization. **D)** The intense hydrothermal activity produces strong hydrothermal alteration in all rock units outcropping in the mine. Potassic alteration prevails in the Llamo porphyry, phyllic in the Zaldívar porphyry, and propylitic in the andesites. **E)** Supergene argillic alteration related to the secondary enrichment process, overprints the phyllic and potassic alterations.

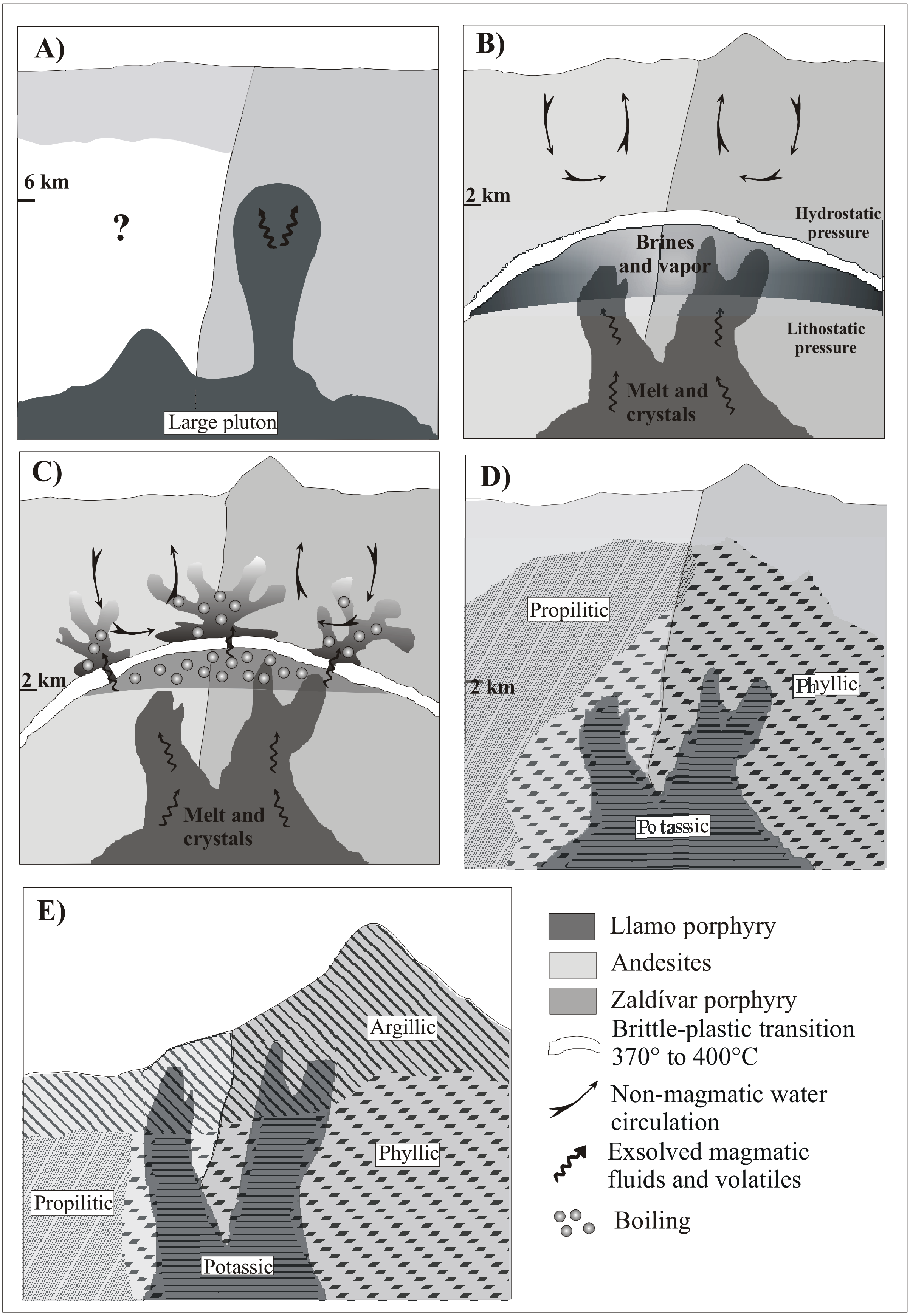
A)
6 km
?
Large pluton
B)
2 km
Hydrostatic pressure
Brines and vapor
Lithostatic pressure
Melt and crystals
C)
2 km
Melt and crystals
D)
Propilitic
2 km
Phyllic
Potassic
E)
Argillic
Phyllic
Propilitic
Potassic
Llamo porphyry
Andesites
Zaldívar porphyry
Brittle-plastic transition 370° to 400°C
Non-magmatic water circulation
Exsolved magmatic fluids and volatiles
Boiling

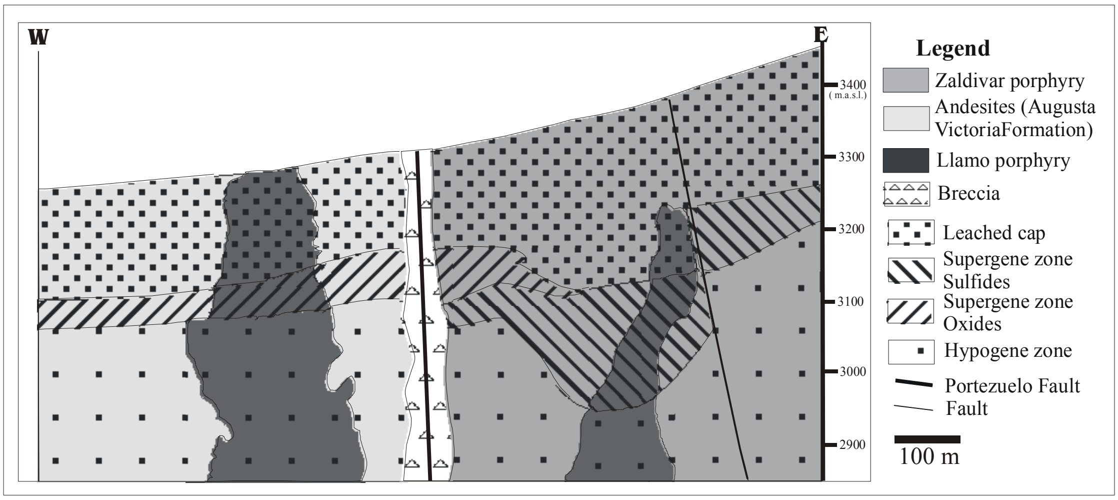

Figure 11-3. Profile showing the present day distribution of rocks units outcropping in the Zaldívar mine, and the distribution of hypogene and supergene mineralization.

11.3 The source of metals

A major sub-crustal source, associated with subduction-related processes, has been proposed for the origin of metals and volatiles during the formation of PCDs. These components are largely independent from the thickness and composition of the continental crust, and they are also incompatible with an origin by partial melting or wholesale assimilation of continental crust (e.g., Sillitoe, 1972). The continental crust will thus have minor importance as a source of copper, it will only be important as the site for magma differentiation (Sillitoe, 1986, and ref. therein).

The amount of metals potentially available for mineralization in a porphyry copper system depend on the contribution of the subducted oceanic crust and the pelagic sediment, as well as the mantle wedge above the subducted slab. Metals and volatiles incorporated by dehydration of the subducted slab and partial melting of the mantle wedge ascend to the upper crust as components of calc-alkaline magmas, these magmas become water-saturated as they reach upper levels in the crust, a process that ultimately will concentrate metals in chloride-rich fluid phases associated with the roof-zones of the parental intrusives.

11.4 Why is the Llamo porphyry Cu-rich?

Hypogene copper mineralization in the Zaldívar deposit is genetically related to the latest Oligocene Llamo porphyry. The intrusive presents several distinguishing features when compared to the other rock units outcropping in the mine (the Zaldívar porphyry and the Andesites), namely a) more acidic composition, b) extremely high magmatic temperatures, c) abundance of brines, and finally d) high copper content. These different points will be discussed in some detail:

a) Rhyolitic composition

As described in chapter 10, section 10.4 and in the previous section 11.1.3, the original magma from which the Llamo porphyry originated was formed in the asthenospheric mantle wedge, triggered by the dehydration and partial melting of the subducted slab. The mantle-derived magma was then strongly modified by large-scale interactions with the continental crust in magma reservoirs in the mantle-crust transition.

The magma evolution described above coincides with deformation peaks associated with a tectonic setting in which compression leads to crustal shortening and thickening, over a shallow subducted slab. Under compressional conditions magmas intruded into a thickened crust could not easily migrate upwards and therefore were trapped and evolved at depth leading to high intrusive/extrusive ratios (Kay et al., 1999).

Entrapment of the modified mantle-derived magma in the middle upper crust resulted in the production of highly differentiated magmas caused by extensive magmatic differentiation and magma-crust interaction in an intermediate magma chamber due to a long residence time in the crust (Davidson et al., 1991).

b) Anomalously high magmatic temperature

During the time of emplacement in the upper crust, the temperature of the Llamo intrusive was up to 1000°C, as estimated from melt and MS-type inclusions microthermometry. These values are higher than the solidus temperature commonly accepted for granitic magmas (about 850° - 950°C, Tuttle and Bowen, 1958), and they are more in line with magmatic differentiation than with crustal assimilation. Anatexis (crustal rock melting) is a strongly endothermic process, which will buffer magmatic temperatures at values commonly encountered during crustal anatexis, about 750°C (Spear, 1993).

The West Fissure represents a favorable geodynamic environment that served as a pathway for a rapid ascent of deep hot magmas towards the surface, favoring the generation of the extremely high homogenization temperatures measured in melt inclusions (Fig. 11-1-E).

Chloride contents would also have an important effect on the magma displacement through the crust as they will decrease magma viscosity (Kirstein et al., 2001), favoring a fast ascent of melt along the thickened crust.

c) High brine content

During a shallow subduction regime, fluids and volatiles produced by dehydration of the subducted slab are concentrated in the cooling mantle above the subducted slab and constitute a major source of fluids (namely water and chlorides) for future mineralization (Kay et al., 1999). Subsequent melting of the hydrated mantle promotes the generation of fluid-rich magmas intruding into a thickened crust under a compressional regime.

A fast thickening of the crust causes the fluids, expelled from the magma and intruded into the lower crust, to be accumulated in the high-conductivity zone (HCZ) indicated in figure 10-5-A. This zone (Fig. 11-1-D and E) has been related to the occurrence of interstitial brines and or melt (per. com. ANCORP'96, GFZ, Postdam, Germany) and an important source for the brines also typical in the Llamo porphyry.

The high brine contents of these magmas facilitates metal sequestering from the crystallizing magma and subsequent transport during the hydrothermal regime.

d) Copper enrichment

Metals in the Llamo porphyry, mainly copper, were originally derived from the mantle and incorporated in the oceanic crust created at the ocean ridges. The oceanic lithosphere moves laterally towards the ocean trenches and finally is subducted in the margins of the oceanic basins (Sillitoe, 1972). The copper content was further enriched by fluids and pelagic sediments incorporated in the subducted slab (Fig. 11-1-E).

The subducted slab, consisting of water-saturated oceanic crust plus sediments, contained metals and volatiles that were expelled by dehydration and partial melting as it sank into the mantle (e.g., Sillitoe, 1972; Oyarzun and Frutos, 1980). The flux of volatiles generated by dehydration of the oceanic crust subsequently induced magma production by partial melting of the mantle wedge above the subducted slab. The melting of this mantle portion also constituted a source of metals (Sillitoe, 1972).

Normal calc-alkaline magmas contain sufficient chlorine and copper to produce an economic mineralization if copper behaves as an incompatible element and is not incorporated in crystalline phases, or if water saturation occurs early during magma crystallization (Cline, 1995). Furthermore, Cline and Bodnar (1991) have demonstrated that this type of melt, containing approximately 4 wt. % of water and crystallizing at about 1 kilobar pressure (approximate conditions for the formation of a porphyry copper deposit), require less than 15 cubic kilometers of magma to produce 250 millions tons of 0.75 wt % Cu.

In consequence the development of the copper mineralization associated with the Llamo porphyry is mainly a result of processes that operated during cooling and crystallization of hydrous felsic magmas in a shallow crustal environment.

11.5 Concluding remarks

The Zaldívar mine is a good example of a porphyry copper deposit, and turns out to be an excellent site to study the processes involved in the magmatic-hydrothermal transition in a typical Cu-porphyry system. Some of the positive aspects of this deposit are the small size, rather simple geology and good exposure of the mineralizing intrusive. Another key factor is that the mineralizing intrusive (the Llamo porphyry) it is only affected by the high temperature potassic hydrothermal alteration overprinted by supergene argillic alteration. This fact allows the preservation of magmatic remnants.

The present investigation shows that quartz phenocrysts can preserve very well the magmatic and hydrothermal remnants that would reflect a wide range of melt/fluid/mineral interaction phenomena. The careful study of these phenocrysts and their hosted features, can shed light on the evolution of a PCD and most important of all, can potentially constrain the magmatic-hydrothermal transition. As a consequence, this line of research has shown to be a powerful tool for investigating the metallogenesis of PCDs, therefore it is suggested that a similar approach should be applied to other PCDs.

Furthermore, the application of high temperature microthermometry to the study of melt and MS-type inclusions in porphyry copper systems, has shown to be a most useful technique that should be more widely applied to the study of orthomagmatic ore deposits.

The extremely high homogenization temperatures of melt and MS-type inclusions, above the commonly accepted solidus temperatures for felsic magmas, remains a problem that requires to be investigated by further studies.

A good continuation of the present study would also be the study of apatite fission tracks. This result, combined with the thermochronological data already available, could better constrain the geochronology of cooling and uplift of the Zaldívar deposit.

APPENDIX 1

Tables of petrographic description

Abreviations used in the following tables

PXX : phenocrysts
GMS : groundmass
K-feld : potassium feldspar
Plag : plagioclase
Qz : quartz
Bio : biotite
Ru : rutile
Zr : zircon
Ru : rutile
Ap : apatite
Alt : alteration type
Al : albite
Ser : sericite
Ag : clay minerals
Chl : chlorite
Ep : epidote
Pot : potassic alteration
Phy : phyllic alteration
Arg : argillic alteration
Pro : propylitic alteration
Sil : silicification
P:A : porcentage of primary and alteration minerals
? : mineral probably present
10? : content unknown
S-35 (141) : Sample name (meters below the surface). For location see figure 3-1.

Table 4-1. Petrographic description of samples from the Zaldívar Porphyry unit.

		Prymary minerals								Alteration minerals						
Sample		%	Size (mm)	K-feld	Plag	Qz	Bio	Minor	P : A	K-feld	Bio	Ser	Qz	Al?	Ar	Alt
S-35 (141)	PXX	50	< 5	30	60	10	<1?	Ru, Zr,	40:60			30	?		60	Phy
	GMS	50		20	70	?						20	?		10	
S-36 (276)	PXX	50	< 2	30	60	10		Zr, Ap, Ru	60:40			50	?		40	Phy
	GMS	50		-	-	-						10	40	20	30	
S-50 (243)	PXX	40	< 3	10?	40?	50		Ru, Zr,	30:70			40	?		60	Phy
	GMS	60		-	-	-						20	70		10	
S-38 (410)	PXX	30	< 4	10?	40?	50		Ru, Zr, Ap	20:80			20	10	40	30	Phy (Sil)
	GMS	70		-	-	-						10	70			
S-34 (341)	PXX	30	< 4	10?	40?	50		Zr, Ap	20:80			10	10	50	30	Phy (Sil)
	GMS	70		-	-	-						20	70		10	
S-43 (420)	PXX	30	< 3	10	50	40		Zr, Ap	30:70			30	10	40	30	Phy (Sil)
	GMS	70		-	-	-						30	60		10	
S-02 (O)	PXX	20	< 3	10?	40?	50		Zr, Ap	20:80			10	10	50	30	Phy (Sil)
	GMS	80										30	60		10	
S-33 (361)	PXX	30	< 2	10?	50?	30		Ru, Zr, Ap	10:90			50	10	30	10	Phy (Sil)
	GMS	70		-	-	-						30	60		10	
S-01 (0)	PXX	30	<5	?	?	50?		Zr, Ap, Ru	10:90			80	20			Phy
	GMS	70		-	-	-						50	50			
S-34 (202)	PXX	25	< 2	?	?	40?		Zr, Ap	10:90			80	20			Phy
	GMS	75		-	-	-						40	50		10	
S-35 (26)	PXX	25	< 2	?	?	40?		Zr, Ap, Ru	10:90			60	20		20	Phy
	GMS	75		-	-	-						40	40		20	
S-36 (180)	PXX	30	< 3	?	?	40?		Zr, Ap, Ru	10:90			80	10		10	Phy
	GMS	70		-	-	-						50	40		10	
S-38 (139)	PXX	40	< 2.5	?	?	40?		Zr, Ap	10:90			70	10		20	Phy
	GMS	60		-	-	-						40	50		10	
S-39 (260)	PXX	30	< 3	?	?	40?		Zr, Ap	10:90			80	10	10		Phy
	GMS	70		-	-	-						40	60			
S-37 (230)	PXX	30	< 2	?	?	40?		Ru, Zr, Ap	10:90			90	10			Phy
	GMS	70		-	-	-						60	40			
S-43 (10)	PXX	20	< 3	?	?	40?		Zr, Ap,	10:90			90	10			Phy
	GMS	80		-	-	-						50	40		10	
S-50 (155)	PXX	50	< 4	?	?	20?		Ru, Zr, Ap	10:90			80	10		10	Phy
	GMS	50		-	-	-						60	40			
S-50 (316)	PXX	40	< 3	?	?	20?		Zr, Ap, Ru	10:90			70	10		20	Phy
	GMS	60		-	-	-						40	50		20	
S-45 (200)	PXX	20	< 4	?	?	20?		Zr, Ap, Ru	10:90			90	10			Phy
	GMS	80		-	-	-						60	40			
S-39 (135)	PXX	40	< 2	?	?	20?		Zr, Ru	10:90			70	10		20	Phy
	GMS	60		-	-	-						60	20		20	
S-39 (365)	PXX	60	< 3	?	?	-		Zr	5:95			40	60		10	Phy
	GMS	40														
S-45 (283)	PXX	30	< 2	?	?	20?		Zr, Ru	10:90			80	20			Phy
	GMS	70		-	-	-						70	30			

Table 4-2. Petrographic description of samples from the Andesite unit.

		Primary minerals								Alteration minerlas							
Sample		%	Size (mm)	K-feld	Plag	Qz	Bio	Minor	P : A	Feld	Ser	Qz	Chl	Ar	Al	Ep	Alt
S-46 (235)	PXX	40	< 2	10?	90			Ap, Zr	60:40		10	5	30	40	10	5	Pro
	GMS	60		10?	90							15	50	30		5	
S-48 (118)	PXX	40	< 2	-	-	-	-	Zr	0:100		20	40	30				Phy
	GMS	60		-	-	-	-										
EC-Z1 (432)	PXX	30	< 1		80?			Zr	0:100		30	50	10	10			Pro
	GMS	70										40	50	10		10	(Pro)
S-48 (289)	PXX	30	<3						0:100		20	40	10	20	10		Phy
	GMS	70									10	50	40				(Pro)
S-31 (260)	PXX	60	< 2		60?		20		5:95		10	60	30	10			Phy
	GMS	40															(Sili)

Table 4-3. Petrographic description of samples from the Llamo porphyry unit.

		Primary minerals								Primary minerals							
Sample		%	Size (mm)	K-feld	Plag	Qz	Bio	Minor	P : A	Feld	Ser	Qz	Chl	Ar	Al	Ep	Alt
S-42 (225)	PXX	60	< 6	30	60	< 5	10	Ap, Ru, Zr,	80:20		20		10	10	50		Pot
	GMS	40		20	70		10				30	20	30	20			
S-48 (10)	PXX	60	< 5	20?	60	< 5?	10	Zr, Ap,	60:40		30		20	10	30	<5	Pot
	GMS	40		20	70		10				30	20	20		20	< 5	
S-34 (324)	PXX	40	< 6	20?	70	5?	10?	Zr, Ap	40:60		40	10	20	30	10		Pot (Arg)
	GMS	60		?	60?	20	10?				40	10	20	10	20		
S-05 (0)	PXX	60	< 2	20?	70	5	5	Zr, Ap	40:60		40	10?	30		20	< 5	Pot (Arg)
	GMS	40		20?	60	20					10	50	20		10	<5	
S-26a (0)	PXX	60	< 2		60?	5	5?	Ap, Zr	30:70		20		10	20	40	10	Pot (Arg)
	GMS	40		20?	70?	5					20		10	20	?	20	
S-52 (280)	PXX	50	< 5	20	70	5	5?	Ap, Zr	30:70				20	10	60	20	Pot
	GMS	50		-	20	-						30	20	40		10	
S-33 (211)	PXX	60	< 4	20?	60	5	10	Zr, Ap	20:80		30		10	50		5	Pot (Arg)
	GMS	40									10	70	5	10		5	
S-30 (0)	PXX	60	< 5	?	?	10	10	Zr, Ap	10:90		30			60	10		Pot (Arg)
	GMS	40									10	80		10			
S-47 (168)	PXX	40	< 4	20?	60	5		Zr	10:90		30		10	40	20		Pot (Arg)
	GMS	60		20?	70?	10					10	10	10	70			
S-41 (160)	PXX	60	< 5	20?	60?	5	5	Zr	10:90		20		20	60			Pot (Arg)
	GMS	40								5	10	50	5	30			
S-40 (115)	PXX	60	< 5	20?	70?	5	5	Zr	10:90		10		10	80			Pot (Arg)
	GMS	40									10	70		20			
S-41 (53)	PXX	60	< 5	20?	70?	5	5	Zr, Ap	10:90		10	10	5	70			Pot (Arg)
	GMS	40									20	60		20			
S-47 (168)	PXX	40	< 5	20?	70	5?	< 5	Zr	70:30		10		20	40	30		Pot (Arg)
	GMS	60		20?	60?	10					30	10	20		40		
S-38 (110)	PXX	60	< 5	20?	70?	<5	<5?	Zr	20:80		40		10	50			Pot (Arg
	GMS	40			60?						30	50	10	10			
S-43 (198)	PXX	60	< 3	?	?	5	?	Zr	10:90		60			30			Phy (Arg)
	GMS	40									10	40		50			
S-43 (250)	PXX	40	< 6	?	60?	< 5	?	Zr, Ap	30:70		40		10	50			Arg (Phy)
	GMS	60			50?						20	20		60			
S-35 (280)	PXX	40	< 4	?	?	< 5		Zr	20:80		30			70			Arg (Phy)
	GMS	60									20	70		10			
S-35 (341)	PXX	40	< 4	?	?	10		Zr, Ap	20:80		30		10	60			Arg (Phy)
	GMS	60		-	-	-					10	50	10	30			
S-12 (0)	PXX	60	< 4	?	?	5	?	Ap, Zr	20:80		60		10	20	10		Phy
	GMS	40		?	10	5	?				10	70	10	10			
S-37 (27)	PXX	40	< 5	?	?	5		Zr	5:95		80			10			Phy
	GMS	60		-	-	-					60	30		10			
S-45 (340)	PXX	40	< 3	?	?	5		Zr, Ru, Ap	5:95		90			10			Phy
	GMS	60		-	-	-					60	40					
S-34 (281)	PXX	40	< 5	-	-	5	-	Zr	5:95		70			30			Phy (Arg)
	GMS	60		-	-	-	-				50	40		10			
S-37 (375)	PXX	60	< 4	-	-	5	-	Ap, Ru, Zr	5:95		70						Phy
	GMS	40		-	-	-	-				40	60					
S-42 (110)	PXX	?	?	?	?	5		Ap, Ru, Zr	5:95			20		80			Arg
	GMS	?		-	-							40		60			
S-38 (20)	PXX	30	< 2		100				40:60		20	20		60			Arg (Phy)
	GMS	70										50	40	10			
S-31 (220)	PXX	50	< 2	30?	60?		10?		0:100		20		20	30	30		Pot (Arg)
	GMS	50									10	50	10	30			

APPENDIX 2

Electron microprobe analysis on mineral inclusions

Table 4.4 EPMA analysis of plagioclase grains hosted in quartz phenocrysts from Llamo porphyry unit. Concentration is in wt. %.

Sample	SiO_2	TiO_2	Al_2O_3	FeO	MnO	MgO	CuO	CaO	Sro	Na_2O	K_2O	P_2O_5	SO_3	F	Cl	Total
S-30	59.64	0.00	24.34	0.02	0.01	0.00	0.03	7.99		7.02	0.27	0.00	0.01	0.00	0.05	99.36
S-30	65.68	0.04	20.83	0.05	0.00	0.00	0.00	1.93		10.50	0.23	0.00	0.00	0.01	0.00	99.29
S-37 (27)	57.56	0.03	25.87	0.24	0.00	0.01	0.00	8.67	0.23	6.43	0.30	0.00	0.00	0.04	0.00	99.41
S-37 (53)	62.82	0.00	21.56	0.09	0.00	0.01	0.03	3.77	0.11	8.16	0.14	0.03	0.00	0.02	0.02	96.77
S-30	65.62	0.00	22.36	0.12	0.01	0.00	0.00	4.98	0.11	6.37	0.36	0.00	0.02	0.00	0.00	99.95
S-37 (53)	62.69	0.00	23.82	0.18	0.01	0.00	0.02	5.61	0.08	7.36	0.14	0.00	0.01	0.05	0.00	99.97
S-11	66.70	0.01	20.67	0.00	0.00	0.00	0.00	1.88	0.10	9.45	0.13	0.00	0.01	0.00	0.00	98.96

Table 4.5 EPMA analysis of K-feldspar grains hosted in quartz phenocrysts from Llamo porphyry unit. Concentration is in wt. %.

Sample	SiO_2	TiO_2	Al_2O_3	FeO	MnO	MgO	CuO	CaO	Sro	Na_2O	K_2O	P_2O_5	SO_3	F	Cl	Total
S-30	63.34	0.02	18.64	0.04	0.01	0.00	0.00	0.04		1.18	14.87	0.00	0.00	0.04	0.08	98.28
S-37 (27)	63.00	0.06	16.97	2.20	0.04	2.70	0.00	2.45		1.12	12.25	1.12	0.00	0.02	0.01	98.50
S-37 (27)	65.50	0.03	18.38	0.00	0.00	0.00	0.02	0.22		1.12	12.25	1.12	0.00	0.00	0.02	98.67
S-37 (53)	62.79	0.03	18.01	0.14	0.00	0.00	0.00	0.02	0.13	1.66	13.96	0.01	0.01	0.00	0.01	96.75
S-30	64.86	0.03	18.98	0.07	0.00	0.00	0.01	0.12	0.13	2.25	12.48	0.00	0.00	0.00	0.00	98.92
S-30	68.81	0.03	15.17	0.04	0.00	0.00	0.00	0.00	0.04	1.86	10.96	0.32	0.00	0.00	0.07	97.26
S-37 (27)	67.68	0.05	17.77	0.06	0.00	0.01	1.51	0.13	0.14	1.77	10.44	0.03	0.01	0.00	0.06	99.67

Table 4.6 EPMA analysis of fresh biotite grains hosted in quartz phenocrysts from Llamo porphyry unit. Concentration is in wt. %.

Sample	SiO_2	TiO_2	Al_2O_3	FeO	MnO	MgO	CuO	CaO	Sro	Na_2O	K_2O	P_2O_5	SO_3	F	Cl	Total
S-30	39.14	2.44	14.61	13.97	0.21	16.36	0.01	0.00		0.13	9.75	0.00	0.02	1.22	0.29	98.73
S-30	37.54	3.61	14.63	12.84	0.21	16.29	0.00	0.00		0.23	8.94	0.00	0.04	0.56	0.10	95.24
S-41 (53)	39.39	1.25	13.76	12.82	0.36	18.70	0.01	0.02	0.02	0.19	8.80	0.00	0.02	0.33	0.23	96.07

APPENDIX 3

Whole-rock major elements from Llamo and Zaldivar porphyries

Sample	SiO_2	TiO_2	Al_2O_3	FeO	MnO	MgO	CaO	Na_2O	K_2O	P_2O_5	Total
Lla-1	69.74	0.47	17.67	4.19	0.06	1.16	0.65	2.29	3.61	0.15	99.99
Lla-2	71.15	0.42	17.87	3.90	0.05	0.90	0.33	1.19	4.06	0.12	99.99
Lla-3	70.36	0.47	17.25	4.45		0.82	0.49	1.54	4.46	0.16	100.00
Lla-4	70.98	0.45	16.94	4.33		0.74	0.40	1.38	4.66	0.12	100.00
Lla-5	69.49	0.51	17.61	4.63		0.94	0.62	1.79	4.18	0.23	100.00

Sample	SiO_2	TiO_2	Al_2O_3	FeO	MnO	MgO	CaO	Na_2O	K_2O	P_2O_5	Total
Zal-1	73.35	0.39	16.98	2.83	0.02	0.35	0.23	1.85	3.79	0.18	99.97
Zal-2	77.25	0.17	15.73	1.21	0.03	0.20	0.09	0.88	4.35	0.08	99.99
Zal-3	76.89	0.26	15.00	2.97	0.04	0.38	0.08	0.57	3.73	0.08	100.00
Zal-4	77.67	0.15	15.28	1.53	0.04	0.19	0.08	0.99	4.02	0.04	99.99
Zal-5	78.36	0.20	13.70	2.79		0.27	0.09	0.33	4.16	0.08	99.98
Zal-6	77.57	0.19	14.58	2.80		0.26	0.09	0.35	4.16	0.01	100.01
Zal-7	76.86	0.30	15.03	2.81		0.37	0.09	0.19	4.23	0.12	100.00

APPENDIX 4

Electron microprobe analysis on quenched glasses

Table 6-2. Electron microprobe major element composition of quenched glass from Llamo porphyry

Sample	Inclusion	SiO_2	TiO_2	Al_2O_3	FeO	MnO	MgO	CuO	CaO	SrO	Na_2O	K_2O	P_2O_5	SO_3	F	Cl	Total
S-37 (27)	c39-4	72.72	0.10	15.30	0.46	0.01	0.06	0.10	2.48	0.10	2.73	5.76	0.08	0.01	0.00	0.06	99.99
S-37 (27)	c32-1d	70.26	0.05	18.95	0.56	0.09	0.09	0.05	1.92	0.04	3.07	4.68	0.05	0.00	0.10	0.11	100.00
S-37 (27)	c32-6d	70.81	0.05	18.46	0.52	0.08	0.08	0.04	1.72	0.03	3.47	4.54	0.00	0.00	0.11	0.10	100.00
S-37 (27)	c32-1	77.31	0.07	14.58	0.46	0.07	0.06	0.02	0.83	0.00	1.35	5.17	0.00	0.00	0.00	0.08	99.99
S-37 (27)	c43-18e	73.95	0.04	16.45	0.21	0.10	0.00	1.37	0.89	0.13	0.71	5.68	0.00	0.00	0.00	0.47	100.00
S-37 (27)	c21b-3	74.19	0.02	16.39	0.06	0.00	0.00	0.01	2.26	0.04	3.02	3.95	0.00	0.01	0.00	0.07	100.00
S-37 (27)	c44-10b	76.99	0.06	14.66	0.36	0.02	0.05	0.03	1.36	0.09	2.38	3.79	0.00	0.01	0.07	0.11	100.00
S-37 (27)	c24-7	76.66	0.10	14.31	0.44	0.03	0.06	0.08	0.88	0.05	3.41	3.75	0.01	0.00	0.12	0.09	100.00
S-37 (27)	c32-1	75.28	0.04	15.10	0.46	0.04	0.07	0.00	1.10	0.03	2.31	5.46	0.02	0.00	0.02	0.06	100.00
S-37 (27)	c43-18d	74.81	0.07	16.34	0.26	0.07	0.01	0.96	1.03	0.15	1.50	4.53	0.01	0.00	0.00	0.25	100.00
S-37 (27)	c32-2	74.63	0.08	14.79	0.55	0.03	0.07	0.05	1.14	0.05	2.96	5.48	0.02	0.04	0.02	0.09	100.00
S-37 (27)	c32-2b	69.76	0.06	17.65	0.59	0.08	0.11	0.06	2.20	0.07	3.80	5.32	0.03	0.02	0.11	0.12	100.00
S-37 (27)	c24-7b	77.67	0.06	14.74	0.40	0.04	0.06	0.06	0.78	0.06	2.45	3.56	0.00	0.00	0.07	0.07	100.00
S-37 (27)	c45-5b	74.97	0.00	16.43	0.03	0.01	0.00	0.04	2.82	0.09	2.00	3.51	0.02	0.04	0.00	0.03	100.00
S-37 (27)	c21b-1	72.84	0.02	16.75	0.02	0.00	0.00	0.00	1.46	0.02	2.95	5.56	0.21	0.09	0.04	0.04	100.00
S-37 (27)	c43-7b	72.15	0.06	16.62	0.20	0.07	0.02	1.42	0.92	0.14	2.99	5.16	0.01	0.00	0.00	0.23	100.00
S-37 (27)	c43-6	75.95	0.03	13.09	0.15	0.07	0.00	1.05	0.34	0.10	1.71	7.28	0.01	0.02	0.03	0.17	100.00
S-37 (27)	c43-19d	75.30	0.04	14.05	0.17	0.08	0.01	1.22	0.58	0.09	1.45	6.70	0.00	0.00	0.10	0.20	100.00
S-37 (27)	c43-7	72.59	0.03	15.03	0.22	0.07	0.02	1.40	0.84	0.12	1.91	7.50	0.00	0.02	0.02	0.24	100.00
S-37 (27)	c43-6b	73.65	0.03	14.93	0.16	0.08	0.00	1.22	0.40	0.11	1.94	7.23	0.00	0.00	0.00	0.25	100.00
S-41 (53)	c77-2	77.12	0.03	14.60	0.10	0.02	0.01	0.05	0.89	0.05	3.12	3.76	0.00	0.01	0.03	0.22	100.00
S-41 (53)	c83-4	76.99	0.00	13.60	0.28	0.08	0.01	0.00	2.18	0.02	3.11	3.54	0.00	0.01	0.00	0.19	100.00
S-41 (53)	c81-3	76.63	0.12	14.85	0.60	0.00	0.10	0.10	0.71	0.08	3.10	3.55	0.00	0.01	0.01	0.13	100.00
S-41 (53)	c78-4	73.49	0.04	17.15	0.27	0.12	0.02	0.00	0.07	0.01	3.43	4.89	0.14	0.02	0.00	0.36	100.00
S-41 (53)	c84-1	75.07	0.40	14.40	1.47	0.07	0.23	0.04	2.43	0.09	2.33	3.17	0.00	0.01	0.07	0.23	100.00
S-41 (53)	c76a-4	73.66	0.00	15.59	0.13	0.01	0.08	0.00	1.40	0.05	4.00	4.96	0.00	0.02	0.00	0.10	100.00
S-41 (53)	c81-1	76.66	0.10	14.68	0.54	0.00	0.09	0.10	0.98	0.07	3.23	3.30	0.00	0.02	0.05	0.18	100.00
S-41 (53)	c84-3	73.97	0.22	16.99	0.64	0.05	0.12	0.01	1.22	0.02	2.97	3.49	0.00	0.01	0.05	0.24	100.00
S-41 (53)	c81-2	73.36	0.01	16.65	0.05	0.00	0.00	0.07	1.64	0.08	3.10	4.96	0.00	0.01	0.00	0.06	100.00
S-30	15c	72.73	0.17	16.95	2.18	0.01	0.24	0.15	0.67	0.00	0.95	5.63	0.00	0.07	0.09	0.16	100.00
S-30	c95-1	73.21	0.20	18.31	0.99	0.00	0.10	0.00	0.07	0.00	2.37	4.61	0.00	0.01	0.00	0.13	100.00
S-30	c96-1	77.59	0.29	15.39	0.45	0.02	0.22	0.02	0.01	0.01	2.20	3.54	0.00	0.00	0.04	0.23	100.00
S-30	c99-2	76.90	0.31	17.70	1.01	0.01	0.33	0.00	0.04	0.06	2.69	4.71	0.00	0.03	0.00	0.18	103.97
S-30	c3-9	74.77	0.16	15.77	1.61	0.08	0.41	0.01	0.28	0.02	1.53	4.92	0.08	0.00	0.09	0.27	100.00
S-30	c100-1	77.08	0.03	14.69	0.29	0.05	0.02	0.05	2.01	0.11	0.56	4.60	0.00	0.01	0.00	0.50	100.00
S-11	c106-1	72.19	0.01	19.69	0.14	0.00	0.00	0.00	0.27	0.03	2.91	4.68	0.00	0.02	0.05	0.01	100.00
S-11	c110-1	75.65	0.06	15.89	0.43	0.08	0.19	0.05	0.75	0.03	2.64	3.78	0.14	0.00	0.05	0.24	100.00
S-35 (26)	c-122b	71.19	0.09	16.83	0.15	0.03	0.72	0.04	2.13	0.04	3.76	4.71	0.00	0.11	0.17	0.03	100.00
S-45 (238)	c15-4	78.98	0.09	13.95	0.79	0.04	0.16	0.19	0.04	0.02	1.36	3.85	0.00	0.02	0.09	0.42	100.00

Table 6-3. Electron microprobe major element composition of quenched glass from Zaldivar porphyry

Sample	Inclusion	SiO_2	TiO_2	Al_2O_3	FeO	MnO	MgO	CuO	CaO	SrO	Na_2O	K_2O	P_2O_5	SO_3	F	Cl	Total
S-43 (420)	c74-3	71.00	0.02	19.65	0.77	0.04	0.05	0.00	0.40	0.02	1.99	6.03	0.02	0.00	0.00	0.00	100.00
S-43 (420)	c72-3	72.67	0.03	18.96	0.22	0.04	0.17	0.00	0.00	0.02	2.87	4.79	0.00	0.00	0.02	0.20	100.00
S-43 (420)	c61-9	71.94	0.02	18.97	0.38	0.09	0.03	0.02	0.20	0.01	2.04	6.16	0.13	0.01	0.00	0.00	100.00
S-43 (420)	c74-4	75.20	0.03	17.36	0.29	0.09	0.17	0.01	0.23	0.03	2.42	2.97	0.10	0.57	0.04	0.50	100.00
S-43 (420)	c65-1b	74.17	0.02	17.22	0.75	0.03	0.03	0.00	0.14	0.01	4.66	2.57	0.11	0.04	0.05	0.22	100.00
S-43 (420)	c67-1b	74.34	0.11	16.55	0.34	0.04	0.23	0.00	0.15	0.03	3.58	4.36	0.15	0.00	0.04	0.09	100.00
S-43 (420)	c67-1c	75.16	0.48	12.69	2.02	0.01	1.10	0.02	0.28	0.00	1.85	5.69	0.00	0.04	0.10	0.55	100.00
S-43 (420)	c74-11	75.97	0.05	13.18	0.59	0.00	0.11	0.00	0.00	0.01	3.15	6.68	0.03	0.01	0.04	0.18	100.00
S-43 (420)	c63-5	76.12	0.02	13.57	0.60	0.01	0.02	0.00	0.08	0.02	2.62	6.54	0.20	0.01	0.01	0.20	100.00
S-43 (420)	c65-1	76.09	0.22	15.33	0.73	0.03	0.03	0.03	0.12	0.03	2.42	4.64	0.06	0.00	0.02	0.25	100.00
S-43 (420)	c61-7	76.92	0.00	11.91	1.53	0.08	0.10	0.00	1.24	0.02	1.81	5.96	0.03	0.01	0.00	0.38	100.00
S-43 (420)	c61-2a	77.21	0.02	12.66	0.43	0.00	0.04	0.02	0.04	0.00	3.43	5.98	0.05	0.02	0.00	0.10	100.00
S-43 (420)	c61-2b	77.86	0.00	12.57	0.41	0.02	0.05	0.01	0.04	0.04	2.69	6.11	0.05	0.00	0.05	0.10	100.00
S-43 (420)	c72-4	77.99	0.17	14.18	0.86	0.02	0.37	0.02	0.03	0.03	2.51	3.43	0.04	0.00	0.06	0.30	100.00
S-43 (420)	c72-2	77.70	0.08	13.84	1.10	0.01	1.00	0.00	0.07	0.02	1.96	3.80	0.08	0.01	0.05	0.28	100.00
S-43 (420)	c61-1	78.65	0.00	14.33	0.40	0.01	0.02	0.02	0.03	0.00	1.79	4.61	0.03	0.01	0.00	0.09	100.00
S-43 (420)	c67-2	77.24	0.02	14.66	0.19	0.00	0.10	0.00	0.02	0.03	1.24	6.19	0.07	0.00	0.07	0.17	100.00

APPENDIX 5

Microthermometry data for MS-type inclusions

Table 7-1. Representative microthermometric data for MS-type inclusions from the Llamo porphyry.

Grain	Inclusion	Solid 1	Sylvite	Halite	Th
C19	3c	145	252	519	993
C23	1	112	250	478	1010
C27	1	130	211	389	1000
C28	1	130	300	550	1032
C29	1	148	329	450	976
C30	2	140	245	575	990
C33	1	110	369	557	913
C33	2	95	372	532	1010
C42	1	150	250	466	870
C42	2	152	247	472	840
C42	5	149	345	448	
C42	6	146	326	440	
C42	7	129	258	414	744
C42	8	125	230	380	
C42	10	130	230	403	873
C42	11	132	240	380	860
G78	1		215	570	1030
C-89	4		260	500	890
C-98	1		300	490	830
C-89	2		240	470	800
C-89	3		260	470	880
C37	2	130		510	880
C31	1	121		521	1030
C26	1	80		560	1000
G78	2	120		575	1000
C-89	1	180		470	780
C21	10	145		409	1064
C23	18	150		468	1082
G2	2				920
G2	4				1000
G2	5				770
C32	1				890
C32	2		230		870
C32	3				860
C32	4				953
C42	12				988
C23	19	145		475	1095
G27	1	112		410	845
G47	1	113		400	733
C29	2	146		435	928
G12	1	120		430	830
G1	1				919
C127	5	160	283	400	880
C127	6	130	250		840
C127	7	156	250	315	940
C127	8	159	255	300	940
C127	9	155	250	330	940
C128	2	162	255	312	1050
C128	3	166	248	280	1040
C128	7	146	260	363	990
C125	2	157	240	429	1010
C126	1	158	250	412	992
C126	2	150	250	400	830
C126	3	140	250	397	940

APPENDIX 6

Metal abundance in MS-type inclusions

Table 7-2. Relative abundance of elements in MS-type fluid inclusions as defined by PIXE microanalyses. -: scarce, *: abundant, # most abundant

	C23	C21-ca	C27-1	C27-2b	C34-a	C40-1	C68-a	C40-6	C29-1	MI2-6a	C40-7	C21-aa	C19-1	C34-4	C25
Cl	#	*	*	*	*	*	*	-	-	-	-	-	-	-	-
K	*	*	*	*	*	*	*	-	-	-	-	-	-	#	#
Mn	*	#	*	*	*	*	*	*	*	-	-	-	*	-	
Fe	#	#	#	#	*	#	*	#	#	#	*	*	#	#	#
Cu	*	#	#	*	#	*	#	*	-	*	-	*	*	-	-
Zn	*	*	*	*	*	*	*	*	*	*	-	-	-	-	-
	C21-cb	MI2-6a	MI2-2a	MI2-3a	C9-1	C21-ab	C134d	C37-a	MI2-1a	C128b	C128c	C127a	C128a	C132c	
Cl			-	-	*			-		-	-	-	-		
K				-	*	*		#	-	-	-	-	-		
Mn	*	-	-		*				-						
Fe	#	#	-	-	#	#	#	#	#	*	*	#	#	*	
Cu	#	*						*	*	#	#	#	#	*	
Zn	*	-			*	*	#	-	*						

APPENDIX 7

$^{40}Ar/^{39}Ar$ Incremental heating data

Biotite S-03

Laser power (Watts)	$^{36}Ar_{(a)}$	$^{37}Ar_{(Ca)}$	$^{38}Ar_{(Cl)}$	$^{39}Ar_{(K)}$	$^{40}Ar_{(r)}$	$^{40}Ar_{(r)}$ (%)	$^{39}Ar_{(K)}$ (%)	K/Ca ± 2σ	Age ± 2σ (Ma)
0.3	0.06277	0.00000	0.00197	0.66904	3.66048	16.48	17.28	0.000 ± 0.000	29.05 ± 2.39
0.5	0.02415	0.00000	0.00186	0.75225	4.88570	40.64	19.43	0.000 ± 0.000	34.43 ± 1.26
0.7	0.01021	0.13920	0.00145	0.45970	3.20875	51.53	11.87	1.420 ± 2.946	36.98 ± 1.04
0.9	0.00654	0.00000	0.00076	0.32375	2.19277	53.14	8.36	0.086 ± 0.000	35.89 ± 1.34
0.11	0.00228	0.11423	0.00040	0.13215	0.89879	57.19	3.41	0.497 ± 1.280	36.04 ± 3.26
0.14	0.01497	0.25379	0.00179	0.70985	4.67663	51.38	18.33	1.203 ± 1.260	34.92 ± 0.83
Fusion	0.01628	0.36533	0.00132	0.82557	5.54032	53.52	21.32	0.972 ± 0.838	35.57 ± 0.74
Σ	0.13721	0.87254	0.00955	3.87232	25.06343				

Age plateau S-03 = 35.55 ± 0.72 Ma

Biotite S-05

Laser power (Watts)	$^{36}Ar_{(a)}$	$^{37}Ar_{(Ca)}$	$^{38}Ar_{(Cl)}$	$^{39}Ar_{(K)}$	$^{40}Ar_{(r)}$	$^{40}Ar_{(r)}$ (%)	$^{39}Ar_{(K)}$ (%)	K/Ca ± 2σ	Age ± 2σ (Ma)
0.3	0.00552	0.00000	0.00035	0.16469	0.98841	37.71	3.45	0.000 ± 0.000	31.84 ± 3.41
0.5	0.00441	0.00000	0.00168	0.46869	3.03083	69.92	9.83	0.000 ± 0.000	34.29 ± 1.10
0.7	0.00192	0.00000	0.00263	1.04929	7.42359	92.88	22.00	0.000 ± 0.000	37.48 ± 0.52
0.9	0.00035	0.00000	0.00141	0.75233	5.45756	98.14	15.77	0.000 ± 0.000	38.42 ± 0.77
0.11	0.00023	0.00000	0.00079	0.37841	2.74041	97.56	7.93	0.000 ± 0.000	38.35 ± 1.20
0.14	0.00027	0.00000	0.00053	0.32326	2.31178	96.71	6.78	0.000 ± 0.000	37.88 ± 1.42
Fusion	0.00091	0.00000	0.00347	1.63268	11.55998	97.70	34.23	0.000 ± 0.000	37.51 ± 0.39
Σ	0.01362	0.00000	0.01086	4.76935	33.51256				

Age plateau S-05 = 37.68 ± 0.40

Biotite S-06

Laser power (Watts)	$^{36}Ar_{(a)}$	$^{37}Ar_{(Ca)}$	$^{38}Ar_{(Cl)}$	$^{39}Ar_{(K)}$	$^{40}Ar_{(r)}$	$^{40}Ar_{(r)}$ (%)	$^{39}Ar_{(K)}$ (%)	K/Ca ± 2σ	Age ± 2σ (Ma)
0.3	0.04574	0.00000	0.00264	0.63467	3.28383	19.54	16.60	0.000 ± 0.000	27.48 ± 2.43
0.5	0.01684	0.00000	0.00102	0.53137	3.49589	41.26	13.90	0.000 ± 0.000	34.88 ± 1.26
0.7	0.00915	0.00000	0.00132	0.58669	4.11629	60.35	15.35	0.000 ± 0.000	37.17 ± 1.03
0.9	0.00674	0.00000	0.00086	0.46703	3.25819	62.05	12.22	0.000 ± 0.000	36.96 ± 1.04
0.11	0.00337	0.00000	0.00022	0.17936	1.23849	55.46	4.69	0.000 ± 0.000	36.59 ± 2.55
0.14	0.00497	0.13040	0.00091	0.36978	2.62771	64.15	9.67	1.219 ± 2.670	37.64 ± 1.34
Fusion	0.01910	0.13243	0.00280	1.05397	7.35499	56.57	27.57	3.422 ± 7.393	36.97 ± 0.73
Σ	0.10592	0.26283	0.00977	3.82288	25.37539				

Age plateau S-06 = 37.08 ± 0.51 Ma

Biotite S-11

Laser power (Watts)	$^{36}Ar_{(a)}$	$^{37}Ar_{(Ca)}$	$^{38}Ar_{(Cl)}$	$^{39}Ar_{(K)}$	$^{40}Ar_{(r)}$	$^{40}Ar_{(r)}$ (%)	$^{39}Ar_{(K)}$ (%)	K/Ca ± 2σ	Age ± 2σ (Ma)
0.3	0.00391	0.18056	0.00073	0.23523	1.39924	54.78	8.47	0.560 ± 0.835	31.56 ± 2.05
0.5	0.00115	0.38408	0.00085	0.52527	3.59748	91.36	18.91	0.588 ± 0.488	36.29 ± 1.05
0.7	0.00076	0.00000	0.00067	0.33917	2.31375	91.19	12.21	0.000 ± 0.000	36.15 ± 1.73
0.9	0.00072	0.20923	0.00065	0.28292	1.90097	89.95	10.19	0.581 ± 0.891	35.61 ± 1.68
0.11	0.00019	0.00000	0.00020	0.28573	2.00535	97.23	10.29	0.000 ± 0.000	37.18 ± 1.82
0.14	0.00005	0.00000	0.00071	0.31076	2.17556	99.27	11.19	0.000 ± 0.000	37.09 ± 1.67
Fusion	0.00019	0.00000	0.00101	0.79863	5.51729	98.96	28.75	0.000 ± 0.000	36.60 ± 0.59
Σ	0.00697	0.77387	0.00482	2.77772	18.90964				

Age plateau S-11 = 36.52 ± 0.48 Ma

Biotite S-16

Laser power (Watts)	$^{36}Ar_{(a)}$	$^{37}Ar_{(Ca)}$	$^{38}Ar_{(Cl)}$	$^{39}Ar_{(K)}$	$^{40}Ar_{(r)}$	$^{40}Ar_{(r)}$ (%)	$^{39}Ar_{(K)}$ (%)	K/Ca ± 2σ	Age ± 2σ (Ma)
0.3	0.00718	0.05257	0.00036	0.14767	0.77867	26.86	1.35	1.208 ± 6.531	28.01 ± 3.75
0.5	0.01155	0.00000	0.00210	0.79596	5.39028	61.23	7.28	0.003 ± 0.000	35.89 ± 0.77
0.7	0.00423	0.24800	0.00390	1.71587	11.82169	90.43	15.69	2.975 ± 3.446	36.51 ± 0.33
0.9	0.00102	0.08450	0.00226	0.91170	6.19494	95.37	8.33	4.640 ± 18.117	36.01 ± 0.57
0.11	0.00047	0.00000	0.00118	0.57558	3.93791	96.56	5.26	0.001 ± 0.000	36.25 ± 0.83
0.14	0.00062	0.10278	0.00128	0.75398	5.13035	96.56	6.89	3.154 ± 9.268	36.06 ± 0.66
Fusion	0.00201	0.49444	0.01187	6.03769	40.86561	98.55	55.20	5.251 ± 2.917	35.87 ± 0.17
Σ	0.02707	0.98230	0.02295	10.93845	74.11945				

Age plateau S-16 = 36.01 ± 0.28 Ma

Biotite S-30

Laser power (Watts)	$^{36}Ar_{(a)}$	$^{37}Ar_{(Ca)}$	$^{38}Ar_{(Cl)}$	$^{39}Ar_{(K)}$	$^{40}Ar_{(r)}$	$^{40}Ar_{(r)}$ (%)	$^{39}Ar_{(K)}$ (%)	K/Ca ± 2σ	Age ± 2σ (Ma)
0.3	0.11942	31.67767	0.00864	1.62172	11.28032	24.22	37.08	0.022 ± 0.003	36.85 ± 2.63
0.5	0.08559	0.00000	0.00361	1.35154	9.03506	26.32	30.90	0.000 ± 0.000	35.43 ± 1.88
0.7	0.00457	0.00000	0.00072	0.22017	1.59249	54.12	5.03	0.000 ± 0.000	38.31 ± 2.46
0.9	0.00399	0.00000	0.00000	0.16034	1.13647	49.10	3.67	0.000 ± 0.000	37.55 ± 3.13
0.11	0.00613	0.00494	0.00070	0.23312	1.64182	47.55	5.33	20.283 ± 1334.625	37.31 ± 2.31
0.14	0.00784	0.05353	0.00069	0.29602	2.01077	46.45	6.77	2.378 ± 12.498	36.00 ± 1.54
Fusion	0.01281	0.00000	0.00177	0.49095	3.16846	45.57	11.22	0.005 ± 0.000	34.22 ± 1.09
Σ	0.24034	31.73614	0.01614	4.37387	29.86539				

Age plateau S-30 = 36.57 ± 0.89 Ma

Biotite S-40

Laser power (Watts)	$^{36}Ar_{(a)}$	$^{37}Ar_{(Ca)}$	$^{38}Ar_{(Cl)}$	$^{39}Ar_{(K)}$	$^{40}Ar_{(r)}$	$^{40}Ar_{(r)}$ (%)	$^{39}Ar_{(K)}$ (%)	K/Ca ± 2σ	Age ± 2σ (Ma)
0.3	0.00382	0.00000	0.00044	0.13690	0.82560	42.23	1.66	0.000 ± 0.000	31.99 ± 3.65
0.5	0.00420	0.05084	0.00208	0.88879	6.01176	82.89	10.80	7.517 ± 40.076	35.85 ± 0.71
0.7	0.00260	0.00000	0.00236	1.12720	7.68339	90.90	13.69	0.000 ± 0.000	36.12 ± 0.59
0.9	0.00030	0.30355	0.00096	0.53042	3.74539	97.68	6.44	0.751 ± 0.706	37.41 ± 0.97
0.11	0.00224	0.04366	0.00249	1.24023	8.70670	92.91	15.07	12.216 ± 96.725	37.19 ± 0.44
0.14	0.00084	0.17855	0.00194	0.76658	5.37868	95.56	9.31	1.846 ± 3.069	37.17 ± 0.60
Fusion	0.00191	0.00000	0.00745	3.54164	24.42302	97.73	43.02	0.005 ± 0.000	36.54 ± 0.23
Σ	0.01591	0.57660	0.01773	8.23176	56.77455				

Age plateau S-40 = 36.64 ± 0.40 Ma

$^{36}Ar_{(a)}$ = atmospheric component in ^{36}Ar
$^{37}Ar_{(Ca)}$ = calcium derived ^{37}Ar
$^{38}Ar_{(Cl)}$ = chlorine-derived component in ^{38}Ar
$^{39}Ar_{(K)}$ = potassium-derived component in ^{39}Ar
$^{40}Ar_{(r)}$ = sum of radiogenic and atmospheric components in ^{40}Ar
$^{40}Ar_{(r)}$ (%) = percentage radiogenic component in ^{40}Ar
$^{39}Ar_{(K)}$ (%) = increment size expressed as the percentage of $^{39}Ar_K$ compared to the total amount of $^{39}Ar_K$ released during the experiment
K/Ca = molar K/Ca ratio
J value = 0.002967

APPENDIX 8

^{40}Ar/^{39}Ar Spot fussion data

Biotite S-05

	$^{36}Ar_{(a)}$	$^{37}Ar_{(Ca)}$	$^{38}Ar_{(Cl)}$	$^{39}Ar_{(K)}$	$^{40}Ar_{(r)}$	$^{40}Ar_{(r)}$ (%)	$^{39}Ar_{(K)}$ (%)	K/Ca ± 2σ	Age ± 2σ (Ma)
C	0.00076	1.18391	0.00015	0.00573	0.19103	46.12	2.77	0.002 ± 0.054	36.85 ± 2.63
G	0.00351	0.10826	0.00008	0.00358	0.10115	8.89	1.73	0.014 ± 0.000	35.43 ± 1.88
J	0.00012	1.17654	0.00016	0.02642	0.62480	94.53	12.77	0.010 ± 0.670	38.31 ± 2.46
L	0.00202	1.23285	0.00012	0.01470	0.39218	39.64	7.10	0.005 ± 0.560	37.55 ± 3.13
O	0.00032	0.00000	0.00007	0.02795	0.56062	85.70	13.51	0.000 ± 0.437	37.31 ± 2.31
S	0.00155	0.00000	0.00025	0.08904	1.73599	79.16	43.04	0.000 ± 0.000	36.00 ± 1.54
V	0.01048	0.00000	0.00004	0.03275	0.54072	14.86	15.83	0.000 ± 0.000	34.22 ± 1.09
Y	0.00114	0.00000	0.00001	0.00671	0.12242	26.57	3.24	0.000 ± 0.000	
Σ	0.01989	3.70156	0.00089	0.20689	4.26890				

Biotite S-30

Spot	$^{36}Ar_{(a)}$	$^{37}Ar_{(Ca)}$	$^{38}Ar_{(Cl)}$	$^{39}Ar_{(K)}$	$^{40}Ar_{(r)}$	$^{40}Ar_{(r)}$ (%)	$^{39}Ar_{(K)}$ (%)	K/Ca ± 2σ	Age ± 2σ (Ma)
F	0.00571	0.00000	0.00000	0.02877	0.42369	20.08	10.43	0.000 ± 0.000	26.21 ± 0.58
G	0.00451	0.00000	0.00000	0.02373	0.32630	19.65	8.60	0.000 ± 0.000	24.49 ± 2.84
I	0.00186	0.44578	0.00004	0.00809	0.14215	20.59	2.93	0.008 ± 0.018	31.22 ± 19.71
J	0.01098	0.48445	0.00019	0.06512	1.17378	26.56	23.60	0.058 ± 0.149	32.04 ± 3.12
L	0.03124	0.59516	0.00010	0.08309	1.40067	13.17	30.11	0.060 ± 0.275	29.98 ± 5.21
Q	0.00816	0.29281	0.00011	0.01324	0.28264	10.48	4.80	0.019 ± 0.061	37.84 ± 11.13
R	0.00756	0.00000	0.00006	0.01953	0.38204	14.60	7.08	0.000 ± 0.000	34.74 ± 3.63
T	0.00500	0.10543	0.00015	0.01670	0.30788	17.23	6.05	0.068 ± 0.687	32.75 ± 9.92
U	0.00133	0.00000	0.00005	0.00650	0.14106	26.46	2.36	0.000 ± 0.000	38.50 ± 8.91
W	0.00294	0.00000	0.00000	0.01117	0.19503	18.34	4.05	0.000 ± 0.000	31.05 ± 4.10
Σ	0.07929	1.92363	0.00071	0.27596	4.77505				

$^{36}Ar_{(a)}$ = atmospheric component in ^{36}Ar
$^{37}Ar_{(Ca)}$ = calcium derived ^{37}Ar
$^{38}Ar_{(Cl)}$ = chlorine-derived component in ^{38}Ar
$^{39}Ar_{(K)}$ = potassium-derived component in ^{39}Ar
$^{40}Ar_{(r)}$ = sum of radiogenic and atmospheric components in ^{40}Ar
$^{40}Ar_{(r)}$ (%) = percentage radiogenic component in ^{40}Ar
$^{39}Ar_{(K)}$ (%) = increment size expressed as the percentage of $^{39}Ar_K$ compared to the total amount of $^{39}Ar_K$ released during the experiment
K/Ca = molar K/Ca ratio
J value = 0.002967

References

Ahmad S. N., and Rose A., 1980, Fluid inclusions in Porphyry and Skarn ore at Santa Rita, New Mexico: *Economic Geology*, v. 75, p. 229-250.

Alpers, H. C., and Brimhall, G. H., 1988, Middle Miocene climatic change in the Atacama Desert, northern Chile: Evidences from supergene mineralization at La Escondida: *Geological Society of America Bulletin*, v 100, p. 1640-1656.

Anderson, A. J., Clark, A. H., Xin-Pei, M., Palmer, G. R., MacArthur, J. D., and Roedder E., 1989, Proton-induced X-ray and gamma-ray emission analysis of unopened fluid inclusions: *Economic Geology*, v. 84, p. 924-939.

Andriesssen, P. A. M., and Reuter, K. J., 1994, K-Ar and fission track mineral age determinations of igneous rocks related to multiple magmatic arc systems along the 23°S latitude of Chile and NW Argentina: *Tectonics of the southern central Andes.* Reuter, J. K., Scheuber, E., and Wigges, P. J., editors, p. 141-153, Springer Verlag.

Audétat, A., and Günther, D., 1999, Mobility and H_2O loss from fluid inclusions in natural quartz crystals: *Contributions to Mineralogy and Petrology*, v. 137, p. 1-14.

Audédat, A., Günter, D., and Heinrich, C. A., 2000, Magmatic-hydrothermal evolution in a fractionating granite: A microchemical study of the Sn-W-F-mineralized Mole granite (Australia): *Geochimica et Cosmochimica Acta*, v. 64, No. 19., p. 3373-3393.

Beane R. E., and Titley S. R., 1981, Porphyry Copper Deposits, Part II: Hydrothermal Alteration and Mineralization: *Economic Geology*, 75th Anniversary Issue, p. 214-269.

Bean, R. E., and Bodnar, R, J., 1995, Hydrothermal fluids and hydrothermal alteration in porphyry copper deposits: *in* Pierce, F. W. and Bohm, J. G., Porphyry copper deposits of the American Cordillera: Tucson, AZ, Arizona Geological Society Digest, v, 20p. 83-93.

Bin, F., 2002, Fluid regime during high- and ultrahigh-pressure metamorphism in the Dabie-Sulu terranes, Eastern China: A stable-isotope and fluid-inclusion study: *PhD thesis Vrije Universiteit Amsterdam*, p. 164.

Breirkreutz, C., Bahlburg, H., and Zeil, W., 1988, The Paleozoic evolution of northern Chile: Geotectonic implications, *in* Bahlburg, H., et al., eds. The Southern Central Andes: Lecture notes in earth sciences, Number 7: *Heidelberg, Germany, Springer-Verlag*, p. 87-102.

Bodnar, R. J., and Bean, R. E., 1980, Temporal and spatial variations in hydrothermal fluid characteristics during vein filling in preore cover overlying deeply buried Porphyry Copper-type mineralization at Red Mountain, Arizona: *Economic Geology*, v. 75, p. 876-893.

Bodnar, R., 1993, Revised equation and table for determining the freezing point depression of H_2O-NaCl solutions: *Geochimica et Cosmochimica Acta*, v. 57, p. 683-684.

Bodnar, R., and Vityk, M. O., 1994, Interpretation of microthermometric data for H_2O fluid inclusions, *in* De Vivo, B., and Frezzotti, M. L., eds. *Fluid inclusions in minerals: Methods and applications*: Blacksburg, VA, Virginia Polytechnic Institute and State University, p. 117-130.

Campos, E., Touret, J. L. R., Nikogosian, I., and Delgado, J., 2001, Overheated, Cu-bearing magmas in the Zaldívar porphyry-Cu deposit, Northern Chile. Geodynamic consequences: *Tectonophysics*, v. 345, p. 229-251

Cathles, L. M., 1977, An analysis of the cooling of intrusives by ground-water convection which includes boiling: *Economic Geology*, v. 72, p. 804-826.

Candela, P. A., and Holland, H. D., 1984, The partitioning of copper and molybdenum between silicate melts and aqueous fluids: *Geochimica and Cosmochimica Acta*, v. 48, p. 373-380.

Clark, A. H., Archibald, D. A., Lee, A. W., Farrar, E., and Hodgson, C. J., 1998, Laser probe ^{40}Ar/^{39}Ar ages of early- and late-stage alteration assemblage, Rosario porphyry copper-molybdenum deposit, Collahuasi District, I Region, Chile: *Economic Geology*, v. 93, p. 326-337.

Cline, J. S., and Bodnar R. J., 1991, Can economic porphyry copper mineralization be generated by a typical calc-alkaline melt?: *Journal of Geophysical Research*, v. 96, N° B5, p. 8113-8126.

Cline, J. S., 1995, Genesis of porphyry copper deposits: the behavior of water, chloride, and copper in crystallizing melts: *Arizona Geological Society Digest*, v. 20, p. 69-82.

Coira, B., Davison, J., Mpodozis, C., Ramos, V., 1982, Tectonic and magmatic evolution of the Andes of northern Argentina and Chile: *Earth Sciences Reviews*, Linares, E., Cordani, U. G., and Munizaga, F., eds., v. 18, N 3-4, p. 303-332.

Cornejo, P., Tosdal, R. M., Mpodozis, C., Tomlinson, A. J., Rivera, O., and Fanning C. M., 1997, El Salvador, Chile porphyry copper deposit revisited: Geologic and geochronology framework: *International Geology Review*, v. 39, p. 22-54.

De Bruijne, C. H., 2001, Denudation, intraplate tectonics and far field effects; and integrated apatite fission track study in central Spain: *PhD thesis Vrije Universiteit Amsterdam*, p. 164.

Damman, A. H., Kars S. M., Touret J. R. L., Fieffe E. C., Kramer J. A. L. M., Vis R. D., and Pintea I., 1996, PIXE and SEM analysis of fluid inclusions in quartz crystals from the K-alteration zone of the Rosia Poieni porphyry-Cu deposit, Apuseni Mountains, Rumania: *European Journal of Mineralogy*, v. 8, p. 1081-1096.

Davidson, J. P., Harmon, R. S., and Wörner, G., 1991, The source of central Andean magmas; some considerations: *in* Harmon, R. S., and Rapela, C. W., eds., Andean magmatism and its tectonic setting: *Boulder, Colorado, Geological Society of America, Special Paper 265*, p. 233-243

Deer, W. A., Howie, R. A., and Zussman, J., 2001, Rock-forming minerals: framework silicates: Second edition, volume 4A. Geological Society London., p. 972.

Dickin, A. P., 1997, Radiogenic isotope geology: *Cambridge University Press*, Cambridge, p. 452.

Eastoe, C. J., 1978, A fluid inclusion study of Panguna porphyry copper deposit, Bougainville, Papua New Guinea: *Economic Geology*, v. 73, p. 721-748.

Eastoe, C. J., and Eadington, P. J., 1986, High-temperature fluid inclusions and the role of the biotite granodiorite in mineralization at the Panguna porphyry copper deposit, Bougainville, Papua New Guinea: *Economic Geology*, v. 81, p. 478-483.

Einaudi, M. T., Moore, W. J., and Wilson, J. C., eds. 1978, An issue devoted to the Bingham mining district: *Economic Geology Special Issue*, v. 73, p. 1215-1365.

Einaudi, M. T., 1997. Porphyry copper and epithermal systems. *Short course. Instituto de Geología Económica Aplicada. Universidad de Concepcion*. Chile.

Espinoza, S., Véliz, H., Esquivel, J., Arias, J., and Moraga, A., 1996, The cupriferous province of the Coastal Range, Northern Chile: *In* "Andean copper deposits: new discoveries, mineralization, styles and metallogeny": Soc. Econ. Geologist Special Publication No. 5, Camus, F., Sillitoe, R. H., and Petersen, R., eds., p. 19-32.

Fleischer, R. L., Price, P. B., and Walker, R. M., 1965, Tracks of charged particles in solids. *Science*, v. 149, p. 383-393.

Flint, S., Turner, P., Jolley, E. J., and Hartley, A. J., 1993, Extensional tectonics in convergence margin basins: An example from the Salar de Atacama, Chilean Andes: *Geological Society of America Bul.*, v. 105, p. 603-617.

Fonarev, V. I., Touret, J. L. R., and Kotelnikova, Z. A., 1998, Fluid inclusions in rocks from the Central Kola granulite area (Baltic Shield): *European Journal of Mineralogy*, v. 10, p. 1181-1200.

Fournier, R. O., 1967, The porphyry copper deposit exposed in the Liberty open-pit mine near Ely, Nevada. Part II. The formation of hydrothermal alteration zones: *Economic Geology*, v. 62, p. 207-227.

Fournier, R. O., 1999, Hydrothermal processes related to movement of fluid from plastic into brittle rock in the magmatic-epithermal environment: *Economic Geology*., v. 94, p. 1193-1211.

Frei, R., 1996, Sulfur in bulk rock and igneous apatite; tracing mineralized and barren trends in intrusions: *Schweizerische Mineralogische und Petrographische Mitteilungen*, v. 76, p. 57-73.

Fu, B., 2002, Fluid regime during high- and ultrahigh-pressure metamorphism in the Dabie-Sulu terranes, Eastern China: A stable-isotope and fluid-inclusion study: *PhD thesis Vrije Universiteit Amsterdam*, p. 164.

Galbraith, R. F., 1990, The radial plot: Graphical assessment of spread in ages: *Nucl. Tracks Radiat. Meas*., v, 17, p. 207-214.

Gallagher, K., Brown, R., and Johnson, C., 1998, Fission track analysis and its application to geological problems. *Annu. Rev. Earth Planet. Sci*., v. 26, p. 519-572.

Goldstein, R. H., and Reynolds, T. J., 1994, Systematics of fluid inclusions in diagenetic minerals: Society for Sedimentary Geology Short Course 31, p, 199.

Gustafson, L. B., and Hunt, J. P., 1975, The porphyry copper deposits at El Salvador, Chile: *Economic Geology*, v. 70, p. 857-912.

Gustafson L. B., 1978, Some Major Factors of Porphyry Coppers Genesis: *Economic Geology*, v. 73, p. 600-607.

Gustafson, L. B., and Titley, S. R., 1978, eds., Porphyry copper deposits of the southwestern Pacific Islands and Australia: *Economic Geology Special Issue*, v. 73, p. 597-986.

Halter, W. E., Pettke, T., Heinrich, C. A., and Rothen-Rutishauser, B., 2002, Major to trace element analysis of melt inclusions by laser-ablation ICP-MS: methods of quantification: *Chemical Geology*, v. 183, p. 63-86.

Harrison, T. M., Duncan, I., and McDougall, I., 1985, Diffusion of ^{40}Ar in biotite: Temperature, pressure and compositional effects: *Geochimica et Cosmochimica Acta*, v. 49, p. 2461-2468.

Hedenquist, J. W., and Lowenstern, J. B., 1994, The role of magmas in the formation of hydrothermal ore deposits: *Nature*, v. 370, p. 519-527.

Heinrich, C. A., Gunther, D., Audétat, A., Ulrich, T., and Frischknecht, R., 1999, Metal fractionation between magmatic brine and vapor, determined by microanalysis of fluid inclusions: *Geology*, v. 27; N. 8; p. 755-758.

Heinrich, C. A., Ryan G. C., Mernagh, T. P., and Eadington, P. J., 1992, Segregation of ore metals between magmatic brine and vapor: A fluid inclusion study using PIXE microanalysis: *Economic Geology,* v. 87, p. 1566-1583.

Henley, R. W., and McNabb, A., 1978, Magmatic vapor plumes and ground-water interaction in Porphyry Copper emplacement: *Economic Geology*, v. 59, p. 538-569.

Hildreth, W., and Moorbath, S., 1988, Crustal contribution to arc magmatism in the Andes of Central Chile: *Contributions to Mineralogy and Petrology*, v. 98, p. 455-489.

Hurford , A. J., and Green, 1983, The Zeta age calibration of fission-track dating: *Isotope Geoscience*, v. 1, p. 285-317.

Kay, S. M., Ramos, V. A., Mpodozis, C., and Suroga, P., 1989, Late Paleozoic to Jurassic silicic magmatism at the Gondwana margin: Analogy to the middle Proterozoic in North America: Geology, v. 17, p. 324-328.

Kay, S. M., Mpodozis, C., and Coira, B., 1999, Neogene magmatism, tectonism, and mineral deposits of the Central Andes (23° to 33° S Latitude): *in* Skinner, B. J. (ed.) Geology and ore deposits of the Central Andes. *Society of Economic Geology special publication,* N 7, p, 27-59.

Kilinc, I. A., and Burnham C. W., 1972, Partitioning of chloride between a silicate melt and coexisting aqueous phase from 2 to 8 kilobars: *Economic Geology*, v. 67, p. 231-235.

Kirstein, L. A., Hawkesworth, C. J., and Garland, F. G., 2001, Felsic lavas or rheomorphic ignimbrites: is there a chemical distinction?: *Contribution to Mineralogy and Petrology*, v. 142, p. 309-322.

Koppers, A. A. P., 1998, ^{40}Ar/^{39}Ar Geochronology and isotope geochemistry of the West Pacific seamounts province: *PhD thesis Vrije Universiteit Amsterdam*, p. 262.

Kamenetsky, V. S., Wolfe, R. C., Eggins, S. M., Mernagh, T. P and Bastrakov, E., 1999, Volatile exsolution at the Dinkidi Cu- porphyry deposit, Philippines: A melt-inclusion record of the initial ore-forming process: *Geology*, v. 27, p. 691-694.

Le Bas, M. J., Le Maitre, R. W., and Wooley, A. R., 1992, The construction of the total alkali-silica chemical classification of volcanic rocks: *Mineralogy and Petrology*, v. 46, p. 1-44.

Le Maitre, R. W., Bateman, P., Dudek, A., Kller, J., Lameyre, J., Le Bas M. J., Sabine P. A., Schmid, R., Sorensen, H., Streckeisen, A., Wolley, A. R., and Zanettin, B., 1989, A classification of igneous rocks and glossary of terms. *Blackwell, Oxford*, p. 193.

Lowell, J. D., and Guilbert, J. M., 1970, Lateral and vertical alteration-mineralization zoning in porphyry ore deposits: *Economic Geology*, v. 65, p. 373-408.

Lowenstern, J., 1995, Application of silicate melt inclusions to the study of magmatic volatiles, *In* Thompson, J.F.H., ed, Magmas, fluids and ore deposits: *Mineralogical Association of Canada Short Course*, v. 23, p. 71-99.

MacLean, W. H., and Hoy, L., 1991, Geochemistry of hydrothermally altered rocks at the Horne mine, Noranda, Quebec: *Economic Geology*, v. 86, pp. 506-528.

Maksaev, V., Gardeweg, M., Ramirez, C. F., and Zentilli, M., 1988, Aplicación del método trazas de fision (fission track) a la datación de cuerpos de magnetita de el Laco e Incahuasi en el Altiplano de la Región de Antofagasta: *V Congreso Geológico Chileno*, v. 1, p. B1-B23.

Maksaev, V., and Zentilli, M., 1999, Fission track thermochronology of the Domeyko Cordillera, Chile: Metallogenetic implications for Andean porphyry copper metallogenesis. *Exploration and Mining Geology, Special Issue on Latin American Mineral Deposits*, v. 8, No. 1 & 2, pp. 65-89.

Marinovic, N., Smoje, I., Maksaev, V., Herve, M., and Mpodozis, C., 1995, Hoja Aguas Blancas, Region de Antofagasta: *Servicio Nacional de Geologia y Mineria*, Carta Geologica de Chile, v. 70, p 150.

Maturana, M., and Zaric, N., 1991, Geología y mineralización del yacimiento tipo pórfido cuprífero Zaldívar, en los Andes del Norte de Chile: *Revista Geológica de Chile*, v. 18, p. 109-120.

Mpodozis, C., and Kay, S. M., 1992, Late Paleozoic to Triassic evolution of the Gondwana margin: Evidence from Chilean frontal cordillera batholiths (28°S-32°S): *Geological Society of America Bulletin*, v. 104, p. 999-1014.

Moore, W. J., and Nash, J. T., 1974, Alteration and fluid inclusion studies of the Porphyry Copper ore body at Bingham, Utah: *Economic Geology*, v. 69, p. 631-645.

Nash, J. T., and Theodore, T. G., 1971, Ore fluids in the Porphyry Copper Deposit at Copper Canyon, Nevada: *Economic Geology*., v. 66, p. 385-399.

Nash, J. T., 1976, Fluid inclusions petrology - data from porphyry copper deposits and application to exploration: *U.S. Geological Survey Professional Paper* 907-D, p. 16.

Norton, D., 1978, Sourcelines, sourceregions, and pathlines for fluids in hydrothermal systems related to cooling plutons: *Economic Geology*, v. 73, p. 21-28.

Norton, D., and Knight, J. E., 1977, Transport phenomena in hydrothermal systems - cooling plutons: *American Journal of Sciences*, v. 277, p. 937-981.

Oyarzun, J., and Frutos, J., 1980, Metallogenesis and porphyry deposits of the Andes (southeastern Pacific region): *in* Mineral resources. *Bur Rech Geol Min Mem*, v, 106, p. 50-62.

Peccerillo, R., and Taylor, S. R., 1976, Geochemistry of Eocene calc-alkaline volcanic rocks from the Kastamonu area, northern Turkey: *Contribution to mineral petrology*, v. 58, p. 63-81.

Pichavant, M., Ramboz, C., and Weisbrod, A., 1982, Fluid immiscibility in natural processes: use and misuse of fluid inclusion data. I. Phase equilibria analysis - a theoretical and geometrical approach: *Chemical Geology*, v. 37, p. 1-27.

Pintea, I., 1993, Microthermometry of the hydrosaline melt inclusions from copper-porphyry ore deposits (Apuseni Mountains, Rumania). *Archiwum Mineralogiczne*., v. XLIX, p. 165-167. Warsaw, Poland.

Pintea, I., 1995, Fluid inclusions evidence for magmatic immiscibility between hydrous salt melt and silicate melt as a primary source of ore metals in porphyry-copper systems from Apuseni Mountains, Rumania: *Boletín de la Sociedad Española de Mineralogía*, v. 18-1, p. 184-186.

Potter, R. W. II, Clynne, M. A. and Brown, D. L., 1978, Freezing point depression of aqueous sodium chloride solutions: *Economic Geology*, v. 73, p. 284-285.

Quan, R. A., Cloke, P. L., and Kesler, S. E., 1987, Chemical analyses of halite trend inclusions from the Granisle porphyry copper deposit, British Columbia: *Economic Geology*, v. 82, p. 1912-1930.

Rayn, C. G., Cousens, D. R., Heinrich, C. A., Griffin, W. L., Sie, S. H. and Mernagh, T. P., 1991, Quantitative PIXE Microanalysis of fluid inclusions based on a layer yield model: *Nuclear Instruments Methods*. B, v. 54, p. 292-297

Richards, J. P., Noble, S. R., and Pringle, M., 1999, A revised late Eocene age for porphyry copper magmatism in the Escondida Area, Northern Chile: *Economic Geology*, v. 94, p. 1231-1248.

Reynolds, P., Ravenhurst, C., Zentilli, M., and Linsay, D., 1997, High precision ^{40}Ar/^{39}Ar dating of two consecutive hydrothermal events in the Chuquicamata porphyry copper system, Chile: *Geological Association of Canada-Mineralogical Association of Canada*, Program with abstracts, v. 22, p. A-125.

Roedder, E., 1967, Metastable superheated ice in liquid-water inclusions under high negative pressure: *Sciences*, v. 155, p. 1413-1417.

Roedder, E., 1971, Fluid inclusion studies on the Porphyry-type ore deposits at Bingham, Utah, Butte, Montana, and Climax, Colorado: *Economic Geology*, v. 66, p. 98-120.

Roedder, E., 1984, Fluid Inclusions: *Reviews in Mineralogy*, v. 12, p.1-644.

Roedder, E., 1992, Fluid inclusion evidence for immiscibility in magmatic differentiation: *Geochimica et Cosmochimica* Acta, vol. 56, p. 5-20.

Rollinson, H., 1993, Using geochemical data: Evaluation, presentation, interpretation: *Longman, Essex*, p. 352.

Rose, A. W., 1970, Zonal relations of wallrock alteration and sulfide distribution in porphyry copper deposits: *Economic Geology*, v. 65, p. 920-936.

Sanders, C. A. E., 1998, Tectonics and erosion; competitive forces in a compressive orogen. A fission track study of the Romanian Carpathians: *PhD thesis, Vrije Universiteit Amsterdam*, p. 204.

Sawkins F. J., 1984, Metal Deposits in Relation to Plate Tectonics. *Berlin, Springer-Verlag.*

Schiffries, C. M., 1990, Liquid- absent aqueous fluid inclusions and phase equilibria in the system $CaCl_2$-NaCl-H_2O: *Geochimica et Cosmochimica Acta*, v. 54, p. 611-619.

Shepherd, T. J., Rankin, A. H., and Alderton D. H. M., 1985, A practical guide to fluid inclusions studies. *Blackie*, p. 239.

Sillitoe, R. H., 1972, A plate tectonic model for the origin of porphyry copper deposits: *Economic Geology*, v. 67, p. 184-197.

Sillitoe, R. H., 1973, The Tops and Bottoms of Porphyry Copper Deposits: *Economic Geology*, v. 68, p. 799-815.

Sillitoe R. H., 1986, Metallogenic Implications. Geology and Metallogeny of Copper Deposits: G. H. Friederich et al., editors. *Springer-Verlag,* p. 235-250.

Sillitoe, R. H., 1988, Epochs of intrusion-related copper mineralization in the Andes: *Journal of South American Earth Sciences*, v. 1, p. 89-108.

Sobolev, A.V., Barkusov, V. L., Nevsorov, V. N., and Slutsky, A. B., 1980, The formation conditions of the high-magnesian olivines from the monomineralic fraction of Luna 24 regolith., *Proceedings of the 11th Lunar Science Conference*, p. 105-116.

Sobolev, A. V., 1996, Melt inclusions in minerals as a source of principal petrological information: *Petrology*., v. 4, p. 209-220.

Sobolev, A. V., and Danyushevsky L. V., 1994, Petrology and geochemistry of boninites from the north termination of the Tonga Trench: constraints on the generation conditions of primary high-Ca boninite magmas: *Journal of Petrology*, v. 35, p.1183-1213.

Sourirajan, S., and Kennedy, G. C., 1962, The system H_2O-NaCl at elevated temperatures and pressures: *American Journal of Science*, v. 260, p. 115-141.

Spear, F. S., 1993, Metamorphic Phase Equilibria and Pressure-Temperature-Time paths: *Mineralogical Society of America*, Monograph. 800 p.

Tagami, T., Carter, A., and Hurford, A. J., 1996, Natural long-term annealing of zircon fission-track system in the Vienna Basin deep borehole samples: constrains upon partial annealing zone and closure temperature: *Chemical Geology*, v. 130, p. 147-157.

Titley, S. R. and Hicks, C. J., 1966, Geology of the porphyry coppers deposits, southwestern North America: *Tucson, University of Arizona Press*, 287 p.

Titley, S. R., and Bean, R. E., 1981, Porphyry Copper Deposits. Part I: Geologic settings, petrology, and tectonogenesis: *Economic Geology*. 75 th Anniversary, p. 214-249.

Thomas, R., Rhede, D., and Trumbull, R. B., 1996, Microthermometry of volatile-rich silicate melt inclusions in granitic rocks: *Zeitschrift fur Geologische Wissenchaften*, v. 24, p. 507-528.

Touret, J. L. R., and Frezzotti, M. L., 1993, Magmatic remnants in plutonic rocks: *Bull. Soc. Geol.* France, v. 164, p. 229-242.

Touret, J. L. R., and Marquis, G., 1994, Fluides profonds et conductivité électrique de la croûte continentale inferieur: Académie des Sciences Paris. t. 318, série II, p. 1469- 1482.

Touret, J. L. R. and Huizenga J. M., 1999, Precambrian intraplate magmatism: high temperature, low pressure crustal granulite: *Journal of African Earth Sciences*, v. 28, p. 367-385.

Tuttle, O. F., and Bowen, N. L., 1958, Origin of granite in the light of experimental studies in the system $NaAlSi_3O_8$-$KalSi_3O_8$-SiO_2-H_2O: *Geological Society of America*, Memoir 74, p. 153.

Ulrich, T., Günter, D., and Heinrich, C. A., 2001, The evolution of a porphyry Cu-Au deposit, based on La-ICP-MS analysis of fluid inclusions: Bajo de la Alumbrera, Argentina: *Economic Geology*, v. 96, p. 1743-1774.

Vanko, D. A., Sutton, S. R., Rivers, M. L., and Bodnar, R. J., 1993, Major-element ratios in synthetic fluid inclusions by synchrotron X-ray fluorescence microprobe: *Chemical Geology*, v. 109, p.125-134.

Vis, R. D., Kramer, J. L. A. M., Tros, G. H. J., van Langevelde, F., and Mars, L., 1993, The upgraded Amsterdam nuclear microprobe: *Nucl. Instr. Meth*, v. B77, p. 41-44.

van Soest, M. C., 2000, Sediment subduction and crustal contamination in the Lesser Antilles Island Arc. The geochemical and isotopic imprints on recent lavas and geothermal fluids. *PhD thesis, Vrije Universiteit Amsterdam*, p. 287.

Wagner, G. A., and Van den Haute, P., 1992, Fission-track dating: Kluwer, Dordrecht, p. 285

Wijbrans, J. R., Pringle, M. S., Koppers, A. A. P., and Scheveers, R., 1995, Argon geochronology of small samples using the Vulkaan argon laserprobe. Proceedings Koninklijke Nederlandse, v. 98, p. 185-218.

Wilson, W. J., Kesler, S. E., Cloke, P. L., and Kelly, W., 1980, Fluid Inclusion Geochemistry of the Granisle and Bell porphyry copper deposits, British Columbia: *Economic Geology*, v. 75, p 45-61.

Wilson, M., 1989, Igneous Petrogenesis: *Chapman and Hall*, p. 466.

Yang, K., and Bodnar, D., 1994, Magmatic-hydrothermal evolution in the "Bottoms" of Porphyry Copper Systems: Evidence from silicate melt and aqueous fluid inclusions in granitoid intrusions in the Gyeongsang Basin, South Korea: *International Geology Review*., v. 36, p. 608-628

Zen, E-an., 1986, Aluminum enrichment in silicate melts by fractional crystallization: some mineralogic and petrographic constrains: *Journal of Petrology*, v. 27, p.1095-1117.